

https://dspace.org/

Structure of the fada-gourma shear zone Eastern Burkina Faso

Sehloho, Pulane Relebohile

2018

https://hdl.handle.net/10539/26175

Sehlobo, Pulane Relebohile (2018) Structure of the Fada-Gourma Shear Zone, Eastern Burkina Faso, University of the Witwatersrand, Johannesburg, <http://hdl.handle.net/10539/26175>

Downloaded from a DSpace repository. https://dspace.org/

STRUCTURE OF THE FADA-GOURMA SHEAR ZONE, EASTERN BURKINA FASO

A Dissertation submitted to the Faculty of Science, University of Witwatersrand in the fulfilment of the requirements for the degree of Master of Science

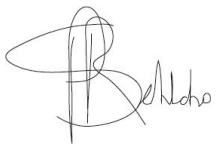
Pulane Relebohile Sehloho
Person Number: 417621

2018



Declaration

I declare that this Dissertation is my own, unaided work. It is being submitted for the Degree of Master of Science at the University of Witwatersrand, Johannesburg. It has not been submitted before for any degree or examination at any other University.



Pulane Relebohile Sehloho

04 June 2018

Date

Abstract

The Baoulé-Mossi Domain in eastern Burkina Faso is a greenstone belt-granitoid terrane, formed in a volcanic arc tectonic environment. Volcanism and magmatism were coeval at around 2239 Ma, and this formed the basement rocks of the Fada-Gourma Shear Zone (FGSZ) region. Crosscutting relations observed in the field, aided by zircon U-Pb age data reveal that pluton emplacement continued to post-2167±12 Ma. The youngest units are NW-trending dolerite dykes, dated at 1814±26 Ma in eastern Burkina Faso.

The study area has five defined deformation events. D1 is responsible for the remnant NW-trending S1 foliation in some of the granite gneisses and the foliated and gneissic granodiorites outside of the shear zones. The σ1 principal compressive stress orientation was NE-SW. The metamorphic grade associated with D1 is amphibolite facies. D2 had a NW-SE oriented compressive stress direction, and this resulted in thrust faulting and the NE-trending dominant structural grain in the study area. The associated metamorphic grade for D2 is lower amphibolite facies.

D3 involved a dextral-reverse slip along faults with a NE trend, with southeast-block-up displacement. The principal compressive stress axis was ENE-WSW to ESE-WNW directed. Metamorphic grade associated with D3 is greenschist facies to lower amphibolite facies.

D4 caused the sinistral reactivation of the NE-trending D3 structures. The sinistral shear overprint the dextral displacement and a sigmoidal foliation related to D4 is discernible on the aeromagnetic imagery data. The principal compressive stress axis during D4 was NNE-SSW to N-S oriented. The metamorphic grade during D4 was greenschist facies.

D5 is a late-stage brittle deformation that led the formation of NW-trending extensional fracture cleavage planes.

The imagery data was integrated with field data to aid in establishing the orientation of foliations, and the kinematic and geometric information at map scale and at outcrop scale. Petrographic descriptions provided information at a micro-scale where available.

The study area is host to gold mineralization, and there is a network of active artisanal mines in the northern domains of the study area. Tambiga Hill is one of the larger actively mined quartz stockwork vein deposits in the Gourma region. Gold

mineralization is concomitant with quartz veins, and is hosted either adjacent to the quartz veins, or within the veins. Gold is either invisible, or occurs as nuggets. Pyrite, tourmaline, ankerite and minor malachite are also present as accessory minerals within the quartz veins. Gold mineralization is associated with the late stages of D2, and D3.

Acknowledgements

I would like to thank Dr. Asinne Tshibubudze for supervising this project, for the guidance and invaluable insight. Thank you to Prof. Kim A. A. Hein for the support.

Thank you to my bursar, JB Marks Education Trust Fund. Thank you to WAXI (West African Exploration Initiative), the AMIRA and its sponsors for the funding that made this research project possible.

Thank you to Gryphon Minerals Limited and Teranga Gold Corporation for funding field work, transportation and hosting in Ouagadougou for the April 2016 field work phase. Thank you to Wilfred Da and Bilem Souleymane for all the help and guidance in the field, and to our trusted driver Alex Djiguemde. Thank you to our campsite cook, Francis Nikiema, his assistant, and the campsite security. To Elliot Grant from Gryphon Minerals, thank you for allowing us to be hosted at the camp site, for making sure we had all that we needed for a successful field work phase. Thank you to Artue from Ludovic Auto Location Vehicle Rental Company, who was our driver for the 2017 field work phase.

I would like to thank Joe Aphane from the Earth Lab at the University of the Witwatersrand for the help with the sample preparation and mineral separation for geochronology analysis. Thank you to Marlin Patchappa for carrying out the XRF analyses. Thank you to Caiphus Majola and Samuel Tshabalala for preparing the zircon mount and for the petrography thin sections.

Thank you to the staff at University of Johannesburg, in the LA-ICP-MS facilities lab for their help with geochronology analysis; Henriette Ueckerman and Marlina Elburg.

I acknowledge Tom Anderson from the University of Oslo (Geology Department) for the NuAge 2 Excel software used to process raw data for the LA results.

Table of Contents

Declaration……. *i*
Abstract……...…….....…… *ii*
Acknowledgements……. *iv*
Table of Contents…….. *v*
List of Figures…….…….…..*ix*
List of Tables……..……..*xxiv*

CHAPTER 1: Introduction....1
1.1 Preamble....1
1.2 Location and Physiography of the Study Area....3
1.3 Aims and Objectives....4
1.4 Thesis Organization....5
1.5 Abbreviations Used In This Dissertation....6
CHAPTER 2: Overview of the Geology of the WAC and Regional Geology of the Fada-Gourma Region....8
2.1 Lithostratigraphy....8
2.2 Structure....12
2.3 Metamorphism....15
2.4 Metallogenesis....16
CHAPTER 3: Methodology....20
3.1 Desktop Analysis....20
3.1.1 Geophysical Data....20
3.1.2 Google Earth, Landsat and ASTER Imagery Data....25
3.2 Field Work and Data Interpretation....28
3.3 Analytical Work....30
3.3.1 Thin Sections....30
3.3.2 Geochemical Analysis....30
3.3.3 Geochronology....31
CHAPTER 4: Lithologies Proximal to the FGSZ, and the Petrography and Geochemical Analysis on Selected Samples....35
4.1 Meta-Volcanic Rocks....35
4.1.1 Meta-Basalt....35
4.1.2 Meta-Agglomerate....36
4.1.3 Tuffaceous Sequence....36

4.1.4 Pyroclastics 36
4.2 Meta-Sediments and Meta-Volcanic Sediments 39
4.2.1 Meta-Volcaniclastic Greywacke 39
4.2.2 Meta- Sandstone, Meta-Siltstone and Schist Sequences 39
4.3 Intrusive Rocks 42
4.3.1 Pyroxenite 42
4.3.2 Gabbro 45
4.3.3 Granite Gneiss 47
4.3.4 Granodiorites 48
4.3.5 Quartz Diorite 54
4.3.6 Tonalite 54
4.3.7 Granite 55
4.3.8 Feldspar-Quartz Porphyritic Diorite 56
4.3.9 Dolerite Dykes 57
4.3.10 Aplite dykes 58
4.3.11 Pegmatites 58
4.3.12 Migmatite 59
4.4 Geochemical Analysis of Selected Plutonic Rocks 63
CHAPTER 5: Structural Geology of the FGSZ 71
5.1 Domain A 75
5.1.1 Domain A1-The FGSZ 75
5.1.2 Domain A2-The Diabatou Trend 87
5.1.3 Domain A3 92
5.1.4 Summary of the structures and sequence of deformation events in Domain A 97
5.2 Domain B-The Fada-Boulougou Shear Zone 98
5.2.1 Geophysical Imagery Lineaments Map Analysis 99
5.2.2 Foliation- S1 99
5.2.3 Lineation- L1 99
5.2.4 Quartz Veins- V1 100
5.2.5 Faults- F1 100
5.2.6 Foliation- S2 100
5.2.7 Fracture cleavage planes- S3 100

5.2.8 Summary of structures and sequence of deformation events for the FBSZ 101
5.3 Domain C 105
5.3.1 Foliation- S1 105
5.3.2 L-tectonite- L1 105
5.3.3 Faults- F1 and associated myonite 105
5.3.4 Foliation- S2 106
5.3.5 Lineation- L2 107
5.3.6 Quartz veins-V2 108
5.3.7 Fracture planes- S3 108
5.3.8 Summary of structures and sequence of deformation events in Domain C 116
5.4 Domain D 117
5.4.1 Geophysical Imagery Lineaments Map Analysis 117
5.4.2 Foliation-S1 117
5.4.3 Foliation-S2 118
5.4.4 Lineation- L2 122
5.4.5 Fractures planes- S3 122
5.4.6 Summary of the structures and sequence of deformation events in Domain D 125
5.5 Combined Structual Data from all Domains and the Deformation Events for Entire Study Area 126
CHAPTER 6: Geochronology Analysis of Selected Plutonic Samples 128
6.1 Sample Locations, Descriptions and LA-ICP-MS Results 128
6.1.1 Sample GP006 128
6.1.2 Sample GP027 129
6.1.3 Sample GP043 130
6.1.4 Summary of Geochronology Results 140
CHAPTER 7: Interpretation and Discussion of the Tectonic Evolution of the FGSZ 141
7.1 Volcanic Arc activity and Magmatism 141
7.2 Regional Deformations and the Overall Tectonic Evolution 144
7.2.1 Deformation Event- D1 144
7.2.2 Deformation Event- D2 146

7.2.3 Deformation Event- D3.....150
7.2.4 Deformation Event- D4.....153
7.2.5 Deformation Event- D5.....157
7.2.6 Gold Mineralization 157
7.3 Summation of the Tectonic Framework of the FGSZ 158
CHAPTER 8: Conclusion.....160
REFERENCES……..…..161
APPENDIX A: Geological Map 1:1 000 000 (BRGM, 1992)……..……..174
APPENDIX B: Geological Map 1:1 000 000 (BUMIGEB, 1992)…….…....175
APPENDIX C: Geological Map 1:2 000 000 (BRGM, 1992)…..……...176
APPENDIX D: Petrographic Descriptions ……..……..…..177
APPENDIX E : Field Dataset Sample……..183

LIST OF FIGURES

Figure 1.1: The locality map for the study area. The FGSZ is located in eastern Burkina Faso, within the Gourma Province (red filled polygon). The blue filled polygon in the top right map insert outlines the areas of the WAC. The NE trending crustal scale shear zone that extends from beyond Dabanadeni in Burkina Faso, to northern Ghana. Southeast of the FGSZ is the WKSZ (Vegas et al., 2008) and the BNSZ (Block et al., 2016). Southwest of this study area is the Tenkodogo-Yamba pluton studied by Naba et al. (2004). The area in which Ganne et al. (2011) conducted metamorphic studies is indicated by the dotted-line box; this area encloses the current study area.

Figure 2.1: Geological map of the West Africa Craton; modified after Baratoux et al. (2011), de Kock et al. (2012).

Figure 3.1: Lineaments were traced out from the magnetic imagery data, in ArcMap. Structures such as faults could be mapped in the desktop studies, even when not identified in the field due to scarcity of outcrops.

Figure 3.2: (a) The Google Earth image mosaic with the villages, roads and drainage patterns that were extracted as attributes from the images. (b) Landsat imagery was used to delineate the drainage patterns in detail, and the dams in the study area.

Figure 3.3: Surface lineaments were extracted from Landsat, ASTER and Google Earth images. Polygons were also made at regions that show features of interest to be targeted during field work (ROI= region of interest). Although the worm map for surface lineaments is scattered and not as cohesive as the magnetic data worm map in Figure 3.1, general NE and NW trends are discernible.

Figure 3.4: The outlined study area and the dots representing station points. The blue dots indicated station points from the first field work phase in 2016. The yellow dots represent station points from the second phase of field work, 2017. The background geophysical image is the Airborne Magnetic TMI 1st Vertical Derivative of eastern Burkina Faso.

Figure 3.5: Backscatter electron (BSE) images of zircons from samples (a) GP006, (b) GP027and (c) GP043.

Figure 3.6: CL images of zircons from sample (a) GP006, (b) GP043 and (c) GP027. The zircons from sample GP006 had contrasting oscillatory zoning. A few of

the grains with zoning were targeted for analysis of the rims to get a metamorphic age. Both sample GP006 and GP043 had some grains with darker cores, and these may be inherited cores. Sample GP027 did not yield clear CL images, and internal structures could not be observed (c). For this sample, the centres of the grains were targeted as the cores, for a magmatic age.

Figure 4.1: (a) Flow banding is evident in some meta-basalt outcrops, although not well preserved. Some of the outcrops do not have these features preserved and are just massive, or schistosed. (b) The amygdales in the amygdaloidal meta-basalts are slightly flattened. (c) An agglomerate with large mafic clasts of up to ~30cm in length. These clasts are imbricated. These units outcrop as upright, angular blocks up to 1.7m tall.

Figure 4.1 *Continued:* (d) The foliated tuffaceous unit. The main, S1, foliation is NE trending. A second foliation crosscuts S1 in a NW orientation. (e) Stockwork quartz veining hosted in the tuffaceous sequence. The tuffaceous sequence and the quartz veins have undergone Fe-enrichment. (f) A pyroclastic sub-outcrop with sub-angular clasts in a medium grained matrix. Clasts vary in size, and are poorly sorted.

Figure 4.2: Image (a) is of the meta-volcaniclastic greywacke with sub-angular clasts in a mafic matrix. (b) A micrograph of sample GP011; the clasts are mainly plagioclase and quartz. The clasts are sub-angular to sub-rounded in shape. (c) The meta-volcaniclastic greywacke is host to granitic xenoliths; this suggests that the basement rocks to the greenstone belts were granitic.

Figure 4.2 *Continued*: (c) A low lying siltstone outcrop. This unit has a pervasive NE trending foliation (local orientation for this outcrop is 070°/52° SE) crosscutting it. (d) A meta-sandstone unit with weak fabrics and alteration textures. (e) A graphitic schist with euhedral andalusite crystals. The andalusite crystals are ~5mm in length, and have a generally even distribution.

Figure 4.3: (a and b) Mega-crystic pyroxenite outcrops with cumulate pyroxenes of ~3cm in size. In (b), a NNE trending foliation crosscuts this unit. (c and d) A compositional layering is preserved in the massive pyroxenite outcrops. The layering is dominated by coarse grained pyroxene crystals (~2cm in size).

Figure 4.3 *Continued*: (e) A pyroxenite outcrop with assimilation textures; the leucocratic unit has a pegmatitic composition. This outcrop has a coarse grained, with crystal sizes up to 5cm. (f) A thin section micrograph with a clino-pyroxene in a

matrix of fine grained feldspar “laths”. (g) A coarse grained pyroxenite containing both clino- and ortho-pyroxenes. The pyroxenes have feldspar inclusions.

Figure 4.4: (a) A micrograph of a gabbro. It is a fine to medium grained unit with igneous textures such as poikilitic pyroxenes. It is mainly made up of pyroxenes and feldspars. (b) A gabbro and pyroxenite xenolith within a granodioritic gneiss host rock. The contact between the pyroxenite and gabbro is not sharp but rather gradational. The xenolith and the granodioritic gneiss are crosscut by a pegmatite vein. (c) The intrusive contacts between the gabbro and the meta-basalt. The gabbro is massive, and shows no fabrics.

Figure 4.5: (a) A thin section micrograph of the granite gneiss. The composition is mainly plagioclase, quartz and hornblende. There is minor biotite and the accessory mineral zircon. (b) The granite gneiss in outcrop. This unit is fine grained (<1-3mm). It has a pink appearance, indicating the presence of k-feldspar. This unit is crosscut by fracture cleavage planes.

Figure 4.6: (a) The micrograph of sample GP006; the quartz grains are either fine grained, or have undulose extinction in the larger grains (Passchier and Trouw, 2005). The hornblende has a preferred orientation, and defines the foliation. (b) A hbd-bt granodiorite outcrop with foliation defined by compositional banding of leucocratic and melanocratic minerals. The calculated average orientation of the foliation is 293°/74° S. (c) A gneissic foliation crosscuts the hbd-bt granodiorite in a NE orientation of 041°/88° SE. This gneissic zone has the same composition as the surround unit; the minerals underwent a grain size reduction to form the gneissic foliation (Passchier and Trouw, 2005). (d) The hbd-bt granodiorite is crosscut by a fine grained vein with similar composition, and lastly by the plg-qtz granodiorite. The edges of the plg-qtz granodiorite have a pegmatitic composition. (e) The plg-qtz granodiorite intrudes into the hbd-bt granodiorite, and encloses it as an enclave. (f) The foliated hbd-bt granodiorite is crosscut by a pegmatite vein.

Figure 4.7: The plg-qtz granodiorite with weak foliation defined a preferred mineral alignment; this unit has a fine to medium grain size of 1 to 5mm. This unit has an elongate mafic inclusion/xenolith. (b) In thin section, the quartz grains show an equilibrated texture (Passchier and Trouw, 2005) and 3-point boundaries. Few grains have grain boundary migration textures. (b) Mafic inclusions are characteristic in the plg-qtz granodiorite, and in image (a), the inclusion is elongate parallel to the weak

preferred mineral orientation foliation (oriented 320°/70 W). (c) An outcrop of the non-foliated granodiorites; this unis has a grain size of ≤1-3mm. (d) The non-foliated granodiorite intrudes into the hbd-bt granodiorite, and branches out as thin veins in the hbd-bt granodiorite. This unit is crosscut by pegmatite veins.

Figure 4.8: (a) The porphyritic granodiorite has feldspars that are up to 3cm in size. The porphyries randomly distributed in the unit. (b) Veinlets that are ~1cm wide with a feldspar composition crosscut the unit. Majority of the porphyries are k-feldspars (c) The porphyritic granodiorite has a sharp contact with the non-foliated granodiorite. The hbd-bt granodiorite is a xenolith in the porphyritic granodiorite, and a sharp contact separates the two suites, as shown in image (e). (f) The hbd-bt granodiorite is crosscut by a k-feldspar rich vein that is ~10cm wide.

Figure 4.9: (a) The outcrop of a quartz diorite/granodiorite; the unit is medium grained with a grain size of up to 3mm. The units are massive, and a gneissic foliation is present in some outcrops (no foliation is present in the outcrop in image a). Image (b) is a micrograph of the sample GP043. The quartz grains vary in size; they are either fine grained (~10μm) and have grain boundary migration textures, or are larger grains of up to 200μm in size, and have undulose extinction. The hornblende has a weak preferred orientation. (c) The tonalite outcrop; this unit is distinct in the field by its light appearance. The grain size is ~2mm. (d) The tonalite in thin section; the plagioclase grains are euhedral in shape, and the chlorite is interstitial in between the plagioclase and quartz grains.

Figure 4.10: (a) A granite outcrop with an a slight pink appearance, with a equigranular textures. This unit does not show any pervasive fabrics. (b) A micrograph of a granite thin section; the quartz grains have three-point boundries, and have well-developed boundaries. Few grains show recrystallization textures, and the minerals have a more equilibrated texture (Passchier and Trouw, 2005), and majority of the quartz grains do not have undulose extinction.

Figure 4.11: (a) Aplite dyke with strike orientation of 012° crosscutting a gneissic unit with NE trending compositional banding with a strike orientation of 045°. (b) Aplite dykes crosscutting a hbd-bt granodiorite gneiss.

Figure 4.12: Aluminium classification diagrams that discriminate between peraluminous, peralkaline, and metaluminous type granitoids. (a) A ternary diagram that uses the Al2O3, Na2O+K2O and CaO molecular mass percentages. (b) A binary

classification diagram using the ratios A/CNK on the x-axis and A/NK on the y-axis. Both diagrams classify sample GP027 and GP043 as metaluminous, I-type granitoids, and GP006 as a peraluminous, S-type granitoid (Chappell and White, 1974; Chappell and White, 2001).

Figure 4.13: (a) A pegmatite vein with a slightly pink appearance, indicating a K-feldspar composition. The grain size is approximately ~2cm. (b) The pegmatites crosscut the granite gneiss, the granodioritic suite, and the dolerite dykes. In this image, the pegmatite crosscuts both the hbd-bt granodiorite and the plg-qtz granodiorite.

Figure 4.14: (a) The migmatites have distinct leucocratic and melanocratic layers/bands in outcrops. Some outcrops have complex patterns, and others have a constant, NNW to NNE orientation as in images (b) and (c) (calculated average orientation of 020°/80° E).

Figure 4.15: The TAS diagrams modified after (a) Cox et al. (1979) and (b) Middlemost (1994). Diagram (b) was applied to aid in refining the classification of sample GP043. Sample GP006 plotted as a granodiorite (or quartz diorite) in both diagrams. Sample GP027 plots as a granite. Sample GP043 plots in between a granite and a granodiorite in (a), and as a quartz monzonite in (b).

Figure 4.16: The AFM diagram classifies all samples as Calc-Alkaline. Modified after Irvine and Baragar (1971).

Figure 4.17: Aluminium classification diagrams that discriminate between peraluminous, peralkaline, and metaluminous type granitoids. (a) A ternary diagram that uses the Al2O3, Na2O+K2O and CaO molecular mass percentages. (b) A binary classification diagram using the ratios A/CNK on the x-axis and A/NK on the y-axis. Both diagrams classify sample GP027 and GP043 as metaluminous, I-type granitoids, and GP006 as a peraluminous, S-type granitoid (Chappell and White, 1974; Chappell and White, 2001).

Figure 4.18: Classification diagrams after Pearce et al. (1984); (a) The Nb vs Y (ppm) tectonic environment discriminant diagram, separating Oceanic-Ridge, Within-Plate and Volcanic-arc+ syn-Collisional granitoids. All samples plot as Volcanic-arc+ syn-Collisional tectonic regime plutons. (b) The Rb vs (Y+ Nb) (ppm) diagram; this diagram gives a separation of the syn-Collisional and Volcanic-arc

granitoids, revealing that all the samples are likely plutons emplaced in a volcanic-arc setting.

Figure 5.1: A summary structural interpretation worm map of the study area showing geographical locations of the structural domains. Domain A has been sub-divided into A1, A2 and A3; A1 is the northeast extension of the FGSZ and A2 is the DT. Sub-domain A3 is located between A1 and A2. Domain B is the northeast extension of the FBSZ. Domain C encloses the southwest extensions of the FGSZ and the FBSZ. Domain D is the southernmost region of the study area. Structural data is analysed based on the domains, and the local fabrics (foliation, lineation) and structures (folds, faults, fractures, veins) are described in each domain. The overall regional tectonic evolution of the shear zones will be summarized at the end of the chapter, and all local structures will be put into regional context for the study area.

Figure 5.2: Lineaments map incorporating structural information gathered from field data including schists, dolerite dykes orientations, faults and mylonite zones. The GGB is bounded by the FGSZ and the DT. A dilation bend with dextral shear sense has been interpreted from aeromagnetic data around the GGB, and this makes up domain A. Domain B is the Fada-Boulougou Shear Zone. The Tanbaougou Trend (TT) is on the western boundary of the Tambouana Greenstone Belt.

Figure 5.3: Stereoplots of foliation and lineation in domain A are shown in the inserts (a), (b), (c), (d), (e) and (f). S1 has a NE trend with calculated average orientation 032°/66° SE, and is dominant in the schist units proximal to the shear zones. S1 also occurs as a gneissic foliation in the intrusive units located between the shear zones. The NW to E-W trending S2 crosscuts S1 as a crenulation foliation, or as a schistosed foliation. The lineation L1 is a mineral lineation. The orientation of L1 is generally shallow plunging to the NE and SW along the NE trending foliation as shown in the stereoplots. L2 is an E- to W-plunging defined by fold axes. The orientations of the buck quartz veins are mainly NE trending and have a calculated strike orientation average of 039°, as shown in the stereoplot for V1.

Figure 5.4: (a) The chl-bt-qtz schist dominates the FGSZ, and is a low lying, outcrop that weathers easily unless it has been silicified. The S1 foliation along the schist is NE trending, and the orientation of the outcrop in the image is 051°/60° SE. This outcrop has boudin quartz veins that are parallel to the foliation. (b) The chl-bt-

qtz schist has inclusions of disseminated pyrite. (c) Chlorite, biotite and hornblende define the NE trending foliation. (d) An image of a silicified chl-bt-qtz schist in outcrop that has preserved the NE trending S1 (020°/58° W) and a stretch mineral lineation oriented 24°→224°.

Figure 5.5: An L-tectonite unit is hosted between the FGSZ and the FBSZ. The rock type is a tuff, with Fe-enrichment. There is minor pyrite that has crystallized in this unit. The outcrops of the L-tectonite can be up to ~1.2m in height, and have sub-horizontal fracture planes, as shown in images (a) and (b). The azimuth of the lineation, illustrated by the red arrows in image (a), is SW, and the plunges are steep, as shown by the strereoplot in image (c).

Figure 5.6: (a) An illustration of the tight folded schistosed tuffaceous sequence located near the intersection zone of the FGSZ and the DT. The folds are doubly plunging, and have a SE vergence. The lineations on the folds is indicated by the red arrows in the cross section, and in stereoplot, have calculated average orientations of 29°→045°, and 41°→259. These folds have wavelengths of ~3m. The hinges of the folds have stockwork quartz veins. (b) The veins at the hinges of the folds are folded, and the fold axes of the quartz veins are NE and SW plunging. (c) Some veins boudinaged. The boudins are parallel to the NE trend of the fold axis. Folding of the schistosed tuffaceous sequence developed under a NW-SE shortening regime.

Figure 5.7: (a) An iron-enriched schist with a NE trending S1 foliation, oriented 040°/82° SE is crosscut be a crenulation cleavage S2 oriented 086°/82° S. The required stress axis for this S2 foliation to develop is N-S as illustrated. (b) An image of outcrop with an S1 cleavage (020°/58° W) crosscut by an S2 cleavage oriented 272°/80°. (c) Sample GP037 is also a chl-bt-qtz schist with feldspar clasts within the fine grained matrix. Although not well defined, the rotated fractures within the feldspar clasts indicate a dextral shear sense. (d) Striations and slickenside lineations on the surfaces of a buck quartz vein. The lineations are NE plunging, and the slickenside indicate that the northern block (according to north arrow in image D) was displaced upwards (NBU=north block up).

Figure 5.8: (a) The micrograph of sample GP009 shows micro-folds that formed around the quartz and plagioclase clasts. The foliation is defined by a compositional banding of fine grained (μm scale) leucocratic minerals and minimal

biotite. (This sample is not oriented). (b) A micrograph of sample GP010 A shows micro-folds, and plagioclase and quartz clasts. Sample GP010 B also has micro-folds, and sub-euhedral plagioclase and quartz grains. Weak shear sense indicators have developed in sample GP010 B; the plagioclase delta clasts have with a dextral shear sense as illustrated in image (d).

Figure 5.9: (a). The granitic gneisses have fracture cleavage planes. The fracture cleavage planes crosscut the gneissic foliation in the granite. The orientation of the dominant fractures at this outcrop has an orientation of 290°/88° NE. (b). The stereoplot of the fracture cleavage planes measured along FGSZ in domain A; the calculated average orientations are 310°/70° SW and 001/82° W.

Figure 5.10: (a) A chl-bt-qtz schist outcrop along the DT; these outcrops are low lying, and erode easily, unless they are silicified and/or Fe-enriched. This outcrop has an S-C fabric, and the measured S1 orientation is 024°/78° SE, and the C1 orientation is 036°/40° NW. The S-C fabric displays a dextral displacement, consistent with a NW-SE directed σ1. The schist is crosscut by a quartz vein, then subsequently underwent brittle deformation. (b) In thin section, sample GP002, whose location is indicated in Figure 5.2, is fine grained (~1μm). Chlorite, biotite and quartz ribbon define the foliation. Zircon is present as an accessory mineral. (c) An Fe-enriched schist outcrop, with two foliation sets S1 and S2. The S1 orientation measured at this outcrop is 024°/72° SE, and the S2 orientation is 068°/88° NW. This dextral displacement along the NE trending foliation is also consistent with a NW-SE directed σ1.

Figure 5.11: (a) Lineations L1 along the DT are observed on the NE trending S1 surface of the Fe-enriched schist. The orientations on this outcrop are; S1 030°/68° SE, L1 10°→022°. (b) The L2 lineations are E plunging, and have calculated average orientation of 50°→090°.

Figure 5.12: An Fe-enriched schist with a NE trending S1 foliation oriented 026°/80° SE, crosscut by a ENE-WSW trending S2 foliation oriented 082°/82° NW. The stress axis changed from NW-SE for S1, to NNW-SSE for S2.

Figure 5.13: A few of the station points within A3 had structural data, and the S1, S2 and L1 data is presented in the stereoplots. The S1 foliation has a calculated average orientation of 039°/68° SE. The S2 foliation crosscuts S1 in a NW orientation, calculated average 327°/73° SW. The lineation is defined by stretching

clasts in a meta-volcaniclastic greywacke, and they have a calculated average orientation of 37°→065°.

Figure 5.14: A summation of the structures identified in sub-domain A3; (a) The overall sense of shear along the area of sub-domain A3 is sinistral, with rotational lineaments discernible on and extracted from aeromagnetic data. The principal stress axis responsible for this displacement is NNW-SSE oriented. The entire GGB is interpreted to be an overturned synform, and the fold hinge lineaments were traced and extracted from aeromagnetic imagery data, and the fold axis has a NE strike orientation of ~050°. The fold may have formed under a more NW –SE oriented σ1. (b) The meta-volcaniclastic greywacke has S-C fabric shear sense indicators. The sense of displacement is dextral, and the principal stress axis is NW-SE directed. (c) The L1 lineation on a NNE trending S1 plane; the lineation is defined by stretching clasts in a meta-volcaniclastic greywacke. The S1 orientation in this outcrop is 020°/44° SE, and L1 is 40°→060°. The station points to which the outcrop images (a) and (b) belong are indicated in the map.

Figure 5.15: This map shows the locations of the artisanal mine sites that were identified in the field, and using Google Earth images. The artisanal mines are located on the buck quartz veins, and mining occurs along strike of the veins. The pits of the artisans are ~1m wide and can be several meters deep. Tambiga Hill is indicated on the map by the green star symbol; it is located in the middle of sub-domain A3.

Figure 5.16: (a) A gold nugget that is hosted within the fractures of a quartz vein; the sample is from an artisanal mine along the DT. (b) An image of an artisanal pan with heavy minerals including gold; the gold sinks to the bottom of the pan and is separated out.

Figure 5.17: This lineaments map illustrates the sinistral shear sense indicators along the domains A2 and B. The lineaments from aeromagnetic imagery data reveal a sigma structure between the DT and the FBSZ, and S-C fabrics along each shear zone. The pattern of S-C fabric is consistent in between the shear zones, although not always strongly defined.

Figure 5.18: Stereoplots of foliation and lineation in domain B, and additional station points along domain A2, south of the Gourma camp site. The data reveals a consistency in the NE trend of S1. Stereoplots along the DT have limited lineation

and quartz veins measurements. The location of the L-tectonite unit, discussed in domain A is between the FGSZ and the FBSZ. The stereonet for the fracture cleavage planes along the FBSZ indicates as NW trending set of fractures.

Figure 5.19: A foliated granodiorite with an S1 orientation of 058°/80° SE crosscut by a meso-scale (cm) dextral shear zone. The strike orientation of the meso-scale shear zone is 284. The σ1 orientation along the dextral shear is NW-SE.

Figure 5.20: (a) An outcrop of a brecciated quartz vein; the veins have also undergone late stage brittle deformation and a fractured and fragmented. (b) The quartz veins are crosscut by NW trending fractures. (c) A pyroxenite unit is crosscut by N-S and WNW-ESE trending faults. The fault planes have been infilled by pegmatites. Image (c) is rotated to north facing up, and illustrates the displacement along the faults. These faults have a sinistral displacement along them. The σ1 orientation is NW-SE oriented.

Figure 5.21: Domain C encloses the trend of the FGSZ and the FBSZ. The Bogueli Mylonite Zone is located on the western boundary of the FGSZ. In the eastern parts of domain C, a NW trending gneissic foliation is dominant. Domain D is in the southern most region of the study area. Domain D encloses the Bounpa Mylonite Zone, the Silmitenga Trend and the Bosangre Trends.

Figure 5.22: The migmatites and gneissic foliation have a NW trending S1. S2 is NE trending, consistent with the northern domains. Lineation has been sub-divided into L2a, L2b and L2c, as all measurements were taken on the NE trending S2 planes. The orientations suggest that the lineation sets formed under different stress regimes (Passchier and Trouw, 2005).

Figure 5.23: Granodiorite outcrops with a NW-trending S1 foliation, calculated average orientation of 300°/65° SW, defined by (a) preferred mineral orientation, and (b) weak compositional banding. (c) An outcrop image of a foliated granodiorite displays a folding of the S1 foliation (measure orientation 298°/84° SW); the orientation of the fold axial plane is NE trending with orientation 076°/60° SE. The σ1 orientation for the displacement is N-S directed.

Figure 5.24: An L-tectonite unit is located between the FGSZ and the FBSZ. The rock type is an ultra-fine grained (<1mm) tuff with Fe-enrichment. There are euhedral pyrite crystals that have crystallized as accessory minerals in this unit. The outcrops of the L-tectonite can be up to ~1.2m in height, and have sub-horizontal

planes is presented in images (d). The azimuth of the lineation, illustrated by the red arrows in image (a), is SE with the steep plunges. The calculated average orientation is 81°→155°. The stereoplot for the lineation is shown in image (d).

Figure 5.25: (a) The stereoplot of the faults that cross a foliated granodiorite unit in domain C. (b) A NE trending faults have a dextral shear sense, and have meso-scale dilational jogs in which quartz veins have precipitated. The calculated average orientation is 068°/88° SE. (c) A NNW to NNE trending set of faults have a calculated average orientation of 004°/85° E. A mylonitic foliation has developed along the strike of these faults with rotated delta clasts. The shear sense indicators along the clasts are weakly developed, and have a sinistral displacement.

Figure 5.26: (a). A NE trending mylonitic shear zone ~30cm in width. This mylonitic shear zone is strongly foliated, and is hosts delta clasts and tight micro-folds. Adjacent to the mylonitic shear zone is a quartz vein with a dilation jog. All the shear sense indicators in the mylonitic zone are dextral. (b) An up close look at one of the mylonitic shears. The mylonite is hosts sigma quartz clasts with a dextral displacement. The mylonite foliation has shear planes and shear bands all consistent with dextral shearing. Late stage quartz veins crosscut the mylonite.

Figure 5.27: (a) The felsic mylonite outcrop, with a pink appearance indicating the presence of K-feldspar in the mineral composition. (b) A NE trending minor mylonitic shear zone ~20cm wide within the mylonite outcrop. The felsic mylonite hosts en echelon quartz veins with a dextral displacement.

Figure 5.28: A gneiss granite outcrop with stretching mineral lineation defined by hornblende and feldspar. The S2 orientation along this outcrop is 076°/72° NW, and the L2a orientation is 70°→324°.

Figure 5.29: An interpretation of the trends in domain D; the orientations are consistent with a subsidiary shear fracture system of Riedel shears. These trends fall within the study area, and may be part of a regional sinistral shear deformation. The Silmitenga Trend represents the Riedel shear, and the NNE Bosangre trend represents the synthetic P shear. No structural data was collected along the trend and interpretation is based mainly of the lineaments extracted from aeromagnetic imagery data. The subsidiary shear fracture system fits the sinistral shearing on the NE trending foliation observed in other domains in a NNW-SSE to N-S directed σ1.

Figure 5.30: Stereoplots of the foliation, lineation and fracture cleavage planes in domain D. Similar to domain C, S1 in domain D is defined by a NW-trending gneissic and migmatitic foliation in the granodiorites and granite. Lineation on the S2 planes is sub-divided into L2a and L2b based on the clusters with different orientations. The fracture cleavage planes have a NW trend, and they crosscut all other fabrics.

Figure 5.31: The migmatite outcrops are dominant in domains C and D. (a) A migmatite outcrop with complex folding of leucocratic and melanocratic band. Images b, c and d are of migmatite outcrops with a near N-S oriented anatexis texture. The strike orientation of the banding is ~020°. Some outcrops have meso-scale folded bands as shown in image d.

Figure 5.32: The Bounpa Mylonite Zones outcrops; (a) The mylonite has a pink appearance in outcrop. The dominant foliation is NE trending, and the S1 orientation measured at this outcrop is 040°/70° SE. The shear sense in zone 1 is dextral, as illustrated by the S-C fabric. The σ1 orientation required for this displacement is NW-SE. (b) The second mylonite outcrop is weathered, and fine grained (<1mm grain size). An S-C fabric has developed in this outcrop; the S1 orientation is 070°/60° SE and the C1 orientation is 042°/52° SE. The shear sense in this mylonite outcrop is sinistral under a NNW-SSE stress axis.

Figure 5.33: A migmatite outcrop with a NNE trending anatexis banding and a crenulation lineation; the orientation of the foliation is 020°/88° SE and the crenulation lineation L2b is 54°→028°.

Figure 6.1: Locality map of the three geochronology samples, and the zircon U-Pb ages of each sample.

Figure 6.2: Sample GP006; (a) Field outcrop of the quartz diorite. (b) Thin section of sample GP006 with plagioclase, quartz, hornblende and minor muscovite and biotite. The quartz has undulose extinction, and has a seriate texture with finer grained crystals, and coarser grained, recrystallized quartz grains. (c) Zircons analysed for LA. The black circles indicate where core ablations were made, and the red circles indicate where rim ablations were made. The numbers relate to the suffix numbers in the table of results (Table 2) for sample GP006. (d) The Concordia diagram gave an age of 2210±8.7Ma.

Figure 6.3: Sample GP027; (a) the field outcrop of the gneissic granite, with intrusive contacts with the granodiorite. (b) The hand sample of the granite gneiss. This sample was cut for thin section, crushed for XRF and underwent mineral separation for zircons. (c) The fine grained gneiss in thin section. The matrix is quartz and feldspar dominates, with minor hornblende and mica content. (d) The black circles indicate where ablation was done, and the number correlated with the sample number suffixes in the sample names in Table 4. (e) The Concordia age attained for sample GP027 is 2239±13Ma.

Figure 6.4: Sample GP043; (a) The younger granodiorite that intruded into an older amphibolitic unit. (b) Sample GP043 in thin section. It has a fine to medium grain size. (c) The zircons analysed in LA. The black circles represent were ablation was done, and the numbers correlate with the sample name suffix in Table 5. (d) The Concordia diagram for sample GP043, with an age of 2167±12Ma.

Figure 7.1: An interpretation of the volcanic arc regime during which volcanic activity was coeval with magmatism; volcanic activity is constrained at 2240Ma or older (Castaing et al., 2003; Gasquet et al., 2003; Lompo, 2010; Tshibubudze et al., 2013). For the current study area, the oldest dated rock is the granite gneiss aged at 2239±13Ma. It is interpreted that magmatism was continuous, and the oldest granodiorite suite for this study area was emplaced ~29Ma later. The meta-sediments, the pyroclastics and meta-volcaniclastic sediments all accumulated during continued volcanic activity, and form part of the greenstone belts.

Figure 7.2: A simplified stratigraphic column illustrating the relationships between the greenstone belt rocks, the meta-sediments and the intrusive rocks for this study. Age data of plutons from other studies in Burkina Faso have been included in the geochronological sequence (Castaing et al., 2003; Vegs et al., 2008; Jessell et al., 2015).

Figure 7.3: An interpretation of the D1 event; a NE-SW oriented σ1 lead to the development of the NW trending S1 foliation. This foliation has a calculated average orientation of 300°/65° SW. This foliation pre-exists the NE trending structures.

Figure 7.4: The interpreted geological map for the study area. The lineaments extracted from aeromagnetic data show the pervasive NE trending fabric. The thrust planes are located mainly at the contacts of the greenstone belts and the plutons.

Synforms are interpreted to have developed in the greenstone belts (cross-section A-B in Figure 7.5).

Figure 7.5: Cross sections A-B and C-D as indicated in Figure 7.4. illustrating the coaxial shortening and thrusting deformation is in a NW-SE direction. Thrust folding of sequences occurred. The basalt, meta-volcaniclastics, pyroxenites and gabbros were all emplaced during the ≥2239Ma volcanic event. The ages of the plutons are an indicator of syn-tectonic plutonism during accretion at ~2167Ma.

Figure 7.6: An illustration of D3 stress axis orientation; the σ1 varies from WSW-ENE to NW-SE. This was a non-coaxial shortening and it lead to dextral shear sense along the thrust fault planes. The FGSZ developed a right stepping dilation bend with the DT on the eastern margin of the bend. Another dextral dilation bend is discernible in geophysical imagery data, but has been overprinted by subsequent sinistral shears.

Figure 7.7: An interpretation of the possible relation of the NW-trending foliation to the dominant NE fabrics. (a) One outcrop shows the NW foliation being folded and sheared (dextral shear sense). This may be part of the Riedel fault system that develops in a sinistral shear zone with NNE-SSE directed σ1. This orientation is consistent with the sinistral shear defined in D4 for this study area. (b) Southwest of the FGSZ study area, is the WKSZ as defined by Vegas et al., 2008. The Koure pluton was emplaced within a tonalitic host rock, and is dated at 2128±6Ma. The high temperature emplacement of the pluton led to the re-melting and development of the gneissosity in the tonalite, and rotation fabrics formed. Although the original orientation of the pre-existing foliation before rotation could be determined, Vegas et al. (2008) suggest that the layering before deformation was at an angle to the NNE/NE shear zones, and underwent rotation during sinistral shearing and emplacement of the pluton. The NW-trending migmatite foliation in the FGSZ study area may have developed under similar tectonic environments. For this study, NNE-SSW directed σ1 is defined as part of the D4 event.

Figure 7.8: A schematic summation of the tectonic evolution, pluton emplacement sequence incorporated with published data from other studies in Burkina Faso. The ages attained from this study reveal that the basement rocks for the Birimian terrane in the FGSZ area were granitic (granite gneiss). The crystallization age of the granite gneiss and the quartz diorite/granodiorite is within

the constrained volcanic arc activity ages between 2250Ma and 2200Ma (Lompo, 2010). This suggests that magmatism was coeval with volcanic activity. Deformation event D1 is comparable with the D1 defined in NE Burkina Faso as the Tangaean event by Tshibubudze et al. (2009), Hein (2010), Tshibubudze et al. (2015). D2 and D3 form part of the early stages of the Eburnean Orogeny in eastern Burkina Faso, dominated by compression and crustal thickening. The dominating NE trending structural grain resulted from the NW-SE shortening direction. D4 is a reactivation of the shear zones during a sinistral shear sense regime. D5 is a late stage brittle deformation resulting in fracture cleavage planes. Plutons were emplaced through the deformation events. The youngest units are the dolerite dykes that crosscut all other lithologies and the structures. The dolerite dykes in Burkina Faso are dated at 1814±26Ma by Castaing et al. (2003).

LIST OF TABLES

Table 1: A summary of the magnetic signatures and features that were identified as characteristic for each lithology during desktop studies. Some units could not be clearly identified in the geophysical imagery, and no representative polygons could be interpreted from the imagery data alone. Field data took precedence over imagery data, and this aided in increasing the accuracy of interpretations based on ground truth. The scale of the images in the table is at a length of ~2km.

Table 2: The standard samples used during LA-ICP-MS, their ages and source publication.

Table 3: Major (wt%) and trace (ppm) element data and analysed samples GP006, GP027 and GP043 (d.l = below detection limit).

Table 4: Summary of the structures and deformation events in domain A.

Table 5: Summary of the structures and deformation events in domain B.

Table 6: Summary of the structures and deformation events in domain C.

Table 7: Summary of the structures and deformation events in domain D.

Table 8: Combined summary of the structures and deformation events in the study area.

Table 9: L A- ICP-MS U-Pb analysis of sample GP006, the quartz diorite. The last four analyses (in red) are rim analyses.

Table 10: LA-ICP-MS U-Pb analysis of sample GP027, the gneissic granite.

Table 11: LA-ICP-MS U-Pb analysis of sample GP043, the granodiorite.

Table 12: Summary of the conventions of the naming of structures from a local to regional context.

Table 13: A completed summary of all defined deformation events for this study. All fabrics have been put in a regional context.

CHAPTER 1: INTRODUCTION

1.1 PREAMBLE

The West Africa Craton (WAC) covers countries including: Burkina Faso, Guinea, Ivory Coast, Liberia, Ghana, Gambia, Mali, Mauritania, Senegal, Niger, Sierra Leone and Togo (Figure 1.1). The West Africa Exploration Initiative (WAXI) and geological surveys in West African countries have undertaken a program of mapping of the WAC, and building a broad geological database that is available for research use and mineral exploration. This includes geological and structural maps, geophysical data, GIS interpolations of field data and satellite imagery, and metallogenic maps indicating locations of the different types of deposits hosted within the Craton.

Macro-scale, first order crustal scale faults and shear zones that possibly extend to the lithosphere and resolve displacements of tens of kilometers (Le Pape et al., 2014) have been studied in Burkina Faso. These include the Sabce Shear Zone, which is a 10m wide crustal scale shear zone with sinistral displacement that formed during the Eburnean Orogeny in the Goren Greenstone Belt, north of Ouagadougou in Burkina Faso (Hein, 2010). The steeply dipping Markoye Shear Zone in northeastern Burkina Faso is also a first order crustal scale shear zone that has undergone at least two phases of deformation (Tshibubudze et al., 2009). The NE trending West Koaure Shear Zone (WKSZ) in eastern Burkina Faso (Figure 1.1) is a shear zone adjacent to the syn-tectonically emplaced Kouare pluton aged at 2128±6Ma (Vegas et al., 2008). The reported displacement along the WKSZ is sinistral.

The WKSZ extends into northwestern Ghana as the Bole-Nangodi Shear Zone (BNSZ), as shown in Figure 1.1. The BNSZ is a major shear structure that is on the margins of and transects the Bole-Bulenga domain of northern Ghana (de Kock et al., 2012). Both the WKSZ and the BNSZ are part of the crustal scale shear zone in the eastern region of the WAC that extends from the Niger-Burkina Faso border to NW Ghana over a distance of ~ 500km (Figure 1.1). The studies by Naba et al. (2004), Vegas et al. (2008), Ganne et al. (2011), de Kock et al. (2012) and Block et al. (2015) have revealed a minimum of two deformation phases and multiple intrusive events along and/or adjacent to the crustal scale structure.

The NE trending Fada-Gourma Shear Zone (FGSZ) is located in the Gourma Province (Figure 1.1). For this study, the FGSZ extends from Dabanadéni to Bounpa, south of Fada N'Gourma in eastern Burkina Faso. The study area is composite of granitoid batholiths and arcuate, NE trending volcanic belts. The structure of the FGSZ in this region has not been the focus of any study thus far. Based on geophysical data alone, the shear zones, rotational fabrics and shear bands reveal a complex succession of tectonic, and related intrusive events. This study will investigate the phases of deformation that occurred within the study area, and give a comprehensive geotectonic evolution. This will add on to the interpretations made along the WKSZ and the BNSZ. Interpretations made based on the geophysical data and field data will be further supported by geochemical and geochronological analysis on the intrusive units. The plutons in between and adjacent to the volcanic belts have not been dated. Age data for these units will put the deformations in geochronological context. This will assist in concluding whether the deformation events for this study are consistent with regional deformations defined in other study areas in the WAC, especially in Burkina Faso.

The greenstone belt-granitoid assemblages and shear zones of the WAC, and more specifically in Burkina Faso, are concomitant with gold mineralization (Feybesse et al., 2006; Tshibubudze and Hein, 2013; Hein, 2016; Vearncombe and Zelic, 2015). Artisanal mining is very active in the Gourma region, and confirms the presence of gold mineralization in the eastern regions of Burkina Faso. The exploration company Gryphon Minerals Limited and Teranga Gold jointly own a tenement located in the NE region of the FGSZ, and are exploring for gold. Gold deposits found within the tenement include the Tambiga Hill deposit and the Diabatou Trend deposit, both of which are active artisanal mining sites. Part of this study's objective is to establish the metallogenic controls with respect to the geology and tectonic evolution. Artisanal mining is abundant in this area, with both active and mined-out sites easily accessible. These sites were useful for lithology descriptions, structural measurements and sampling, and they indicate where gold mineralization may occur.

The geological maps available for the FGSZ are only at regional scale (1:2 000 000), for example that of the Bureau de Recherches Géologiques et Minières (BRGM) by Milesi et al. (1992). Part of WAXI's mandate is updating the geological

maps of the WAC. Sampling of the different intrusive units and their petrographic descriptions (hand samples and thin sections) and geochemical analysis aided with the detailed mapping of the study area. Outcrops were however, limited, and field data had to be used in conjunction with geophysical data interpretations. This aided in producing a detailed geological map for this region, contributing to the WAXI database.

1.2 LOCATION AND PHYSIOGRAPHY OF THE STUDY AREA

The study area for this research project is located in eastern Burkina Faso, in the Gourma Province as shown in Figure 1.1. It has an area of ~4500km^2, extending from Dabanadéni, southwest of the Niger border (~30km from border) towards the city Fada N'Gourma, along the northeast trending shear zone, covering a distance of ~200km. The region is a fairly low lying area, with elevation highs of no higher than 290 meters above sea level (hills often capped with laterite formations), and lows of ~260 meters above sea level which are mainly river drainages. Ground coverage is of low shrubs and trees, and ploughed land near villages or dwelling spaces used for domestic farming. Where there are no outcrops or vegetation, an extensive flat landscape covered by soil is common.

Burkina Faso has a tropical climate with two main seasons, a 7-month long dry season, and a 5-month rainy season. The rainy season lasts from May to September, and it is during July, August and September that the country receives 80% of the rainfall (Roncoli et al., 2002; 2009). November to March is the dry season. Between March and May, the harmattan, a dry east wind brings with it hot conditions. Maximum temperatures range from 40°C to 45°C from the months of May to October, and minimum temperatures recorded in January range between 7°C and 13°C (Ouedraogo et al., 2012).

Access to the field area was by use of the national roads in-between the town and villages, in addition to the local gravel roads that connect the smaller villages, and off-road driving. The scarcity of outcrops may be one of the limitations of the project, and strategic routes and traverses were planned to reach key areas of interest so as to maximize field work outcomes.

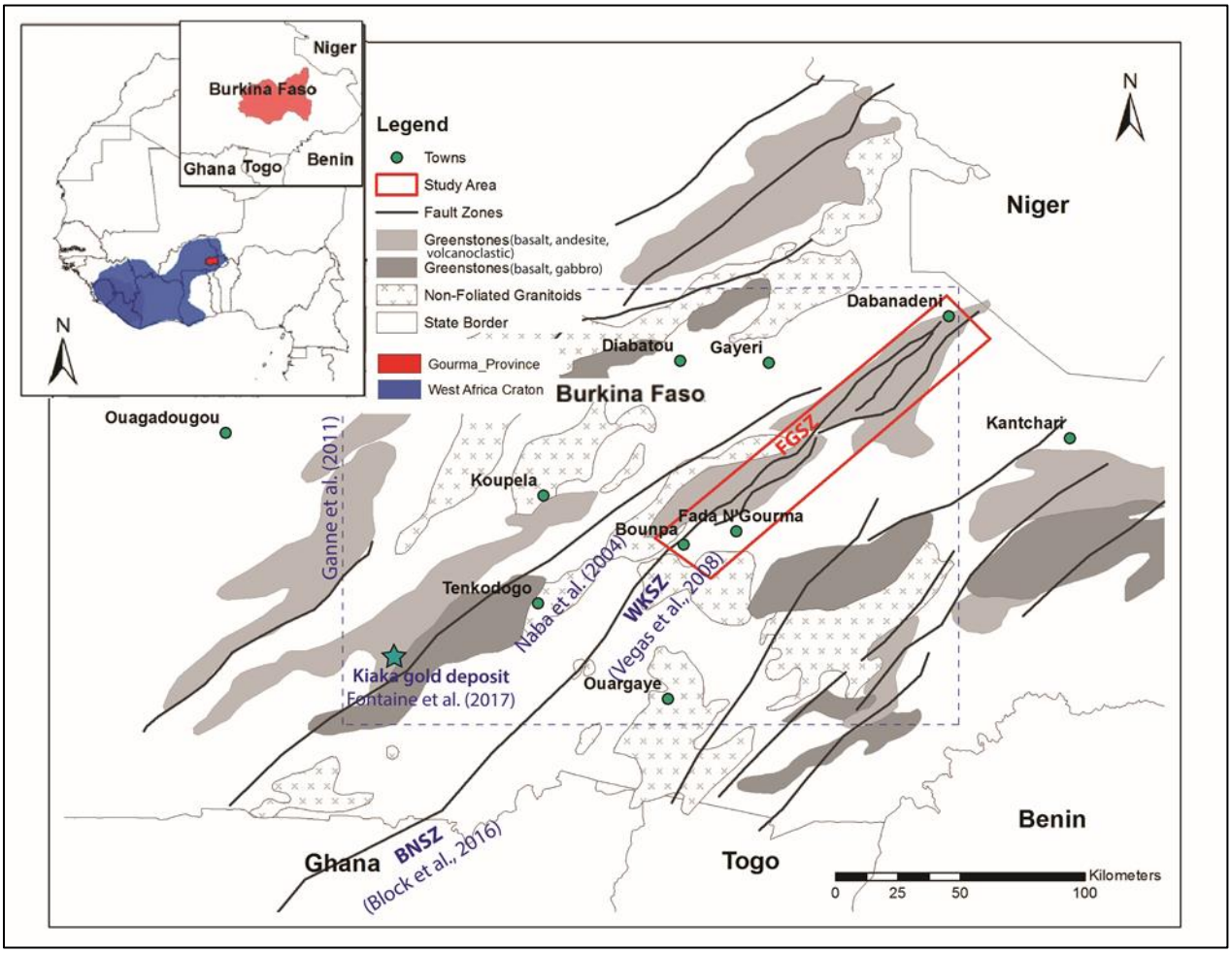


Figure 1.1: *The locality map for the study area. The FGSZ is located in eastern Burkina Faso, within the Gourma Province (red filled polygon). The blue filled polygon in the top right map insert outlines the areas of the WAC. The NE trending crustal scale shear zone that extends from beyond Dabanadeni in Burkina Faso, to northern Ghana. Southeast of the FGSZ is the WKSZ (Vegas et al., 2008) and the BNSZ (Block et al., 2016). West to SW of this study area is the Tenkodogo-Yamba pluton studied by Naba et al. (2004). The Kiaka gold deposit studied by Fontaine et al. (2017) is indicated by the star symbol. The area in which Ganne et al. (2011) conducted metamorphic studies is indicated by the dotted-line box; this area encloses the current study area.*

1.3 AIMS AND OBJECTIVES

The geology, structure, metamorphism and metallogenesis of the FGSZ will be investigated within the following aims and key objectives;

- To determine and characterize the different lithological units along the structure using outcrop field data and interpolation and infilling using characteristic feature in imagery data.

- Defining the metamorphic facies, and the change in metamorphic grade observed along and across the trend of the shear zone.
- Attaining the ages of the intrusive rocks (determined through absolute geochronology) in the FGSZ, and determining when intrusions occurred relative to the regional deformation phases.
- Establishing crosscutting relationships of micro-, meso-and macro-scale structures and fabrics, based on field data collected along traverses taken across the shear zone, and from desktop studies.
- Defining the deformations that the FGSZ underwent based on the geometric, kinematic and dynamic information.
- Determining the overall tectonic evolution of the FGSZ and to establish whether this interpretation is consistent with the regional tectonics that dominated the Palaeoproterozoic terranes of the WAC in Burkina Faso.
- To determine the metallogenic controls, that is, whether gold mineralization was structurally controlled.

1.4 THESIS ORGANIZATION

This thesis is organized into eight chapters, including the Introduction. A summary of each chapter subsequent to the Introduction are listed below;

Chapter 2 is the overview of the geology of the West Africa Craton, and the regional geology of eastern Burkina Faso, with particular focus on the Gourma Province region.

Chapter 3 explains the methodology followed to achieve the aims and objectives for the project. This includes desktop studies, field work and analytical work on the rock samples collected.

Chapter 4 describes the petrography that makes up the study area. This includes descriptions of outcrops in the field, hand samples, and thin sections. This chapter also presents the geochemical data from XRF analysis of the plutonic units found in the study area. The results serve to classify the intrusive rock types.

Chapter 5 focuses on and describes the dominant structures along the FGSZ. Cross cutting structures were used to make interpretations of the possible deformations that occurred in the study area.

Chapter 6 is the geochronological analysis of the selected plutonic samples. This data will give intrusive ages, and also aid in constraining the age of tectonic events, based on cross cutting relationships observed within each unit.

Chapter 7 discusses and synthesizes the results so as to achieve the aims and objective set out for this thesis, based on the interpretations made. The tectonic evolution of the FGSZ will be determined.

Chapter 8 is a summation of the conclusions made on the findings.

1.5 ABBREVIATIONS USED IN THIS DISSERTATION

Au - Gold

BNSZ - Bole Nangodi Shear Zone

Bt – Biotite

BRGM – Bureau de Recherches Geologiques et Minieres

°C – Degrees Celsius

Ca - Calcium

Chl – Chlorite

C-pyx - Clinopyroxene

D1; D2; D3; D4; D5 – Successive deformation events 1 to 5

DT - Diabatou Trend

FBSZ - Fada-Boulougou Shear Zone

Fldsp - Feldspar

Fe - Iron

FGSZ - Fada-Gourma Shear Zone

GGB - Gourma Greenstone Belt

Hbd - Hornblende

Hz – Hertz

J/cm^2 – Joules per centimetre squared

K-feldspar – Potassium feldspar

Kbar - Kilo bar

L1; L2; L3; L4 – Successive lineation sets 1 to 4

LA-ICP-MS - Laser Ablation Inductively Coupled Mass Spectrometry

LANDSAT - Land Remote-Sensing Satellite

Ma - Mega-annum, millions of years

Mg - Magnesium

Mus - Muscovite

µm - micrometre

MSZ - Markoye Shear Zone

Nb - Niobium (trace element)

O-pyx - Orthopyroxene

Plg - Plagioclase

Ppm – parts per million

Pyx - Pyroxene

Qtz - Quartz

Rb - Rubidium

RMI - Residual Magnetic Intensity

RTP - Reduced To Pole

S0 – Primary bedding/foliation

S1; S2; S3; S4; S5 – Successive foliation sets 1 to 5

TGB - Tanmbouana Greenstone Belt

Th - Thorium

TMI - Total Magnetic Intensity

TT - Tanbaougou Trend

TTG - Trondjhemite-Tonalite-Granodiorite

U-Pb - Uranium-Lead

WAC - West Africa Craton

WKSZ - West Kouare Shear Zone

Wt% - Weight percentage

Y - Yttrium (trace element)

CHAPTER 2: OVERVIEW OF THE GEOLOGY OF THE WAC AND REGIONAL GEOLOGY OF THE FADA-GOURMA REGION

2.1 LITHOSTRATIGRAPHY

The WAC consists of an Archaean block to the west of the craton referred to the Kenema-Man Domain, and the Palaeoproterozoic Baoulé-Mossi Domain to the east (Figure 2.1) (Doumbia et al., 1998; Beziat et al., 2000; Egal et al., 2002; Thieblemont et al., 2004; Metelka et al., 2011; Parra-Avila et al., 2016). The Kenema-Man Domain is comprised of gneisses, granitic complexes and banded iron formations all aged between ~3400Ma and ~2700Ma (Hirdes et al., 1996; Thieblemont et al., 2004; De Waele et al., 2015; Kouamelan et al., 2017). Greenstone belts, granitoids and belts of volcano-sedimentary and volcaniclastic rocks, collectively commonly referred to as the Birimian terranes, make up the Baoulé-Mossi Domain (Feybesse et al., 2006; Lompo, 2010; Baratoux et al., 2011; Parra-Avila et al., 2016). The ages reported for the terranes of the Baoulé-Mossi Domain are Palaeoproterozoic (Hirdes et al., 1996; Doumbia et al., 1998;

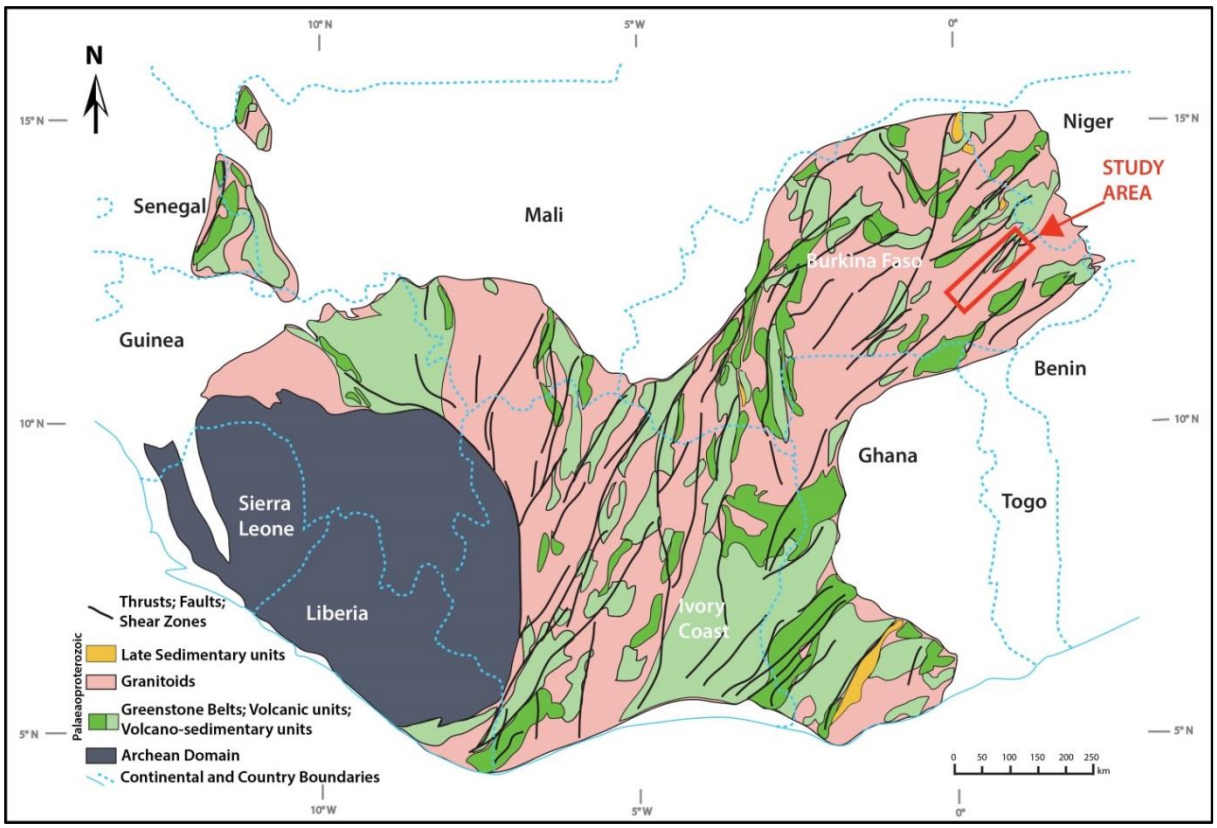


Figure 2.1: *Geological map of the West Africa Craton; modified after Milesi et al. (2004), Baratoux et al. (2011) and de Kock et al. (2012).*

Thieblemont et al., 2004; Feybesse et al., 2006; Hein, 2010; Tshibubudze and Hein, 2013; Tshibubudze et al., 2015). Magmatism is revealed to have commenced as early as 2300Ma (Gasquet et al., 2003; Block et al., 2016), and was coeval with volcanic activity in other regions that occurred between 2250Ma and 2100Ma (Gueye et al., 2008; Lompo, 2010; Tshibubudze et al., 2013; Baratoux et al., 2015; Block et al., 2016).

The lithostratigraphy in Burkina Faso is composite of N-S, NNE-SSW, NW-SE and NE-SW trending greenstone belts and granitoid batholiths and plutons (Hirdes et al., 1996; Hein, 2010; Baratoux et al., 2011; Tshibubudze et al., 2015). In the Fada-Gourma region, eastern Burkina Faso, the NE trending greenstone belt extends for ~200km on published geological maps (Milesi et al., 1989; Baratoux et al., 2011). The Tarkwaian sediments unconformably overlie the Birimian sequences, and deposition of the sediments is constrained between 2133Ma and 2017Ma (Hout et al., 1987; Davis et al., 1994; Pigois et al., 2003; Perrouty et al., 2012; Fontaine et al., 2017). There is no single comprehensive geochronological interpretation of the lithostratigraphy of the entire Baoulé-Mossi Domain, as the stratotectonic evolution differs across the various regions in the domain.

Baratoux et al. (2011) illustrates the lithostratigraphic sequences for three greenstone belts from east to west; Boromo belt (and associated Lawra belt), Houndé belt and the Banfora belt, all located in the northern to central part of the WAC, in southwest Burkina Faso. The belts trend north to northern-northeast and are composite of bimodal tholeiitic basalts (often pillowed) and interbedded calc-alkaline volcanics, dolerites and gabbros, with interlaying immature detrital meta-sediments, carbonates, volcaniclastics, turbidites and mudstones (Beziat et al., 2000; Baratoux et al., 2011; Metelka et al., 2011; Hein, 2016). The lithostratigraphic columns constructed for studied regions in Burkina Faso show the intercalation between the major volcanic and volcano-sedimentary sequences, such as the columns drafted by Hout and Sattran (1987) for the Boromo Greenstone Belt, and by Hein et al. (2004) along the Boromo-Goren Greenstone Belt. The composition of the volcanic and plutonic units evolved from similar Palaeoproterozoic magmatic suites (Beziat et al., 2000; Lompo, 2010; Baratoux et al., 2011).

Ultramafic plutons with cumulate pyroxenite dykes also form part of the greenstone belts, representing the remains of a crystallized magma chamber at the

base of a volcanic island arc (Beziat et al., 2000; Lompo, 2010). The U-Pb zircon ages obtained from the Goren greenstone belt (central Burkina Faso) and the Houndé greenstone belt are between 2240Ma and 2170Ma (Castaing et al., 2003). There are associated granitioid and TTG (tonalite, trondhjemite, granodiorite) plutons and batholiths, and sedimentary basins (Tarkwaian) in some regions, between the greenstone belts (Debat et al., 2003; Baratoux et al., 2011; Block et al., 2016). Doleritic and gabbroic dykes intrude into and cross cut all of the Birimian units (Lompo, 2010; Metelka et al., 2011; Jessell et al., 2015).

Granitoid batholiths and plutons make up more than half of the Birimian rocks, contributing significantly to the continental crustal growth of the Baoulé-Mossi Domain during the orogenic events referred to as the Eburnean Orogeny (Egal et al., 2002; Naba et al., 2004; Pawlig et al., 2006; Baratoux et al., 2011). Three magmatic cycles during which major granitoid emplacement occurred are at 2200Ma, 2160-2130Ma, and at 2100-2070Ma (Feybesse et at., 2006; Lompo, 2009; Vidal et al., 20009; Lompo, 2010; Tshibubudze et al., 2013; Ganne et al., 2014). Emplacement of the granitoids together with the regional transcurrent deformation and northwest to southeast shortening separated the greenstone belts into folded, linear segments trending north/north-northeast (Pons et al., 1995; Naba et al., 2004; Vegas et al., 2008; Lompo, 2009).

A number of the Birimian granitoids in northeastern Burkina Faso and western Niger were studied based on the geochemical and geochronological data, including studies by Pons et al. (1995), Naba et al. (2004), Vegas et al. (2008) and Ganne et al., 2014. The classification of the Palaeoproterozoic plutonic units studied in Burkina Faso includes foliated tonalite-granodiorite-monzogranitic and the alkali granite suites, composed of quartz, albite, microcline and hornblende (Pons et al., 1995; Lompo, 2009; Tshibubudze et al., 2013). Lompo (2009; 2010) distinguishes between two series of grainitoids present in the Baoulé-Mossi Domain; amphibole bearing group of granitoid batholiths, some with a gneissic texture, aged at 2200Ma to 2020Ma, and the biotite (and minor muscovite) bearing group of granitoids without amphiboles, dated at 2150Ma to 1950Ma.

In northwestern Ghana, the granitoid domains comprise of high-grade (mafic) ortho-and para-gneisses, granodiorites, and late stage (potassic) granites (Block et al., 2016). TTG's (foliated) emplaced at ~2210Ma make up the oldest granitoids, and

they were subsequently intruded by non-foliated granites at between 2150Ma and 2095Ma. The alkaline granitoids are the youngest to intrude of the three groups of granitoids in this region, between ~1890Ma to 1820Ma (Naba et al., 2004; Vegas et al., 2008). The batholith studied by Naba et al. (2004) in Fada N'Gourma, west of the FGSZ is composite of hornblende tonalites, trondjhemite and granodiorites, and is host to a biotite granite pluton (the Tenkodogo-Yamba elongate pluton). Based on compositional similarities, this batholith is comparable to the gneissic and sodic calc-alkaline granitoids studied by Hirdes et al. (1996) and Doumbia et al. (1998) in Côte d'Ivoire. The Tenkodogo-Yamba elongate pluton is comparable to the biotite granodiorite and peraluminous granitoids of central Côte d'Ivoire (Naba et al., 2004).

Erosion of the older Proterozoic (and Archaean) domains that were undergoing accretion along a major thrust zone between the Kenema-Man Domain and Baoulé-Mossi Domain served as a source from which the first sediments in intra-cratonic basins were derived (Feybesse and Milesi, 1994; Thieblemont et al., 2004; Kouamelan et al., 2017). Volcaniclastic eruptions and turbidites of tephra and ash from the volcanic belts aged between 2185Ma and 2155Ma are also closely associated with sedimentary deposits (Leube et al., 1990; Feybesse and Milesi, 1994; Feybesse et al., 2006; Roddaz et al., 2007). Hein et al. (2004) has described the sedimentary sequences associated with the Boromo-Goren Greenstone Belt, 75km northeast of Ouagadougou in Burkina Faso; the lithostratigraphic column has lower and upper volcano-sedimentary successions, separated by a volcanic sequence. The lower succession, at ~800m thick, is made up of quartzite, weakly bedded meta-tuffaceous greywacke, siltstone and za, all interbedded with quartzo-feldspathic layers and a rare occurrence of discontinuous felsic tuff layers (Hein et al., 2004). The upper succession, almost double that of the lower succession (~1600m), is comprised of siltstone, shale, feldspathic quartzite-gritstone, meta-conglomerate (gravel to boulder sized), and immature volcanic breccia and tuff (Hein et al., 2004). The Birimian volcano-sedimentary and sedimentary sequences were deposited pre-, during and post- the Eburnean Orogeny (Doumbia et al., 1998; Feybesse et al., 2006; Beziat et al., 2008; Davis et al., 2015). In western Burkina Faso, the Tarkwaian sediments are deposited in a north-south trending linear basin within the Houndé Greenstone Belt, that is about 400km long and up to 2km wide (Baratoux et al., 2011; Koffi et al., 2016). The Tarkwaian sedimentary basin in

southwestern Ghana provided a detrital zircon age of 2133±4Ma, which aids in constraining the age of deposition (Pigois et al., 2003).

The dolerite dyke swarms observed across the craton are reported to have been emplaced during a late stage continental breakup in the large igneous provinces of the WAC (Ernst and Jowitz, 2013; Ernst 2014; Jessell et al., 2015). Jessell et al. (2015) reports that there are six generations of mafic dyke emplacement in the WAC. The NW trending dolerite dykes in Burkina Faso are dated at 1814±26Ma (Castaing et al., 2003; Jessell et al., 2015).

2.2 STRUCTURE

The tectonic evolution of the Baoulé-Mossi Domain in Burkina Faso and Ghana can include up to four deformation phases as described by different authors in the different regions. This includes work by Hein (2010), Baratoux et al. (2011), Ganne et al. (2011), de Kock et al. (2012), Tshibubudze and Hein (2013), Block et al. (2015), Tshibubudze et al. (2015) and Fontaine et al. (2017). The first deformation is the Tangaean Event (Tshibubudze et al., 2009; Hein, 2010) or Eoeburnean (Block et al., 2015; Baratoux et al., 2015) dated at 2170-2130Ma. The Eoeburnean defined by de Kock et al. (2012) in Ghana deformed the Birimian rocks that are older than 2150Ma, and is bracketed to have occurred between 2350Ma and 2150Ma (Petersson et al., 2016). The Tarkwaian sequence was not affected by D1 in Ghana (Eisenlohr and Hirdes, 1992; Davis et al., 1994). In the southwest region of Ghana, Allibone et al., (2002) and Perrouty et al. (2012) refer to D1 in this region as Eburnean I (2200-2150Ma). The Eburnean I in southwest Ghana is associated with magmatism, volcanic eruptions and N-S shortening.

D1 in northeastern Burkina Faso is defined by NE-SW compression and crustal shortening, concomitant with the formation of north-northwest trending dextral reverse shear zones, and NW/WNW and NNE/NE trending fold and thrust belts (Tshibubudze et al., 2009; Hein, 2010; Tshibubudze et al., 2015). Tight to isoclinal folds, steep foliation (S1), which is often sub-parallel to the S0 bedding, stretching mineral lineations (L1), and sinistral shear zones are also ascribed to D1 by Feybesse and Milesi (1994), Feybesse et al. (2006), Hein (2010) and Baratoux et al. (2011; 2015). These structures and fabrics have varying intensity across the Baoulé-Mossi Domain, and may not be identified across the entire Domain, as they were overprinted by succeeding deformations (Hirdes et al., 1996; Baratoux et al., 2011).

East-dipping thrusts and shears (and associated branching shear zones) with a dextral reverse shear sense, all trending NW to NNW formed during D1 in northeastern Burkina Faso (Tshibubudze et al., 2009; Tshibubudze and Hein, 2013). Similar structures are reported for the northeastern domain of the Goren Greenstone belt in Burkina Faso (northeast of Ouagadougou) by Hein (2010). This indicates an approximate NE-SW directed σ1 for D1 in NE Burkina Faso (Tshibubudze et al., 2009; Hein, 2010; Tshibubudze et al., 2015). In northern Ghana, D1 is defined by N-S shortening. Regional scale folds with E-W axial planes, shear zones, thrusts, high grade metamorphic banding make up the D1 structures in NW Ghana (Block et al., 2016). The Bole-Nangodi shear zone (BNSZ), a NNW dipping structure is at the contact of the Bole-Bulenga and Maluwe tectono-metamorphic domains. This structure acted as a reverse thrust during D1 in this region (Block et al., 2015; 2016).

The Eburnean Orogeny is a progressive, poly-phase deformation constrained between 2130Ma and 1980Ma based on the radiometric ages from syn-to late-tectonic granitoids and crosscutting relations between structures studied in Burkina Faso and Ghana (Allibone et al. 2002; Naba et al., 2004; Feybesse et al., 2006; Tshibubudze et al., 2009; Hein, 2010; Baratoux et al., 2011, 2015; Metelka et al., 2011; Perrouty et al. 2012; Block et al., 2016; Fontaine et al., 2017). It is regionally defined as D2, and affected the Birimian greenstone-granite belts, the overlying Tarkwaian-type sediments, and reworked some of the structures in the Archaean rocks (Eisenlohr and Hirdes, 1992; Feybesse and Milesi, 1994; Feybesse et al. 2006; Kouamelan et al., 2017). Allibone et al. (2002) refers to D2 as the Eburnean II deformation (dated at 2116-2088Ma) in southwest Ghana, and it similarly affected both Birimian sequences and Tarkwaian sediments, accreting the volcano-sedimentary belts and the plutonic units in a NW-SE shortening direction (Feybesse et al., 2006; Perrouty et al., 2012).

Trans-current faulting and shearing mainly oriented NNE/NE to SSW/SW are the main structures of the Eburnean Orogeny (Naba et al., 2004; Baratoux et al., 2011; de Kock et al., 2012; Block et al., 2016). The dip directions vary and the foliation along these structures are anastomosing to the E and W (Baratoux et al., 2011; de Kock et al., 2012; Fontaine et al., 2017). Some of the D2 structures are re-activated pre-existing D1 structures (Vegas et al., 2008; Fontaine et al., 2017). Crosscutting relations are often difficult to identify in the field due to the overprinting

of D2 on D1 structures. A few low angle (~30°) crosscutting fabrics between D1 and D2 structures are, however, present in some study areas in northern Burkina Faso (Baratoux et al., 2011; Metelka et al., 2011).

The direction of principal stress that acted in D2 varies across different regions. Hein (2010) distinguishes between D1 NW trending thrust folds and shears, and the crosscutting D2 NE trending macroscopic fold axial planes and shear zones in the Goren Greenstone Belt, north of Ouagadougou in Burkina Faso. A crustal scale anticline formed between the Houndé and Boromo greenstone belts in western Burkina Faso, coevally with pluton emplacements between 2160Ma and 2090Ma (Baratoux et al., 2011). Strike-slip N-S and NW-SE trending faults developed on the flanks of the regional scale folding (Feybesse and Milesi, 1994; Baratoux et al., 2011). NE trending micro-and macro-folding, axial planar foliation and a crenulation cleavage also formed during the Eburnean Orogeny (Hein, 2010; Baratoux et al., 2011). Sub-vertical NE-SW trending foliation, which is sub-parallel to S0, is prominent along the Bole Navrongo shear zone in NW Ghana related to the Eburnean event (de Kock et al., 2012).

The ages constrained for D2 and D3 in NW Ghana overlap with the regionally defined Eburnean Orogeny by Feybesse et al. (2006), Tshibubudze et al. (2009) and Amponsah at al. (2015). The Eburnean orogeny is associated with the juxtaposition of terranes onto each other, and N-S extension in the northwestern region of Ghana (Block et al., 2016). The Julie Belt and Bole-Bulenga shear zone in NW Ghana are interpreted to be extensional detachment zones (Block et al., 2016). Regional scale transcurrent faulting with N and NE trends is associated with D2 in Ghana and SW Burkina Faso (Amponsah et al., 2015).

In northeast Burkina Faso, within the MSZ region, NNE-NE trending mylonite zones, shears and folds developed during D2 (Tshibubudze et al., 2009). The MSZ itself underwent a reactivation of D1 structures and displacement was sinistral reverse from dextral in D1 (Tshibubudze and Hein, 2013). Additional shear zone branches formed to the east of the MSZ with sinistral reverse displacement (Tshibubudze et al., 2009; Tshibubudze and Hein, 2013). The direction of shortening for D2 in MSZ region was therefore SE-NW (Tshibubudze et al., 2009) same as that interpretated for southwest and northwestern Ghana (Feybesse et al., 2006; de Kock et al., 2012).

Granitoid plutons that intruded into the greenstone belts in central to western Burkina Faso developed a penetrative S-C fabric and a mylonitic fabric which was interpreted as syn-kinematic with D2 (Hein, 2010; Baratoux et al., 2011). Syn-tectonic granitoid emplacements led to the development of lateral shortening and antiforms at a local scale, and regional scale coaxial compression resulted in the linear greenstone belts (Gasquet et al., 2003; Baratoux et al., 2011). Pluton emplacement of granites in the Fada N'Gourma area, west of the study area has been associated with the Eburnean Orogeny by Naba et al. (2004). The northeast trending Tenkodogo-Yamba elongate pluton was emplaced during late stage brittle deformation associated with D2 in this region (eastern Burkina Faso), where sigmoidal trajectories with a dextral sense of shear formed during magma accent (Naba et al., 2004).

The third deformation, D3, is the Wabo-Tampelse Event. (Hein et al., 2004 ; Feybesse et al., 2006 ; Hein, 2010 ; Baratoux et al., 2011; Perrouty et al., 2012; Tshibubudze and Hein, 2013; Tshibubudze et al., 2015). The age constrains on D3 have not been conclusively determined, but it post-dates D2 and pre-dates the regional NW trending dolerite dykes (Hein et al., 2004; Jessell et al., 2012; Tshibubudze and Hein, 2013). N-S shortening and WNW trending shearing and folds that crosscut older D1 and D2 structures characterize D3 (Hein, 2010). East-west striking crenulation cleavage and chevron folds with east-west striking fold axes crosscut the S1 and S2 cleavage and foliation planes at high angles (Hein, 2010; Baratoux et al., 2011). In northern Burkina Faso, along the Goren Greenstone belt, F3 folds are north verging, with dextral shear zones, and southeast dipping thrusts are interpreted as belonging to D3 (Feybesse et al., 1990; Hein, 2010). Steeply dipping (normal) faults trending NE-SW in western Burkina Faso have been interpreted as D3 structures, but may also have developed in the previous deformation phases D1 and D2, and were reactivated during D3 (Baratoux et al., 2011).

2.3 METAMORPHISM

The Birimian sequences of the Baoulé-Mossi Domain underwent greenschist facies metamorphism on a regional scale, with amphibolite facies and hornblende-hornfels facies reported at local scales (Beziat et al., 2000; Debat et al., 2003; Naba et al., 2004; Feybesse et al., 2006; Ganne et al., 2011; Metelka et al., 2011; de Kock

et al., 2012). Regional metamorphism was concurrent with deformation phases (D1 and/or D2 depending on region) that occurred between 2200Ma and 2090Ma, with more localized ages for successive deformation phases attained for Birimian rocks in Ghana and Burkina Faso (Ganne et al., 2011; Klemd et al., 2002; Block et al., 2015). Shear zones separate the low to high grade tectono-metamorphic domains in northwestern Ghana, along the Bole-Nangodi Shear Zone (Block et al., 2015). In northeast Burkina Faso, the pre-to syn-D1 gneissic units underwent high grade metamorphism i.e. the Dori Batholith of the Oudalan-Gorouol belt reaching granulite facies contact metamorphism (Tshibubudze and Hein, 2013).

The amphibolite facies metamorphic grade was induced by the thermal effect of the emplacement of granitoids at various stages during the Eburnean Orogeny (Debat et al., 2003; Baratoux et al., 2011; Naba et al., 2004). Amphibolite facies is restricted to the proximities of the intrusive contacts with the host rock (Pons et al., 1995; Doumbia et al., 1998). Burial regimes in NW Ghana reached P-T conditions of around granulite facies between 2140Ma and 2110Ma, relating to the regional Eburnean event (Block et al., 2016). Ganne et al. (2011) studied a number of granitoid intrusive contact aureoles within close proximities with the FGSZ. The data revealed two main metamorphic events. The first metamorphic event, M1, was characterized by low temperature and high pressure. This is evident in the mineral assemblage of chlorite and phengite. The second metamorphic event, M2, was a high temperature, medium pressure, and is related to the Eburnean shorterning deformation. Subsequent to M2, a retrogressive phase occurred related to exhumation and hydrothermal alteration (Ganne et al., 2011). Block et al. (2015) states that metamorphic grade changes laterally across domains separated by craton scale shear zones. This is due to exhumation and burial of terranes at different stages of deformation.

2.4 METALLOGENESIS

There are a number of mineralized zones with major types such as Zn-Ag, Cu-Au, diamonds, manganese (or manganese oxides) and Au in Ghana and Burkina Faso (Hastings, 1982; Milesi et al., 1991; Milesi et al., 1992). Copper, nickel and zinc are present in the Birimian units of the Houndé and Boromo greenstone belts and the Eburnean granitoids in Burkina Faso (Hout et al., 1987; Metelka et al., 2011). Magneferrous and carbonate-rich sediments, together with the Fe-Ca-Mg carbonates

and disseminated sulphide mineral deposits are found in sedimentary deposits in Ghana (Leube et al., 1990).

Gold mineralization in the Gourma Province has been associated with the hydrothermal alterations, during which mineralized fluids permeated weaknesses in structures that resulted from deformation. The metamorphogenic origin of the gold deposits in the Boromo and Houndé greenstone belts in Burkina Faso are considered to be derived from an older auriferous source within the volcanic and volcano-sedimentary units of the belts (Hout et al., 1987). Deposits in other parts of the Baoulé-Mossi Domain have been reported to be either post-metamorphism (Leube et al., 1990; Milesi et al., 1992; Klemd et al., 2002), synchonous with metamorphism (Mumin et al., 1996; Oberthur et al., 1996) or post-metamorphism (Mumin et al., 1996).

Gold mineralization in eastern Burkina Faso is related to the Eburnean Orogeny and is confined to the structures that formed during this deformation i.e. shear zones, tension gashes and quartz vein systems (Klemd et al., 1997; Beziat et al., 1998; Feybesse et al., 2006;; Tshibubudze and Hein, 2013; Hein, 2016; Vearncombe and Zelic, 2015). The temperatures at which mineralization in the Daibatou deposit, eastern Burkina Faso, occurred are between 300°C and 380°C, at pressures between 3kbar and 5kbar (Klemd et al., 1997). Fault systems, shear zones and contacts of the greenstone belts and magmatic bodies, are hosts of gold mineralization in the Birimian Terranes (Milesi et al., 1992; Feybesse and Milesi, 1994; Baratoux et al., 2011).

Gold deposits relating to the Eburnean event are also hosted within quartz veins that formed synchronously with deformation and metamorphism (Bourges et al., 1998; Klemd et al., 1997; Beziat et al., 2008). Mineralization resulted from an infiltration of hydrothermal fluids into spaces created by the brittle deformation. These brittle structures are of regional scale, up to 10km (Feybesse et al., 2006). Hydrothermal fluids trapped into faults at the hinges of folds, tension gashes and dilation bends precipitated and formed quartz veins with gold mineralization either hosted within, or adjacent to the veins (Feybesse et al., 2006; Beziat et al., 2008).

Ghana's richest source of gold is found in the NE trending Ashanti belt, southwest Ghana (Leube et al., 1990; Feybesse et al., 2006). It is the largest gold deposit discovered in West Africa to date, with several network deposits located in

brittle-ductile structures (mainly faults) related and adjacent to it (Allibone et al., 2002; Parra-Avila et al., 2015).

The Oudalan-Gorouol volcano-sedimentary belt located in northeastern Burkina Faso hosts gold deposits in metallogenic corridors that are northwest trending, including the Essakane Mine Trend (Tshibubudze and Hein, 2013). Also in northeast Burkina Faso is the Taparko gold deposit, located to the east of the Bouroum-Yalogo greenstone belt, which is hosted by a network of quartz veins in a northern-northwest trending shear zone (Bourges et al., 1998). Mineralization is concentrated at D1 (Tangaean deformation) and D2 (Eburnean Orogeny) structure intersections, where dilated zones developed and fluids infilled the spaces. Sheeted and stockwork veins and (often crosscutting) buck quartz veins developed and host the gold deposits found in the region (Bourges et al., 1998; Tshibubudze and Hein, 2013).

In southern Burkina Faso, metamorphosed volcano-sedimentary units and schists host the Kiaka gold deposit (Fontaine et al., 2017). The deposit has hydrothermal mineral assemblages of sulphides (pyrite, pyrrhotite, chalcopyrite), actinolite, phlogopite, and quartz-carbonate veins during a two-stage mineralization process (Fontaine et al., 2017). The two gold mineralization events are characteristic in Birimian terranes of the WAC (Eglinger et al., 2015; Fontaine et al., 2017). In the Kiaka deposit, the first stage of mineralization is responsible for 80% of the gold deposits present and the second stage gold mineralization is concomitant with alteration caused by a latter deformation (Fontaine et al., 2017). In the north to northeast trending Houndé and Boromo greenstone belts (in west to southwest Burkina Faso), the gold mineralization age is constrained by granitoid intrusion events between 2113Ma and 2097Ma, that lead to the formation of the gold bearing high strain zones (Baratoux et al., 2011; Hein, 2016).

Hein (2016) characterizes mineralization as principally located along the margins of granitoids, and is hosted by quartz veins, small shears and dilational bends in the Bagassi gold deposit, located on the eastern margin of the Houndé greenstone belt. These granitoid plutons intruded into metamorphosed tholeiitic basalt-dolerites and gabbros (Hein, 2016). The highest gold grades are within and along the granitoid pluton contact margins (Hein, 2016). The Wona-Kona gold deposit hosted within the Houndé greenstone belt is one of the largest deposits in

west Burkina Faso, and it occurs within highly strained and sheared rocks (Augustin et al., 2016). Mineralization occurred during polycyclic, long lasting brittle-ductile deformation events, entailing progressive folding of quartz veins and boudinage formation (Augustin et al., 2016).

CHAPTER 3: METHODOLOGY

3.1 DESKTOP ANALYSIS

The desktop studies entailed analysis of geophysical data (Reduced To Pole (RTP) 1st derivative magnetic), satellite and remote sensing images (Landsat, ASTER, Google Earth), and the Digital Elevation Model (Gourma region only) of the study area. Total Magnetic Intensity (TMI) and Residual Magnetic Intensity (RMI) (1:250 000) maps and preliminary interpretation geological map drafted by Gryphon Minerals were also provided by the company. These images were helpful for field work planning i.e. locating outcrops and selecting viable routes to complete traverses.

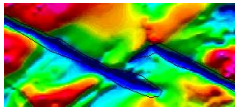
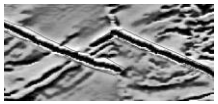
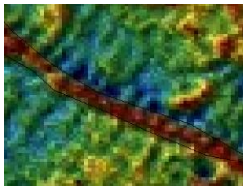
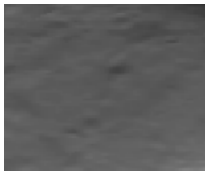
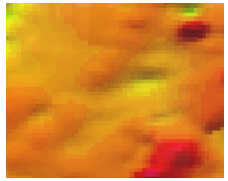
3.1.1 Geophysical Data

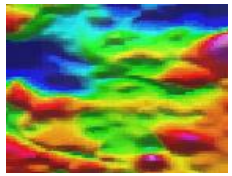
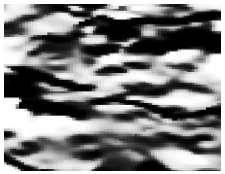
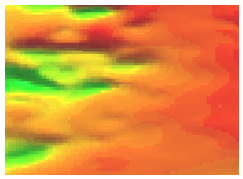
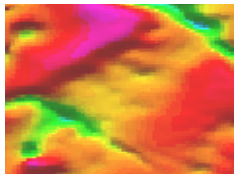
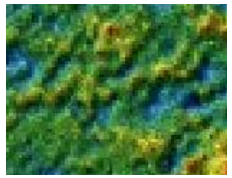
The geophysics magnetic data was used to create a lineaments worm map of the most prominent trends and structures (Figure 3.1). The lineament patterns assisted with the prelimenary interpretation of structures along the FGSZ. The minor shear zones were also delineated using the magnetic imagery, as they have a distinct straited texture, in elongated NE trending bodies. Polygons were created as perliminery interpretaions of different rock types based on magnetic textures and signatures, prior to field work. The different data layers, or shapefiles, were plotted in ESRI ArcGIS®'s ArcMap 10.3 as lines, polygons and points were overlain to create maps in a geographically referenced space. Extisting 1: 2000 000 and 1: 1000 000 geological maps (Appendix A, B, C) and published geological interpretations (BRGM, 1992; BUMIGEB, 1992; Vegas et al., 2008; Naba et al., 2004) were also used as reference maps. These maps were georeferenced (where necessary) and overlaid in ArcMap, to infer lithology types where outcrops were available.

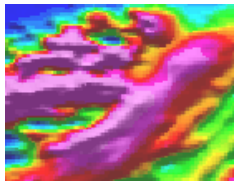
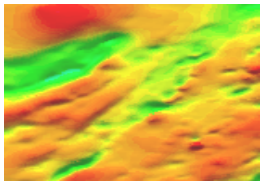
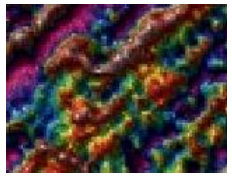
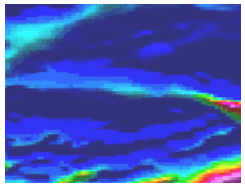
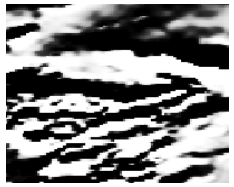
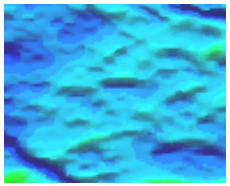
Table 1 summarizes the geophysical charateristics of each rock type. Units that are not extensively outcropping were not easily distinguishable in the geophysical images. These units are the quartz diorite, gabbro, tonalite, meta-volcaniclastic greywacke, tuff and pyroclastic sequences. For these units, field data was used as the primary source of data for detailed, accurate mapping, and reference maps were used as a secondary source to plot and infill representative polygons. The sedimentary sequences were also limited in outcrop. This unit was plotted based mainly on the TMI 1st Vertical Derivative imgery data. The dolerite

dykes were the most discernible units in the magentic images. Their NW-trend is visible on all geophysical data, and outcrops and samples confirmed the location of the dykes. The pyroxenite has a high magnetic signature in the TMI 1st Vertical Derivative image. Field data confirmed the pyroxenite outcrop locations, and inferences were made in the map were similar high magnetic signatures exist. The meta-basalt, granite, granodiorite and gneissic units had sufficient outcrop and sample data to be confidently plotted.

Table 1: *A summary of the magnetic signatures and features that were identified as characteristic for each lithology during desktop studies. Some units could not be clearly identified in the geophysical imagery, and no representative polygons could be interpreted from the imagery data alone. Field data took precedence over imagery data, and this aided in increasing the accuracy of interpretations based on ground truth. The scale of the images in the table is at a length of ~2km.*

Geological Map Legend	**Rock Type**	**RTP RMI Signature/Response**	**TMI 1st Vertical Derivative**	**Comment**	**Airborne Magnetic TMI RTP 1st Vertical Derivative**	**Comment**
	Dolerite Dyke			NW trending low magnetic response, linear bodies.		Linear bodies of high magnetic signature.
	Meta-sedimentary Sequence			Medium to high magnetic response; smooth texture relative to all other lithologies.		Low magnetic response.
	Meta-Volcaniclastic Greywacke; Pyroclastics; Tuff			Not well defined response and texture.	N/A	Not well defined.

	Quartz Diorite			Not well defined response and texture.		Lenses of high magnetic signature, white to red response.
	Tonalite			Not well defined magnetic signature and texture.		Similar signature to granite but not as well defined.
	Granite; Aplites			Highest magnetic signature of all lithologies; smooth texture.		Lenses of high magnetic signature, white to red response.
	Granodiorite (TTG; Gneiss)			Variable magnetic signature from medium to low responses; slightly rough texture.		Low to medium magnetic signature with blue-green response.

	Gabbro			High magnetic signature; rough texture.	N/A	Not well defined.
	Meta-Basalt			Variable magnetic response from medium to low signatures; smooth texture with linear fabrics indicating schistosity and/or tightly folded sequences.		Linear fabric of varying magnetic signatures.
	Pyroxenite			Lowest magnetic signature of all lithologies, rough texture.		Highest magnetic signature with white response.
	Granitic gneiss			Low magnetic signature with blue response; rough and stippled texture plutonic bodies.		Medium to high magnetic signature.

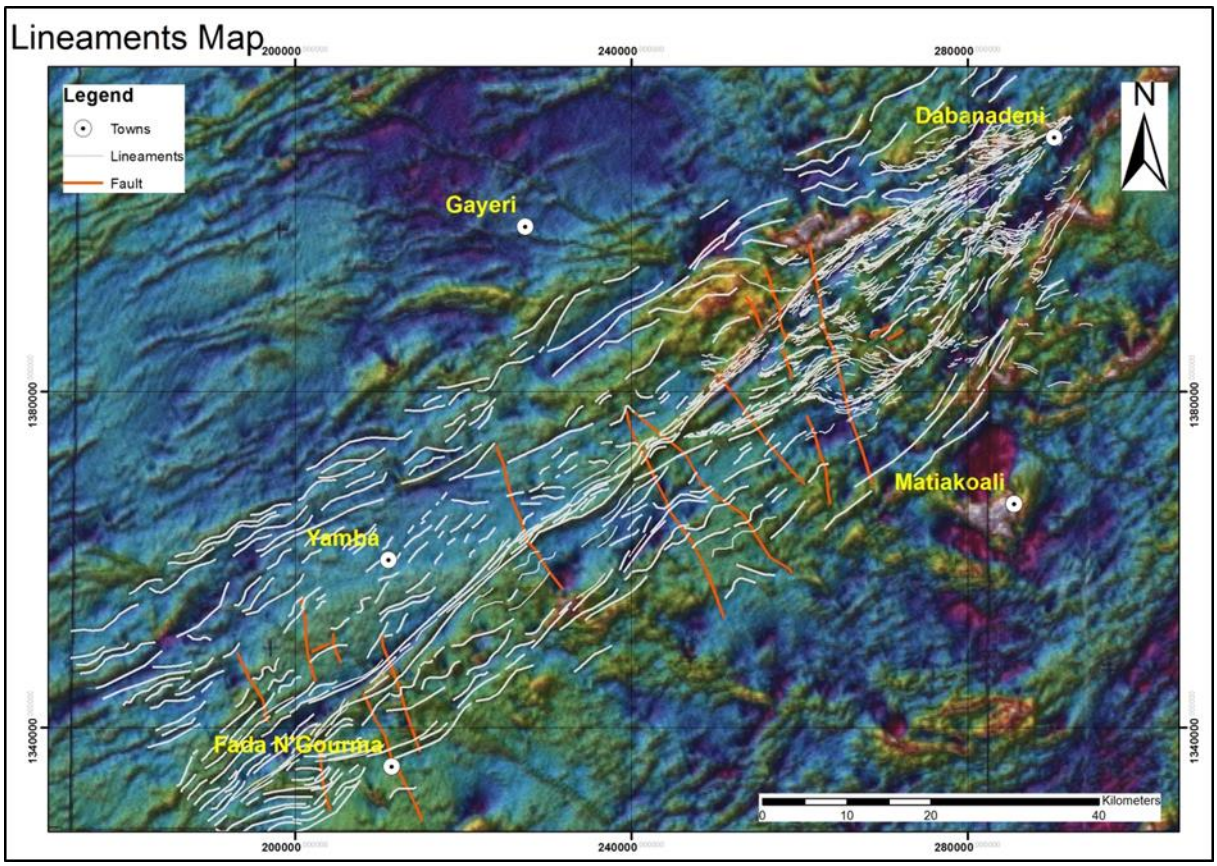


Figure 3.1: *Lineaments were traced out from the magnetic imagery data, in ArcMap. Structures such as faults could be mapped in the desktop studies, even when not identified in the field due to scarcity of outcrops.*

3.1.2 Google Earth, Landsat and ASTER Imagery Data

At a scale of 1:2500, over a distance of ~190km (paralelle to shear zone strike) and an average width of ~60km along the FGSZ, 124 Google Earth images were cropped and saved. These images, with coordinates marked at their corners, were transferred to ESRI ArcGIS®'s ArcMap 10.3, where they were individually georeferenced. A mosaic was then constructed using the images as seen in Figure 3.2 a. This aided in extracting attributes in ArcMap such as village names and roads. Features such as drainage patterns, topographic patterns and outcrops with discernable trends and stuctures were traced out and plotted as individual layers (shapefiles). Drainage patterns are useful as they tend to follow geological structures such as lithological contacts, fault zones, dykes and shear zones.

Not much data could be extracted from the ASTER and Landsat images, expect adding detail to the drainage patterns (Figure 3.2 b). Surface lineaments were traced out using Google Earth, Landsat and ASTER images to supplement the

magnetic data worm map. The surface features are not strongly defined, and the trends can only be traced for a few meters, as shown in Figure 3.3. The trends are not as cohesive as in the magnetics data worm map, but a general NE and NW pattern is discrenible.

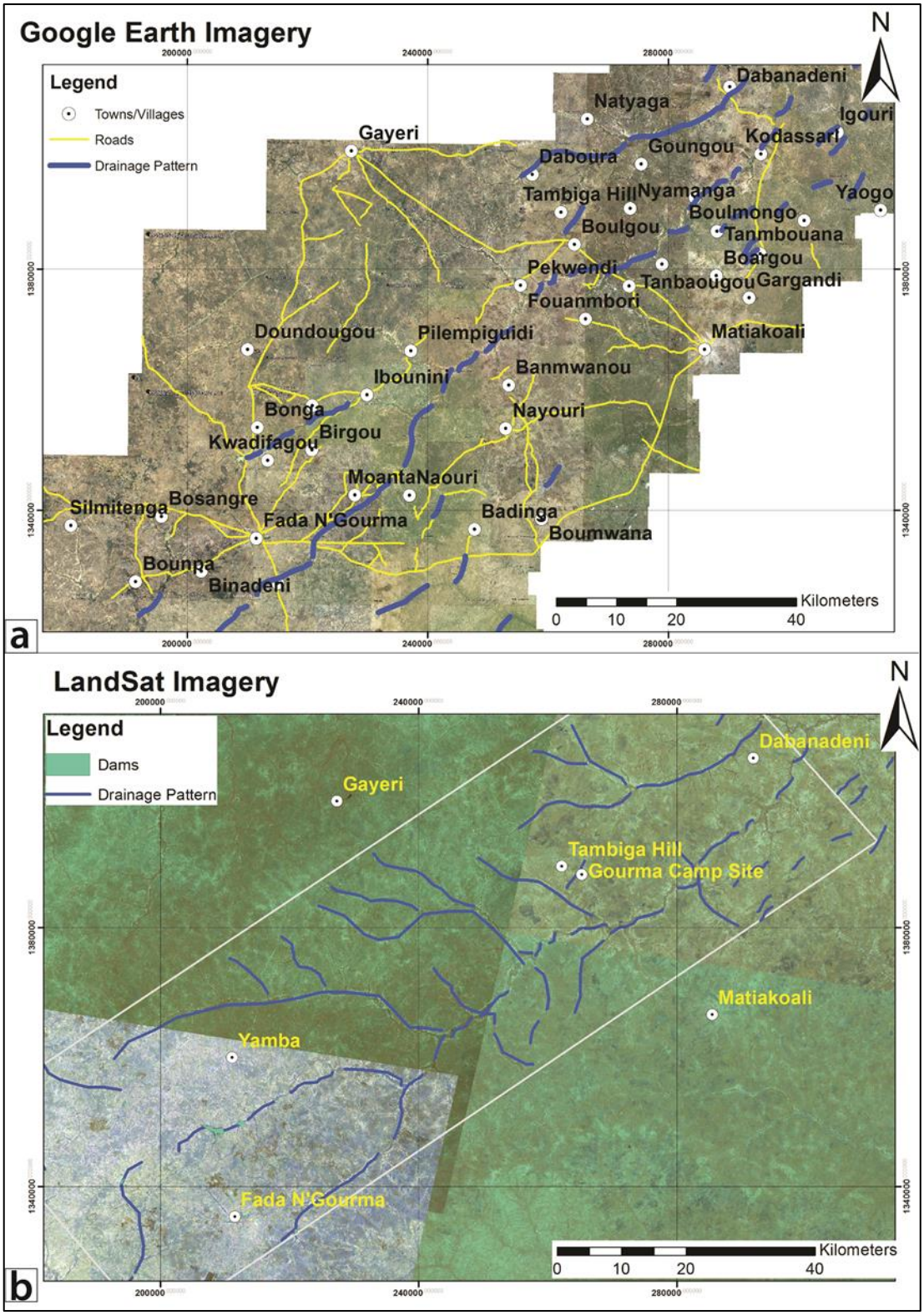


Figure 3.2: *(a) The Google Earth image mosaic with the villages, roads and drainage patterns that were extracted as attributes from the images. (b) LandSat imagery was used to delineate the drainage patterns in detail, and the dams in the study area.*

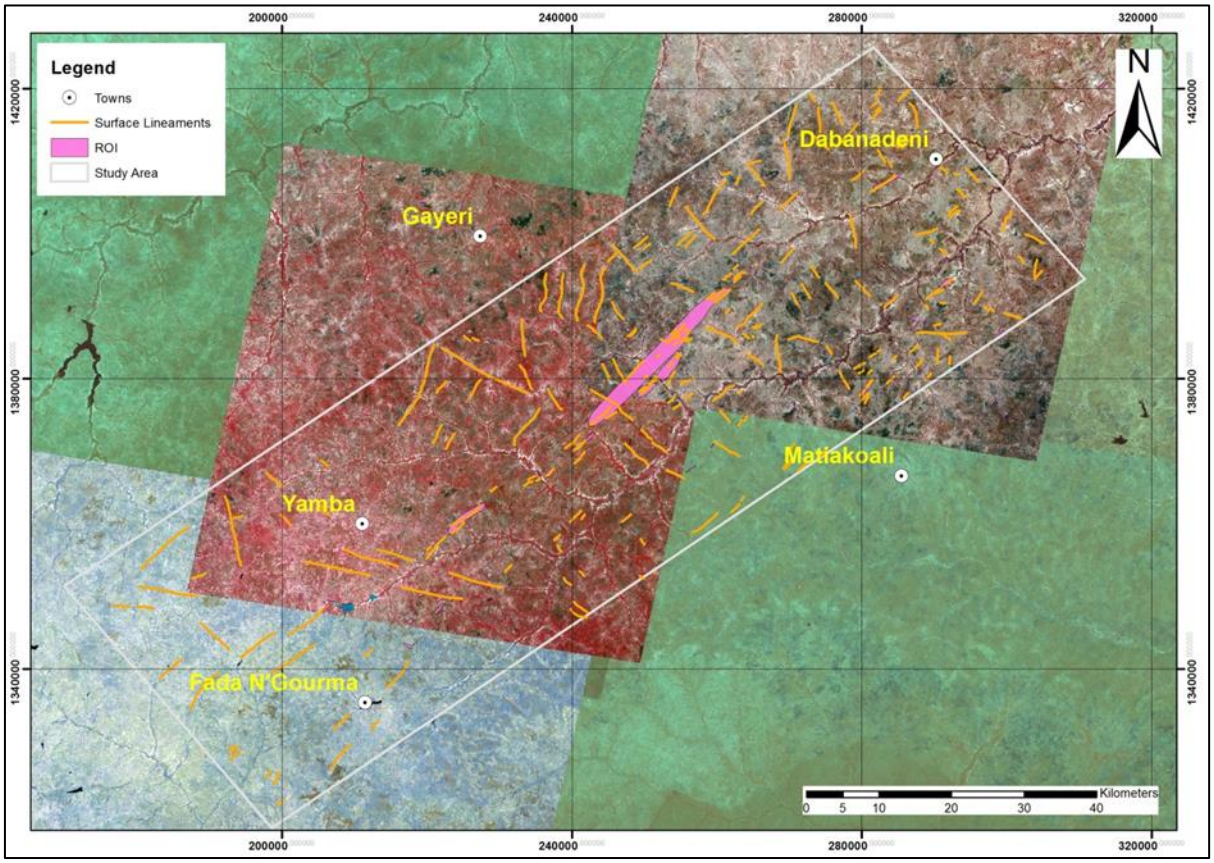


Figure 3.3: *Surface lineaments were extracted from LandSat, ASTER and Google Earth images. Polygons were also made at regions that show features of interest to be targeted during field work (ROI= region of interest). Although the worm map for surface lineaments is scattered and not as cohesive as the magnetic data worm map in Figure 3.1, general NE and NW trends are discernible.*

3.2 FIELD WORK AND DATA INTERPRETATION

Field work was conducted in two phases; April 2016 for 12 days, based in the Gryphon Minerals field camp site, and March/April 2017 for 18 days based in the city of Fada N'Gourma. The exploration company Gryphon Minerals Limited's tenement is located in the Gourma region (Figure 1.1).The FGSZ was mapped over a distance of 150km, via traverses that cross-cut the structure. Accessing the field was done by vehicle, and systematic routes were taken to target regions of interest based on desktop studies and pre-field work planning. The first phase was a reconaissance visit to the Gourma region, but also served as an effective mapping period in the northern half of the study area (blue dots in Figure 3.4). The second phase of mapping was in the southern half of the research area, outside of the tenement, in the region of Fada N'Gourma (yellow dots in Figure 3.4).

Recording of structural measurements, defining geometric and kinematic indicators, rock descriptions and photos of outcrops and GPS coordinates were part of the data collection process in the field. Samples were collected for polished thin sections (oriented and non-oriented), and for geochemical and/or geochronology analysis on selected rock types. The data from field work, including coordinates from the GPS, attributes and sample numbers, was plotted in a Microsoft Excel spreadsheet, and then transferred to ArcMap. The dataset with all station points is on a data disc and can be made avalable if needed (290 station points, 462 data entries due to more than one measurement per station point), but a sample of the dataset is presented in Appendix E. The projection for the study area is WGS 1984 UTM Zone 31 in northern hemisphere. The station points were plotted in ArcMap and used for interpretation, together with the imagery and geophysical data.

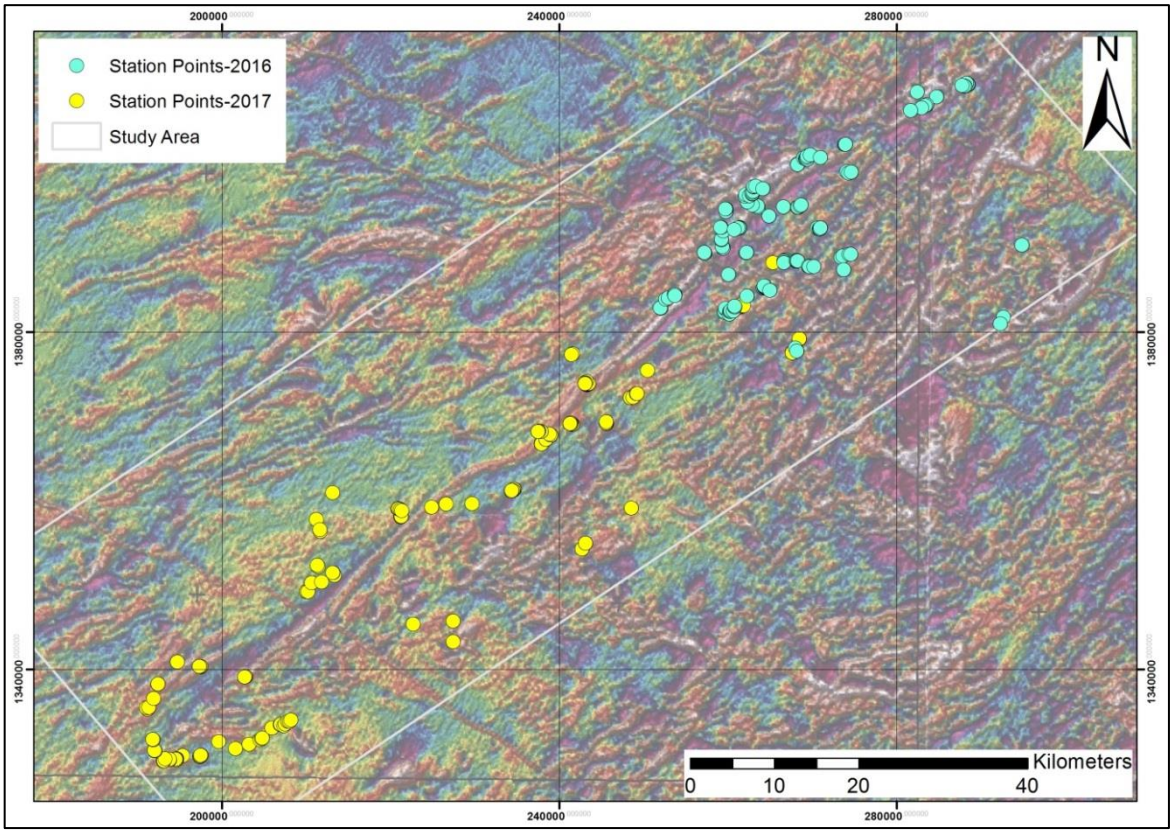


Figure 3.4: *The outlined study area and the dots representing station points. The blue dots indicated station points from the first field work phase in 2016. The yellow dots represent station points from the second phase of field work, 2017. The background geophysical image is the Airborne Magnetic TMI 1st Vertical Derivative of eastern Burkina Faso.*

3.3 ANALYTICAL WORK

A total of 69 samples were collected in the field. However, the last 28 of those samples collected during the second field work phase are lost in transit and could not be retrieved in time for analysis before completion of this study. The field descriptions of these samples still served to suppliment the petrography data for the rock types. Different lithology units within the study area were sampled, and duplicates were collected if a feature was present in the particular unit that distinguished it from other units sampled at different locations, i.e. grain-sizes, fabrics, modal minerology. Analytical work on the samples would serve to classify rock types in the study area.

3.3.1 Thin Sections

Polished thin sections were cut from selected samples for mineral identification under the microscope. Oriented samples were analysed for microstructural analysis, i.e. mineral lineations, foliation, and/or compositional banding. Sample preparation and thin sections cutting was done at the Geosciences Department at the University of the Witwatersrand.

3.3.2 Geochemical Analysis

Three samples were crushed in the jaw crusher, underwent milling and were reduced to a grain size of between 20 and 400 µm. The powder for each of the samples GP006, GP027 and GP043 underwent geochemical analysis to classify the igneous rock type. Inductively coupled plasma mass spectrometry (ICP-MS) instruments with laser ablation systems are used for in situ zircon U-Pb dating, and measurements applied in geochemistry, including measurements of trace elements, radiogenic Pb, Sr, Nd, Hf and Os isotopes, and non-traditional Li, B and Mg isotopes (Fu Yuan, 2010). Whole rock and trace element geochemistry can also be determined using X-ray fluorescence (XRF) spectrometer. The geochemical analytical work was done using the XRF and ICP-MS facilities at the Earth Laboratory (University of the Witwatersrand).

The Excel formated XRF data for whole rock analysis was plotted in the software GCDkit 4.1 (GeoChemical Data Toolkit) for igneous rock classification diagrams (total alkali-silica (TAS) diagram and other ternary diagrams discussed in the geochemistry results section). The TAS diagram for plutonic rocks plots the

weight percentages (wt%) for SiO_2 on the x-axis against Na_2O+K_2O on the y-axis. This diagram subdivides rocks as alkaline or subalkaline/tholeiitic, also as ultrabasic, basic, intermediate or acidic. The wholerock data of each sample plots within the boundaries of a particular rock type according to the wt% the sample is composite of.

3.3.3 Geochronology

The crushed and milled samples GP006, GP027 and GP043 were to undergo further preparation for zircon U-Pb dating. The samples had to undergo mineral separation processes, including the gravity sepration using the Wilfley Table, magnetic separation using the Frantz Magnetic separator (slope 20° and tilt 10°, at intervals of 0.3 amperes (A) with a maximum current of 1.5 A), and gravity separation using heavy liquids (bromoform and diiodomethane). Zircons were picked and mounted onto an epoxy mould, and polished. The mould was carbon coated for imaging of the zircons. Backscatter images were taken using the Scanning Elecron Microscope (SEM) (sample images in Figure 3.5), and Cathodoluminance (CL) images (Figure 3.6) were also taken of the mount, to analyse the internal structures of the zircons (rims and cores) and to identify which zicrons were ideal for laser ablation (LA). The carbon coating was removed prior to LA analysis. Backscatter images were taken at the Microscope and Microanalysis Unit (MMU) facilities, at the University of Witwatersrand, Johannesburg. CL imaging was carried out at the University of Johannesburg, Department of Geology. CL imaging revealed that the zircons had multiple rims around the core. The age from the rims reveal a probable metamorphic age, while the core reveals the probable crystallization age (Pidgeon, 1992; Yuanbao and Yongfei, 2004).

For the laser ablation-induced coupled plasma-sector-mass spectrometry (LA-ICP-MS), a 193nm ArF RESOlution SE excimer laser (Australian Scientific Instruments, Fyshwick) was coupled to a Nu Plasma II MC-ICPMS (Nu Instruments, Wrexham). The Nu Plasma II is equipped with 16 Faraday detectors and 5 ion counting detectors, and all isotopes of interest can be measured simultaneously. All analyses were conducted using a beam with a diameter of 30 µm, a repetition rate of 2.5 Hz and fluence of 1.2 J/cm^2. Data acquisition for each analysis took 95 seconds (about 25 seconds on background, 70 seconds on ablation signal). Raw count rates for ^{206}Pb, ^{207}Pb, ^{208}Pb, ^{232}Th and ^{238}U were collected for age determination. LA-ICP-MS was carried out at the University of Johannesburg, Department of Geology.

Mass bias correction was accounted for by standard bracketing. Primary standards were measured at regular intervals during a measurement batch and used to correct for instrumental mass bias and elemental fractionation. Ten primary standards were analysed at the start of an analysis session, then ten sample analyses, five primary standards, ten sample analyses, five primary standards and the last ten sample analyses for the session. A session is ended with a rerun of ten primary standards. The process was repeated until completion of all three samples. Secondary standards were measured at regular intervals as unknowns to evaluate the accuracy of the measurements. Background signal is collected on mass prior to ablation, and subtracted from the signal. The primary standards used are presented in Table 2;

Table 2: *The standard samples used during LA-ICP-MS, their ages and source publication.*

Sample	Age	Source/Reference
GJ1	608.5±1.5Ma	Jackson et al. (2004)
A1772	2712±1Ma	Huhma et al. (2012); Reinhardt et al. (2015)
A382	1877±2Ma	Huhma et al. (2012) ; Reinhardt et al. (2015)
OGC1	3465.4±0.6Ma	Stern et al. (2009)
The secondary standard sample:		
CDQGNG	1849.8±1.1Ma	Black et al. (2003).

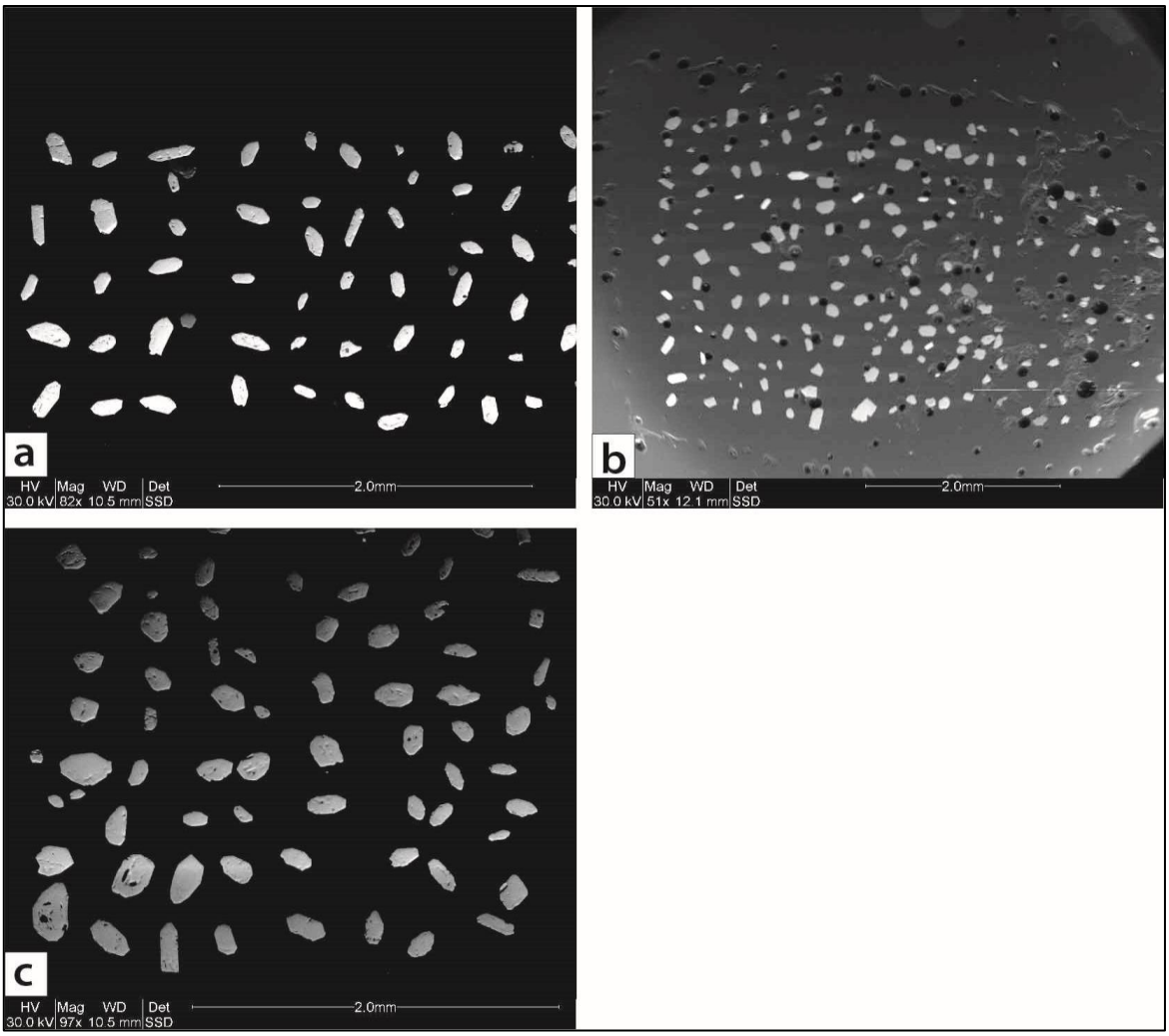


Figure 3.5: *Backscatter electron (BSE) images of zircons from samples (a) GP006, (b) GP027and (c) GP043.*

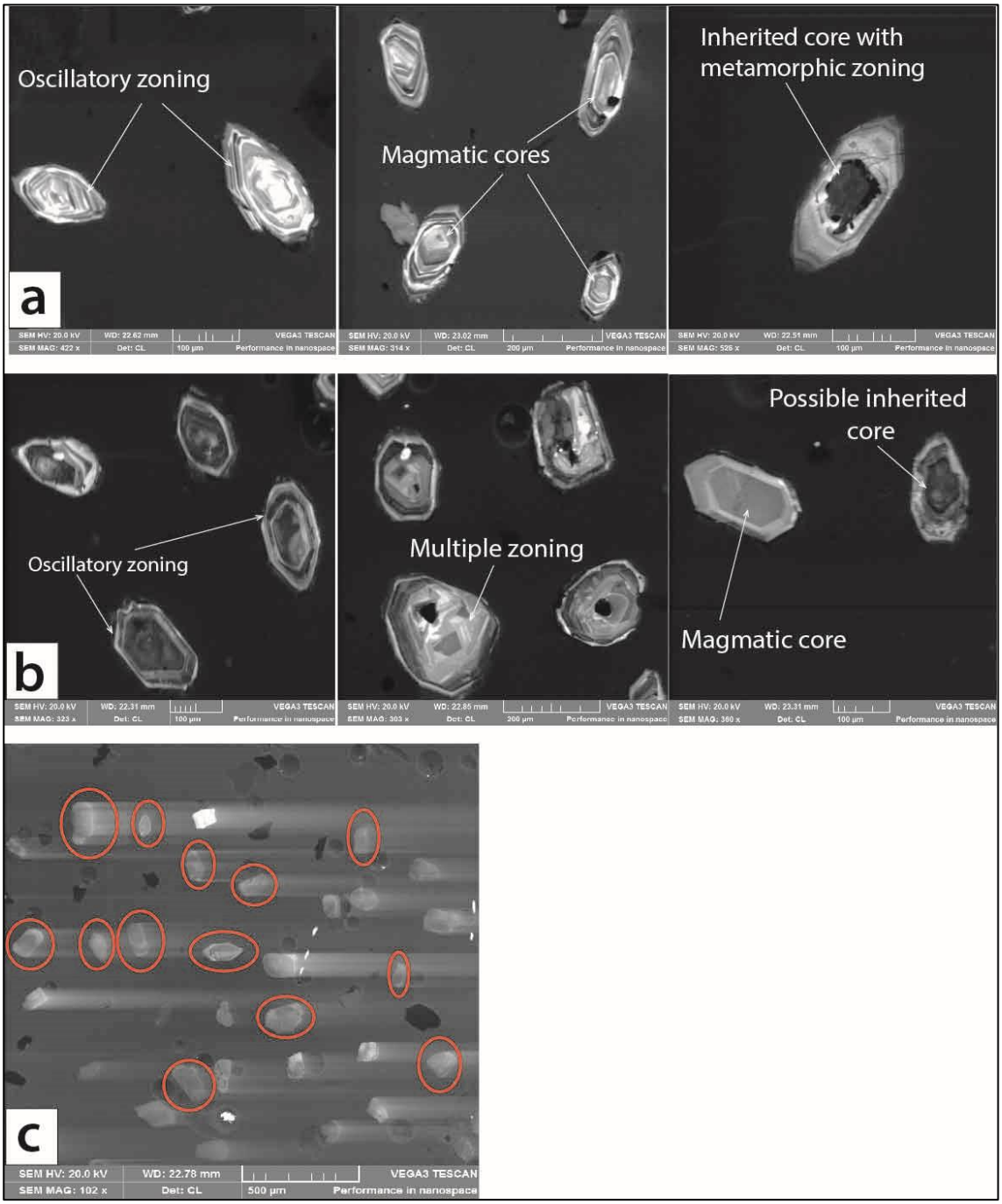


Figure 3.6: *CL images of zircons from sample (a) GP006, (b) GP043 and (c) GP027. The zircons from sample GP006 had contrasting oscillatory zoning. A few of the grains with zoning were targeted for analysis of the rims to get a metamorphic age. Both sample GP006 and GP043 had some grains with darker cores, and these may be inherited cores. Sample GP027 did not yield clear CL images, and internal structures could not be observed (c). For this sample, the centres of the grains were targeted as the cores, for a magmatic age.*

CHAPTER 4: LITHOLOGIES PROXIMAL TO THE FGSZ, AND THE PETROGRAPHY AND GEOCHEMICAL ANALYSIS ON SELECTED SAMPLES

The study area is composite of two NE trending greenstone belts that are parallel to one another, while granite gneiss, granite, granodioritic, dioritic and tonalite plutons are bounded in-between and surround these belts. The granite gneiss and foliated granodioritic units form part of the older rocks found in this study area, and the non-foliated granodiorites, granites, pegmatites and aplite dykes crosscut them. The granite gneiss and foliated granodioritic units are present as clasts in the meta-volcaniclastic greywacke and pyroclastics. Gabbro, pyroxenite, meta-basalt, meta-volcaniclastic rocks and the meta-sedimentary units make up the greenstone belts. The non-foliated granodiorites, granites, tonalites and diorites share intrusive contacts and are closely associated with aplite dykes and pegmatite veins in outcrops. The dolerite dykes cut across all rock units found in the area. All units have undergone a certain degree of metamorphism, and have indicative metamorphic mineral compositions to classify the metamorphic grade.

This chapter focuses on petrographic descriptions of each unit based on the field outcrops, hand samples and thin sections (where available). The lithologies are sub-divided into meta-volcanic rocks, meta-sediments and meta-volcaniclastic sediments, and the intrusive rocks. The last section of this chapter presents the geochemical data from XRF analysis done on selected samples. Presented at the end of this chapter is the interpreted geological map for the study area.

4.1 META-VOLCANIC ROCKS

4.1.1 Meta-Basalt

In outcrop, this unit is massive. The outcrops located <4km to the shear zone have a schistosity that is pervasive. The general orientation of the schist fabric is NE trending, average orientation 032°/66° SE. The meta-basalt is ultra-fine grained, with a grain size of <1mm. The meta-basalt has a metamorphic mineral assemblage of chlorite (40%), muscovite (30%), chloritoid (20%) and minor quartz and sulphides (10%). The outcrops have textural variations. Flow banding can be identified in the massive outcrops. Amygdales are characteristic features in some of the outcrops (Figure 4.1 a and b). The amygdales have quartz, feldspar and carbonate infillings, and the alteration mineral epidote.

4.1.2 Meta-Agglomerate

A volcaniclastic rock that is found in the study area is an agglomerate (Figure 4.1 c). This unit has a conglomerate texture, with rounded, often flattened clasts that are up to ~30cm in size. The clasts have a slight imbrication that indicates a possible volcanic flow direction. The clasts are mafic in composition. They vary in size, and are poorly sorted. The matrix appears to have similar composition to the clasts, and is fine grained (<1mm grain size). The outcrops are ~1.7m high; weather to form upright, angular blocks outcropping on a flat landscape.

4.1.3 Tuffaceous Sequence

The tuff is very fine grained, and has a schistosed fabric with a well-developed foliation (Figure 4.1 d). The foliation is NE trending, with an average orientation of 038°/80° SE. A second foliation, S2, crosscuts S1 at an angle of ~280°/80° SW. There is a compositional layering between Fe-rich laminae (darker in colour) and lighter laminae. The unit has been extremely altered and weathered, but is resistant to erosion due to silicification in some regions. The alteration minerals are mainly micas (biotite and muscovite) and chlorite. The tuff is host to stockwork quartz veins, and there is iron enrichment on the surface of the veins (Figure 4.1 e). There are euhedral crystals of andalusite in the schistosed units, 1mm to 2mm in size that indicate the metamorphic grade reached during related deformation. It hosts euhedral cubic pyrite crystals ranging from mm to cm scales. The tuff is closely associated with a pyroclastic unit.

4.1.4 Pyroclastics

The pyroclastic unit is coarse grained with lithic fragments of up to ~4cm in size, within a fine-grained matrix. The clasts and lithic fragments are angular to sub-angular and poorly sorted (Figure 4.1 f). This unit has a weak foliation that is present in some outcrops. The pyroclastic and tuffaceous sequences are often adjacent to each other in outcrop. There is a difference in susceptibility to weathering between the pyroclastic unit and the tuff; the pyroclastic is softer than the tuff and has a negative weathering profile relative to the tuff. This is due to the tuffaceous sequence being silicified and having Fe-enrichment.



Figure 4.1: *(a) Flow banding is evident in some meta-basalt outcrops, although not well preserved. Some of the outcrops do not have these features preserved and are just massive, or schistosed. (b) The amygdales in the amygdaloidal meta-basalts are slightly flattened. (c) An agglomerate with large mafic clasts of up to ~30cm in length; these clasts are imbricated. These units outcrop as upright, angular blocks up to 1.7m tall.*

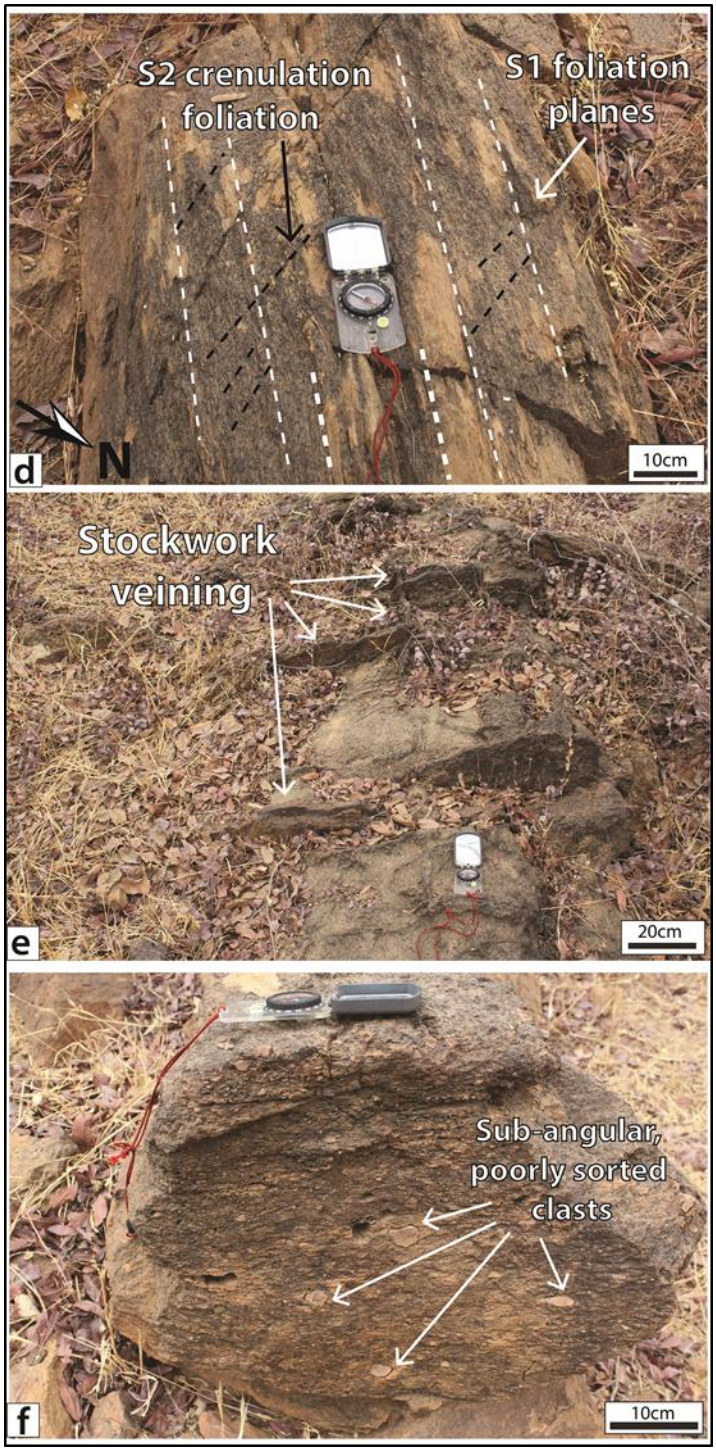


Figure 4.1 Continued: *(d) The foliated tuffaceous unit; the S1 foliation is NE trending. A second foliation crosscuts S1 in a NW orientation. (e) Stockwork quartz veining hosted in the tuffaceous sequence. The tuffaceous sequence and the quartz veins have undergone Fe-enrichment. (f) A pyroclastic sub-outcrop with sub-angular clasts in a medium grained matrix; clasts vary in size, and are poorly sorted.*

4.2 META-SEDIMENTS AND META-VOLCANIC SEDIMENTS

4.2.1 Meta-Volcaniclastic Greywacke

This unit varies from fine grained (clasts of ≤2mm) to coarse grained (clasts up to 15cm in length), with sub-rounded to sub-angular clasts, and elongate clast (Figure 4.2 a). The matrix has a composition of quartz, plagioclase, feldspar, and minor hornblende, epidote, and some outcrops have been silicified (Figure 4.2 b). The clasts are fragments of feldspars, quartz, and some are of granitic composition. A NE trending foliation and compositional banding, and S-C fabrics with dextral shear sense indicators are present in some outcrops. One outcrop has preserved sedimentary features such as downward coarsening of clasts, and cross bedding in the fine grained laminae. This unit is host to gneissic granite clasts and basalt xenoliths (Figure 4.2 c). The xenoliths indicate that the plutonic units and meta-basalts pre-existed the meta-volcaniclastic greywacke.

4.2.2 Meta- Sandstone, Meta-Siltstone and Schist Sequences

The sequences of meta-sandstone, meta-siltstones and graphitic schists are low lying outcrops (Figure 4.2 d). They are foliated, and erode easily.

The sandstone is silica rich, and the minerology is mainly quartz and feldspar (Figure 4.2 e). The grain size is ≤2mm. The siltstone has a finer gained texture, with similar composition as the sandstone. The siltstone has altered into a kaolinite rich unit, and it has a powdery texture. In some outcrops, these units are Fe-enriched and have a dark purple appearance. Some outcrops show primary sedimentary fabrics such as S0 (primary bedding), oriented at an average of 040°/60° and a varying dip direction to the NW and SE.

The schists have a graphitic composition, and have a pervasive fabric in most units. This graphitic schist foliaation has an orientation parallel to the main NE trend. The grain size of the graphitic schist is <1mm. Euhedral andalusite crystals of grain size ~5mm are present in the graphitic schist units (Figure 4.2 f). Outcrops have different characteristics; there are outcrops that have Fe-enrichment in the form of hematite, and others have been silicified.

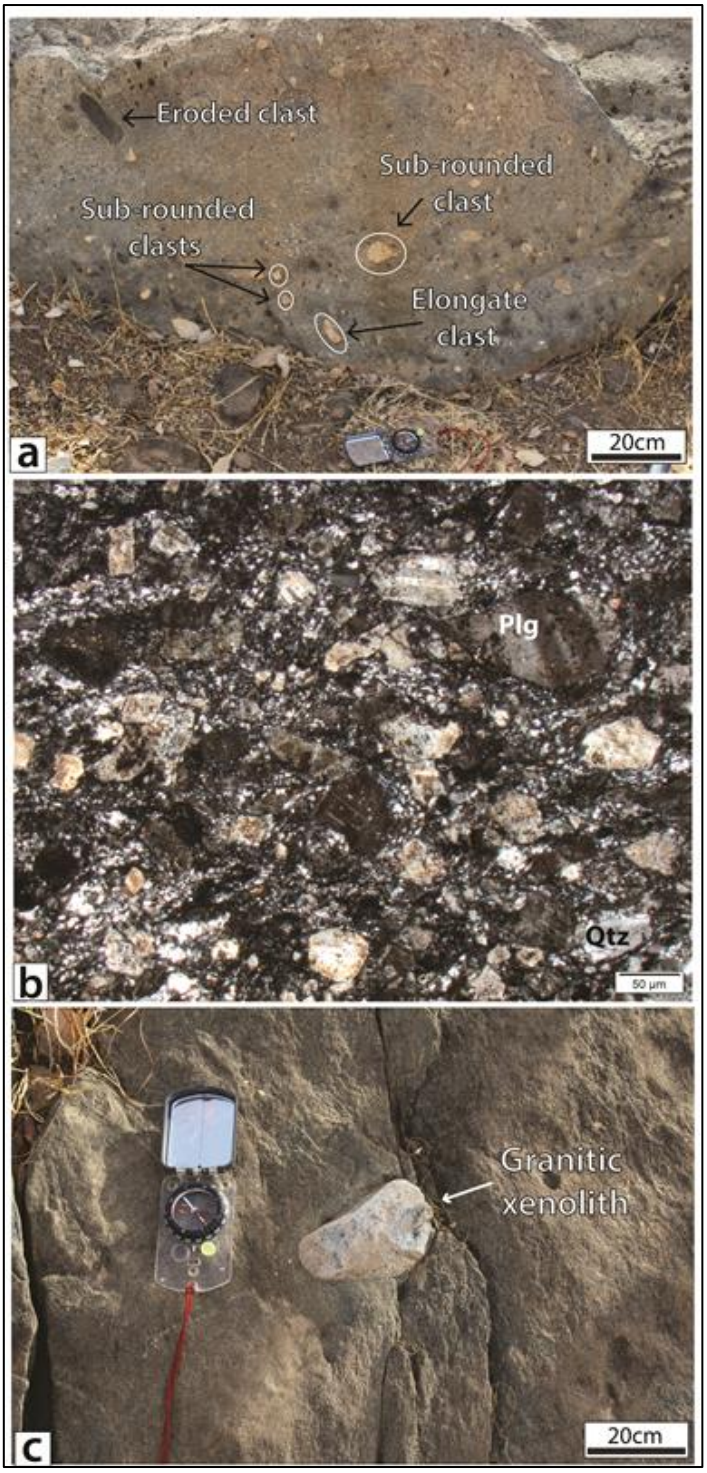


Figure 4.2: *(a) a field photograph of the meta-volcaniclastic greywacke with sub-angular clasts in a mafic matrix. (b) A micrograph of meta-volcaniclastic greywacke sample GP011; the clasts are mainly plagioclase and quartz. The clasts are sub-angular to sub-rounded in shape. (c) The meta-volcaniclastic greywacke is host to granitic xenoliths; this suggests that the basement rocks to the greenstone belts were granitic.*

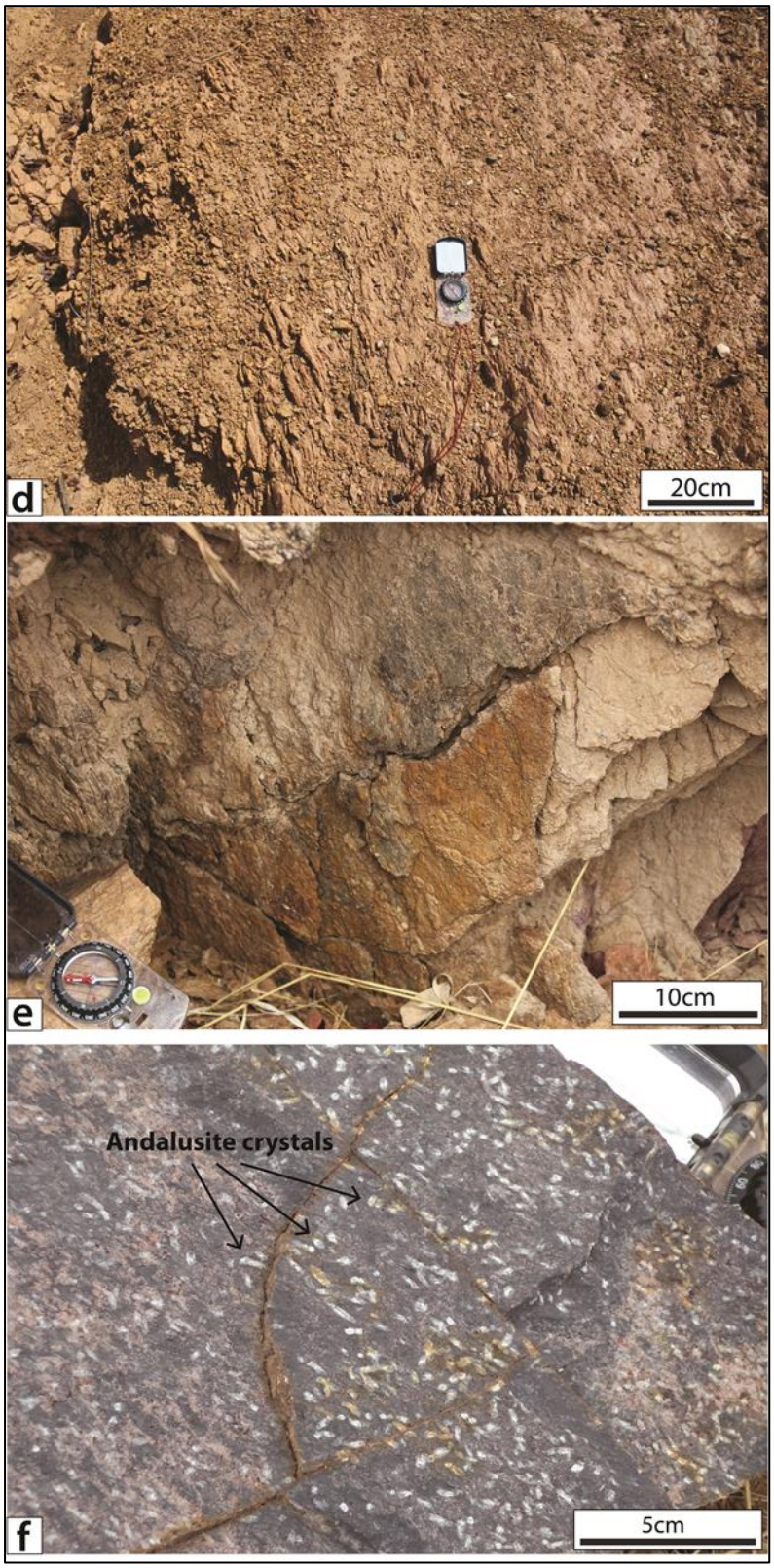


Figure 4.2 Continued: *(d) A low lying siltstone outcrop; this unit has a pervasive NE trending foliation (local orientation for this outcrop is 070°/ 52° SE). (e) A meta-sandstone unit with weak fabrics and oxidation staining, and minor epidote alteration. (f) A graphitic schist with euhedral andalusite crystals; the andalusite crystals are ~5mm in length, and have a generally even distribution.*

4.3 INTRUSIVE ROCKS

4.3.1 Pyroxenite

This unit is mafic to ultra-mafic, with pyroxene, minor olivine and hornblende making up its composition. The modal minerology is pyroxenes 65% (augite, enstatite), hornblende 10%, feldspars 15%, olivine 5% and secondary quartz 5%. It has a varying grain size from fine-grained (1-2mm) to coarse-grained (cm scale). In some outcrops, pyroxenes have crystallized as cumulates of around 3cm in size, forming a mega-crystic texture (Figure 4.3 a and b). A weak NNE to NE trending foliation crosscuts some of the outcrops proximal to the shear zones (Figure 4.3 b).

A compositional layering is also present in the massive outcrops, as shown in Figure 4.3 c and d. The layering has varying thicknesses, and the pyroxene grain textures are identifiable despite the outcrops being extremely weathered. One outcrop in the southern domains has a cumulate, mega-crystic texture (grain size ~5cm), with an intermingling and/or assimilating composition of a leucocratic rock type (Figure 4.3 e). The felsic rock has a feldspar and minor quartz composition, with pegmatitic textures.

In thin section, both clino-(augite and/or omphacite) and ortho-pyroxenes (enstatite) can be identified. The matrix is mainly composed of fine grained feldsparthic laths (anorthite and microcline) (Figure 4.3 f). In other parts of the thin section, the feldspars are interstitial and anhedral in shape. Alteration minerals and textures are visible in thin section, in which pyroxenes altered into hornblende and actinolite, with quartz and feldspar inter-growths. This is indicative of an amphibolite facies metamorphic grade. The pyroxenes have poikiolitic textures with feldspar inclusions (Figure 4.3 g).

The pyroxenites and gabbroic units occur along the NE trending structures. The two units are parallel to the meta-basalt unit. In the southern domains of the study area, the pyroxenites occur as NE trending slivers, parallel to the NE trending structural grain of the study area. These two mafic rock types are found as xenoliths within (migmatized) granodiorites, and are cross cut by late stage pegmatite veins.

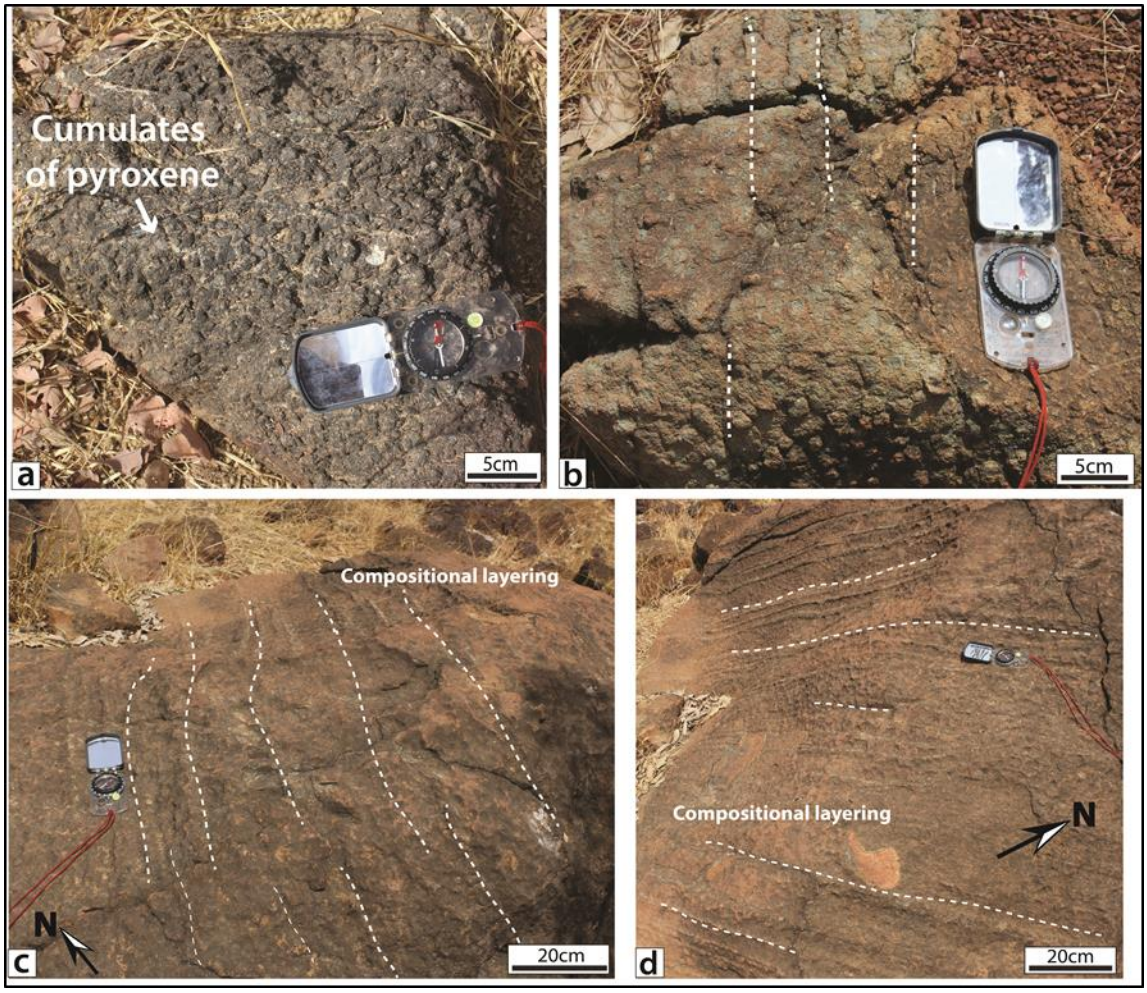


Figure 4.3: *Images (a) and (b) show the mega-crystic pyroxenite outcrops with cumulate pyroxenes of ~3cm in size. In (b), a NNE trending foliation crosscuts this unit. In images (c) and (d) a compositional layering is preserved in the massive pyroxenite outcrops. The layering is dominated by course grained pyroxene crystals (~2cm in size).*

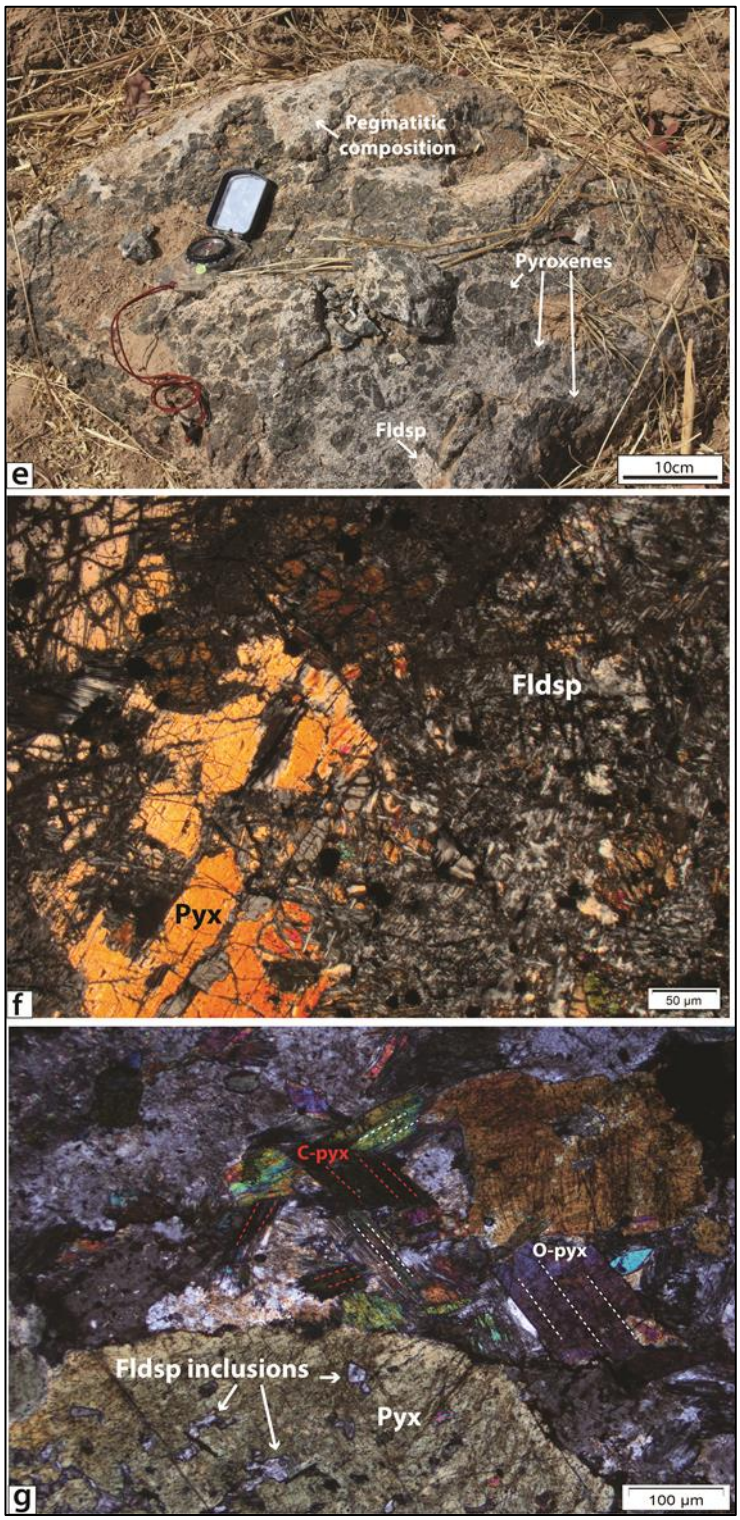


Figure 4.3 Continued: *(e) A pyroxenite outcrop with assimilation textures; the leucocratic unit has a pegmatitic composition. This outcrop is course grained, with crystal sizes up to 5cm. Image (f) shows a thin section micrograph with a clino-pyroxene in a matrix of fine grained feldspar that have a texture resembling "laths". (g) A course grained pyroxenite containing both clino-pyroxenes (C-pyx) and ortho-pyroxenes (O-pyx). The pyroxenes have feldspar inclusions.*

4.3.2 Gabbro

This unit has a grain size of ~2mm, with a composition of pyroxene (40%), feldspar (30%), hornblende (20%), and epidote (10%). In thin section, the minerals are euhedral, and the feldspars are enclosed by the pyroxenes (Figure 4.4 a). The modal minerology does however vary amongst outcrops to a more mafic composition with less leucocratic minerals (80% mafic minerals and 20% plagioclase).

The gabbos are massive, with no fabric crosscutting the outcrops. This unit has limited outcrops in the field. It is intruding into the pyroxenite as described in section 4.3.1, and has gradational composition in a xenolith hosted by a gneissic granodiorite illustrated in Figure 4.4 b. The gabbro has intrusive contacts with the meta-basalt, the meta-volcaniclastic greywacke (Figure 4.4 c). These features aid in correlating the intrusive units to each other; the gabbro intrudes into the meta-basalt, making the meta-basalt relatively older. The gabbro and the pyroxenite also share intrusive contacts, and are xenoliths within a granodioritic gneiss. The granodioritic gneiss is therefore younger than the pyroxenite and gabbro. Pegmatites crosscut all units.

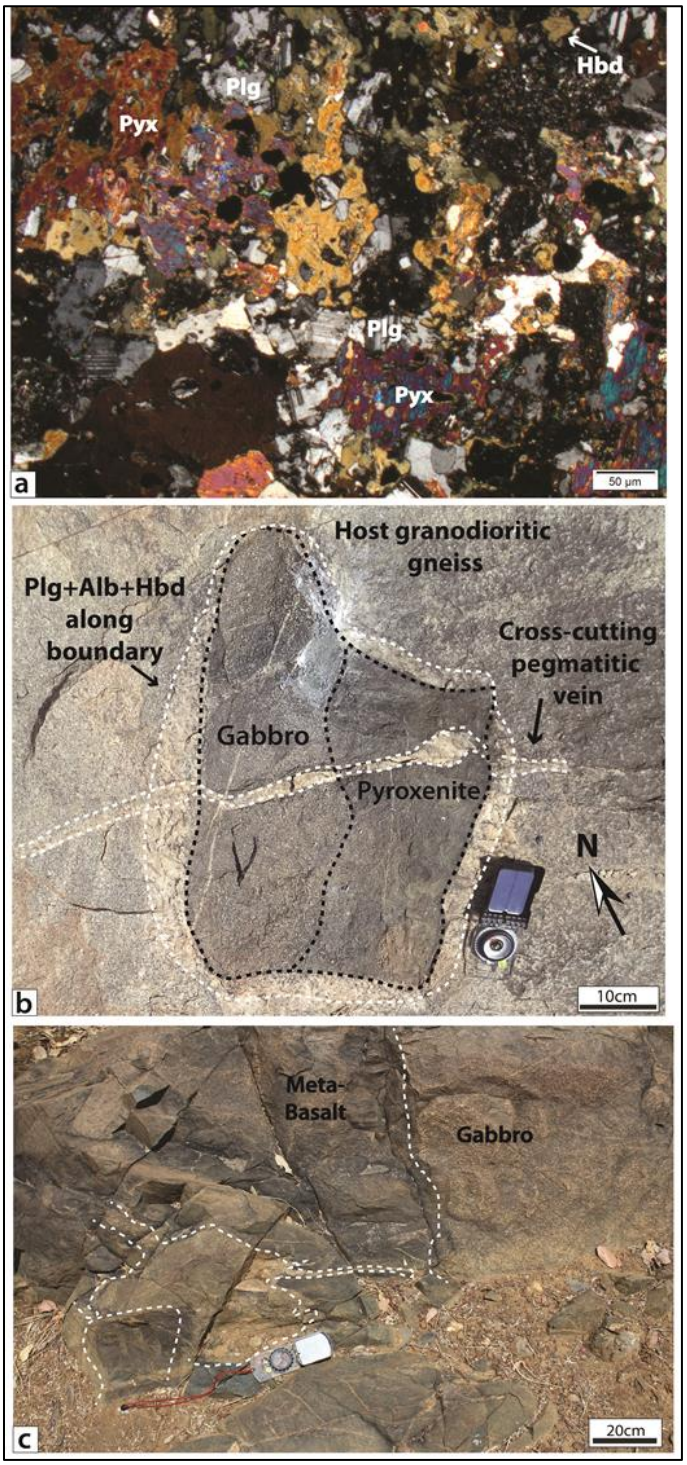


Figure 4.4: *(a) A micrograph of a gabbro; it is a fine to medium grained unit with igneous textures such as poikilitic pyroxenes. It is mainly made up of pyroxenes and feldspars. (b) A gabbro and pyroxenite xenolith within a granodioritic gneiss host rock; the contact between the pyroxenite and gabbro is not sharp but rather gradational. The xenolith and the granodioritic gneiss are crosscut by a pegmatite vein. (c) The intrusive contacts between the gabbro and the meta-basalt; the gabbro is massive, and shows no fabrics.*

4.3.3 Granite Gneiss

The granite gneiss is low lying and massive in outcrop. It has a weak compositional banding defined by segregation of leucocratic and melanocratic layers. The granite gneiss is a fine to medium grained rock (<1-3mm). The modal minerology in thin section is 65% quartz, 20% feldspar, 15% hornblende, and minor chlorite, biotite and pyrite present (Figure 4.5 a). The pyrites have alteration rims around them. The XRF data indicates that the sampled gneiss (GP027) is granitic in composition (presented in section 4.4). The slight pink appearance in outcrop may be due to weathering, or indicates the presence of K-feldspar (Figure 4.5 b).

The K-feldspar appears to be an alteration mineral in some outcrops. It encloses other minerals (i.e. quartz, chlorite), suggesting that it crystallized at a later stage. The quartz grains have three-point boundaries, undulose extinction and in other areas of the thin section grain boundary migration. The larger feldspar grains have poikiolitic textures and minor exsolution lamellae. Hornblende appears as black, foliated grains with preferred orientation. The presence of chlorite suggests a metamorphic imprint lower than amphibolite facies. The granitic gneiss is intruded by the granodioritic units, tonalite and quartz diorite, and occurs as rounded clasts in the meta-volcaniclastic units.

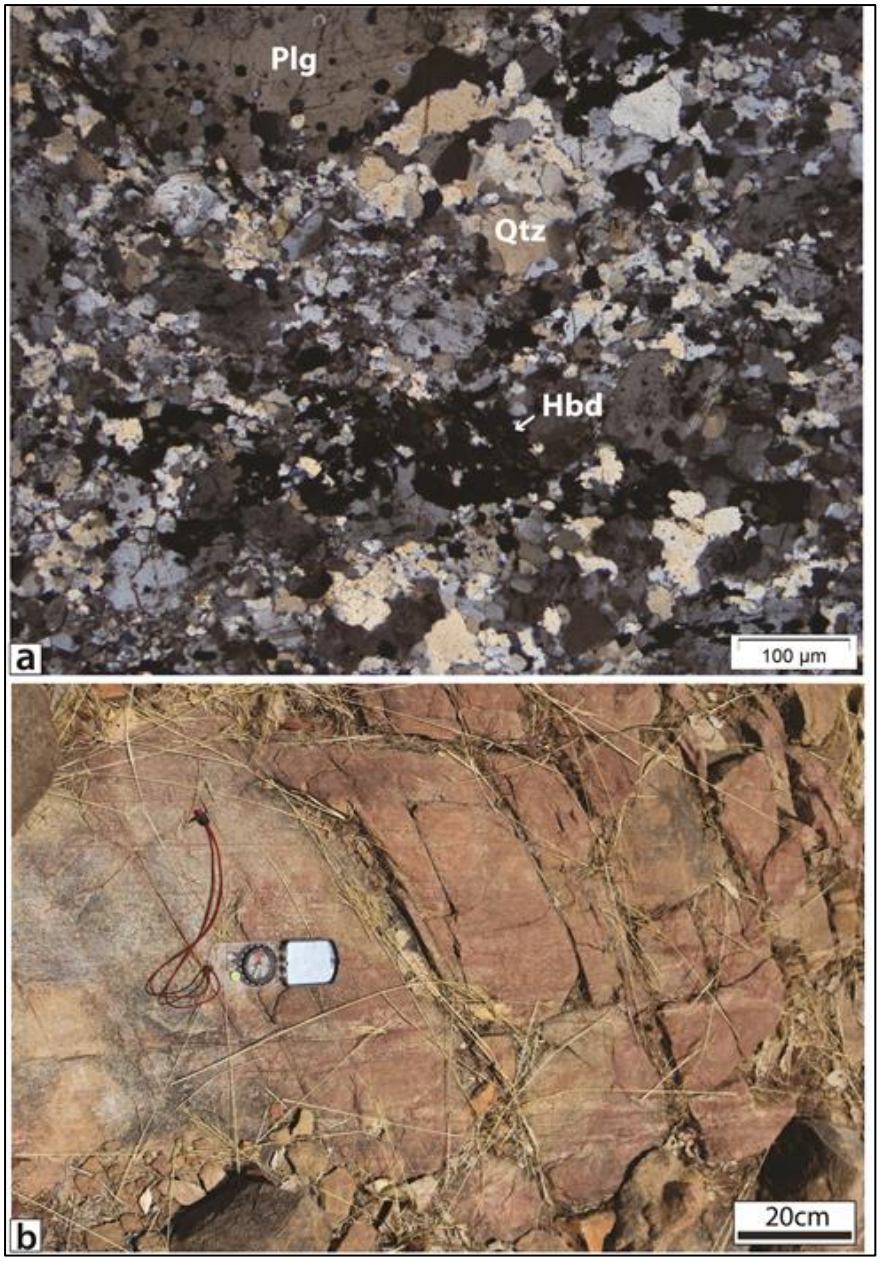


Figure 4.5: *(a) A thin section micrograph of the granite gneiss; the composition is mainly plagioclase, quartz and hornblende. There is minor biotite and the accessory mineral zircon. (b) The granite gneiss in outcrop; this unit is fine grained (<1-3mm). It has a pink appearance, indicating the presence of k-feldspar. This unit is crosscut by fracture cleavage planes.*

4.3.4 Granodiorites

Four different types of granodiorites are classified in the field based on composition and textural characteristics. Crosscutting relations give a sequence of intrusions of each granodiorite suite. The units are described below in sequence of oldest to youngest based on the crosscutting relations observed in the field. These

suites of granodiorites are grouped as part of the Granodiorites layer in the geological map presented at the end of the chapter as Figure 4.19.

The foliated hbd-bt granodiorite

This suite of granodiorites is a hornblende-biotite (hbd-bt) bearing granodiorite, and has a dark appearance in outcrop. These units have a modal minerology 30% biotite, 20% hornblende, 20% plagioclase, 20% quartz and 10% K-feldspar (Figure 4.6 a). Some of the quartz crystals in this unit are fine grained and show recrystallization textures such as sutured boundaries, grain boundary migration and undulose extinction. The composition varies in outcrops, and other outcrops have higher hornblende content.

In some units, there is a weak NW trending foliation with a calculated average orientation of 293°/74° S defined by compositional banding of the amphibole minerals and the felsic minerals (Figure 4.6 b). A gneissic foliation defined by a preferred mineral alignment is also characteristic in the unit. Within ~4km proximal to the shear zones, the gneissic foliation is mainly NE trending (041°/88° SE), and it overprints the weakly foliated outcrop with same composition as shown in Figure 4.6 c.

Crosscutting relationships between the hbd-bt granodiorite and the other suites of granodiorites are observed in the field. Figure 4.6d and e show crosscutting features; the plg-qtz rich granodiorite intrudes into the hbd-bt granodiorite. This unit is amphibolitic in some outcrops, and has a higher amphibole content, with a darker appearance (Figure 4.6 e). Pegmatite veins also crosscut this unit (Figure 4.6 f). From the crosscutting intrusive contacts, it has been established that the hbd-bt granodiorite is the oldest granodiorite. This unit dominates in the southern domains of the study area.

The plg-qtz granodiorite

The plg-qtz rich granodiorite outcrops are massive, and are as high as 1m, or are low lying. The outcrops are extensive, and are up to tens of meters wide. It has a medium to coarse grain size of 1-5mm (Figure 4.7 a). This unit has a composition of 30% plagioclase, 30% quartz, 10% K-feldspar, 20% hornblende and 10% biotite (Figure 4.7 b). The grains are equigranular, and do not show intensive recrystallization textures. There is minor disseminated pyrite content present as an accessory mineral.

This unit hosts amphibolitic enclave as seen in Figure 4.7 a and c that have a composition of ~80% hornblende and ~20% plagioclase. In Figure 4.7 a, that inclusion is elongate in shape, and is parallel to a weak gneissic foliation. The gneissic foliation in some units is defined by a preferred orientation of minerals, and/or weak compositional banding of the leucocratic and melanocratic minerals. The orientation of the foliation in this unit (Figure 4.7 a) is orthogonal to trend at 320°/70 W. The plg-qtz granodiorite crosscuts the hbd-bt granodiorite.

The non-foliated granodiorite

This suite of granodiorite is fine grained (≤1mm to 3mm) and equigranular in texture. The composition of this unit is 40% K-feldspar (microcline), 20% plagioclase, 15% quartz, 15% hornblende and 10% biotite. In outcrop, this unit is low lying, and shows no foliation. This unit crosscuts and has enclaves of the hbd-bt granodiorite (Figure 4.7 d). Pegmatite veins, as shown in Figure 4.7 e crosscut the non-foliated granodiorite. It is difficult to distinguish between the non-foliated granodiorite and the plg-qtz granodiorite in the field, and the intrusive contacts between the two units are faint. Both units are crosscut by the pegmatite veins.

Porphyritic granodiorite

This unit is distinct in outcrop by its porphyritic feldspar texture. The feldspars porphyries are plagioclase and K-feldspar, and they are euhedral as indicated in Figure 4.8 a. The porphyritic granodiorite has a composition of hornblende, biotite, quartz and feldspars (the sample for this unit was not retrieved for analysis, as mentioned in section 3.3). K-feldspar rich pegmatite veins, about 1cm wide, crosscut this unit (Figure 4.8 b). This unit has a sharp contact with the non-foliated granodiorite (Figure 4.8 c). The porphyritic granodiorite has a xenolith of a fine grained hbd-bt granodiorite, with sharp contacts around it (Figure 4.8 d and e). A coarse grained potassium-rich vein, approximately 10 cm wide, crosscuts the xenolith as shown in Figure 4.8 f.

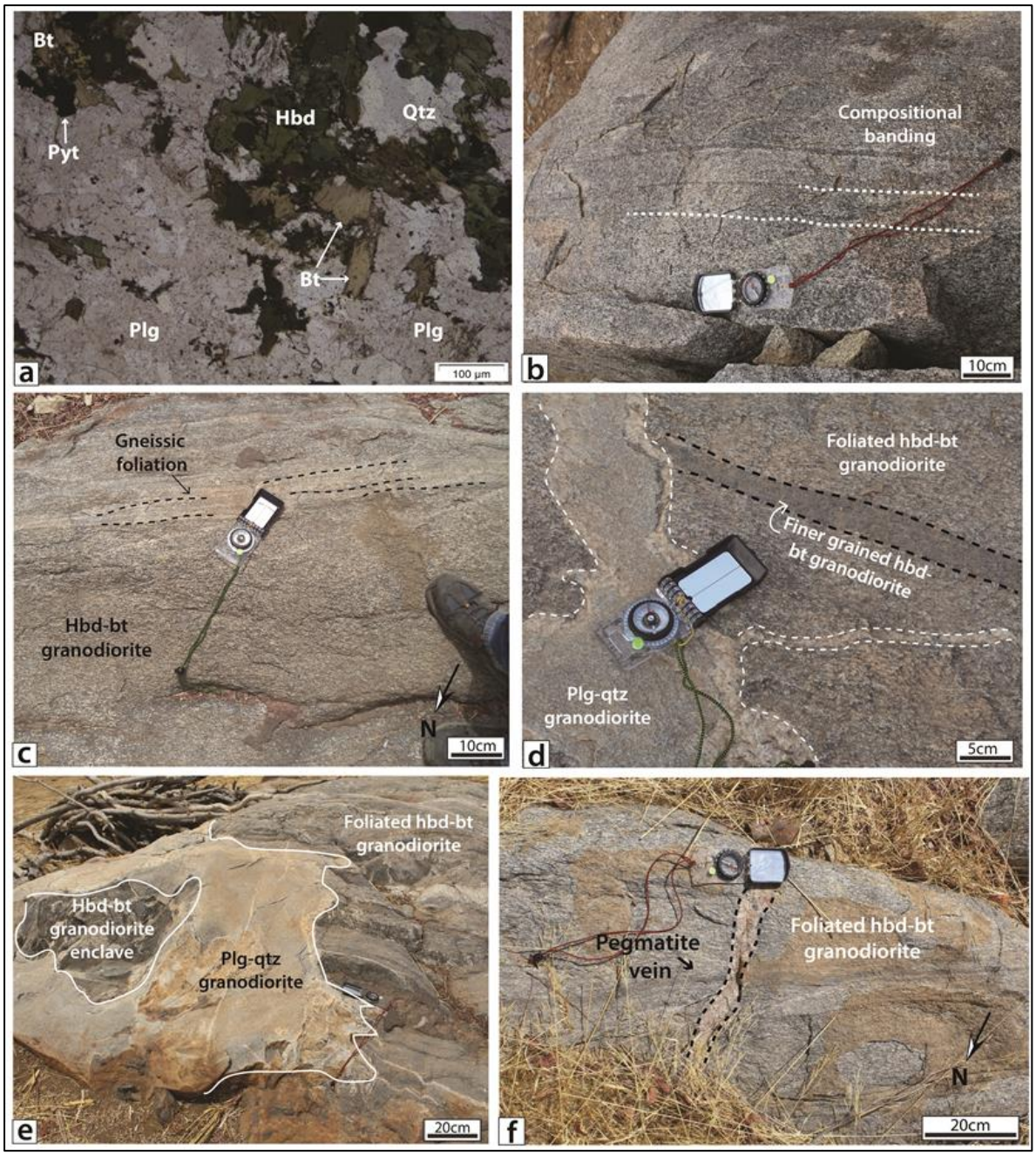


Figure 4.6: *(a) The micrograph of sample GP006 (in plane polarized light- PPL); the quartz grains are either fine grained, or have undulose extinction in the larger grains. The hornblende has a preferred orientation, and defines the foliation. (b) A hbd-bt granodiorite outcrop with foliation defined by compositional banding of leucocratic and melanocratic minerals. The calculated average orientation of the foliation is 293°/74° S. (c) A gneissic foliation crosscuts the hbd-bt granodiorite in a NE orientation of 041°/88° SE. This gneissic zone has the same composition as the surround unit; the minerals underwent a grain size reduction to form the gneissic foliation (Passchier and Trouw, 2005). (d) The hbd-bt granodiorite is crosscut by a fine grained vein with similar composition, and lastly by the plg-qtz granodiorite. The edges of the plg-qtz granodiorite have a pegmatitic composition. (e) The plg-qtz granodiorite intrudes into the hbd-bt granodiorite, and encloses it as an enclave. (f) The foliated hbd-bt granodiorite is crosscut by a pegmatite vein.*

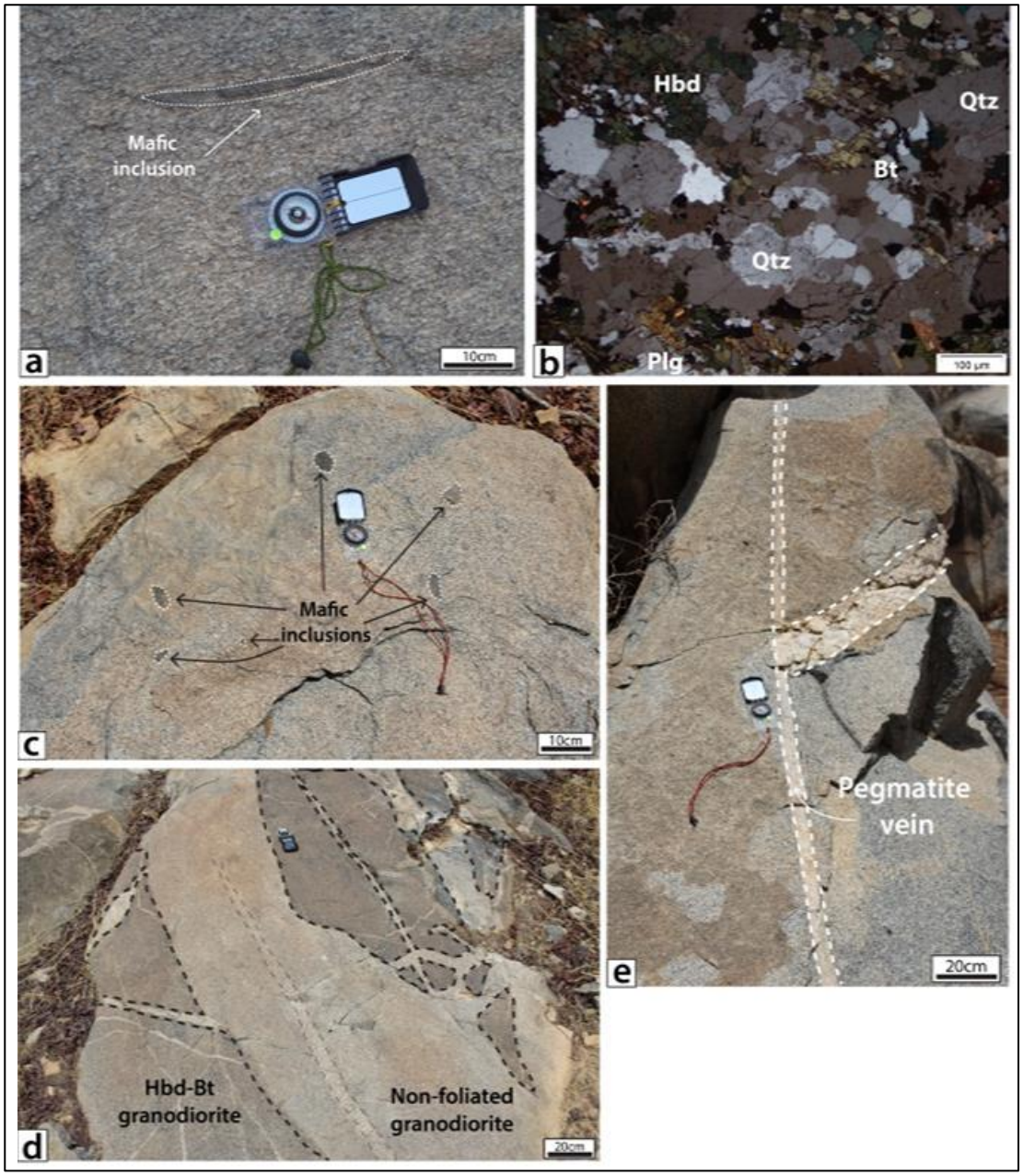


Figure 4.7: *(a) The plg-qtz granodiorite with weak foliation defined a preferred mineral alignment; this unit has a fine to medium grain size of 1 to 5mm. This unit has an elongate mafic inclusion/xenolith. (b) In thin section, the quartz grains show a near-equilibrated texture (Passchier and Trouw, 2005) and 3-point boundaries. Few grains have grain boundary migration textures. (c) Mafic inclusions are characteristic in the plg-qtz granodiorite, and in image (a), the inclusion is elongate parallel to the weak preferred mineral orientation foliation (oriented 320°/70 W). (d) The non-foliated granodiorite intrudes into the hbd-bt granodiorite, and branches out as thin veins in the hbd-bt granodiorite. This unit is crosscut by pegmatite veins. (e) Pegmatite veins crosscut the non-foliated granodiorites.*

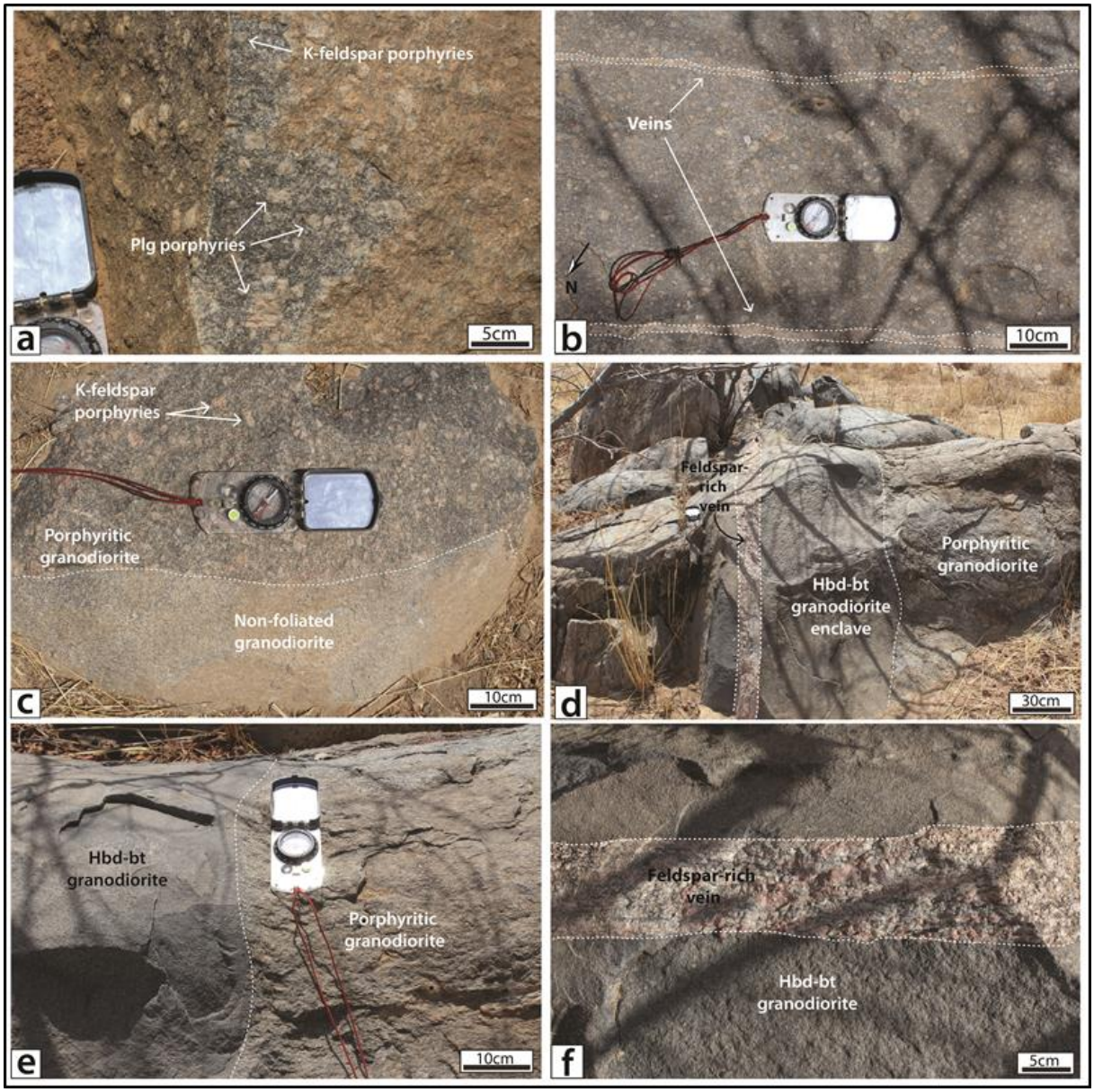


Figure 4.8: *(a) The porphyritic granodiorite has feldspars that are up to 3cm in size. The porphyries randomly distributed in the unit. (b) Veinlets that are ~1cm wide with a feldspar composition crosscut the unit. Majority of the porphyries are k-feldspars. (c) The porphyritic granodiorite has a sharp contact with the non-foliated granodiorite. (d) The hbd-bt granodiorite is closely associated in outcrop with the porphyritic granodiorite, and a sharp contact separates the two suites, as shown in image (e). (f) The hbd-bt granodiorite is crosscut by a k-feldspar rich vein that is ~10cm wide.*

4.3.5 Quartz Diorite

This unit is fine to medium grained with a grain size of up to 3mm, and displays a gneissic texture in some outcrops. The outcrops of this unit are low lying, massive and weakly developed to no foliation (Figure 4.9 a). The composition of the quartz diorite is plagioclase (30%), K-feldspar (30%), hornblende (20%) and quartz (20%) (Figure 4.9 b). The XRF data for sample GP043 plotted between a quartz diorite (granodiorite) and a granite in the classification diagram after Cox et al. (1979), and as a quartz monzonite in the classification after Middlemost (1994). This sample has however been classified as a granodiorite with variable composition from a quartz diorite to a granite depending on each outcrops evolution. The XRF data for the quartz diorite and granodiorite samples are presented in the geochemical section 4.4.

4.3.6 Tonalite

The tonalite is medium to coarse grained, with a grain size of ~2mm. It is a low-lying outcrop, massive with little to no fabrics (Figure 4.9 c). It has a distinct light appearance in outcrop. This unit has a felsic composition of quartz and feldspar (90%) and minor hornblende, biotite and chlorite (10%) present (Figure 4.9 d). The feldspars in this unit are euhedral, and the chlorite in interstitial in between the feldspars and the quartz grains. This unit crosscuts the granite gneiss and is crosscut by the hbd-bt granodiorite. The tonalite outcrops are limited in the field, and majority of the polygons representing this rock type in the geological map are based on interpolation of reference maps as described in the methodology chapter, section 3.1.1. Brittle structures such as fractures that developed into quartz veins crosscut a weak compositional banding in this unit.

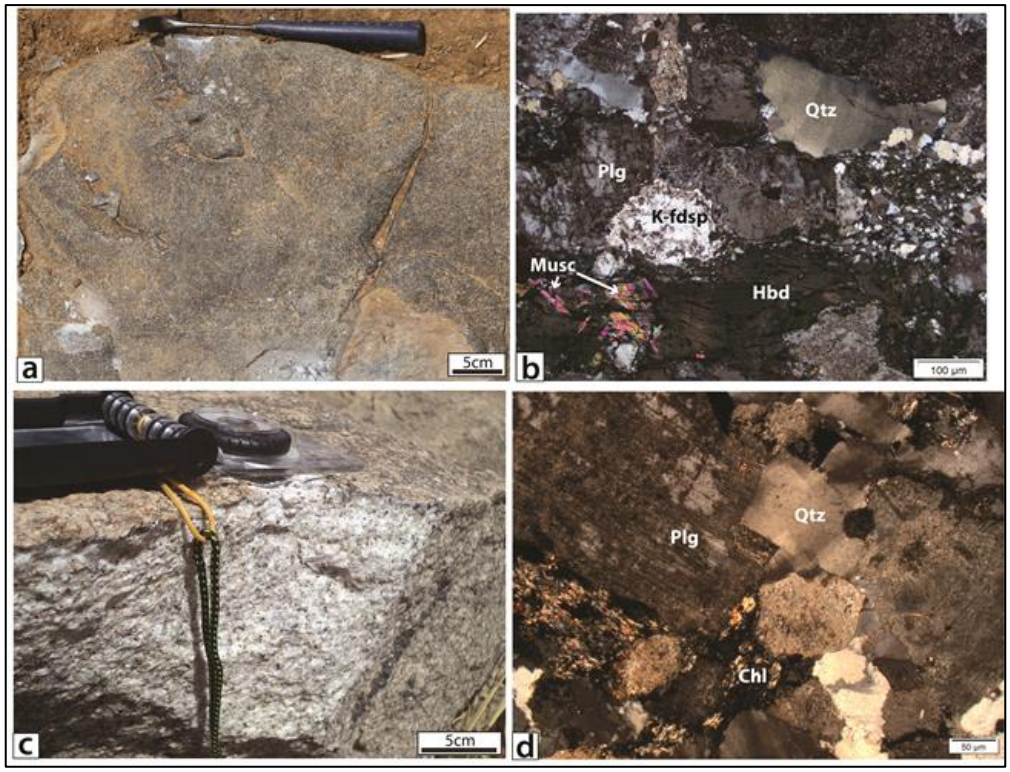


Figure 4.9: *(a) The outcrop of a quartz diorite/granodiorite; the unit is medium grained with a grain size of up to 3mm. The units are massive, and a gneissic foliation is present in some outcrops (no foliation is present in the outcrop in image a). Image (b) is a micrograph of the sample GP043. The quartz grains vary in size; they are either fine grained (~10µm) and have grain boundary migration textures, or are larger grains of up to 200µm in size, and have undulose extinction. The hornblende has a weak preferred orientation. (c) The tonalite outcrop; this unit is distinct in the field by its light appearance. The grain size is ~2mm. (d) The tonalite in thin section; the plagioclase grains are euhedral in shape, and the chlorite is interstitial in between the plagioclase and quartz grains.*

4.3.7 Granite

This unit differs from the granite gneiss by its grain size, and equigranular mineral texture (Figure 4.10 a). The grain size is medium to coarse grained with crystals ≤5mm grain size. The granite unit is composed of plagioclase (30%), quartz (30%), hornblende (20%), K-feldspar (10%), and in some outcrops, biotite and minor muscovite (10%) is present (Figure 4.10 b). The composition does vary into a more alkali feldspar rich granite, and the outcrops have a pink appearance. Some outcrops have been silicified. This suite of granites is distinct from the gneissic granite by having no dominant fabric, and is younger relative to the gneissic granite and the foliated granodiorite, based on crosscutting intrusive contacts. Pegmatites and aplite dykes crosscut this granite suite.

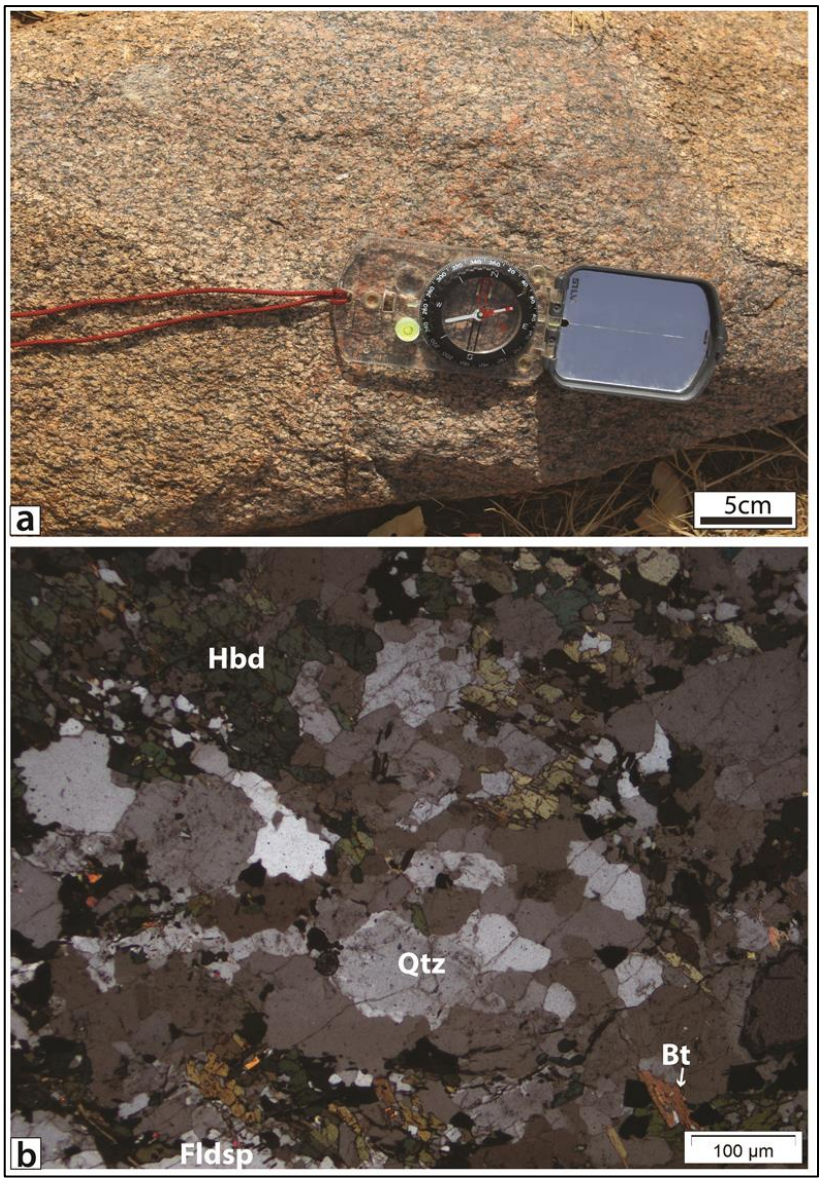


Figure 4.10: *(a) A granite outcrop with an a slight pink appearance, with a equigranular textures. This unit does not show any pervasive fabrics. (b) A micrograph of a granite thin section; the quartz grains have an annealing texture with have well-developed boundaries. Few grains show recrystallization textures, and the minerals have a more equilibrated texture, and majority of the quartz grains do not have undulose extinction.*

4.3.8 Feldspar-Quartz Porphyritic Diorite

These units have a distinct purple colour, and have coarse (1-2cm) feldspars (plagioclase and K-feldspar) grains. The feldspar grains have a weakly defined preferred orientation. The matrix is rich in clay minerals and is fine grained. The composition varies to more chlorite rich outcrops with a green appearance. This unit has the sulphide mineral pyrite. It is also host to buck quartz veins. Tourmaline has

crystallized on the quartz veins. It is in proximity to the chl-mus-qtz schist. Fresh hand samples of this unit were observed at an active artisanal mining site.

4.3.9 Dolerite Dykes

The dolerite dykes have a moderate to high magnetic signature, and are discernible on the magnetic imagery data. There are identified as NW-trending linear bodies, tens of meters wide. Although not abundant, the dykes are found as rounded outcrops a few meters wide, ≤5m (Figure 4.11 a). The high magnetic signature is indicative of a high Fe and Mg content in its mineralogy (Dentith and Mudge, 2014). In some outcrops, the pyroxenes have formed as cumulates within a finer grained mafic matrix of hornblende and minor plagioclase. The sulphide mineral pyrite is also present. Late stage alteration minerals chlorite and epidote developed as minor veins within fractures and joints. The dolerites are crosscut by aplite dykes and pegmatite veins (Figure 4.11 b).

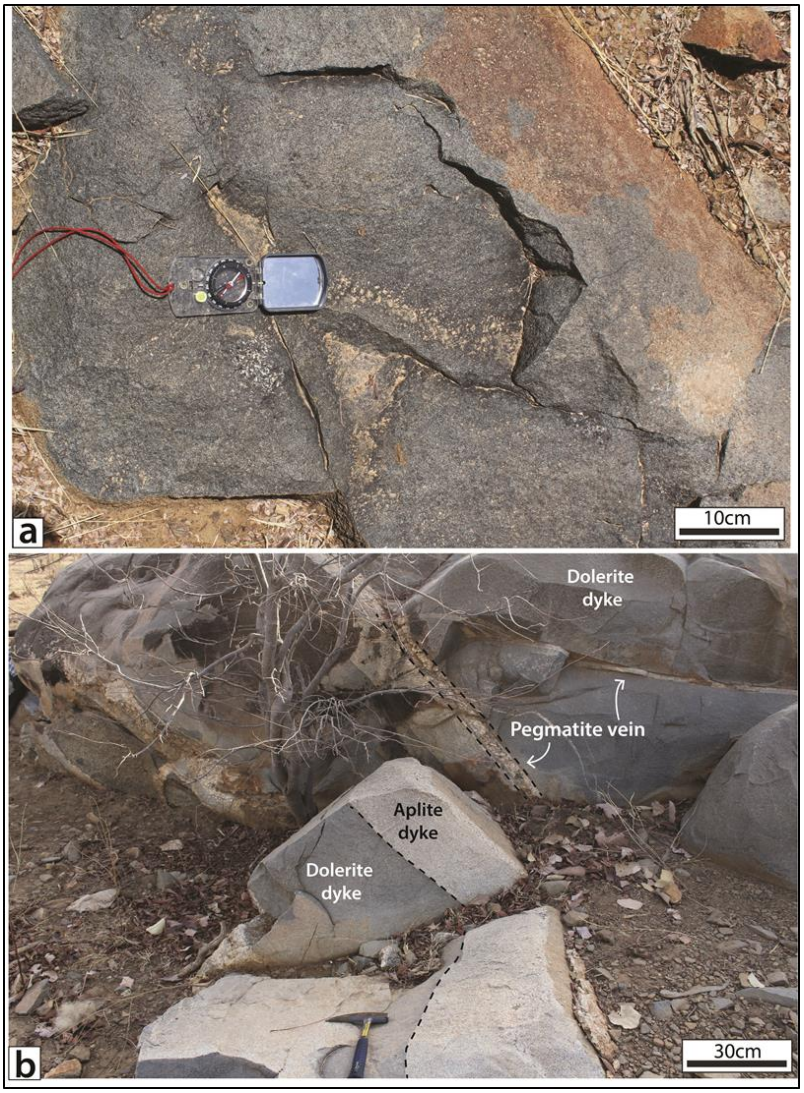


Figure 4.11: *(a) A dolerite dyke outcrop; these units are massive, and have no fabrics. It has a medium grain size of ~3mm. (b) The dolerite dyke outcrop is crosscut by aplite dykes and pegmatite dykes.*

4.3.10 Aplite dykes

This unit is present as minor dykes (of ~30cm width) that crosscut the granite gneiss, granodioritic units and the dolerite dykes (Figure 4.12 a and b). The composition of these dykes is the same as the granites, but the grain size is fine grained (≤1mm). The aplites do have a higher K-feldspar content; the mineralogy is composed of plagioclase (30%), quartz (20%), K-feldspar (20%), hornblende (20%), and biotite and muscovite (10%).

4.3.11 Pegmatites

The main mineralogy of the pegmatite is plagioclase, albite, K-feldspar and quartz crystals. The crystal size varies from medium to coarse, with crystals ~3cm in

length (Figure 4.13 a and b). Crosscutting relations indicate that there might be more than one phase of pegmatite veining. The pegmatites are either crosscutting as veins, or are a transition from a granitic or granodioritic composition to the leucocratic composition. Pegmatitic compositions are observed on the boundaries of plg-qtz granodiorites that intruded in hbd-bt granodiorite, as seen in section 4.3.2 and 4.3.4. Minor content of tremolite, actinolite and biotite is present in some outcrops.

4.3.12 Migmatite

In the southern domains of the study area, there are outcrops with more migmatitic characteristics, with clear leucocratic and melanocratic segregation and banding (Figure 4.14 a, b and c). The migmatites are massive, and extensive over tens of meters along a N to NE strike. The outcrops are up to 5m in width. In outcrop the leucocratic zones are dominated by feldspars and quartz. The melanocratic zones are amphibolitic in composition, with minor biotite. This unit is described in the Structure section, Chapter 5, as part of the structural fabrics that dominate certain domains.

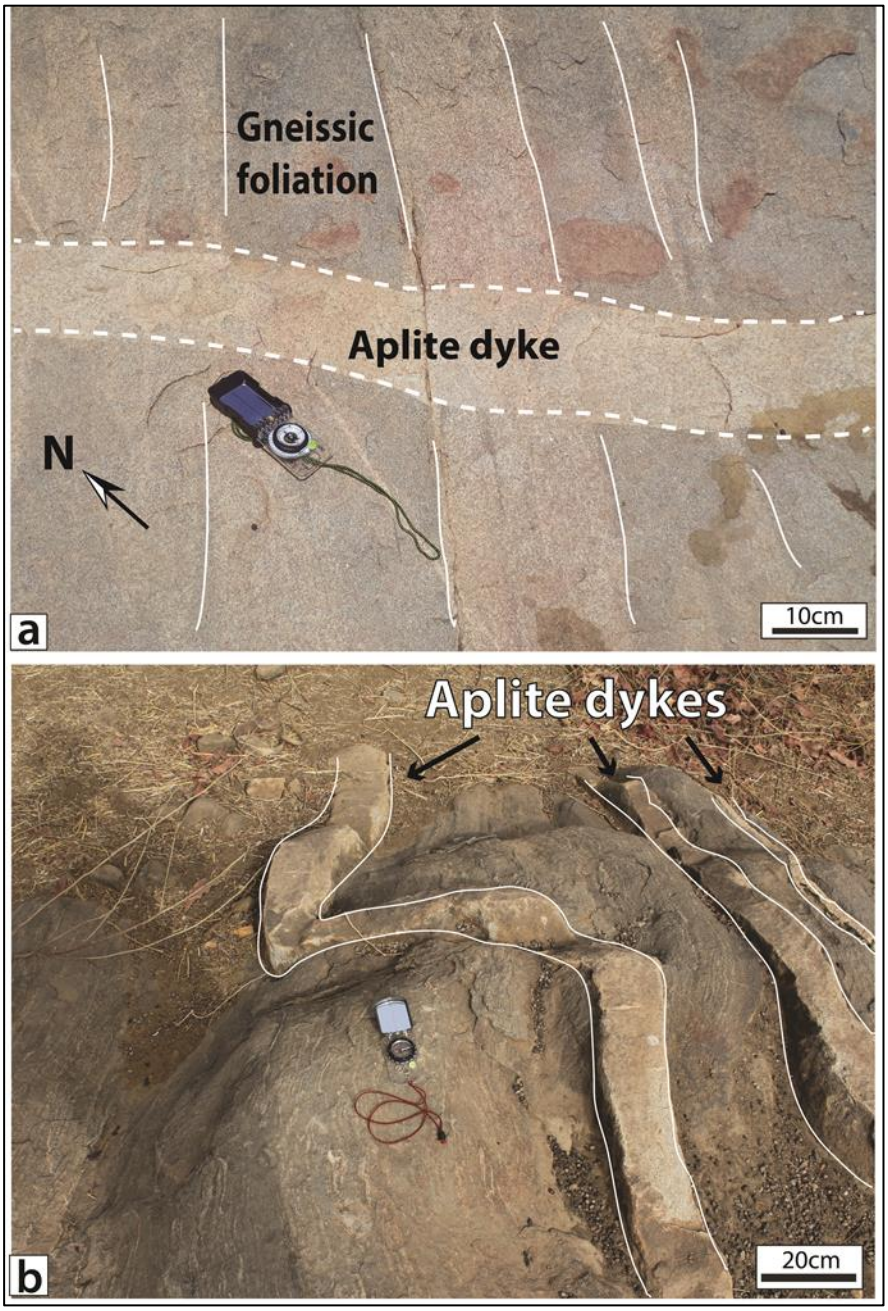


Figure 4.12 : *(a) Aplite dyke with strike orientation of 012° crosscutting a gneissic unit with NE striking compositional banding. (b) Aplite dykes crosscutting a hbd-bt granodiorite gneiss.*

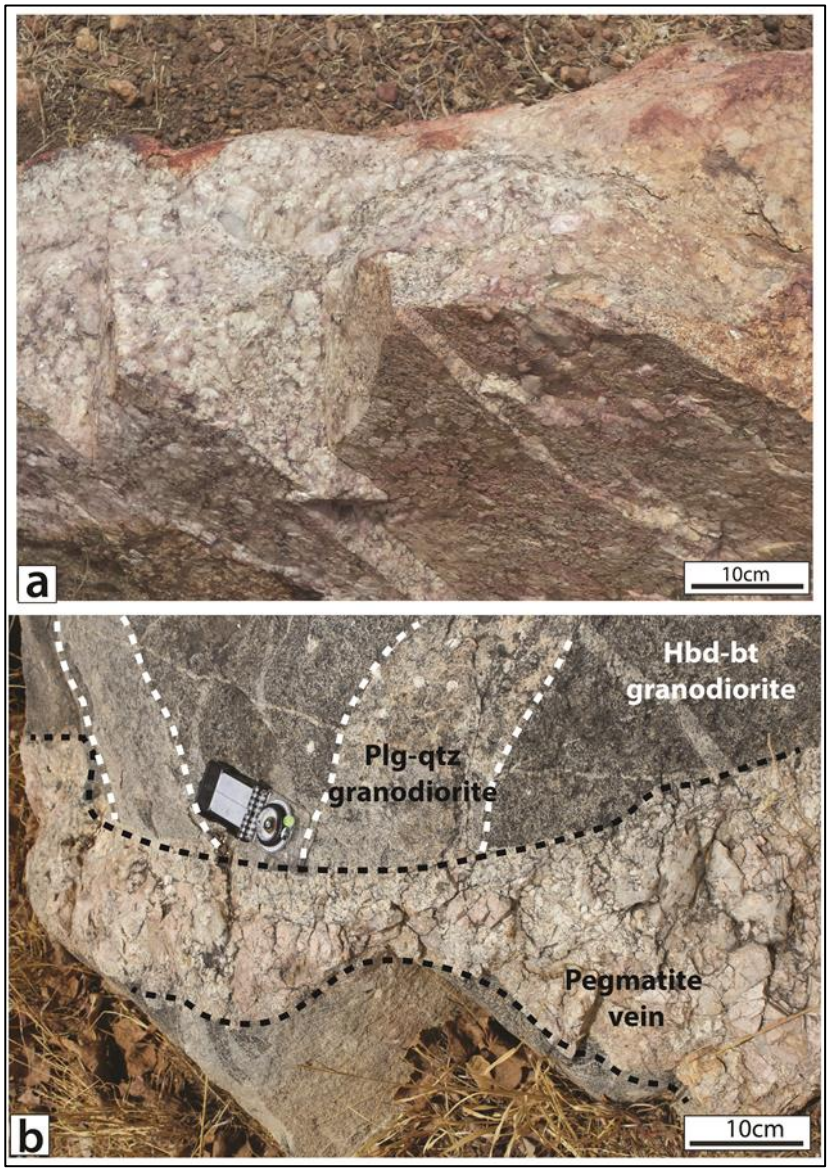


Figure 4.13: *(a) A pegmatite vein with a slightly pink appearance, indicating a K-feldspar composition. The grain size is approximately ~2cm. (b) The pegmatites crosscut the granite gneiss, the granodioritic suite, and the dolerite dykes. In this image, the pegmatite crosscuts both the hbd-bt granodiorite and the plg-qtz granodiorite.*

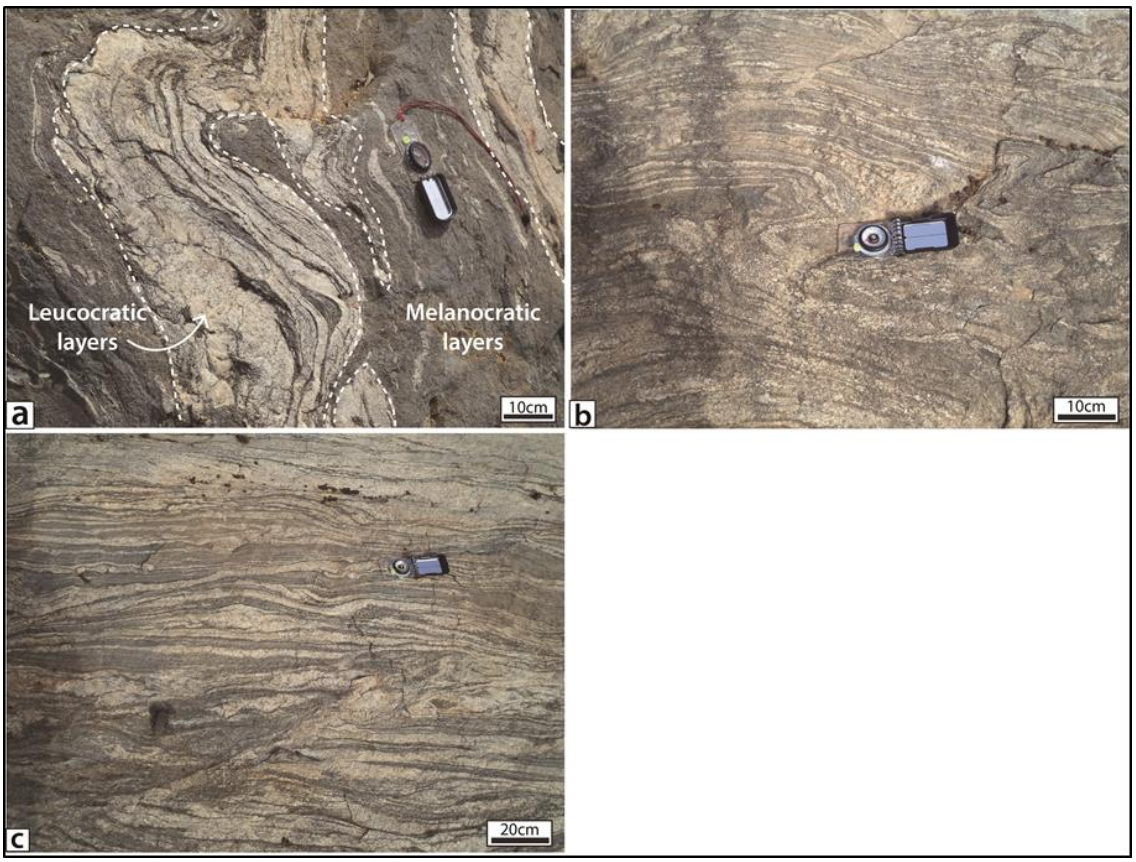


Figure 4.14: *(a) The migmatites have distinct leucocratic and melanocratic layers/bands in outcrops. Some outcrops have complex patterns, and others have a constant (at outcrop-scale), NNW to NNE striking foliations in images (b) and (c) (calculated average orientation of 020°/80° E).*

4.4 GEOCHEMICAL ANALYSIS OF SELECTED PLUTONIC ROCKS

X-ray fluorescence (XRF) analysis on major and trace elements was carried out on samples GP006, GP027 and GP043. These samples were selected for geochronology studies hence the geochemical analysis was completed on them. The results of major elements were plotted in classification diagrams using the software GCDkit 4.1. The major and trace element analytical data is in Table 3. All three samples have a SiO2 content of between 66 and 74 wt%. In the total Alkali-Silica (TAS) diagram for plutonic rocks, all samples plotted as acidic, and under the sub-alkaline subdivision (Figure 4.15 a). Sample GP006 plotted as a quartz diorite (granodiorite) and GP027 as a granite. Sample GP043 plotted on the boundary separating a granodiorite and granite composition. The TAS diagram is modified after Cox et al. (1979) and Wilson (1989). In Figure 4.15 b, the TAS diagram after Middlemost (1994), sample GP043 plots a quartz monzonite.

Other classification diagrams used to analyze the geochemical data also include the AFM (Alkali -Na2O + K2O, Fe Oxides – FeO + Fe2O3, and MgO) diagram, the ternary and bivariate diagram using Al2O3, Na2O, K2O and CaO content, and bivariate diagrams that use trace element data to distinguish between the probable geotectonic environments in which the plutonic units were emplaced.

Table 3: *Major (weight percentage wt%) and trace (ppm) element data of analysed samples GP006, GP027 and GP043 (d.l = below detection limit)*.

wt%	**GP06**	**GP027**	**GP043**
SiO2	66.79	73.80	66.48
Al2O3	16.64	12.12	14.12
Fe2O3	0.34	0.43	0.44
FeO	2.74	3.43	3.56
MnO	0.06	0.07	0.07
MgO	1.56	0.10	2.84
CaO	4.14	1.12	3.47
Na2O	4.63	3.95	4.00
K2O	0.58	3.85	4.01
TiO2	0.30	0.34	0.50
P2O5	0.12	0.04	0.24
Cr2O3	0.00	0.00	0.02
NiO	0.00	0.00	0.00
LOI	2.37	0.30	0.46
Total	100.27	99.54	100.22
ppm			
Sc	8.5	10.3	12.0
V	33.0	d.l.	65.6
Cr	10.2	d.l.	122.2
Co	7.0	d.l.	10.0
Ni	13.7	1.2	39.2
Cu	14.4	13.2	29.3
Zn	45.6	89.8	50.4
Ga	16.2	20.2	17.6
Rb	13.1	84.5	129.1
Sr	530.8	120.0	763.3
Y	6.3	22.1	14.1
Zr	68.8	384.3	176.9
Nb	2.5	3.9	8.3
Mo	d.l.	1.3	1.3
Ba	290.2	1193.7	1426.2
Pb	5.7	15.0	21.0
Th	1.6	6.9	12.3
U	d.l.	d.l.	4.4

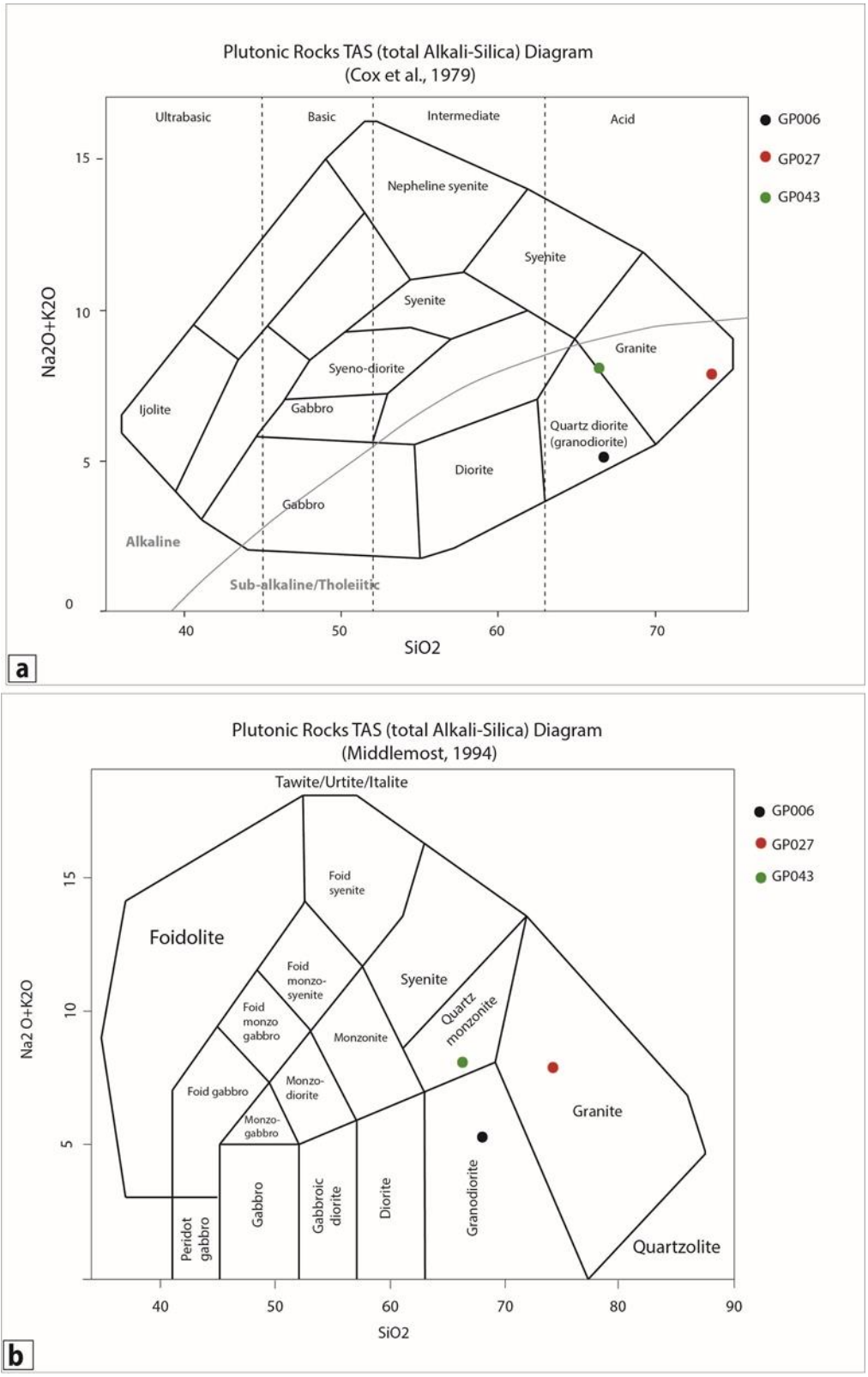


Figure 4.15: *The TAS diagrams modified after (a) Cox et al. (1979) and (b) Middlemost (1994). Diagram (b) was applied to aid in refining the classification of sample GP043. Sample GP006 plotted as a granodiorite (or quartz diorite) in both diagrams. Sample GP027 plots as a granite. Sample GP043 plots in between a granite and a granodiorite in (a), and as a quartz monzonite in (b).*

The XRF data was also plotted in the AFM igneous classification ternary diagram, Figure 4.16 (after Irvine and Baragar 1971). The total Fe oxide values for each sample were calculated as Fe Oxides = FeO + 0.8998*Fe2O3 to compensate for separate oxidation states of iron that were not determined by XRF analytical data (Rollinson, 1993). All samples plot as calc-alkaline, although sample GP027 lies very close to the division line between the tholeiitic and calc-alkaline series.

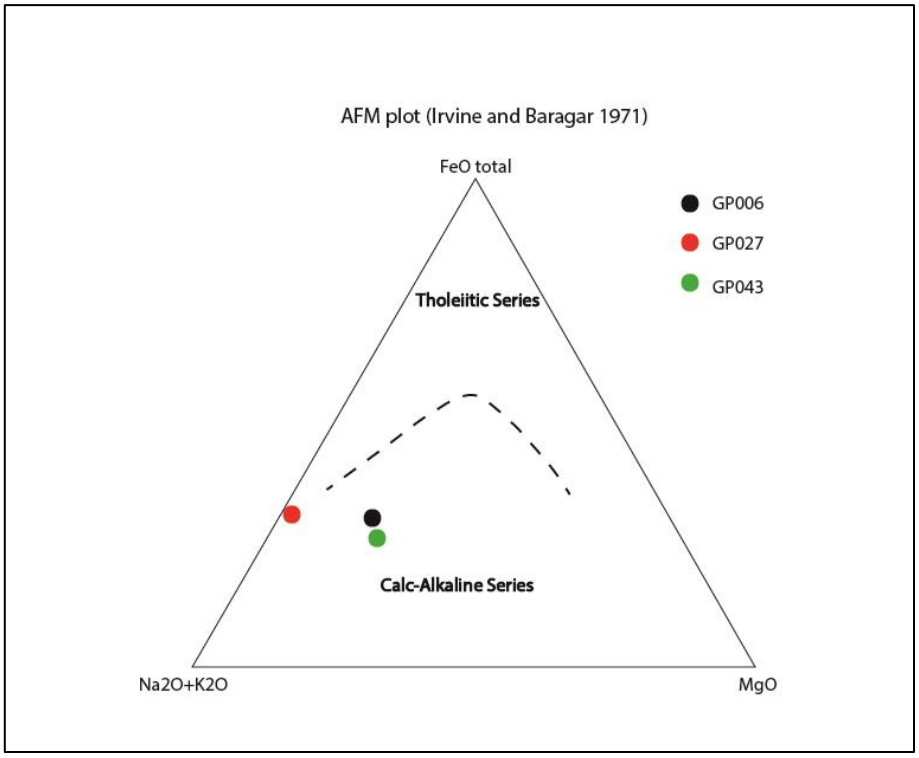


Figure 4.16: *The AFM diagram classifies all samples as Calc-Alkaline. Modified after Irvine and Baragar (1971).*

A further classification of the units as peraluminous, metaluminus or peralkaline using the Al2O3, Na2O, K2O and CaO content was undertaken using two different diagrams. The first (Figure 4.17 a) is a ternary diagram plotted by dividing the mass percentage of each compound by their relative molecular mass, then converted to a new percentage values for each compound from the sum of the four molar amounts, after Gill (2010). The subsequent classification diagram (Figure 4.17 b) is bivariate, with Al2O3/Na2O + K2O (A/NK) on the y-axis and Al2O3/CaO + Na2O + K2O (A/CNK) on the x-axis (Shand, 1943). Both diagrams reveal the sample GP006 is peraluminous, and samples GP027 and GP043 are metaluminous. An associated distinction of granites based on their aluminum content is whether they are I-type, S-type, or A-type granites (Chappell and White, 1974). Peraluminous and

metaluminous granites are classified as S-type and I-type granites, respectively. According to this distinction, sample GP006 is an S-type affiliated granodiorite, and samples GP027 and GP043 are I-type granites. This is therefore indicative of possible different sources for the granitoids found in this study area, a primary igneous protolith for the I-type granites and a sedimentary protolith for the S-type granites (Chappell and White, 1974; Chappell and White, 2001). The plotting of XRF

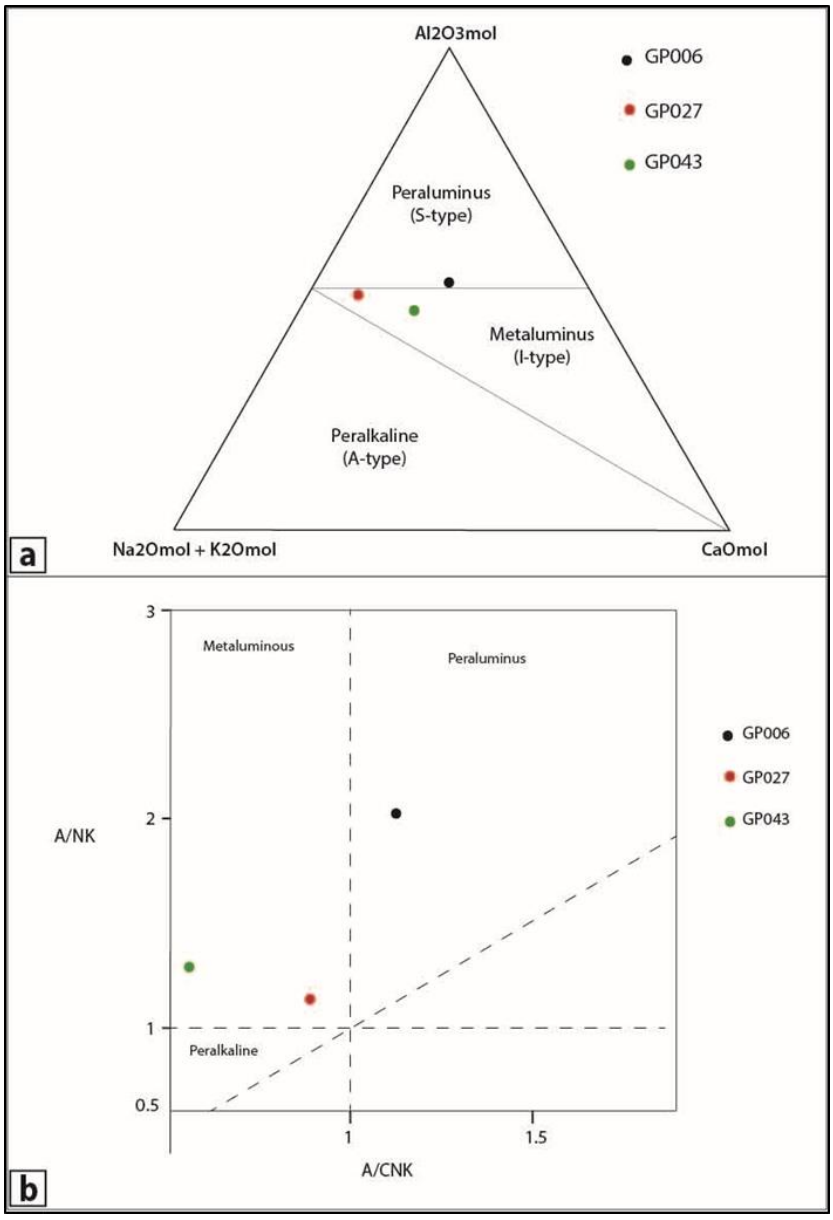


Figure 4.17: *Aluminium classification diagrams that discriminate between peraluminous, peralkaline, and metaluminous type granitoids. (a) A ternary diagram that uses the Al2O3, Na2O+K2O and CaO molecular mass percentages. (b) A binary classification diagram using the ratios A/CNK on the x-axis and A/NK on the y-axis. Both diagrams classify sample GP027 and GP043 as metaluminous, I-type granitoids, and GP006 as a peraluminous, S-type granitoid (Chappell and White, 1974; Chappell and White, 2001).*

data for the granodiorites is used cautiously, as the classification diagrams are mainly used for rocks with a more granitic composition. The classification diagrams only give an indication of what the XRF data can tell about a probable rock's evolution (Rollinson, 1993).

Using Pearce et al. (1984) discriminant diagrams, four tectonic regimes within which granitoids of different trace element compositions could have been emplaced, are defined. These different diagrams are plotted using various combinations of the trace elements Y, Nb, Ta and Yb. The XRF data acquired for the analyzed samples does not have ppm values for Ta and Yb. The Y versus Nb diagram (Figure 4.18 a) subdivides the tectonic environments from which granitoids could be derived into volcanic-arc/syn-collisional, oceanic ridge and within-plate regimes. All three samples plot as volcanic arc/syn-collisional granitoids. The Yb versus Ta diagram further separates volcanic arc granitoids from syn-collisional granitoids, but lack of the relevant trace element data was a limitation to the construction of the diagram. An alternative diagram (Figure 4.18 b) was constructed.

The second discriminant diagram (Figure 4.18 b) uses Rb in addition to Y and Nb. This diagram, with Y + Nb versus Rb axes, separates volcanic arc granitoids from syn-collisional granitoids after Pearce et al. (1984). From this diagram, a distinct classification of the probable regime from which the granitoids were derived is attained, and an enhanced interpretation from the Y-Nb diagram is achieved. All samples plot within the boundaries of volcanic-arc granitoids. It is therefore interpreted that these granitoids were emplaced in a volcanic arc environment. Sample GP006 displays geochemical characteristics, i.e. calc-alkaline, S-type, peraluminous, and quartz-dioritic/granodiorite that are consistent with an orogenic belt tectonic setting such as a volcanic arc with related magmatism during collisional deformation (Pearce et al., 1984).

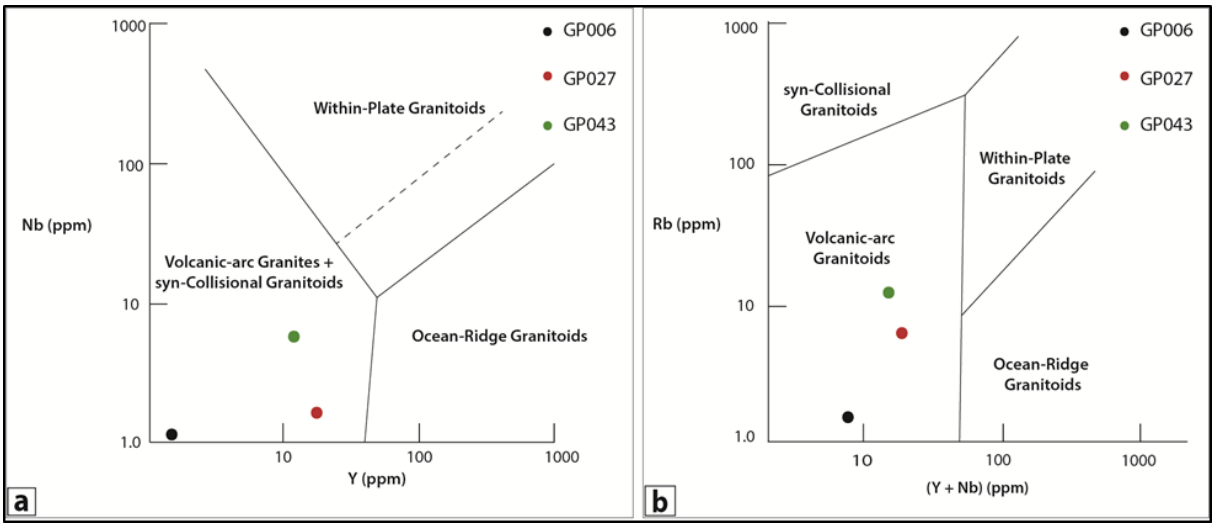


Figure 4.18: *Classification diagrams after Pearce et al. (1984); (a) The Nb vs Y (ppm) tectonic environment discriminant diagram, separating Oceanic-Ridge, Within-Plate and Volcanic-arc+ syn-Collisional granitoids. All samples plot as Volcanic-arc+ syn-Collisional tectonic regime plutons. (b) The Rb vs (Y+ Nb) (ppm) diagram; this diagram gives a separation of the syn-Collisional and Volcanic-arc granitoids, revealing that all the samples are likely plutons emplaced in a volcanic-arc setting.*

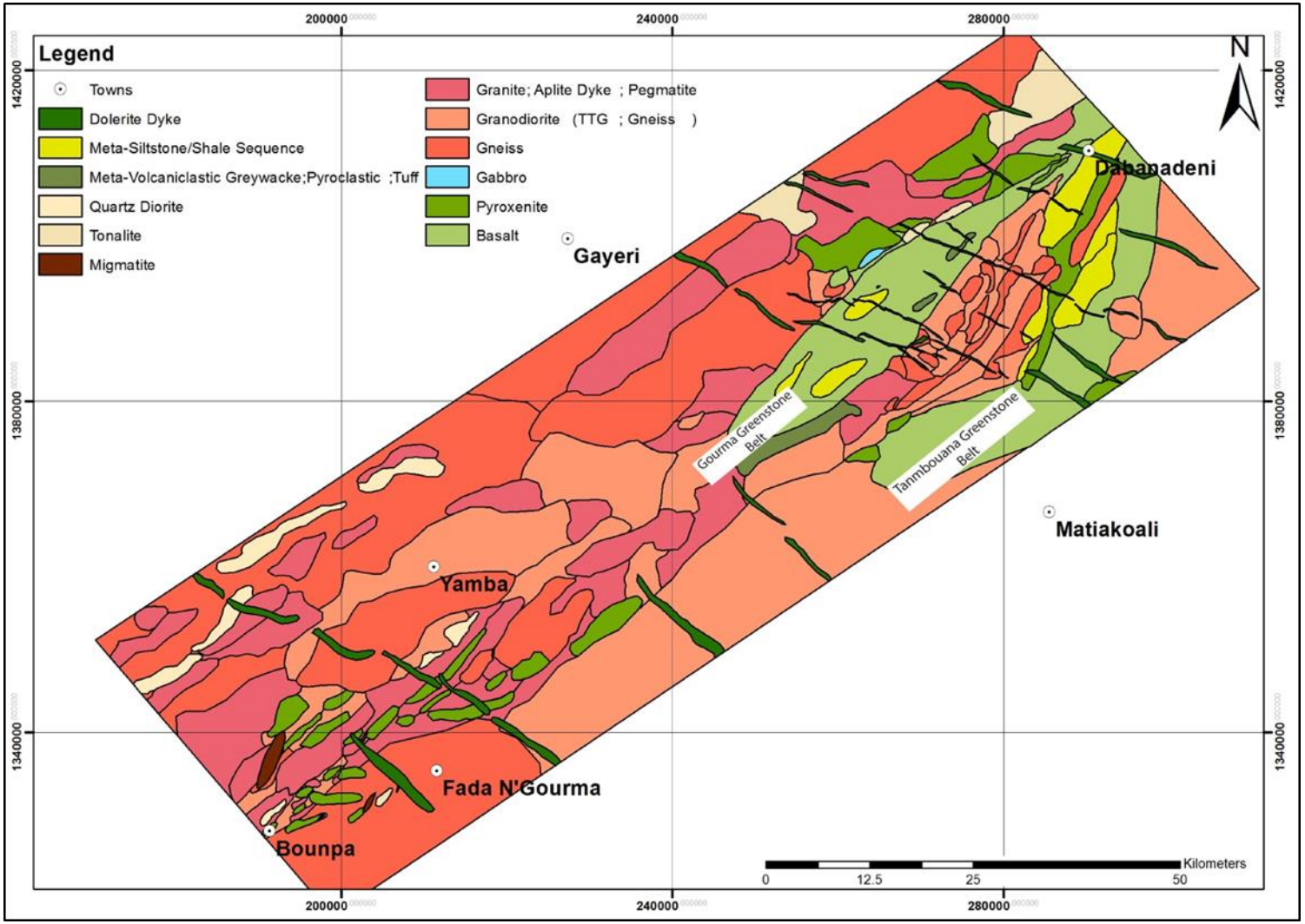


Figure 4.19: *The geological map compiled for the study area using all field data, and incorporating aeromagnetic imagery data and the BRGM (1992) as base maps. The two greenstone belts have been named here as the Gourma greenstone belt (in the centre of the study area) and the Tanmbouana greenstone belt (in the east).*

CHAPTER 5: STRUCTURAL GEOLOGY OF THE FGSZ

The lineaments interpreted as shear zones, faults and foliation were extracted from the aeromagnetic imagery data (RTP 1st derivative magnetic data) from south of the Dabanadeni village in the Gourma Province to Bounpa village, southwest of Fada N'Gourma. Analysis of the structural data collected in the study area is done according to the domain sub-division A, B, C and D as shown in Figure 5.1.

Domain A is inclusive of the FGSZ and the Diabatou Trend- DT. The data along the two structures is sub-divided, and the FGSZ is sub-domain A1 and the DT is sub-domain A2. The FGSZ and the DT are marginal shears on the west and the east of the Gourma Greenstone Belt (GGB), respectively (Figure 5.2). The area between the FGSZ and the DT is analyzed separately as sub-domain A3. Domain B is the Fada-Boulougou Shear Zone (FBSZ). The FBSZ is east of the FGSZ, and the two structures are parallel to one another along a general NE trend.

The easternmost shear is the Tanbaougou Trend (TT). This structure is interpreted based mainly on the aeromagnetic imagery data due to insufficient field data collected along this trend. There is a marked increase in the metamorphic grade south of domains A and B. Domain C is to the south of domains A and B, and enclosed the southwest extension of the FGSZ and FBSZ. Domain D is located in the south of the study area (Figure 5.1).

The dominant structural grain of the study area has an overall NE trend. A northwest trending dyke system is also discernible from geophysics imagery data. The different shear senses interpreted from desktop studies of the geophysics imagery data served as a basis for investigation in the field to determine the possible deformation phases by analyzing the geometric and kinematic information. Kinematic analyses could, however, only be performed on planes parallel to stretching lineation and orthogonal to foliation.

Structural features and data is presented for each domain, and an overall tectonic scheme is illustrated in order to make a cohesive interpretation of the tectonic evolution the study area as a whole.

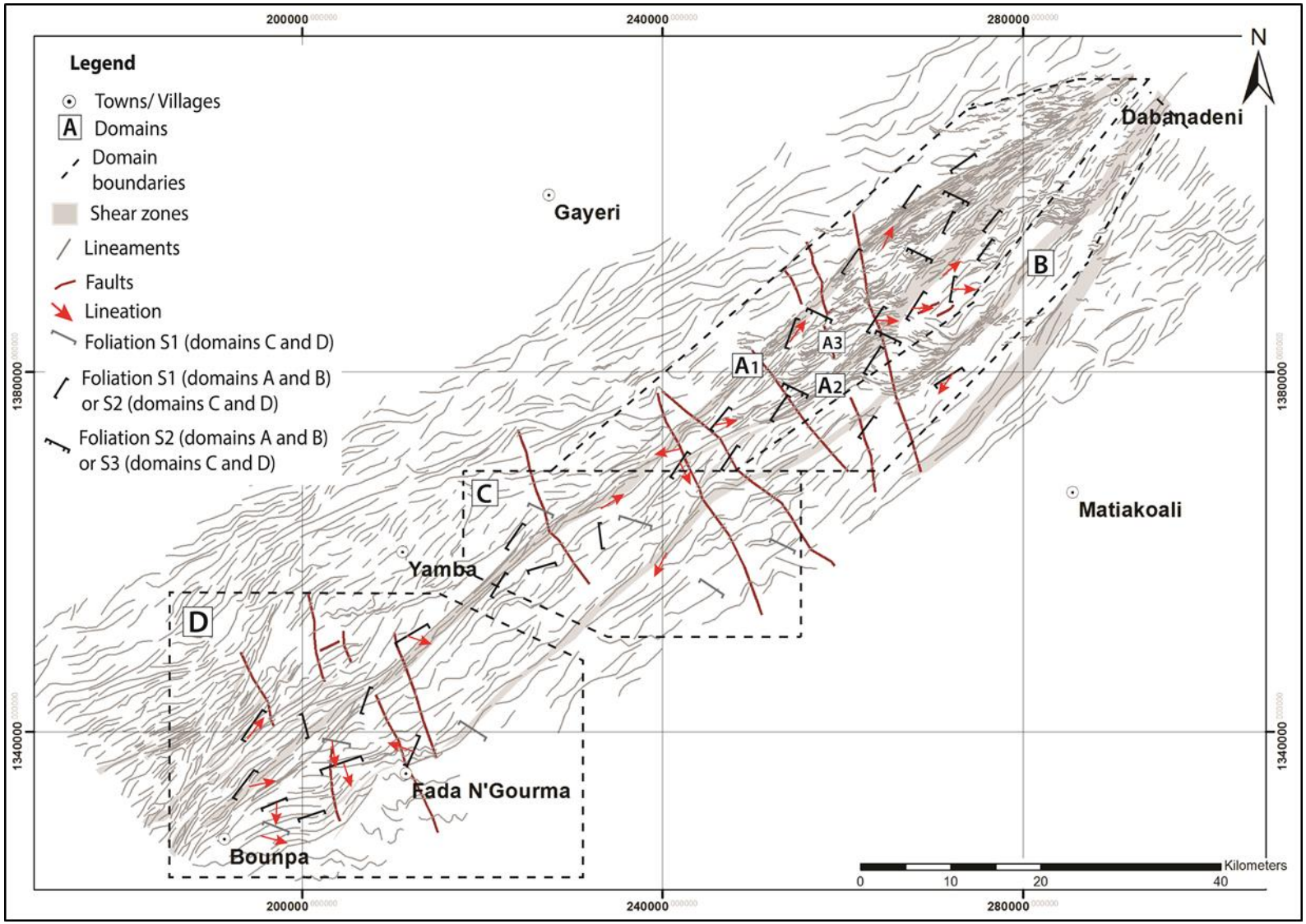


Figure 5.1: *A summary structural interpretation worm map of the study area showing geographical locations of the structural domains. Domain A has been sub-divided into A1, A2 and A3; A1 is the northeast extension of the FGSZ and A2 is the DT. Sub-domain A3 is located between A1 and A2. Domain B is the northeast extension of the FBSZ. Domain C encloses the southwest extensions of the FGSZ and the FBSZ. Domain D is the southernmost region of the study area. Structural data is analysed based on the domains, and the local fabrics (foliation, lineation) and structures (folds, faults, fractures, veins) are described in each domain. The overall regional tectonic evolution of the shear zones will be summarized at the end of the chapter, and all local structures will be put into regional context for the study area.*

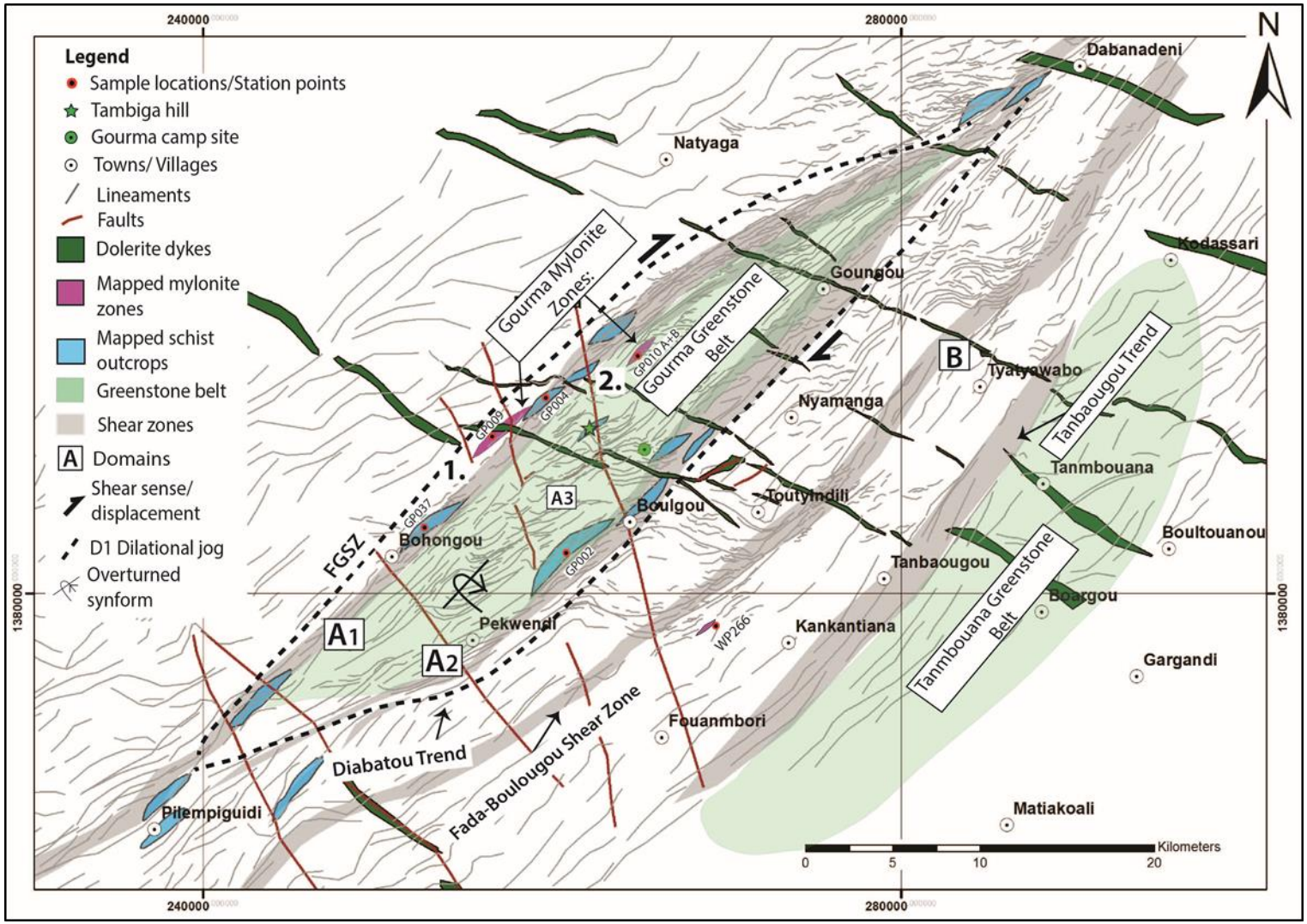


Figure 5.2: *Lineaments map incorporating structural information gathered from field data including schists, dolerite dykes orientations, faults and mylonite zones. The GGB is bounded by the FGSZ and the DT. A dilation bend with dextral shear sense has been interpreted from aeromagnetic data around the GGB, and this makes up domain A. Domain B is the Fada-Boulougou Shear Zone. The Tanbaougou Trend (TT) is on the western boundary of the Tambouana Greenstone Belt.*

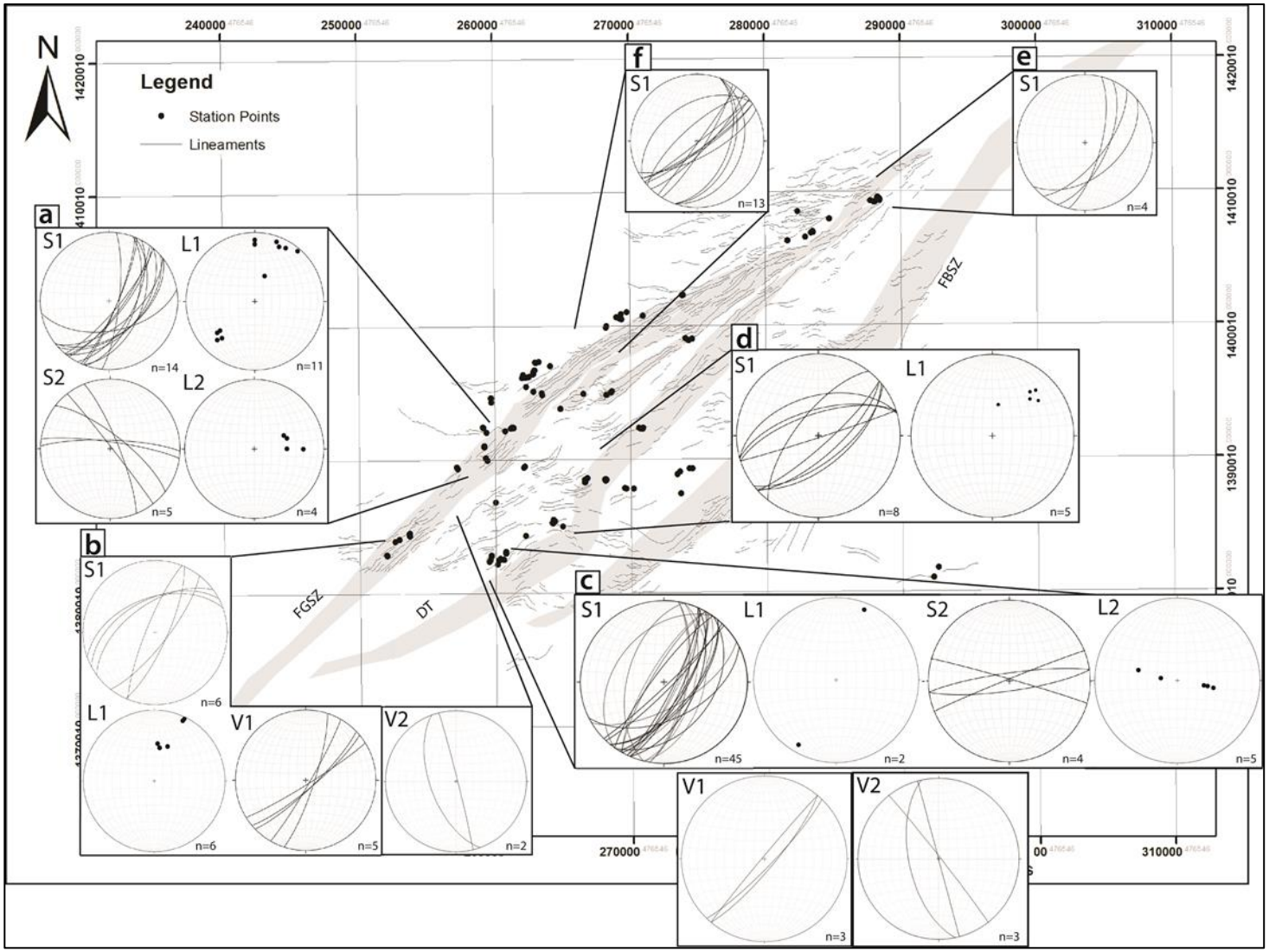


Figure 5.3: *Stereoplots of foliation and lineation in domain A are shown in the inserts (a), (b), (c), (d), (e) and (f). S1 has a NE trend with calculated average orientation 032°/66° SE, and is dominant in the schist units proximal to the shear zones. S1 also occurs as a gneissic foliation in the intrusive units located between the shear zones. The NW to E-W trending S2 crosscuts S1 as a crenulation foliation, or as a schistosed foliation. The lineation L1 is a mineral lineation. The orientation of L1 is generally shallow plunging to the NE and SW along the NE trending foliation as shown in the stereoplots. L2 is an E- to W-plunging defined by fold axes. The orientations of the buck quartz veins are mainly NE trending and have a calculated strike orientation average of 039°, as shown in the stereoplot for V1.*

5.1 DOMAIN A

The FGSZ (domain A1) and the DT (domain A2) are parallel to each other for a strike length of ~50km (Figure 5.2). The two trends coalesce proximal to Dabanadeni village in the north of the study area, and again around Pilempiguidi towards the southwest. The FGSZ is a right-stepping shear zone, and together with the adjacent DT, formed a dilational bend on the margins of the GGB during a dextral shear regime. The outline of the dilation was extracted from geophysical imagery data, and is shown in Figure 5.2. A synform is interpreted to have formed along the GGB in sub-domain A3, based on lineament analysis and lithology sequences suggest that there is folding in between domain A1 and domain A2.

5.1.1 Domain A1-The FGSZ

Within this study area, the FGSZ is continuous from Dabanadeni to Bounpa along a distance of ~130km. The trend of the shear zone continues beyond the Niger border in the NE, and southwards into northwest Ghana. In this sub-domain, the FGSZ is ~2km wide but becomes thinner in domain D to ~300m wide. Field data from this sub-domain indicates a minimum of two sets of foliation, S1 and S2, and the related S1-C1 and S2-C2 fabrics respectively, where present (Figure 5.3). The shear zone is located at the tectonic contact of the plutonic units and the GGB. The following structural features were identified along the shear zone;

Foliation-S1

The rocks within and proximal to the shear zone have been strongly foliated with steep dip angles. S1 has a NE trend with a calculated average orientation of 032°/66° SE (Figure 5.3 inserts a, b, c, d, e and f). The dip direction is mainly SE, but NW dip directions are also present. This anastomosing pattern is observed all along the FGSZ. A schist unit expresses well the S1 foliation, and the schist (Figure 5.4 a and b) dominates along the FGSZ in domain A.

The mapped schist outcrops have a composition of chlorite, biotite, quartz, and minor feldspar. The composition of the schist does vary, and minor muscovite and hornblende content is present in some outcrops. Pyrite is present as an accessory mineral (Figure 5.4 b and c). The schist will be referred to as a chl-bt-qtz schist, unless the composition changes in outcrops being described. Figure 5.4 c

shows a micrograph of sample GP004. Sample location is indicated in Figure 5.2. The outcrop from which sample GP004 is collected has a dark green appearance, and minor chloritoid present in addition to the chl-bt-qtz composition. Hornblende is also identified in outcrop and in thin section. At a microscale, the foliation is defined by a preferred mineral orientation of biotite and hornblende. Sample GP004 has sub-euhedral pyrite grains that are rotated sigma clasts, and chlorite makes up the shear wings of the clasts, indicating a sinistral shear sense of deformation. The orientation of the S1 measured in outcrop is 036°/74° NW. The pervasive NE trending foliation is consistent with a NW-SE directed σ1.

Lineation-L1

Stretch and elongate minerals define lineation L1 (Figure 5.4 d). The orientations of L1 are mainly NE plunging, although there are minor variations with plunge directions to the SW, as seen in Figure 5.3 insert a, b, c and d. The calculated average orientation is 26°→032° for the NE plunging lineation, and 37°→241° for the SW plunging lineation. The changes in azimuth are consistent with the anastomosing pattern observed on the S1 foliation planes. The orientations of L1 indicate a strike slip system (Figure 5.3 insert a and c), and there is a reverse component in some regions with a steeper lineation (Figure 5.3 insert b and d).

Quartz Veins-V1

The chl-bt-qtz schist is host to quartz veins (Figure 5.5 a and b). The main orientation of V1 is NE-SW measuring at an average of 030°/88° SE (V1 strereoplot in Figure 5.3 insert b). Tourmaline has crystalized within some of the quartz veins, and ankerite is present as a brown staining on the surface of some veins. The veins also have disseminated pyrite in the internal fractures. The V1 buck quartz veins are varying in size of ~10 meters in width and up to ~50 meters in length (Figure 5.5 c). The quartz veins are closely associated with gold mineralization, and most artisanal mines are found along the general NE trend strikes of the buck quartz veins.

Smaller veins (cm scale) are present in the schist, and have been boudinaged. The boudins are both symmetrical and asymmetrical as seen in Figure 5.5 a and b. The asymmetrical boudinage quartz veins have a dextral shear sense as indicated in Figure 5.5 b. Such shear sense is consistent with a near E-W directed σ1.

Other outcrops are fractured and jointed indicating a late stage brittle deformation. On the large outcrops, there are pervasive fracture cleavage planes, slickenside lineation and striations on the surfaces of these quartz veins. Complex folding at a scale of ~50cm is observed in some outcrops of the V1, with a fold axis lineation of 30°→230°, and an axial plane orientation measured on another adjacent outcrop is 218°/68° W. The shortening direction required for such folding is NW-SE oriented.

Folds-F1

Near the intersection point between the FGSZ and DT, there is a zone of meso-scale, tight folding. The folds are within the Fe-rich tuff sequences. The fold axes are doubly plunging to the NE and SW; the calculated average orientation of the NE plunging fold axis lineation is 29°→045°, and the calculated average of the SW plunging fold axis lineation is 41°→259°. A cross-section reveals a periclinal buckle characteristic to the folds. The folds have ~3m wide wavelengths and have a SE vergence (Figure 5.6 a). The hinges of these folds have stockwork quartz veining enriched in Fe. The quartz veins have been folded and boudinaged at the limbs of the folds, as shown in Figure 5.6 b and c. The F1 folds formed under a NW-SE compression.

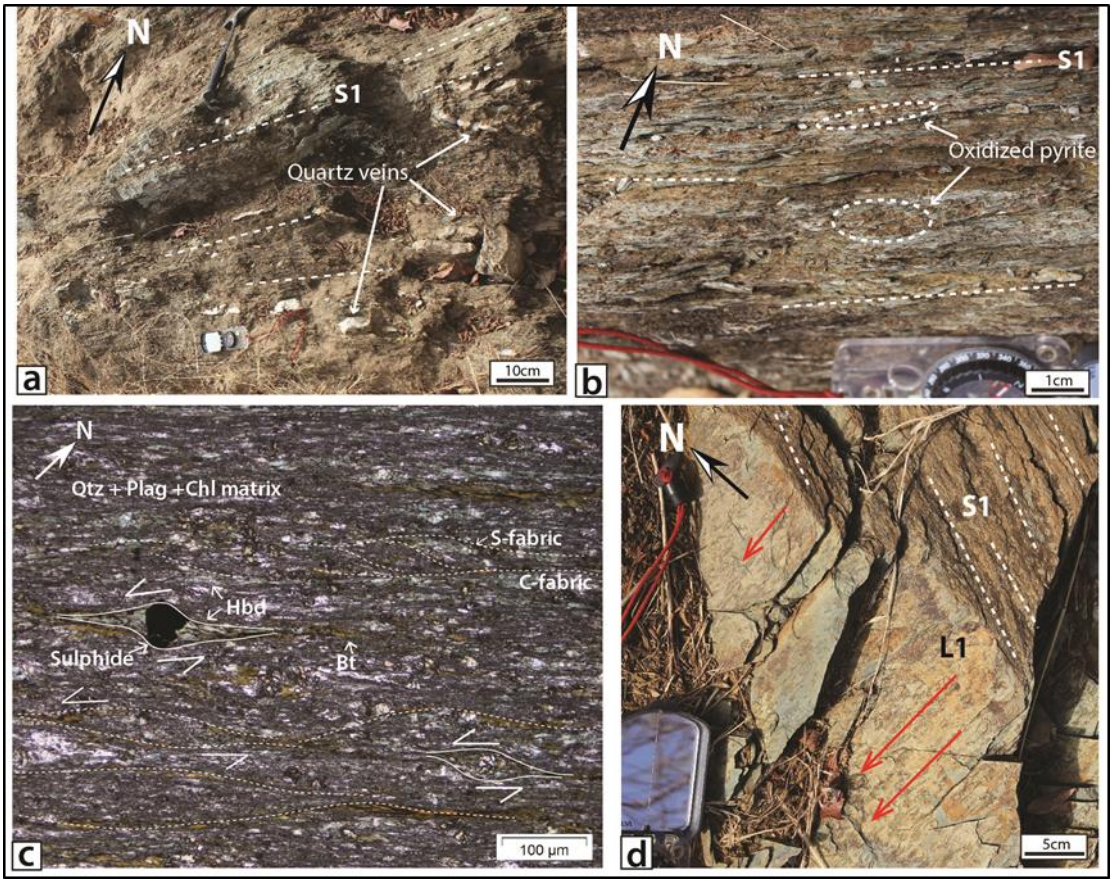


Figure 5.4: *(a) The chl-bt-qtz schist dominates the FGSZ, and is a low lying, outcrop that weathers easily unless it has been silicified. The S1 foliation along the schist is NE trending, and the orientation of the outcrop in the image is 051°/60° SE. This outcrop has boudin quartz veins that are parallel to the foliation. (b) The chl-bt-qtz schist has inclusions of disseminated pyrite. (c) Chlorite, biotite and hornblende define the NE trending foliation. (d) An image of a silicified chl-bt-qtz schist in outcrop that has preserved the NE trending S1 (020°/58° W) and a stretch mineral lineation oriented 24°→224°.*

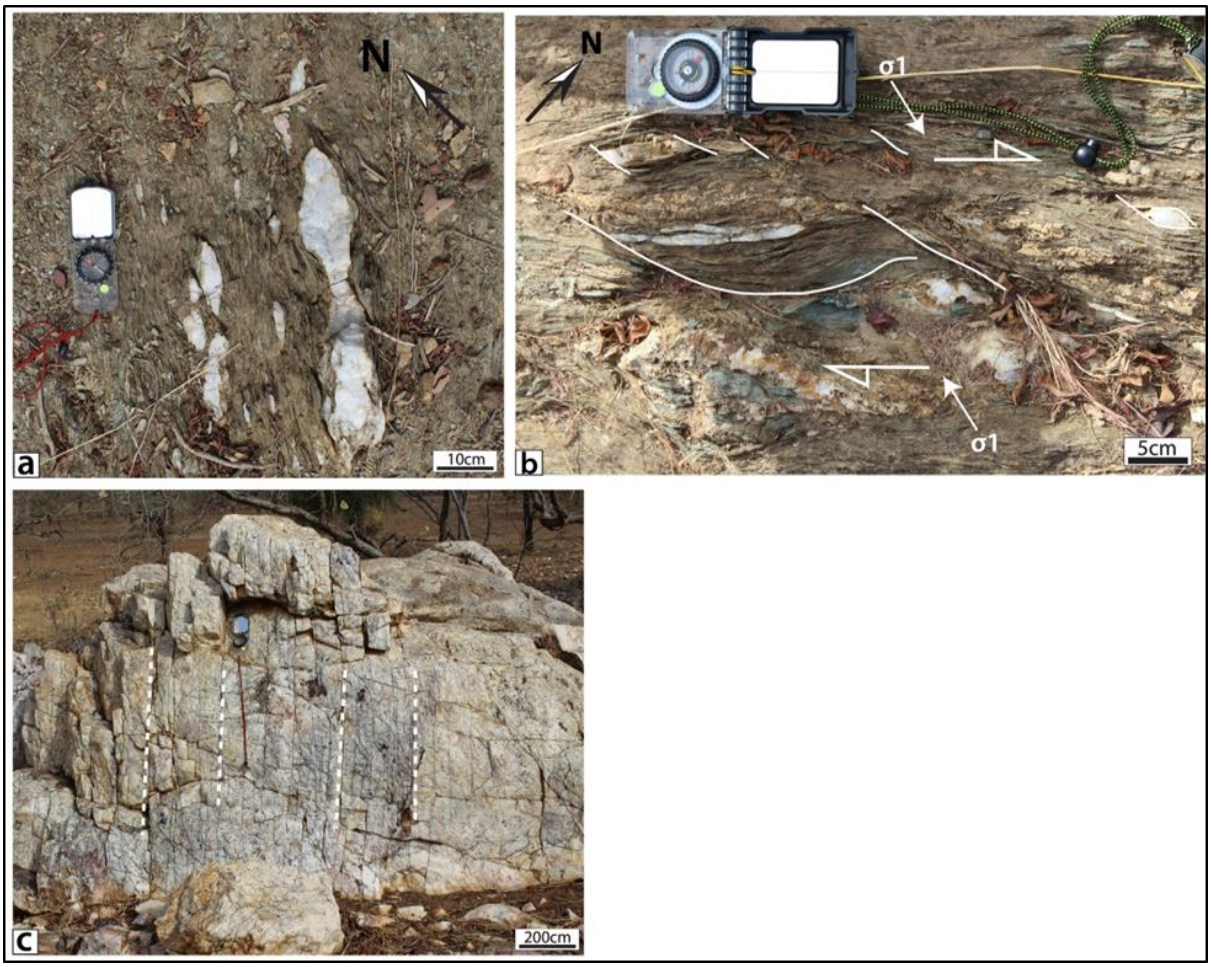


Figure 5.5: *(a) Symmetric boudinage quartz veins V1 hosted by strongly foliated chl-bt-qtz schist. The veins have a NE trend, parallel to the foliation orientation. (b) Asymmetric boudin quartz veins hosted by chl-bt-qtz schist with a dextral shear sense. (c) Buck quartz veins (V1) with the NE trends are ubiquitous within and near the shear zones in domains A and B. These veins have ankerite on the surface. They have been fractured; the fractures have a NW trend.*

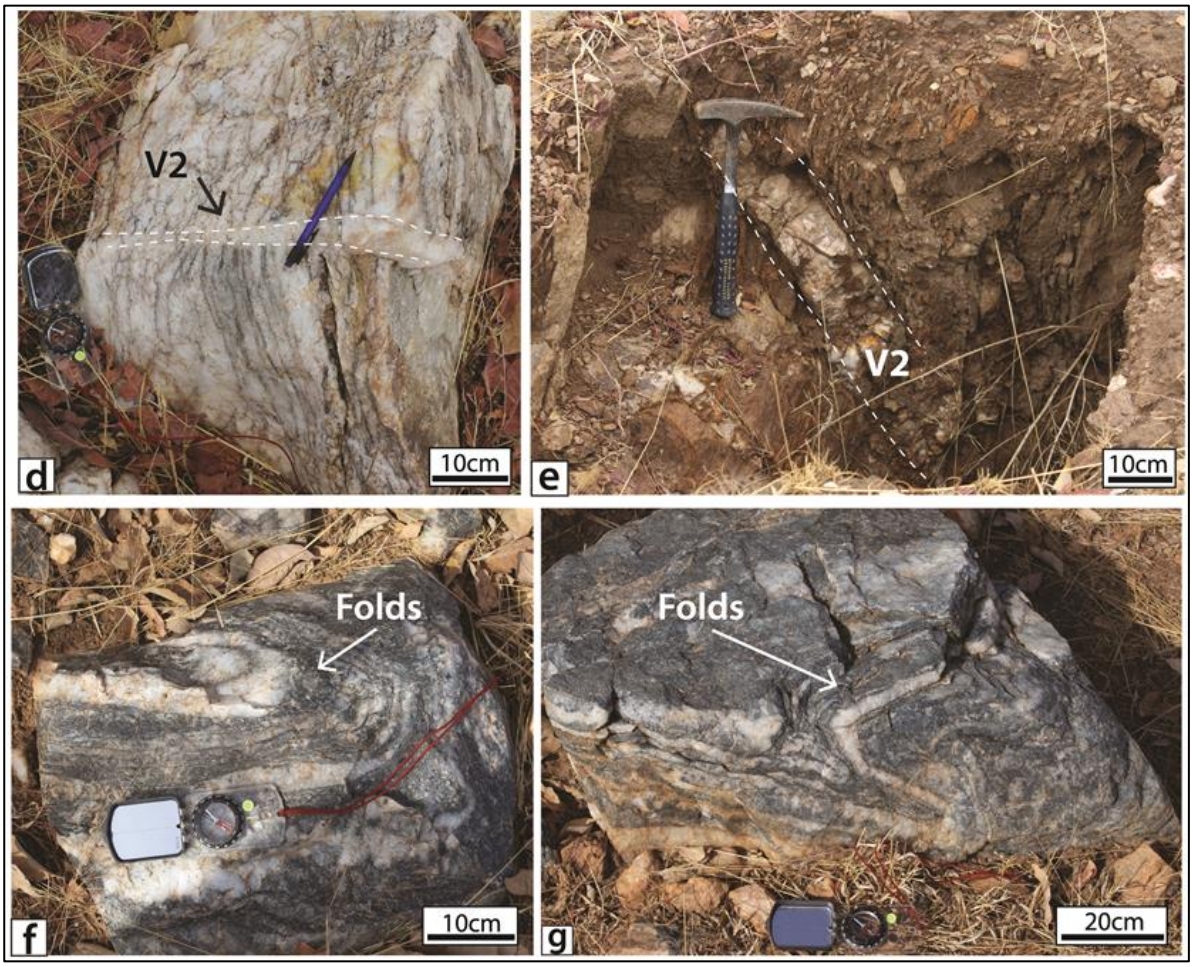


Figure 5.5 Continued: *(d) A ~3cm wide quartz vein, V2, crosscuts V1. (e) A quartz vein crosscutting the schist, with a NW trend (340°/60° E). (f) and (g) Deformed quartz veins that underwent recrystallization during ductile deformation.*

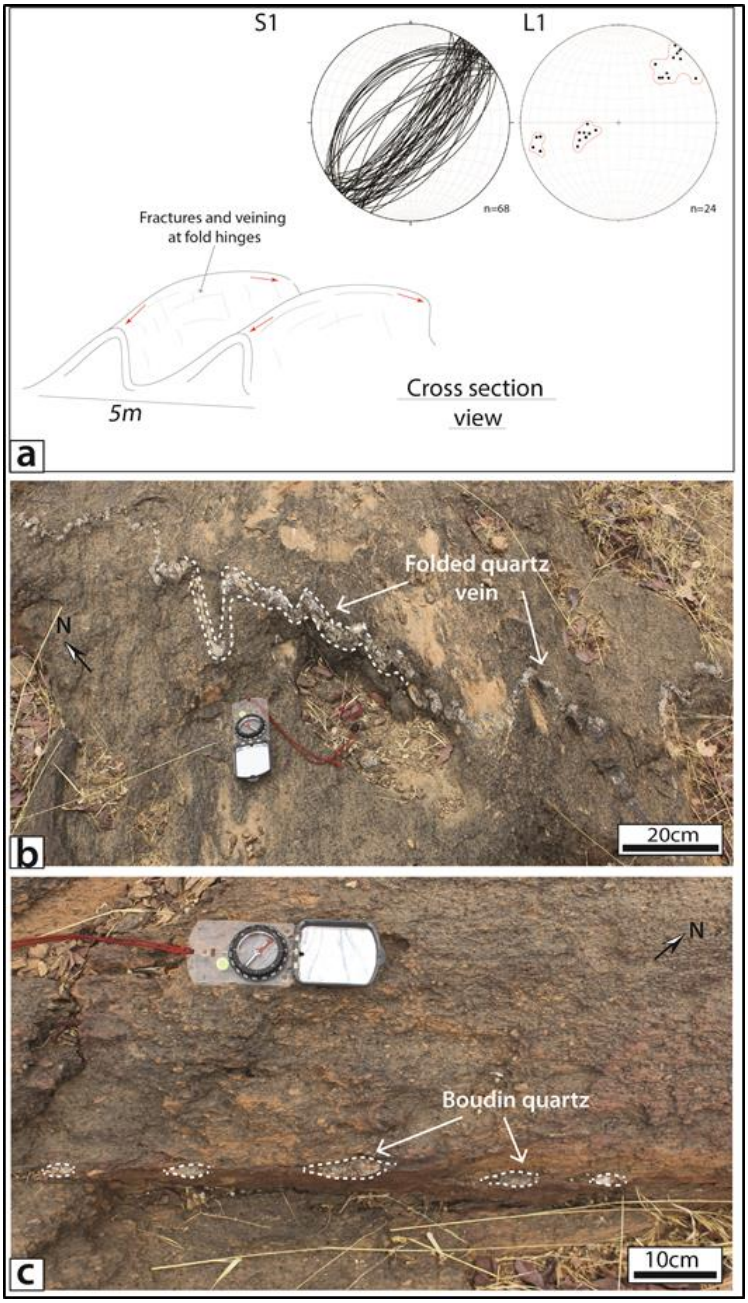


Figure 5.6: *(a) An illustration of the tight folded schistosed tuffaceous sequence located near the intersection zone of the FGSZ and the DT. The folds are doubly plunging, and have a SE vergence. The lineations on the folds is indicated by the red arrows in the cross section, and in stereoplot, have calculated average orientations of 29°→045°, and 41°→259. These folds have wavelengths of ~3m. The hinges of the folds have stockwork quartz veins. (b) The veins at the hinges of the folds are folded, and the fold axes of the quartz veins are NE and SW plunging. (c) Some veins are boudinaged. The boudins are parallel to the NE trend of the fold axis. Folding of the schistosed tuffaceous sequence developed under a NW-SE shortening regime.*

Foliation-S2

The second foliation, S2, is a crenulation cleavage and it folds S1 in a NW-SE trend with minor variations to E-W trends. S2 is not a pervasive foliation in some areas. S2 has a calculated average orientation of 303°/80° SW (Figure 5.3 insert a and c). An E-W trending crenulation cleavage that crosscuts S1 is observed within the siltstone-graphitic schist sequences (Figure 5.7 a). In this outcrop, the S1 orientation is 040°/82° SE, and the crosscutting crenulation S2 has an orientation of 086°/82° S. The crenulation cleavage formed under a sinistral shear sense as illustrated in Figure 5.7 a. The shortening direction required for the crenulation cleavage to form is a N-S to NNW-SSE orientation as illustrated in Figure 5.7 a. The S2 foliation also pervasively cuts through outcrops as shown in Figure 5.7 b, and has an orientation of 272°/80° S.

Sample GP037 is a chl-bt-qtz schist, and it has sub-euhedral feldspar grains (Figure 5.7 c). The location of sample GP037 is indicated in Figure 5.2. The preferred orientation of muscovite and biotite define the foliation. The foliation measured at outcrop location is 344°/48° NE. The rotation around the feldspar grains has a dextral shear sense, and this is consistent with N-S to NNE-SSW directed σ1. In sample GP004, Figure 5.4 c, the shear sense in the pyrite sigma clast is sinistral along the NE trending foliation, and the required σ1 orientation for sinistral shear along a NE plane is NNE-SSW. The sinistral shear in GP004 is attributed to a subsequent deformation D2 to D1 that produced the NE foliation.

Lineation-L2

The second set of lineation, L2, is not abundant in outcrops. L2 has an average orientation of 42°→090°. Stereoplots of L2 measurements in some areas in domain A are shown in Figure 5.3 insert a and c. These measurements are mainly crenulation fold axes lineations. The orientation of the slickenside lineation on the buck quartz vein in Figure 5.4 d is 45°→036°, consistent with the L2 stereoplot in Figure 5.3 insert a.

Quartz Veins-V2

A second set of veins, V2, crosscuts the larger V1 buck quartz veins and the schists. V2 is not abundant in outcrop; the stereoplots for V2 along the FGSZ are in Figure 5.3 insert b. These veins are much smaller than V1 measuring only a few

centimeters (~10cm) wide (Figure 5.5 d). V2 also crosscuts the chl-mus-qtz schist in a NW orientation (340°/60° SW) as seen in Figure 5.5 e. The quartz veins have undergone ductile deformation, and can be distinguished from the older veins that underwent recrystallization and are grey in appearance; the second set of veins is white in appearance (Figure 5.5 f and g).

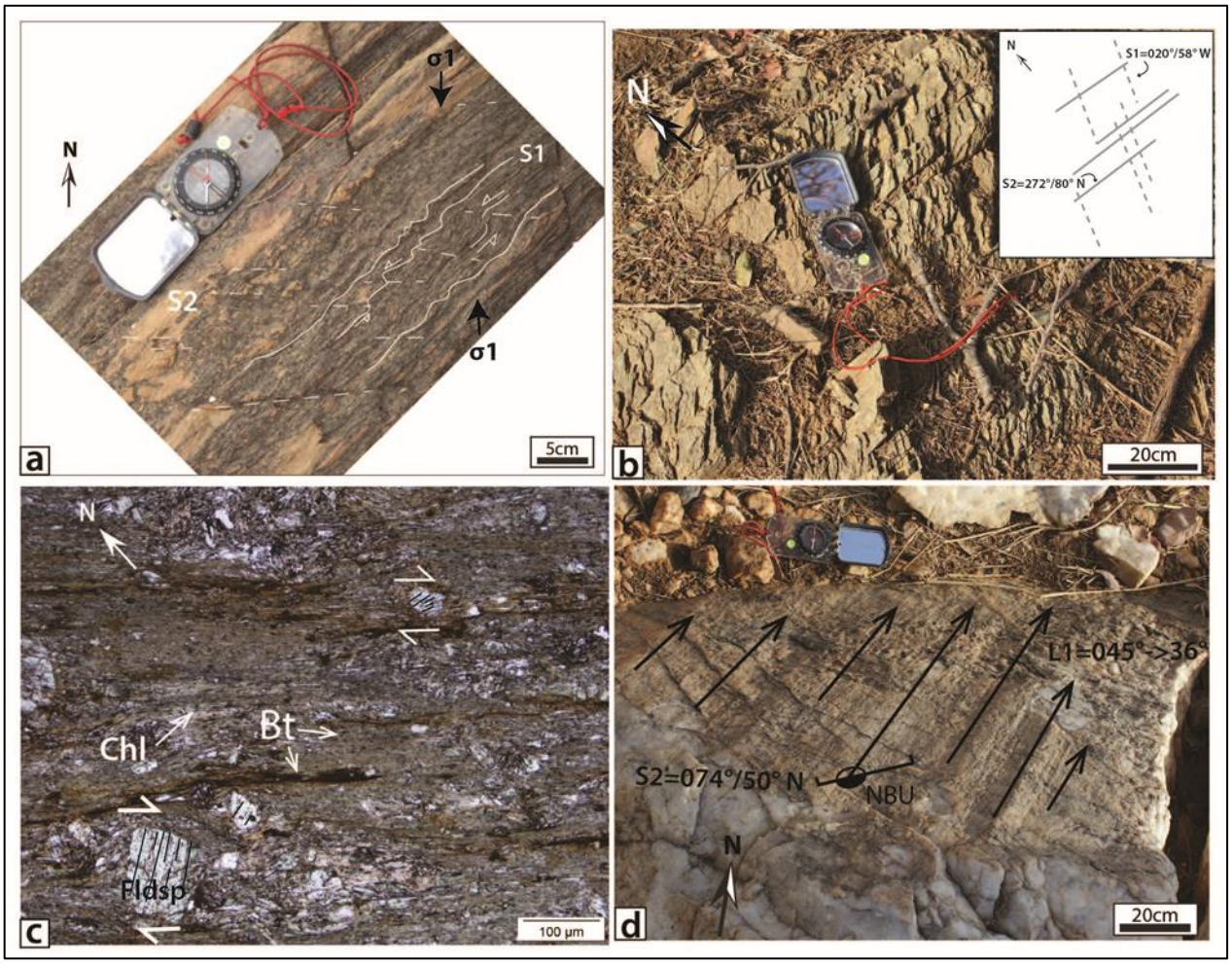


Figure 5.7: *(a) An iron-enriched schist with a NE trending S1 foliation, oriented 040°/82° SE is folded by a crenulation cleavage S2 oriented 086°/82° S. The required shortening direction for this S2 foliation to develop is N-S as illustrated. (b) An image of outcrop with an S1 cleavage (020°/58° W) crosscut by an S2 cleavage oriented 272°/80°. (c) Sample GP037 is also a chl-bt-qtz schist with feldspar clasts within the fine grained matrix. Although not well defined, the rotated fractures within the feldspar clasts indicate a dextral shear sense. (d) Striations and slickenside lineations on the surfaces of a buck quartz vein. The lineations are NE plunging, and the slickenside indicate that the northern block (according to north arrow in image D) was displaced upwards (NBU=north block up).*

The Gourma Mylonite Zone

Mylonitic zones are either isolated outcrops, or they crosscut the plutonic and greenstone outcrops adjacent to the FGSZ (domain A1 in Figure 5.2). The outcrops are low lying, and have a NE trending S1 foliation, and an E-W trending fracture cleavage planes. Some of the outcrops in this mylonite zone are not in-situ. Sample GP009, a proto-mylonite, and samples GP010 a and b, mylonites, are collected in the Gourma Mylonite Zones and their locations are indicated in Figure 5.2.

The mylonite, sample GP009, is from zone 1 as shown in Figure 5.2 (labeled as “1.”). It has quartz and feldspar porphyroclasts that are ~2mm in size, and an ultra-fine grained matrix (µm scale). The quartz grains have undulose extinction and sutured boundaries (Figure 5.8 a). Epidote does occur as part of the ultra-fine grained matrix composition. There is a remnant foliation in thin section and micro folds formed around the porphyroclasts. In hand sample, weak shear sense indicators are observed in the form of sigma clasts, but the outcrop from which this sample was collected is not in situ, therefore its shear sense indicators cannot be interpreted as part of the kinematic information. The S1 foliation measured adjacent to this outcrop has an orientation of 030°/28° NW.

Samples GP010 a and b were collected from zone 2 (labeled as “2.”) as shown in Figure 5.2; the outcrops from which the two samples were collected from are only a few meters apart. These samples are mylonites, containing more matrix than porphyroclasts (Figure 5.8 b), and the porphyroclasts are smaller (<1mm) compared to the proto-mylonite. The compositional variation may equate to an ultra-mylonite due to the matrix making up close to 90% of the rock (Wise et al., 1984). Sample GP010 is an oriented sample, and it has rotated plagioclase clasts (Figure 5.8 b, c, d). The porphyroclasts are quartz and feldspars. The matrix is composed of quartz, feldspar, biotite and ± muscovite and hornblende. The feldspars have simple and pericline twinning. Epidote alteration is present in the mylonites, and there euhedral pyrite crystals visible in thin section.

Samples GP010 a and b have a foliation defined by compositional banding within the matrix. The S1 foliation measured at the outcrop from which GP010 a is collected is 020°/32° NW, and the S1 foliation from the GP010 B outcrop is 048°/72° NW. The outcrop at sample GP010 b has a crosscutting S2 foliation oriented at 308°/74° SW. The foliation has asymmetric micro-folds (Figure 5.8 b). Sigma- and

delta- type clasts are not strongly developed and do not give a conclusive sense of shear. Sample GP010 B has dextral shear sense indicators defined by weakly developed plagioclase sigma clasts (Figure 5.8 d).

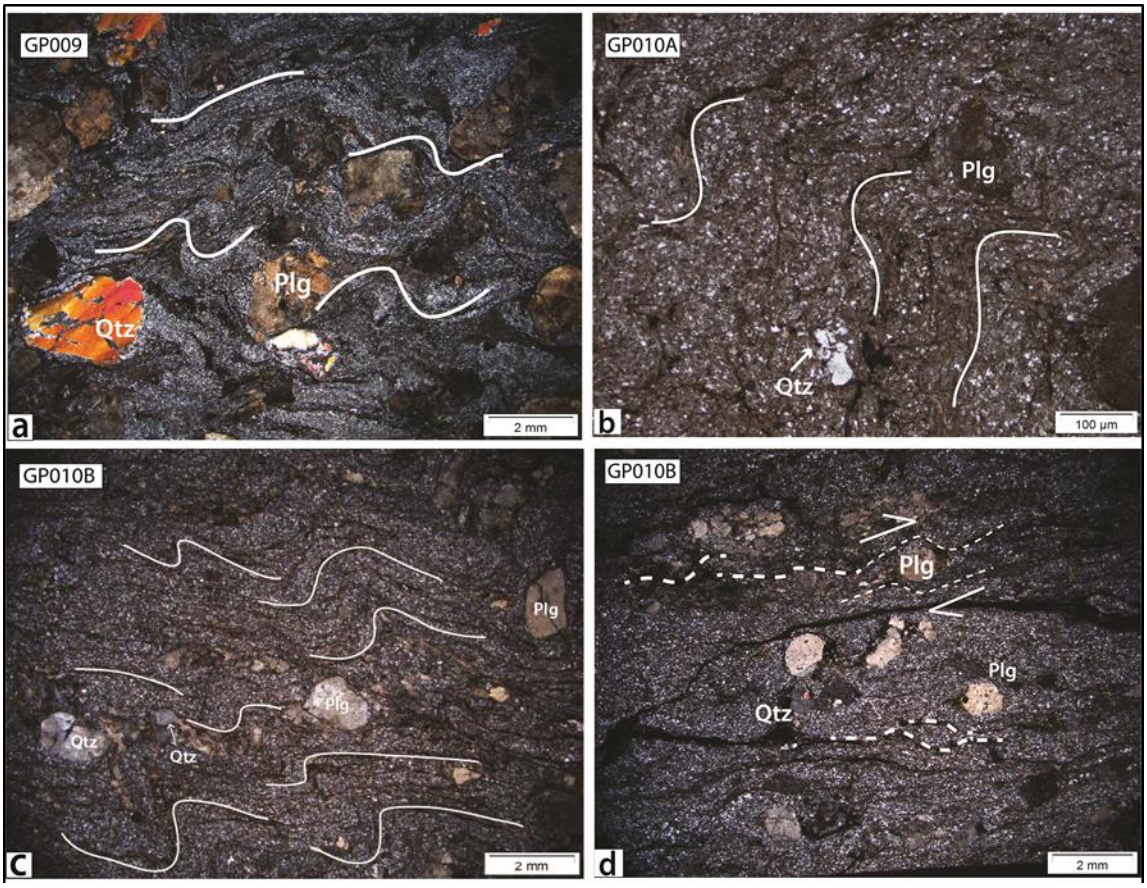


Figure 5.8: *(a) The micrograph of sample GP009 shows micro-folds that formed around the quartz and plagioclase clasts. The foliation is defined by a compositional banding of fine grained (µm scale) leucocratic minerals and minimal biotite. (This sample is not oriented). (b) A micrograph of sample GP010 A shows micro-folds that formed subsequent to mylonitization, and plagioclase and quartz clasts. Sample GP010 B also has micro-folds, and sub-euhedral plagioclase and quartz grains. Weak shear sense indicators have developed in sample GP010 B; the plagioclase delta clasts have with a dextral shear sense as illustrated in image (d).*

Fracture Cleavage Planes- S3

Brittle fracture cleavage planes affect most of the units in the field. In this domain, the fracture cleavage planes are observed on the granite gneiss outcrops (Figure 5.9 a) and some of the buck quartz veins (Figure 5.9 b).The fracture cleavage planes are sub-vertical, and are pervasive. The calculated average strike

orientations of the fracture cleavage planes are 310°/70° SW and 001/82° W (Figure 5.9 b).

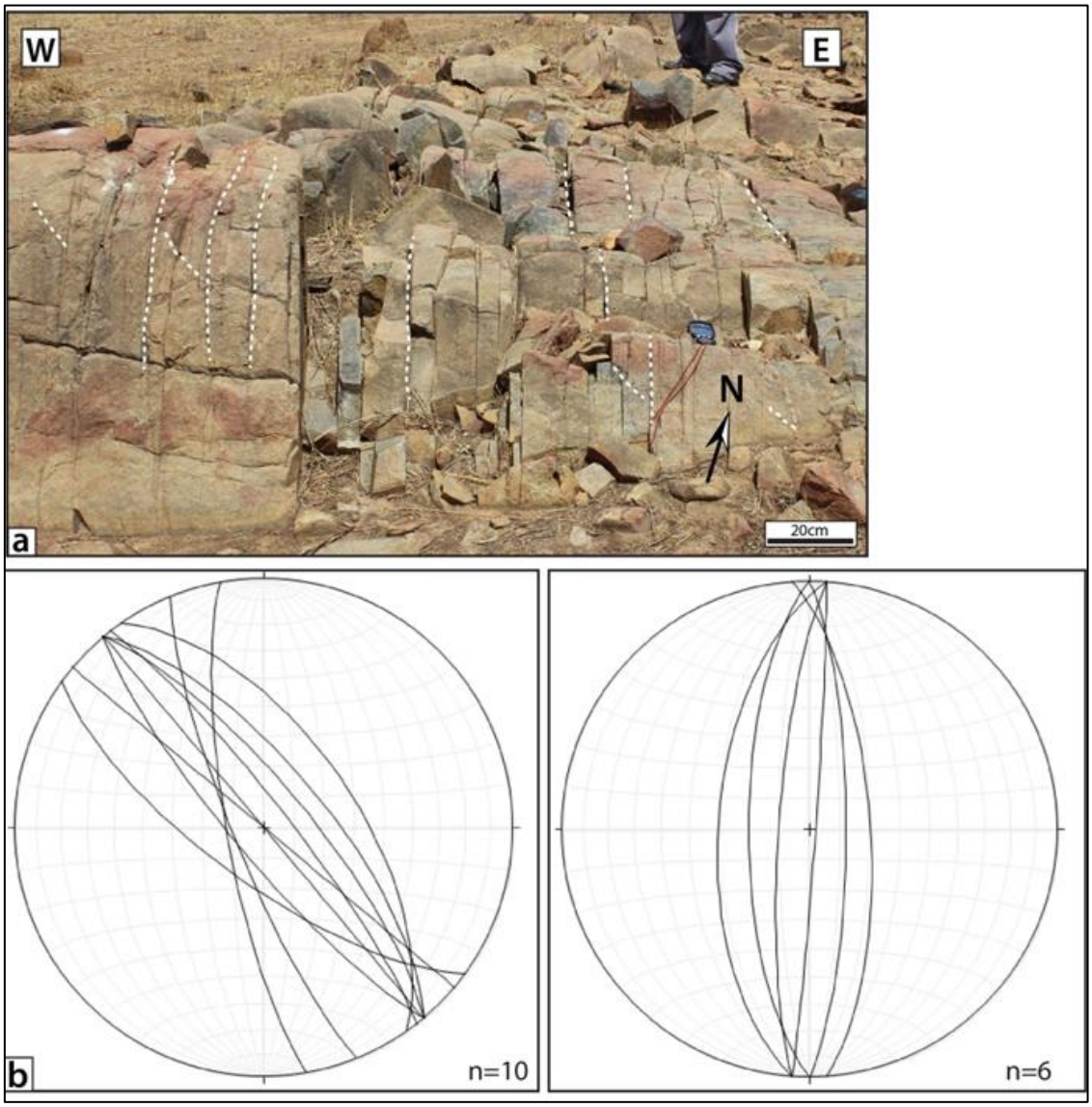


Figure 5.9: *(a). The granitic gneisses are crosscut by fracture cleavage planes. The fracture cleavage planes crosscut the gneissic foliation in the granite. The orientation of the dominant fractures cleavage planes at this outcrop has an orientation of 290°/88° NE. (b). The stereoplot of the fracture cleavage planes measured along FGSZ in domain A; the calculated average orientations are 310°/70° SW and 001/82° W.*

5.1.2 Domain A2-The Diabatou Trend

The DT is on the eastern margin of the Gourma Greenstone Belt (GGB) as shown in Figure 5.2. This trend is part of the overall structure of FGSZ; it makes up the eastern boundary of the FGSZ. Below are the structures and fabrics identified along the trend.

Foliation-S1

This domain, similar to A1, is dominated by a strongly foliated chl-bt-qtz schist (Figure 5.10 a). There are also strongly altered schist that are Fe-enriched, fine grained (≤1mm) and have a red/maroon appearance in outcrops. The schist units have a NNE to NE trending S1 foliation and has a calculated average orientation of 032°/67° SE. The strereoplots for S1 are indicated in Figure 5.3 insert c and d. In thin section, the quartz grain appear as either fine grained matrix with feldspars (<100µm in scale), or as slightly elongate, ribbon quartz grains (Figure 5.10 b). Chlorite and biotite, and the elongate quartz grains define the foliation.

In outcrop, the Fe-enriched schist has a NE trending S1 foliation, crosscut by an ENE trending crenulation S2 formed during a dextral shear sense (Figure 5.10 c). The orientation of S1 is 024°/72° SE, and S2 is 068°/88° NW as shown in Figure 5.10 c. The σ1 orientation required for dextral shearing for the S2 crenulation to form is NW-SE directed, as illustrated in Figure 5.10 c.

At map scale, the DT forms part of the western margin of a sigma structure, and the lineaments that define this structure were extracted from the geophysical imagery data. The general strike orientation of the DT along the sigma structure is 045°. The sigma structure is analyzed under the domain B- FBSZ section.

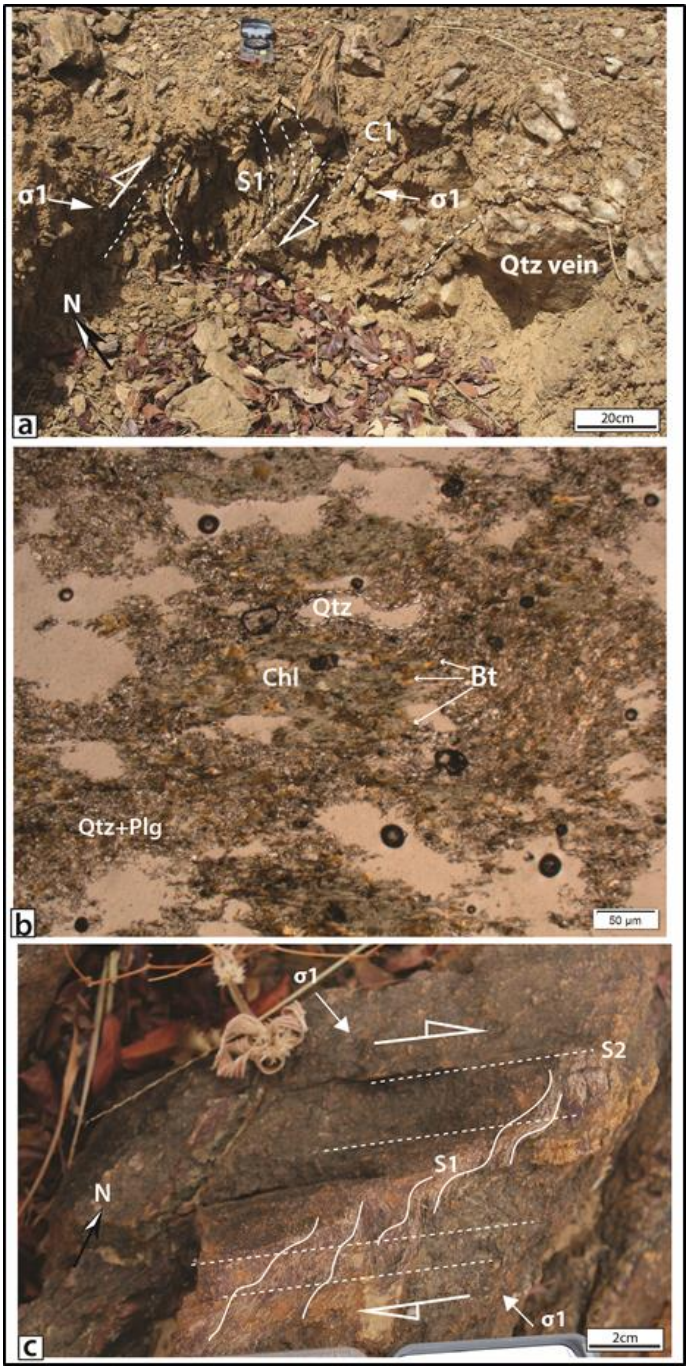


Figure 5.10: *(a) A chl-bt-qtz schist outcrop along the DT; these outcrops are low lying, and erode easily, unless they are silicified and/or Fe-enriched. This outcrop has an S-C fabric, and the measured S1 orientation is 024°/78° SE, and the C1 orientation is 036°/40° NW. The S-C fabric displays a dextral displacement, consistent with a NW-SE shortening direction. The schist is crosscut by a quartz vein, then subsequently underwent brittle deformation. (b) In thin section, sample GP002, whose location is indicated in Figure 5.2, is fine grained (~1µm). Chlorite, biotite and quartz ribbon define the foliation. Zircon is present as an accessory mineral. (c) An Fe-enriched schist outcrop, with two foliation sets S1 and S2. The S1 orientation measured at this outcrop is 024°/72° SE, and the S2 orientation is 068°/88° NW. This dextral displacement along the NE trending foliation is also consistent with a NW-SE directed σ1.*

Lineation-L1

The L1 stereoplots for the DT are in Figure 5.3 insert c and d. Lineation L1 is shallow with NE and SW azimuths; the calculated average orientation for the NE plunging lineation 46°→053°. One lineation has a SW plunge with an orientation of 20°→210°. Slickenside lineation and intersection lineation define L1, as shown is Figure 5.11 a.

Quartz Veins- V1

The chl-bt-qtz schist is host to the V1 and V2 set of quartz veins. The V1 set of veins are massive, buck quartz veins. Similar the veins along the FGSZ, the buck quartz veins are boudinaged within the schist host rock. Fracture cleavage planes crosscut the V1 quartz veins. The stereoplot for the V1 orientations are plotted in the Figure 5.3 insert c.

Ankerite and tourmaline has crystallized within the quartz veins. Disseminated and euhedral pyrite is present in the quartz veins, and is oxidized. In a few outcrops, malachite has crystallized within the veins.

Foliation-S2

S2 has an ENE-WSW trend; the calculated average orientation is 084°/86° S. S2 clearly crosscuts S1 in some Fe-enriched schist outcrops, as shown in Figure 5.12. North-northwest trending quartz veins crosscut the S2 foliation along the DT. The principal stress axis required for an ENE-WSW cleavage is NNW-SSE directed in pure shear.

Lineation-L2

Fold axes on folded buck quartz veins define the second set of lineation. They have an average orientation of 050°→90°. A few measurements are west plunging as shown in Figure 5.3 insert and c. Slickenside lineations similar to those observed on the buck quartz veins along the FGSZ are also present of the buck quartz veins along the DT, and form part of L2.

Quartz Veins- V4

The second set of quartz veins, V2, crosscut the V1 quartz veins, and the NE trending chl-bt-qtz schist. They are smaller in scale, only tens of centimeters wide.

The stereoplot orientations of V2 along the DT are shown in Figure 5.3 insert c. The orientation is NW trending; calculated average orientation is 338°/76° SW.

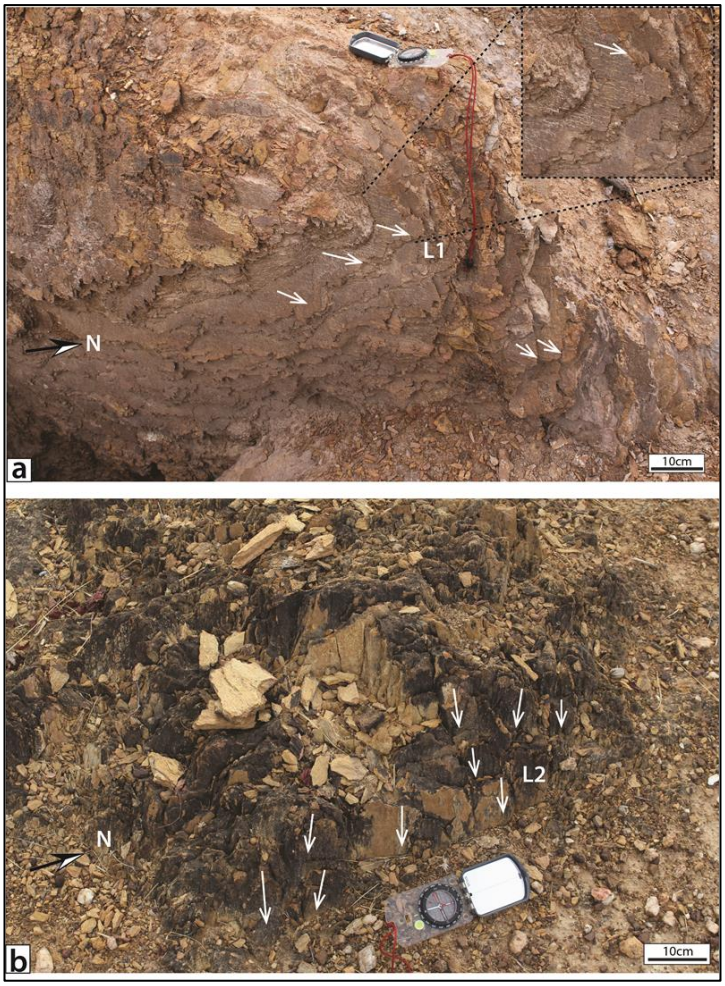


Figure 5.11: *(a) Lineations L1 along the DT are observed on the NE trending S1 surface of the Fe-enriched schist. The orientations on this outcrop are; S1 030°/68° SE, L1 10°→022°. (b) The L2 lineations are E plunging, and have calculated average orientation of 050°→90°.*



Figure 5.12: *An Fe-enriched schist with a NE trending S1 foliation oriented 026°/80° SE, crosscut by a ENE-WSW trending S2 foliation oriented 082°/82° NW. The stress axis changed from NW-SE for S1, to NNW-SSE for S2.*

5.1.3 Domain A3

Domain A3 is located between A1 and A2 (Figure 5.13 and Figure 5.14). This sub-domain makes up the Gourma greenstone belt, GGB, which is comprised of the meta-basalt unit, the meta-volcanoclastic greywacke and the meta-sedimentary rocks. A few data points were collected in between the FGSZ and the DT, and they present kinematic indicators related to the tectonics that occurred along the structures. A few of the outcrops have been schistosed, and developed a pervasive foliation. The foliation S1 and S2 orientations are shown in the stereplots in Figure 5.13.

At map scale, features such S-C foliation and folds are discernable, and were extracted from the aeromagnetics imagery data, as shown in Figure 5.14 insert a. A S1-C1 shear foliation is present in the meta-volcaniclastic greywacke (Figure 5.14 insert b), and the orientation of the S1 foliation is 020°/50° SE, and C1 is oriented 051°/80° SE. The shear sense along the S-C fabric is dextral. The σ1 orientation for dextral displacement along a NE trending S-C foliation is NW-SE, as shown in Figure 5.14 insert b. Stretched clasts in the meta-volcaniclastic greywacke of the sub-domain A3 define a stretching lineation, with average orientation 065/37. Figure 5.14 insert c shows the outcrop image from which lineation L1 measurements were taken.

The lineaments worm map and lithological sequences suggest that there is a regional scale synform in-between domain A1 and domain A2 (Figure 5.13 and Figure 5.14). This fold is an overturned fold with a NW vergence. The trend of this fold and the fold hinge is weakly discernable in the geophysical imagery data. The fold axial plane has a general strike orientation of ~040° measured from aeromagnetic imagery data.

Tambiga Hill is an artisanal mine in the Gourma region located between the FGSZ and the DT, as shown in Figure 5.14 and Figure 5.15. It is the largest active artisanal mine locally. The quartz stockwork-vein deposits are targeted and mined out. Tambiga Hill is located ~500m west of one of the NW-faults extracted from aeromagnetic imagery data (Figure 5.15).

Most of the other active artisanal mines are located along the DT, and their locations are illustrated by the orange polygons in Figure 5.15. Some of the locations of the sites were mapped in the field, and others were extracted from Google Earth imagery data. Some of the sites are inactive, and/or abandoned. The artisanal sites

are located along the strike of buck quartz veins, and the pits are about a meter wide, and are several meters deep. Tourmaline, pyrite, ankerite and minor malachite have crystallized within the fracture structures of the quartz veins.

Gold mineralization occurs as both invisible gold, and as precipitated gold nuggets within the structures of the quartz veins. The artisanal miners crush and mill the quartz, the pan the precipitate in water. The heavy minerals sink to the bottom of the pan and the gold is separated. Figure 5.16 a shows a gold nugget from a quartz vein along the DT, and Figure 5.16 b shows heavy minerals including gold that have sunk at the bottom of a pan after milling.

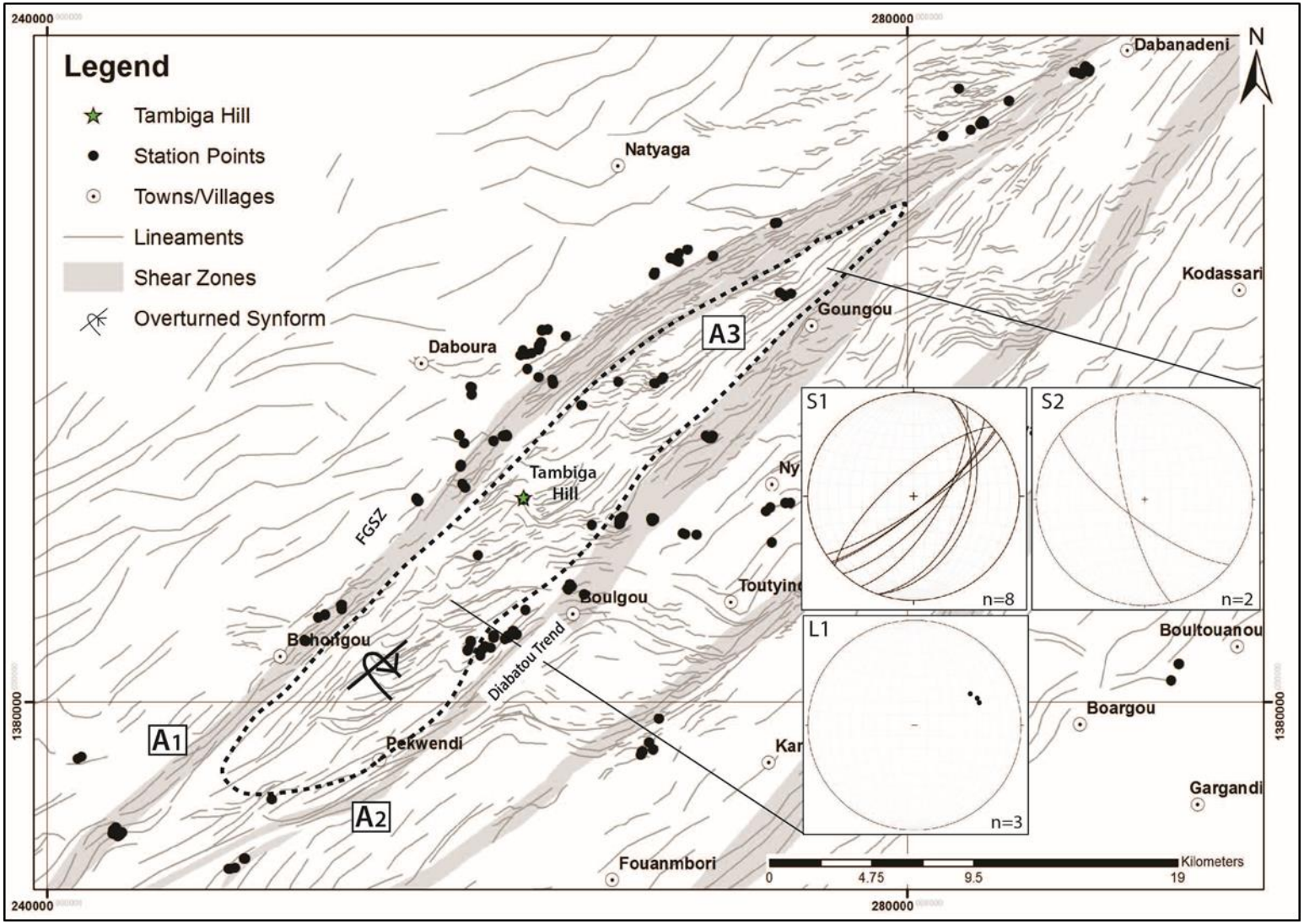


Figure 5.13: *A few of the station points within A3 had structural data, and the S1, S2 and L1 data is presented in the stereoplots. The S1 foliation has a calculated average orientation of 039°/68° SE. The S2 foliation crosscuts S1 in a NW orientation, calculated average 327°/73° SW. The lineation is defined by stretching clasts in a meta-volcaniclastic greywacke, and they have a calculated average orientation of 37°→065°.*

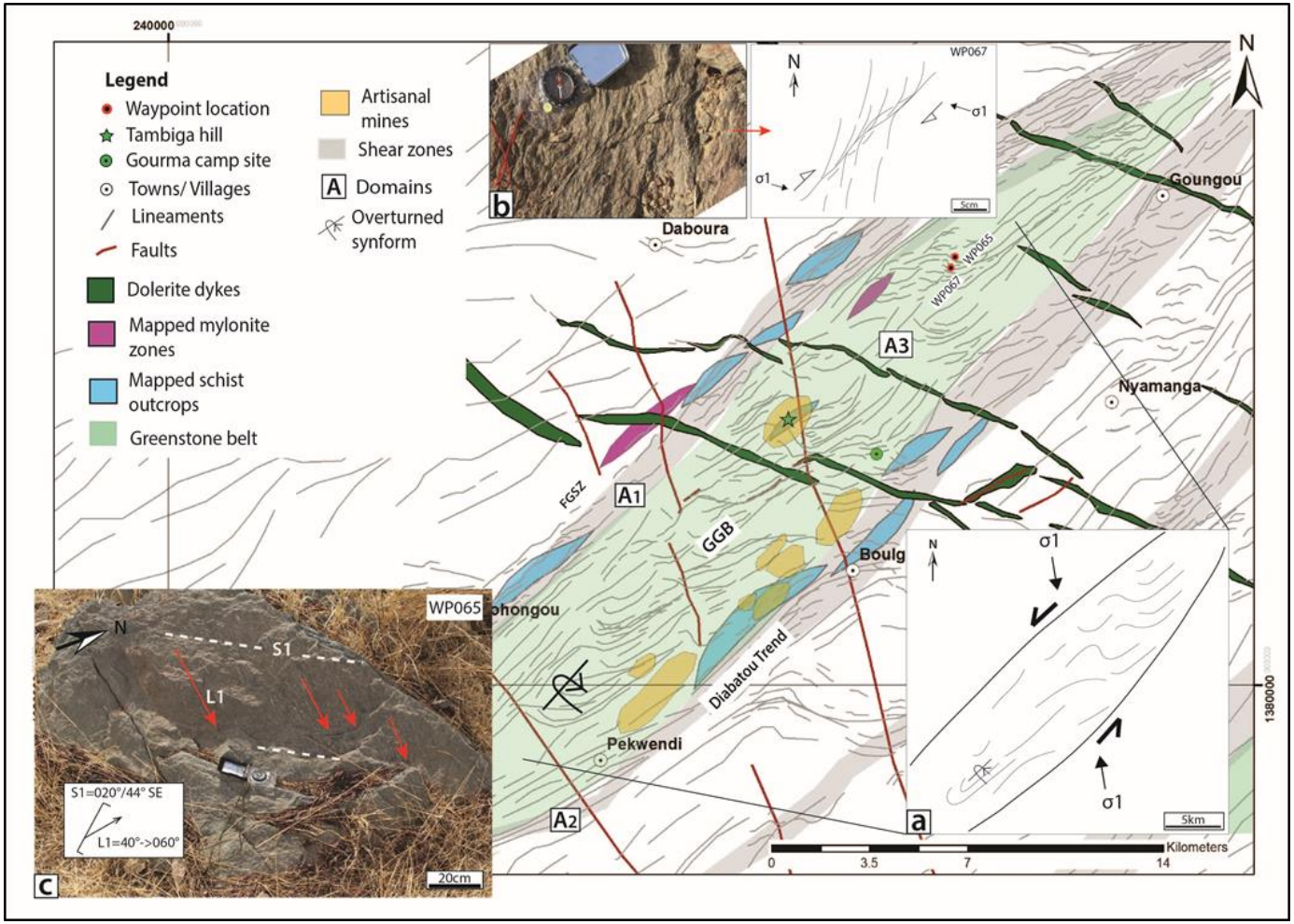


Figure 5.14: *A summation of the structures identified in sub-domain A3; (a) The overall sense of shear along the area of sub-domain A3 is sinistral, with rotational lineaments discernible on and extracted from aeromagnetic data. The principle stress axis responsible for this displacement is NNW-SSE oriented. The entire GGB is interpreted to be an overturned synform, and the fold hinge lineaments were traced and extracted from aeromagnetic imagery data, and the fold axis has a NE strike orientation of ~050°. The fold may have formed under a more NW –SE oriented σ1. (b) The meta-volcaniclastic greywacke has S-C fabric shear sense indicators. The sense of displacement is dextral, and the principle stress axis is NW-SE directed. (c) The L1 lineation on a NNE trending S1 plane; the lineation is defined by stretching clasts in a meta-volcaniclastic greywacke. The S1 orientation in this outcrop is 020°/44° SE, and L1 is 40°→060°. The station points to which the outcrop images (a) and (b) belong are indicated in the map.*

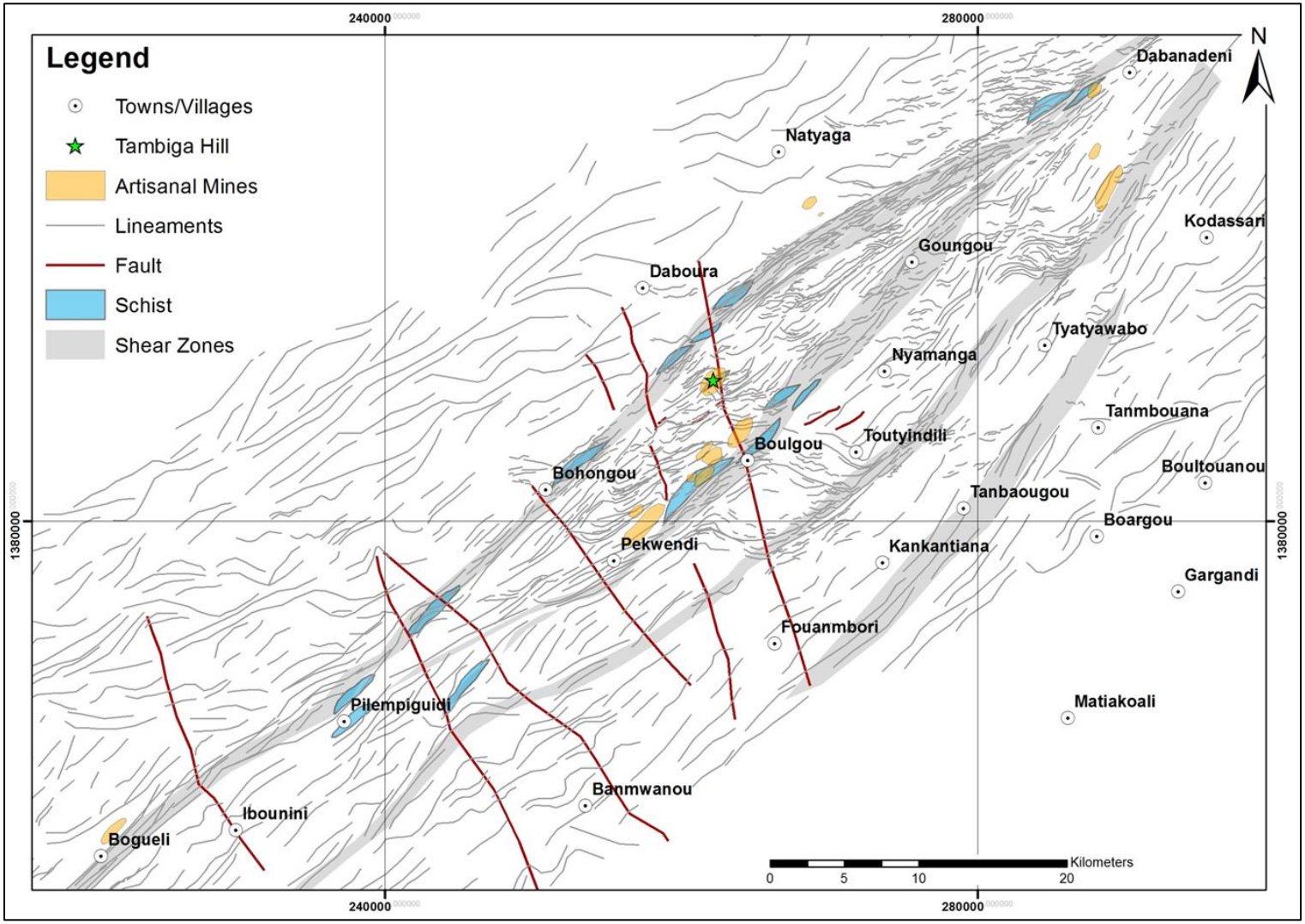


Figure 5.15: *This map shows the locations of the artisanal mine sites that were identified in the field, and using Google Earth images. The artisanal mines are located in association with the buck quartz veins, and mining occurs along strike of the veins. The pits of the artisans are ~1m wide and can be several meters deep. Tambiga Hill is indicated on the map by the green star symbol; it is located in the middle of sub-domain A3.*

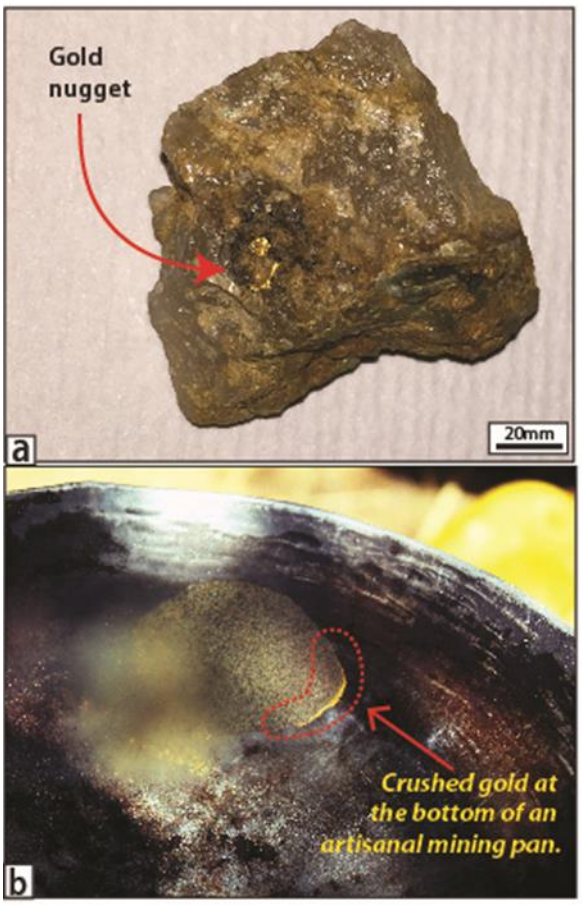


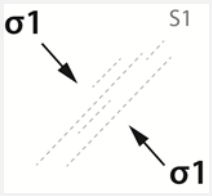
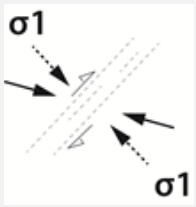
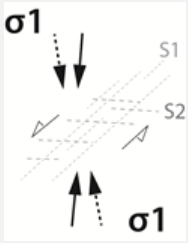
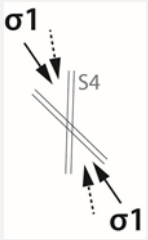
Figure 5.16: *(a) A gold nugget that is hosted within the fractures of a quartz vein; the sample is from an artisanal mine along the DT. (b) An image of an artisanal pan with heavy minerals including gold; the gold sinks to the bottom of the pan and is separated out.*

5.1.4 Summary of the structures and sequence of deformation events in Domain A

Four deformations are identified based on the overprinting relationships. The interpretation includes both the structural data and the magnetic imagery data. The deformation events and the related structures are summarized in Table 4.

Table 4: *Summary of the structures and deformation events in domain A.*

D1	D2 and D3		D4
NE trending S1 foliation	Folding of NE trending S1 foliation	E-W to NW-SE trending S2 foliation	NW trending S4 fracture cleavage planes
Ductile deformation	Ductile deformation	Brittle-ductile deformation	Brittle deformation

	Mylonites	Possible mylonite formation	
Steeply plunging lineation with SE azimuth	NE and SW plunging fold axis L1	E-W plunging L2	
NE trending quartz veins V1	Deformation of V1		NW trending minor quartz veining V4
	Dextral (reverse) displacement ; Dilation bend	Sinistral displacement	
NW-SE directed principal stress axis; coaxial compression 	WNW-ESE to NW-SE non-coaxial principal stress axis 	NNE-SSW trending principal stress axis 	NNW-SSE to NW-SE principal stress axis 

5.2 DOMAIN B-THE FADA-BOULOUGOU SHEAR ZONE

The Fada-Boulougou Shear Zone (FBSZ) is NE trending, and is parallel to the FGSZ. In this study the FBSZ is ~130km in length, from southeast of Dabanadeni to west of Fada N'Gourma. This shear zone is up to 1.9km wide in the Gourma region and thins out to the south, being up to 1km wide. Only the northeast extension of the FBSZ in the Gourma region is analyzed in domain B (Figure 5.17). The southwest extension of the shear zone is analyzed in domains C and D.

Majority of the data analysis for this domain is based on the geophysical data, as not a significant amount of structural station points were collected along the FBSZ.

5.2.1 Geophysical Imagery Lineaments Map Analysis

The NE trending DT and the FBSZ are bounding structures to a regional sigma structure near the Boulgou and Pikwendi villages, as illustrated in Figure 5.17 insert a. The rock type where the sigma structure is located is granitic. The sigma structure is ~9.8km in length along the strike of the shear zones, and ~7.8km wide. The foliation has formed wings around the sigma structure and sinistral shear sense indicators envelope this structure (Figure 5.17 insert a).

There are S-C fabrics along the FBSZ that are discernible in aeromagnetic imagery data. Figure 5.17 insert b illustrates the fabric; the FBSZ is a C-plane to a series of S-planes. The strike orientations of the S and the C foliations are ~290° and ~030°, respectively, as determined from aeromagentic image data. Although weakly developed, a similar pattern is consistent between the TT and the FBSZ. All these fabrics have a sinistral shear sense. The stress axis for sinistral displacement along a NE trending foliation is N-S to NW-SE oriented, as illustrated in Figure 5.17 insert a and b.

5.2.2 Foliation- S1

The structural measurements taken along and adjacent to the FBSZ have a NE trending S1 foliation. The S1 stereoplots are in Figure 5.18 insert a and b. The chl-mus-qtz schist defines the S1 foliation in Figure 5.18 insert a. The S1 foliation measurements in Figure 5.18 insert b is a gneissic foliation in the granite gneiss and the (foliated) plg-qtz granodioritic gneiss in some plutonic units adjacent to the FBSZ. The calculated average S1 orientation is 041°/82° SE. The NE trending S1 foliation is consistent with a NW-SE oriented σ1.

WNW to ESE oriented shears with a dextral shear sense crosscut the S1 foliation as shown in Figure 5.19. The strike orientation of the shear is 284°, and the shear has weakly defined S1-C1 fabrics. The principal stress axis has a NW-SE orientation as illustrated in Figure 5.19.

5.2.3 Lineation- L1

A few lineations are present in the plg-qtz granodiorite outcrop mapped along the FBSZ, and stretching plagioclase and minor hornblende define the lineation. The two mineral lineations stereoplot is in Figure 5.18 a, and the calculated average orientation is 42°→227°.

5.2.4 Quartz Veins- V1

Not many of the buck quartz veins are preserved in outcrop, and most have undergone brittle deformation and are low lying, fragmented sub-outcrops whose orientation cannot be determined. The strereoplot of the vein orientations measured along the FBSZ is in Figure 5.18 insert a. These veins are NW trending, and have a calculated average orientation of 320°/80° NW. This outcrop of veins is brecciated, and later underwent brittle deformation that resulted in crosscutting fractures, as shown in Figure 5.20 a and b.

5.2.5 Faults- F1

One pyroxenite unit proximal to the FBSZ has crosscutting N-S (~000° strike orientation) and WNW-ESE (~280° strike orientation) trending faults that are steeply dipping. The faults are infilled by pegmatitic veins. The faults have a sinistral displacement, as shown in Figure 5.20 inserts c and d. The shortening direction required for the sinistral displacement is NW-SE oriented, as illustrated in Figure 5.20 insert d.

5.2.6 Foliation- S3

One outcrop at station point WP266 as indicated in Figure 5.17 has a proto-mylonitic texture with the composition of hornblende, plagioclase, quartz and K-feldspar. The outcrop has an S3-C3 foliation; the S2 has an orientation of 052°/80° SE and the C3 orientation is 028°/88° SE. The shear sense in the S-C fabric is sinistral, and the orientation of the σ1 required for this displacement is NNW-SSE. At map scale, the S-C fabrics along the FBSZ as illustrated in Figure 5.17 insert b is consistent with the fabric observed at outcrop scale, with a similar NNW-SSE directed σ1 orientation.

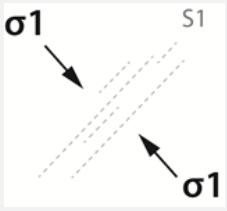
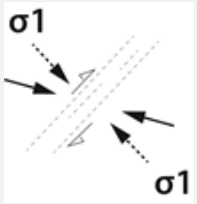
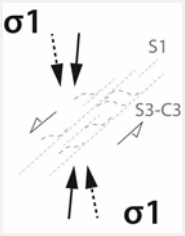
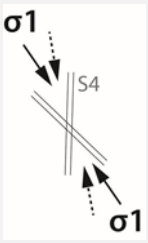
5.2.7 Fracture cleavage planes- S4

Some of the buck quartz veins hosted within the FBSZ, and the granodiorite and granitic units proximal to the FBSZ have fracture cleavage planes that crosscut all other structures. These fractures have a consistent NW trend. The calculated average orientations of the fracture cleavage planes are 293°/83° NW and 346°/79° SW. The stereoplot for the fracture planes is in Figure 5.18 insert c.

5.2.8 Summary of structures and sequence of deformation events for the FBSZ

Structures relating to the northeastern extension of the FBSZ are summarized in Table 5 below, and the deformation events to which each structure belongs are defined based on crosscutting relationships.

Table 5: *Summary of the structures and deformation events in domain B.*

D1 and D2		**D3**	**D4**
NE trending S1	Deformation along NE trending S1-C1 fabric	S3-C3 fabric on NE trending foliation	NW trending S4-fracture cleavage planes
Ductile deformation	Ductile deformation	Ductile deformation	Brittle deformation
NE trending FBSZ	Dextral displacement	Sinistral displacement	
NW-SE directed σ1 	NW-SE to NNW-SSE directed non-coaxial σ1 	N-S to NNW-SSE directed σ1 	NW-SE directed σ1 

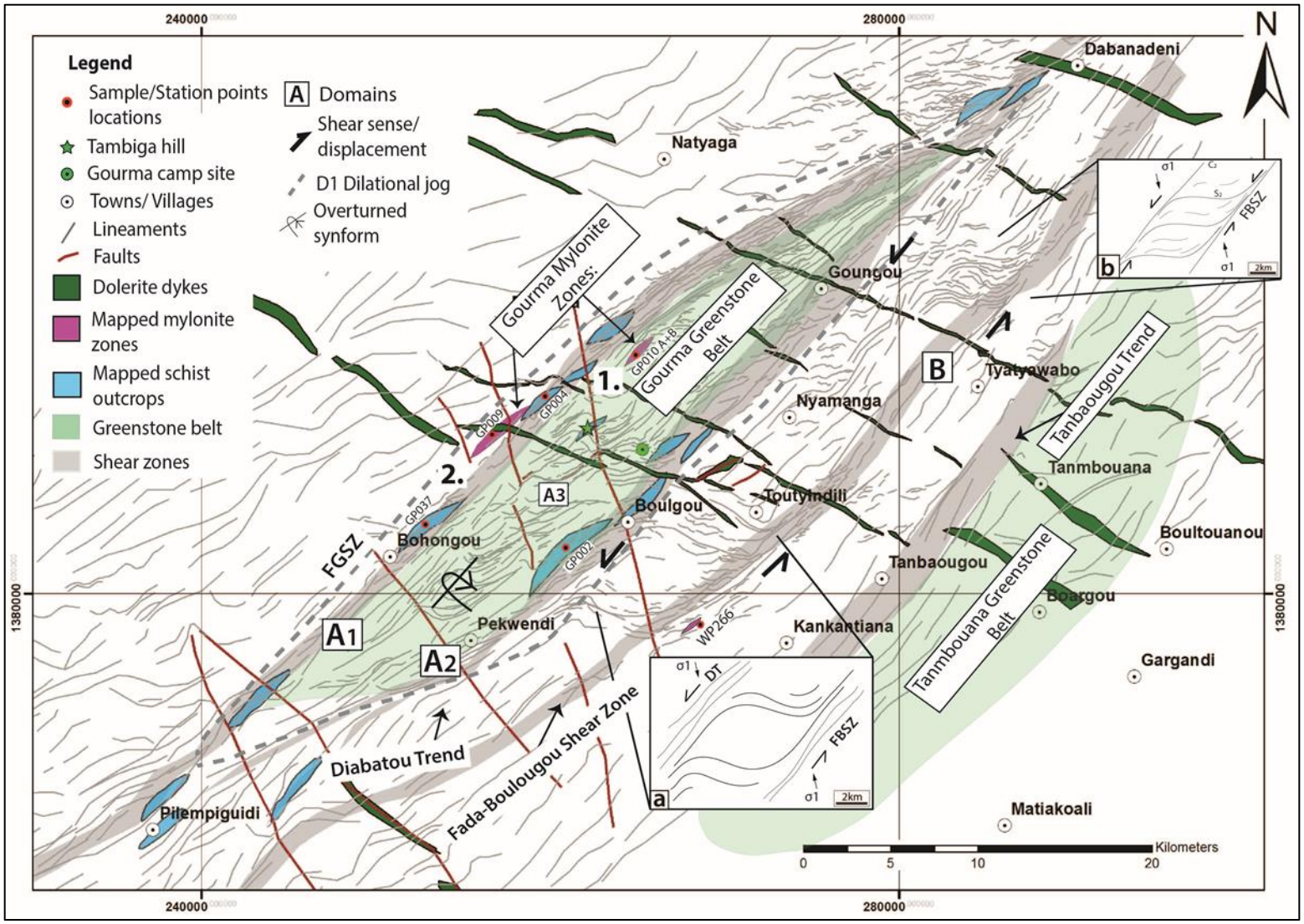


Figure 5.17: *This lineaments map illustrates the sinistral shear sense indicators along the domains A2 and B. The lineaments from aeromagnetic imagery data reveal a regional sigma structure between the DT and the FBSZ, and S-C fabrics along each shear zone. The pattern of S-C fabric is consistent in between the shear zones, although not always strongly defined.*

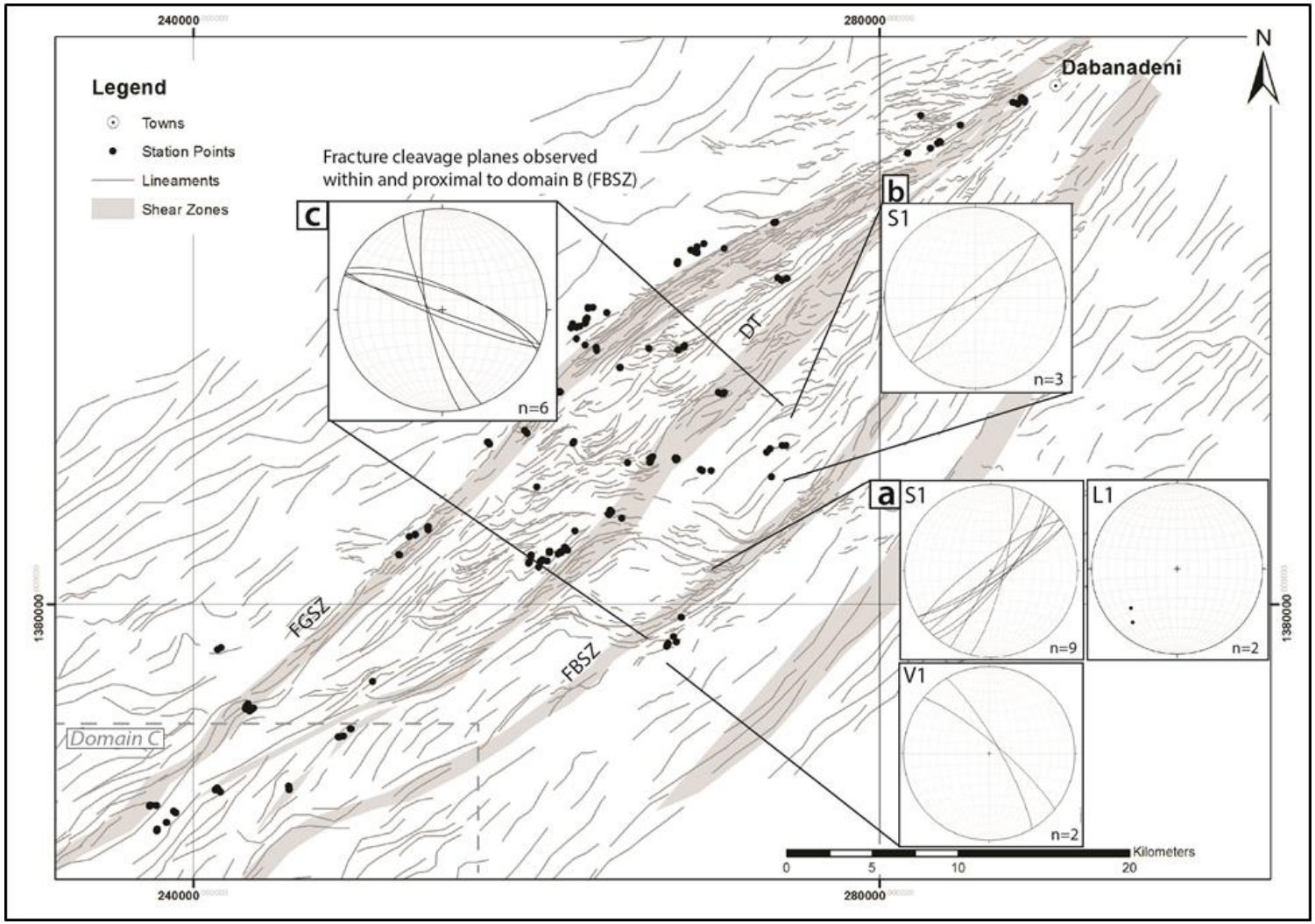


Figure 5.18: *Stereoplots of foliation and lineation in domain B, and additional station points along domain A2, south of the Gourma camp site. The data reveals a consistency in the NE trend of S1. Stereoplots along the DT have limited lineation and quartz veins measurements. The location of the L-tectonite unit, discussed in domain A is between the FGSZ and the FBSZ. The stereonet for the fracture cleavage planes along the FBSZ indicates as NW trending set of fractures.*



Figure 5.19: *A foliated granodiorite with an S1 orientation of 058°/80° SE crosscut by a meso-scale (cm) dextral shear zone (minor S1-C1 fabric). The strike orientation of the meso-scale shear zone is 284. The σ1 orientation along the dextral shear is NNW-SSE.*

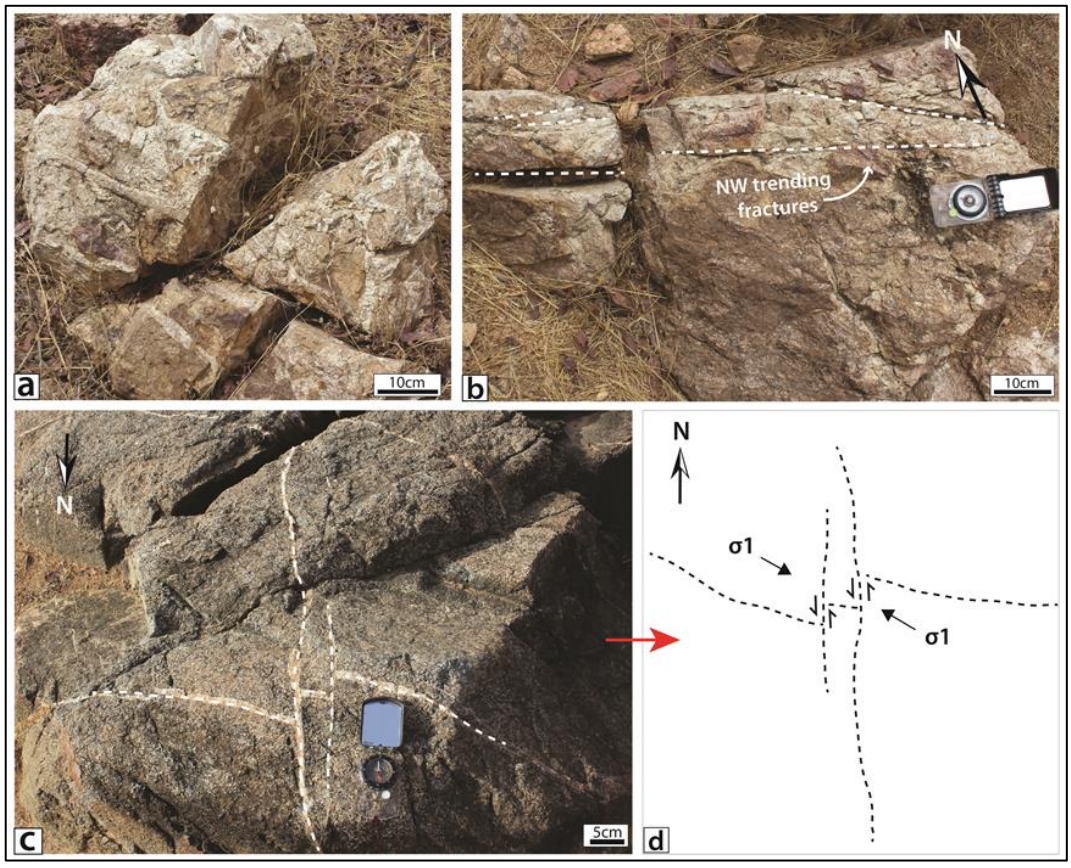


Figure 5.20: *(a) An outcrop of a brecciated quartz vein; the veins have also undergone late stage brittle deformation and a fractured and fragmented. (b) The quartz veins are crosscut by NW trending fractures. (c) A pyroxenite unit is crosscut by N-S and WNW-ESE trending faults. The fault planes have been infilled by pegmatites. Image (d) is an illustration of image (c), and is rotated so that north is facing up. Image (d) illustrates the displacement along the faults. These faults have a sinistral displacement along them. The σ1 orientation is NW-SE oriented.*

5.3 DOMAIN C

This domain is located south of domains A and B and it encloses the trends of the FGSZ and the FBSZ, as shown in Figure 5.21. Domain C continues with structural analysis along the two shear zones; defining the domains along the strike of the NE trending structures made for simplified data analysis and presentation.

5.3.1 Foliation- S1

Granite gneisses and foliated granodiorites dominate domain C. The orientation of S1 is NW trending, calculated average orientation 300°/78° SW (Figure 5.22 insert a and b). The dip direction however does vary from NE to SW. Compositional banding in the gneisses and preferred mineral orientation in the foliated granodiorite defines S1 (Figure 5.23 a and b).

There is little evidence found of any other structural fabric overprinting the NW trending S1 foliation. One outcrop displays meso-folds that formed along the NW trending foliation, as shown in Figure 5.23 c. The orientation of S1 in the outcrop is 298°/84° SW. The fold axial plane along these meso-scale folds is ENE trending, with an orientation of 076°/60° SE. The shortening direction required for folding of the NW trending S1 is either N-S, as illustrated in Figure 5.23 c, or sub-orthogonal to the NW trend between N-S and NE-SW directed.

5.3.2 L-tectonite- L1

The iron-enriched meta-siltstone and graphitic schist units ~2km south of the intersection of the FGSZ and the DT in Pilempiguidi have developed an L-tectonite fabric, with steep plunge angles (Figure 5.24 a). The L-tectonite is crosscut by sub-horizontal fracture planes with a calculated average orientation of 304°/07° NE (Figure 5.24 b and c).The L-tectonite has a calculated average orientation of 81°→155° (Figure 5.24 d). The orientation of the L-tectonite is consistent with a sub-vertical displacement.

5.3.3 Faults- F1 and associated myonite

A set of cm-scale faults crosscut the granite gneiss and the foliated (gneissic) granodiorite. Majority of these faults have quartz infilling and they have displacement indicators. The stereoplot of these faults is in Figure 5.25 a.

Dextral and sinistral shear senses are observed of the faults; the faults with calculated average orientation of 004°/85° E have sinistral displacement (Figure 5.25

b), and the faults with calculated average orientation 068°/88° SE have dextral displacement (Figure 5.25 c). Some of the faults have been mylonitized along the planes of shear, as shown in Figure 5.25 c. These mylonite zones are only a few centimeters wide.

5.3.4 Foliation- S2

In the zone between the FGSZ and the FBSZ, there is a NE trending S2 foliation. Gneissic, mylonitic and minor schist foliation defines S2 in domain C, The calculated average orientation of S2 is 042°/71° SE. The S2 foliation crosscuts the granite gneiss and granodiorite plutonic units that are located proximal to the shear zones. An S2 fold axial plane along NE trending meso-scale folds crosscut S1 with an orientation of 076°/60° SE as illustrated in Figure 5.23. In the siltstone-graphitic schist sequences near Pilempiguidi village (Figure 5.21) have been schistosed, although the primary sedimentary bedding sequences are still preserved. The S0 is parallel to S2, with an orientation of 060°/64° SE.

Two mylonite outcrops were mapped close to the Bogueli village, and the location of the mylonites is here referred to as the Bogueli Mylonite Zone. Both outcrops are strongly foliated. In one outcrop, shown in Figure 5.26, northeast trending mylonitic shear zones of between 10 and 30cm overprint a gneissic granodiorite (Figure 5.26 a). The mylonitic shear zones have a calculated average orientation of 040°/80° SE, and this is sub-parallel to the foliation measured in this outcrop,058°/80° SE.

Quartz sigma clast are present in the mylonitic shears, and they have dextral shear sense indicators (Figure 5.26 a and b). Figure 5.26 a illustrates tight, micro-folds with NE plunging fold axes (azimuth ~30°) and a fold axial plane (a strike orientation of ~050°) within the mylonite shear zones. There are thin (cm scale), NE trending quartz veins with dilation bends that have dextral displacement along them, as illustrated in Figure 5.26 a. Extensional shear bands and planes have developed in the mylonite in Figure 5.26 b, and they also enclose quartz sigma clasts. The overall stress regime for the shear sense indicators observed in this outcrop is a NW-SE to WNW-ESE oriented σ1 with dextral shear sense along the NE trending foliation.

The second mylonite outcrop zone is ~800m southeast from the first outcrop described above. This zone has a few outcrops that are ~1m wide and up to 2m in length. These outcrops are ~50cm in height. This mylonite has a pink appearance and a felsic composition of plagioclase, K-feldspar and quartz and minor hornblende (Figure 5.27 a). The matrix grain size is ultra-fine, less than 1mm, and the feldspar clasts are up to 1cm in size.

The mylonite has a pervasive NE trending foliation with an orientation 060°/87° NW. A weakly defined S2-C2 fabric is present, S2 orientation 040°/87° NW and C2 orientation 055°/88° NW, with dextral shear sense. Lineation is defined by stretching feldspar minerals and have a calculated average orientation of 07°→ 050°. En échelon quartz veins crosscut the mylonite, as shown in Figure 5.27 b. The veins have undergone a dextral shear, and the orientation of the σ1 is NW-SE as illustrated in Figure 5.27 b.

5.3.5 Lineation- L2

Lineation for Domain C is sub-divided into L2a, L2b and L2c. These lineation measurements lie on the NE-trending S2 foliation, but have different orientations in different outcrops (Figure 5.22 insert a). This is an indication that they may represent different deformations events dominated by pure or simple shear, change in flow characteristics along one plane, or have different causes (crenulation lineation or stretch mineral lineation) (Passchier and Trouw, 2005).

Lineation-L2a

L2a is steeply SE or NW punging. Stretching minerals feldspar and minor hornblende define L2a. The granite gneiss outcrop shown in Figure 5.28 has steep dipping S2 foliation (measured orientation 076°/72° NW), and stretching mineral lineation defined by hornblende and feldspars, oriented at 70°→324°.

Lineation-L2b

L2b is a mineral lineation on the S2 plane defined by feldspar and hornblende, and is also defined by fold axes in the micro-folds found in the meso-scale NE trending mylonitic shear zones described in section 5.3.3 and shown in Figure 5.25 a. The calculated average orientations are 66°→047° and 78°→231°.

Lineation-L2c

Stretching minerals plagioclase and minor hornblende define the L2c lineation. L2c is generally shallow plunging. The calculated average orientations are 17°→224° and 08°→048°.

5.3.6 Quartz veins-V2

The quartz veins recorded in the V2 stereoplot in Figure 5.22 insert a represent two veins that crosscut the mylonite zone described under section 5.3.4. These veins have a NW orientation, calculated average orientation 307°/85° NE.

5.3.7 Fracture planes- S4

Extensional fracture cleavage planes crosscut the granite gneiss and foliated granodiorite outcrops. Most of the fracture cleavage planes have been infilled with quartz and formed veins. The calculated average orientations are 307°/88°NE and 356°/88°E.

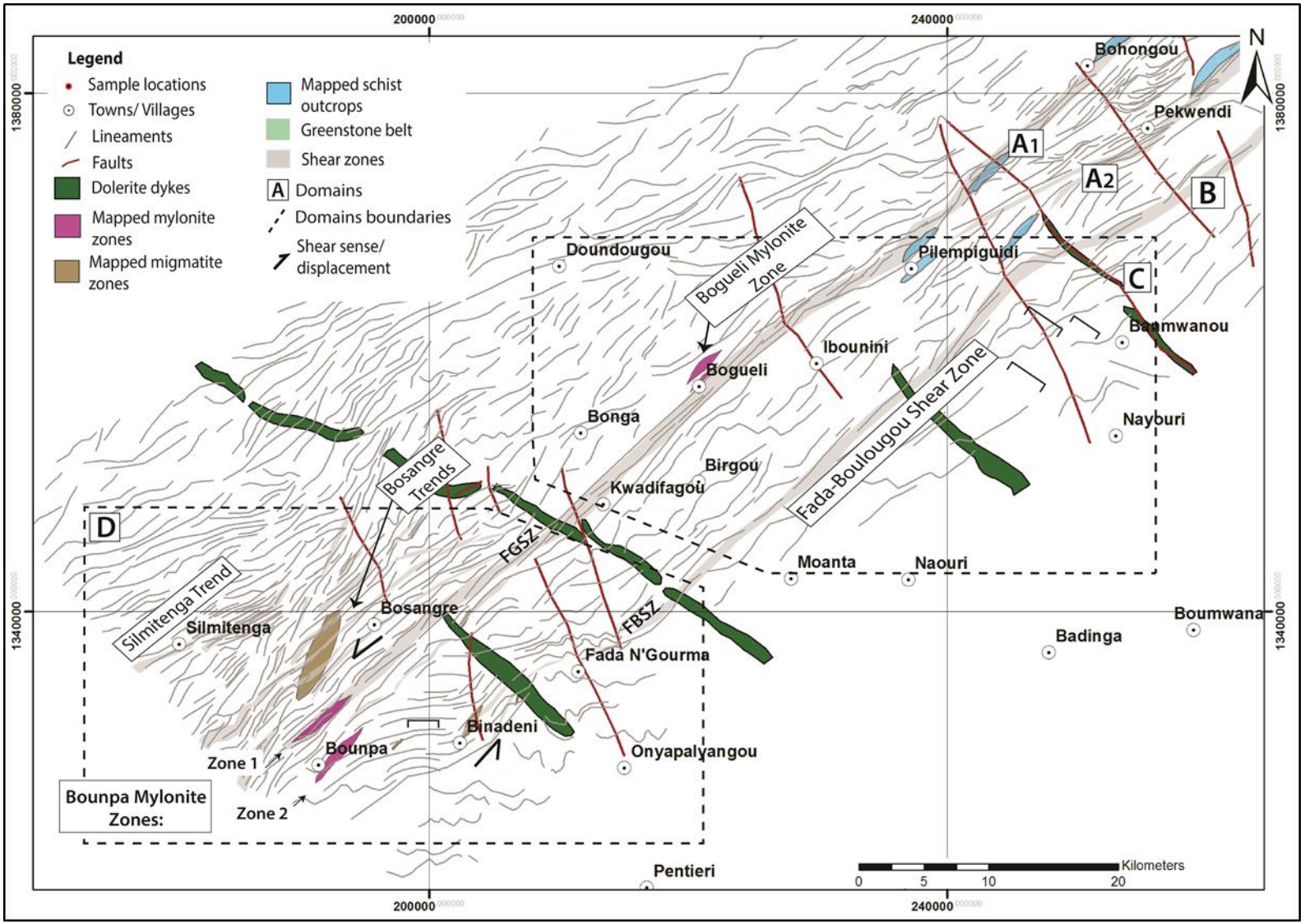


Figure 5.21: *Domain C encloses the trend of the FGSZ and the FBSZ. The Bogueli Mylonite Zone is located on the western boundary of the FGSZ. In the eastern parts of domain C, a NW trending gneissic foliation is dominant. Domain D is in the southern most region of the study area. Domain D encloses the Bounpa Mylonite Zone, the Silmitenga Trend and the Bosangre Trends.*

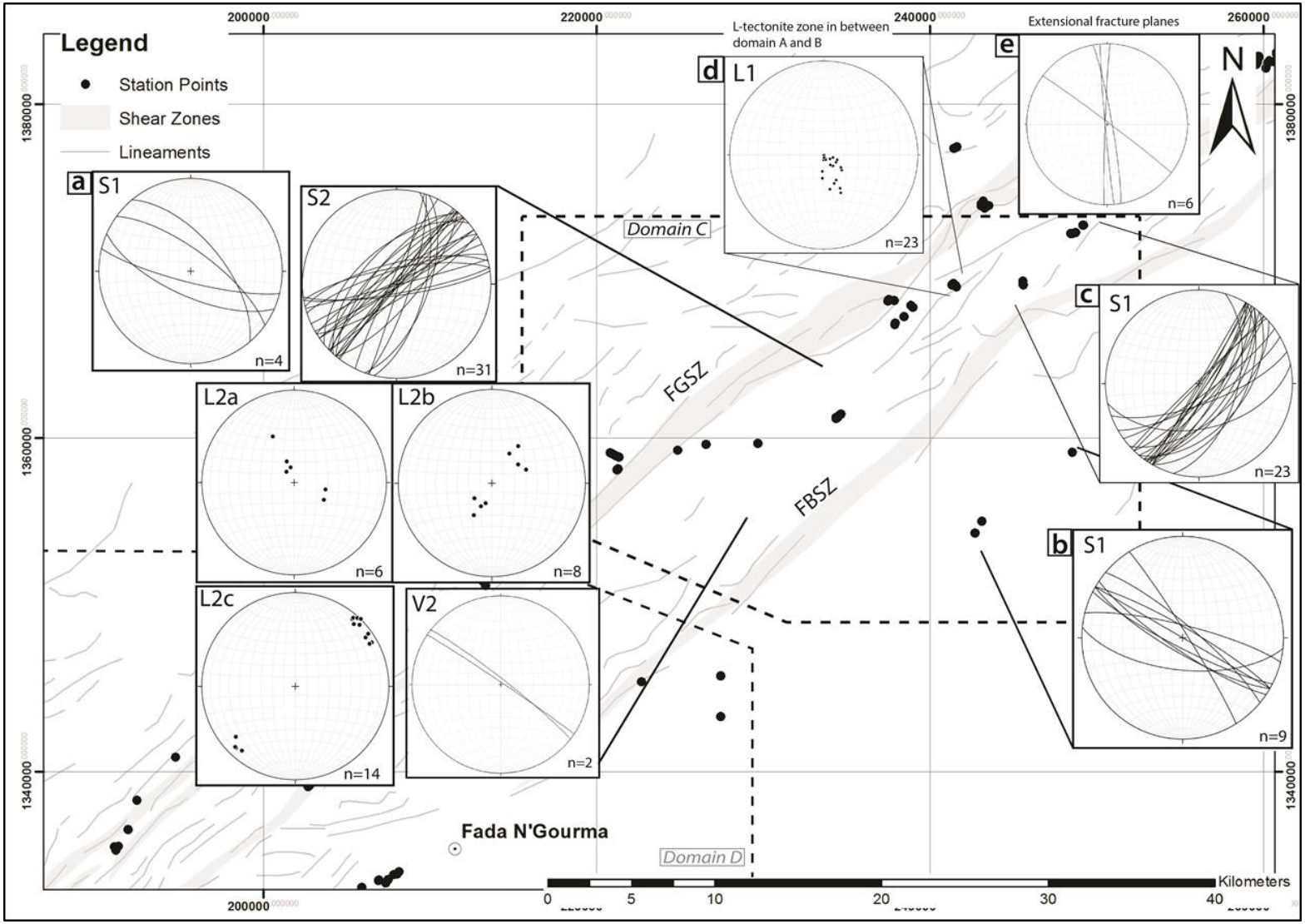


Figure 5.22: *The migmatites and gneissic foliation have a NW trending S1. S2 is NE trending, consistent with the northern domains. Lineation has been sub-divided into L2a, L2b and L2c, as all measurements were taken on the NE trending S2 planes. The orientations suggest that the lineation sets formed under different stress regimes (Passchier and Trouw, 2005).*

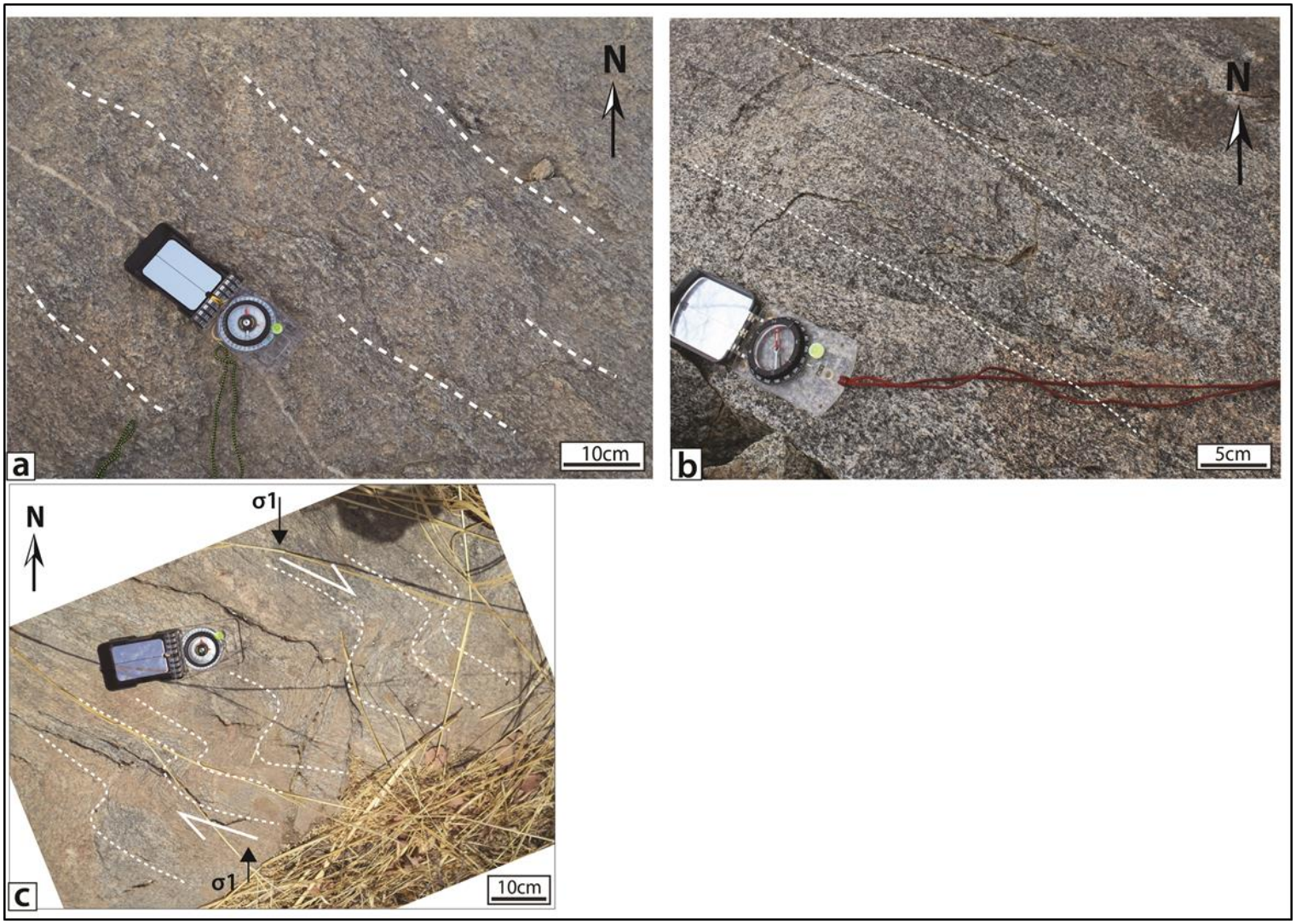


Figure 5.23: *Granodiorite outcrops with a NW-trending S1 foliation, calculated average orientation of 300°/65° SW, defined by (a) preferred mineral orientation, and (b) weak compositional banding. (c) An outcrop image of a foliated granodiorite displays a folding of the S1 foliation (measure orientation 298°/84° SW); the orientation of the fold axial plane is NE trending with orientation 076°/60° SE. The σ1 orientation for the displacement is N-S directed.*

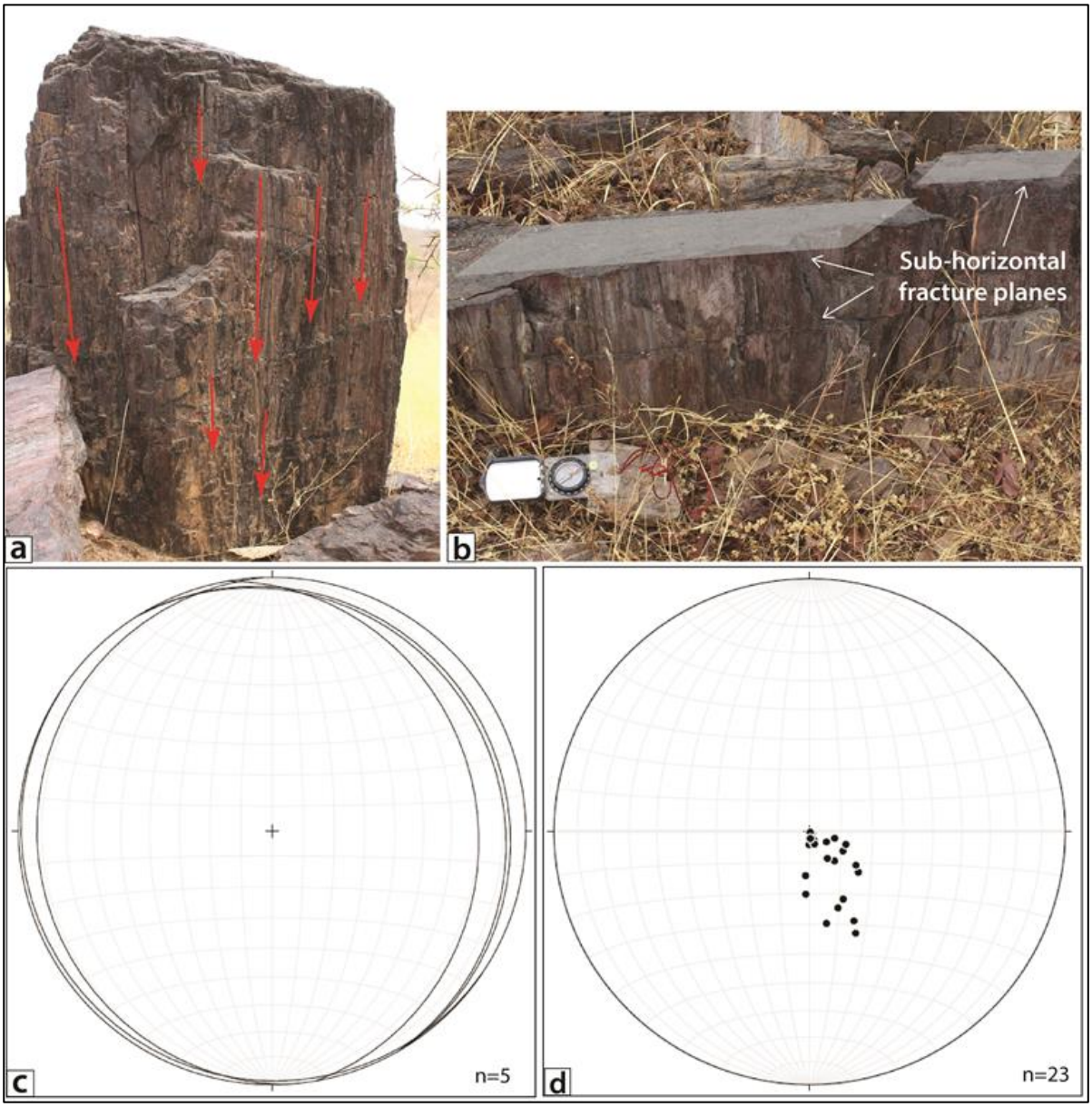


Figure 5.24: *An L-tectonite unit is located near the intersection of the FGSZ and the FBSZ. The rock type is an ultra-fine grained (<1mm) tuff with Fe-enrichment. There are euhedral pyrite crystals that have crystallized as accessory minerals in this unit. The outcrops of the L-tectonite can be up to ~1.2m in height, and have sub-horizontal extensional fracture planes, as shown in images (a) and (b). The stereoplot for the fracture planes is presented in images (d). The azimuth of the lineation, illustrated by the red arrows in image (a), is SE with the steep plunges. The calculated average orientation is 81°→155°. The stereoplot for the lineation is shown in image (d).*

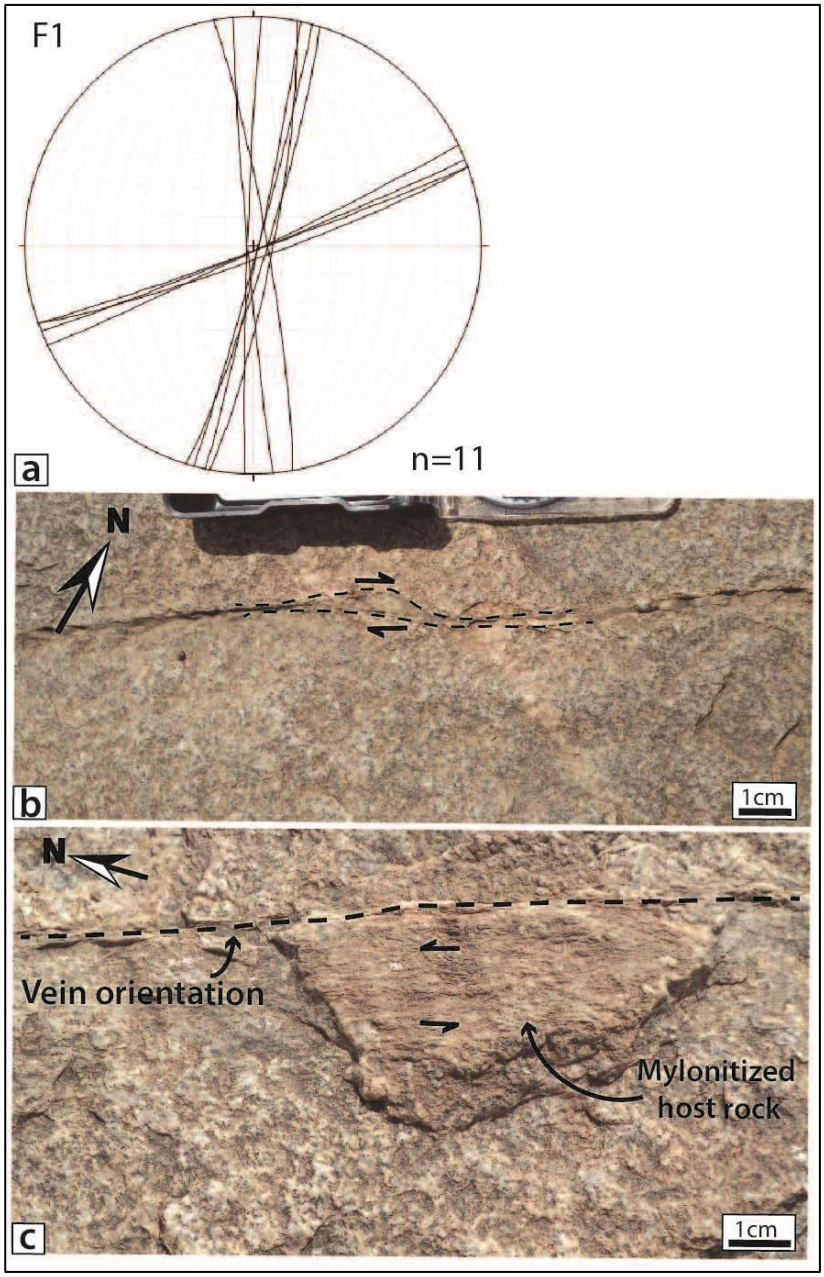


Figure 5.25: *(a) The stereoplot of the faults that cross a foliated granodiorite unit in domain C. (b) A NE trending faults have a dextral shear sense, and have meso-scale dilational jogs in which quartz veins have precipitated. The calculated average orientation is 068°/88° SE. (c) A NNW to NNE trending set of faults have a calculated average orientation of 004°/85° E. A mylonitic foliation has developed along the strike of these faults with rotated delta clasts. The shear sense indicators along the clasts are weakly developed, and have a sinistral displacement.*

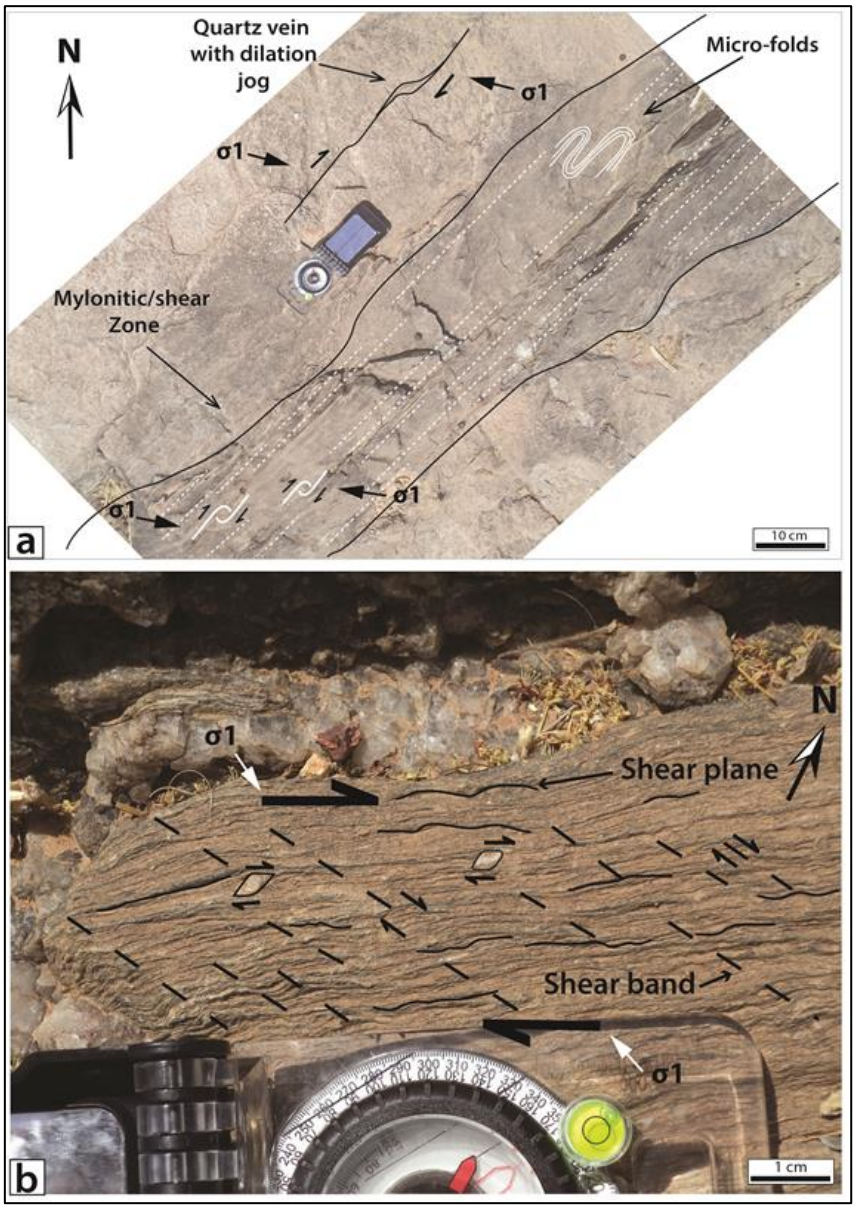


Figure 5.26: *(a) A NE trending mylonitic shear zone ~30cm in width. This mylonitic shear zone is strongly foliated, and is hosts delta clasts and tight micro-folds. Adjacent to the mylonitic shear zone is a quartz vein with a dilation jog. All the shear sense indicators in the mylonitic zone are dextral. (b) The mylonite is hosts sigma quartz clasts with a dextral displacement. The mylonite foliation has shear planes and extensional shear bands all consistent with dextral shearing. Late stage quartz veins crosscut the mylonite.*

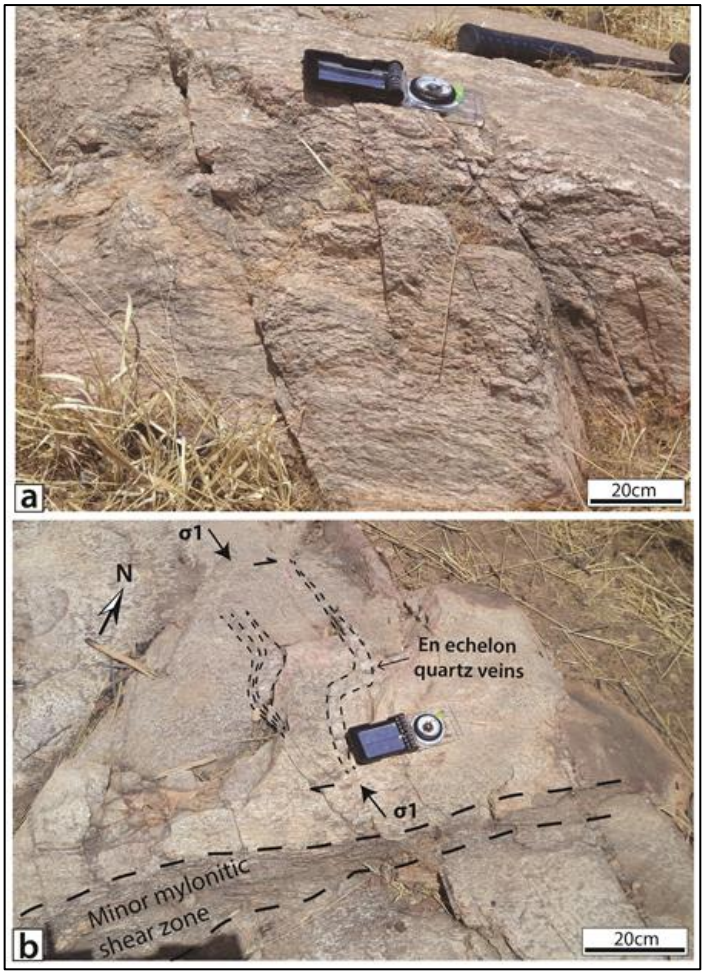


Figure 5.27: *(a) The felsic mylonite outcrop, with a pink appearance indicating the presence of K-feldspar in the mineral composition. (b) A NE trending minor mylonitic shear zone ~20cm wide within the mylonite outcrop. The felsic mylonite hosts en echelon quartz veins with a dextral displacement.*

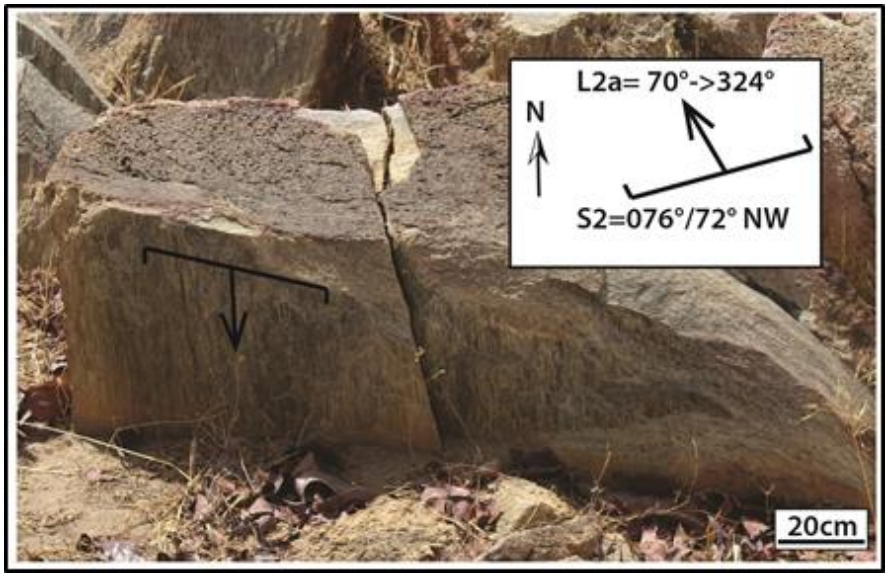
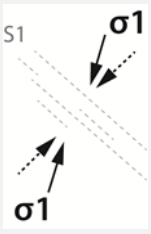
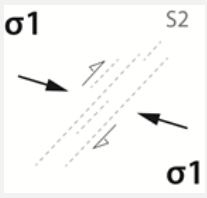
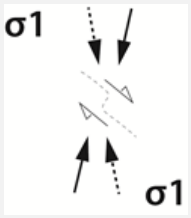
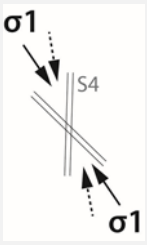


Figure 5.28: *A gneiss granite outcrop with stretching mineral lineation defined by hornblende and feldspar. The S2 orientation along this outcrop is 076°/72° NW, and the L2a orientation is 70°→324°.*

5.3.8 Summary of structures and sequence of deformation events in Domain C

The deformation events for domain C are defined in Table 6 below. Four deformations are defined due to the presence of a NW-trending foliation. A NE trending fold axial plane crosscuts the S1 foliation. The fold axial plane is attributed to the dominant NE trending structural grain, here defined as belonging to D2. The L2a, L2b, L2c lineations belong to more than one deformation event with changing principal stress axes, and therefore cannot conclusively confined to just D2.

Table 6: *Summary of the structures and deformation events in domain C.*

D1	D2	D3	D4
NW-SE trending S1 foliation	NE-SW trending S2 foliation		Fracture planes- S4
Ductile deformation	Ductile deformation	Ductile deformation	Brittle deformation
L-tectonite with steep sub-vertical plunges, SE azimuth; locally isolated as L1	Possibly multiple lineation deformation events; L2a: NW and SE plunging lineation L2b:NE and SW steeply plunging lineation L2c: NE and SW shallow plunging lineation		
	Dextral displacement in Bogueli Mylonite Zone	Dextral displacement along NW trending structures	
NNE-SSW to NE-SW oriented σ1 	NW-SE oriented σ1 	NNW-SSE to NNE-SSW oriented σ1 	NW-SE oriented σ1 

5.4 DOMAIN D

This domain is in the southern region of the study area, and encloses the city of Fada N'Gourma (Figure 5.21). The lithologies found in this domain are mainly plutonic units (granodiorites and granite gneisses), with slivers of NE trending pyroxenite units. The locations of the NNW trending faults in this domain were extracted from geophysical imagery data, and NW trending dolerite dyke locations were plotted using both field data and geophysical imagery data.

5.4.1 Geophysical Imagery Lineaments Map Analysis

The main trend of the FGSZ continues past Bounpa village. The FGSZ thins out, from the average width of ~2km in the northern domains, to ~300m in domain D. The FBSZ trend continues to Fada N'Gourma, and thins out until Binadeni village (Figure 5.21). Smaller branching trends measuring up to ~300m in width occur west of the Bosangre village, and they are here referred to as the Bosangre Trends. The general strike orientation of the Bosangre Trends is NNE (~020°) and NE (~050°), as interpreted from the aeromagnetic imagery data.

A set of E-W trending lineaments were extracted from aeromagnetic data between the Bosangre village and the Binadeni village. The lineaments are bounded by the FGSZ to the west and the faint trend of the FBSZ to the east. The pattern of trends in between the FGSZ and the FBSZ is indicative of a map scale S-C fabric with sinistral displacement (Figure 5.29). The σ1 orientation for sinistral displacement in along the NE trending shear zones is N-S to NNW-SSE.

West to this zone is a NNE oriented lineament crosscutting a NE lineament near Silmitenga village, here referred to as the Silmitenga Trend. The Silmitenga trend is parallel to the FGSZ, and is only traced for a strike length of ~16km within this study area. The Silmitenga Trend and the NNE Bosangre Trend have orientations that are consistent with a subsidiary shear fracture system, in which the Silmitenga Trend is a NE trending Riedel shear, and the NNE trending Bosangre Trend is a synthetic P shear. No structural data was collected along these trends; the interpretation fits a sinistral shear sense with a NNW-SSE directed σ1.

5.4.2 Foliation-S1

The NW trending gneissic foliation in the granite and granodiorite outcrops defines S1 in domain D. Some outcrops have a compositional banding and preferred

mineral orientation of feldspars and hornblende. The average orientation of S1 is 287°/83° S (stereoplots in Figure 5.30 insert a, b and c).

Many of the rocks in the domains C and D have been migmatized, and have developed anatexis textures. The compositional banding is either complex in outcrops (Figure 5.31 a), or has a consistent NNW/NW orientation in most outcrops as shown in Figure 5.31 b, c and d. The calculated average orientation of the migmatitic foliation is 287°/83° S. The migmatites are composite of darker, amphibolitic layers, and lighter, felsic bands.

5.4.3 Foliation-S2

S2 in domain D is defined either by a gneissic foliation (in the granite gneiss and the foliated hbd-bt granodiorite) or by a mylonitic foliation. A few outcrops have a NE trending migmatitic S2 foliation. The S2 is NE trending, and the calculated average orientation is 047°/60° SE (Figure 5.30 insert a, b, c and d).

The mylonite zones mapped in domain D are located near the Bounpa village (Figure 5.21). The mapped outcrops in each zone have different shear sense indicators along the NE trending foliation, and a different principal stress axis. This may indicate that each mylonite zone formed during a different deformation event. Each mapped zone is described below;

Bounpa Mylonite Zone 1

The Bounpa mylonite zone 1 is a low lying mylonite outcrop that is ~20m wide. It has complex deformation textures, evident of high strain tectonic event(s) (Lister and Snoke, 1984). The composition of the mylonite is K-feldspar rich, and has minor hornblende content. The mylonitic foliation has an orientation of ~040°/~88° SE. This mylonite zone has dextral shear sense indicators, and the orientation of the principal stress axis is NW-SE as shown in Figure 5.32 a.

Bounpa Mylonite Zone 2

The outcrops in Bounpa mylonite zone 2 are only ~1m in length and ~0.5m in width. They outcrop at a height of ~40cm. These outcrops have undergone Fe-enrichment and have been weathered resulting in a black discolouration on the surface. The mineral composition of this mylonite zone is K-feldspar, plagioclase, quartz, muscovite and minor hornblende.

The mapped outcrop in this zone has a NE trending S-C fabrics with a sinistral shear sense (Figure 5.32 b). The C-fabric has an orientation of ~050°/58° SE and the S-fabric has an orientation of ~068°/60° SE. The intersection lineation and mineral lineation have a calculated average orientation of 44°→100°. The principal stress axis orientation is N-S to NNE-SSW, as illustrated in Figure 5.32 b.

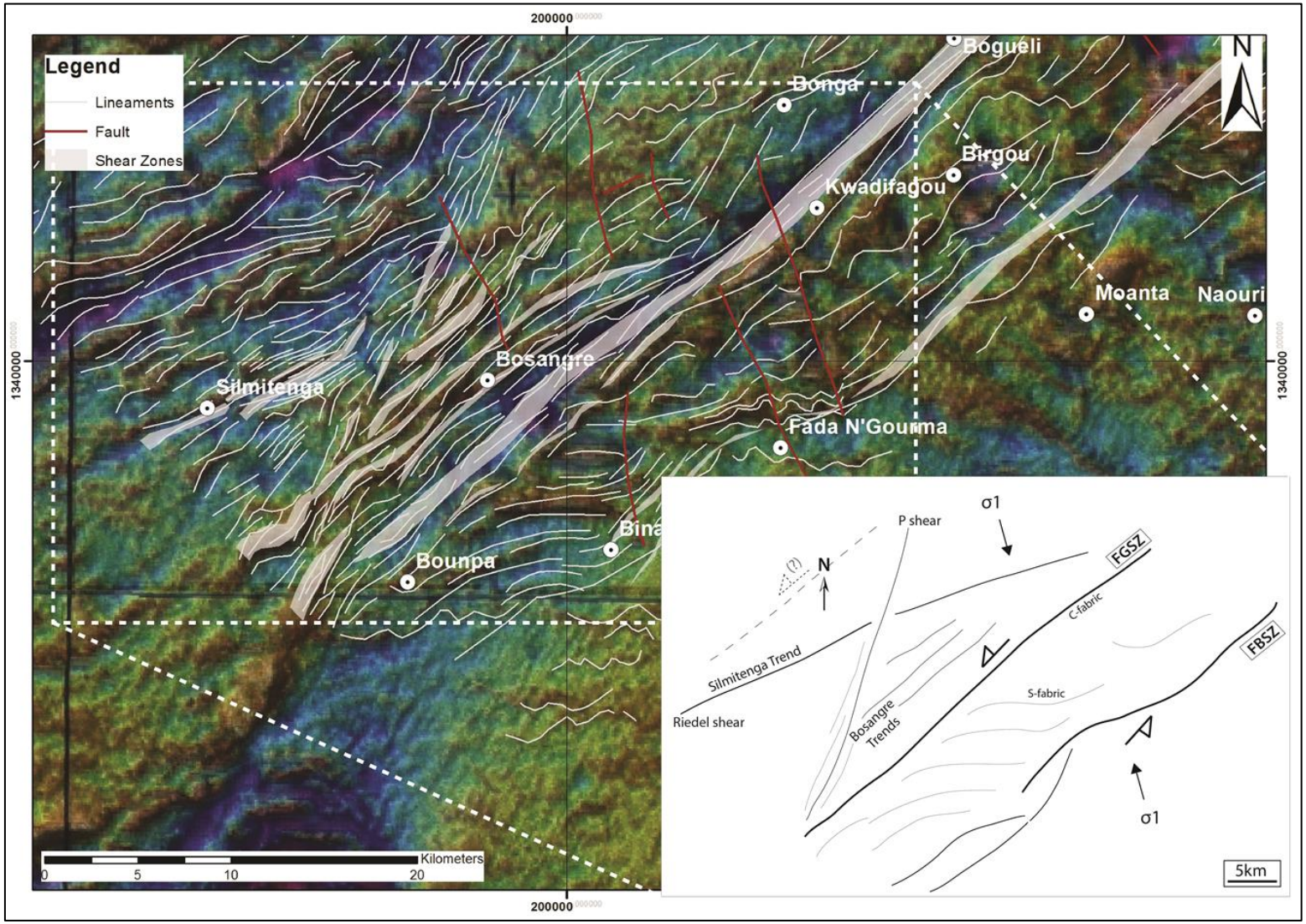


Figure 5.29: *An interpretation of the trends in domain D based on RTP 1st Derivative aeromagnetic imagery data; the orientations are consistent with a subsidiary shear fracture system of Riedel shears. These trends fall within the study area, and may be part of a regional sinistral shear deformation. The Silmitenga Trend represents the Riedel shear, and the NNE Bosangre trend represents the synthetic P shear. No structural data was collected along the trend and interpretation is based mainly of the lineaments extracted from aeromagnetic imagery data. The subsidiary shear fracture system fits the sinistral shearing on the NE trending foliation observed in other domains in a NNW-SSE to N-S directed σ1.*

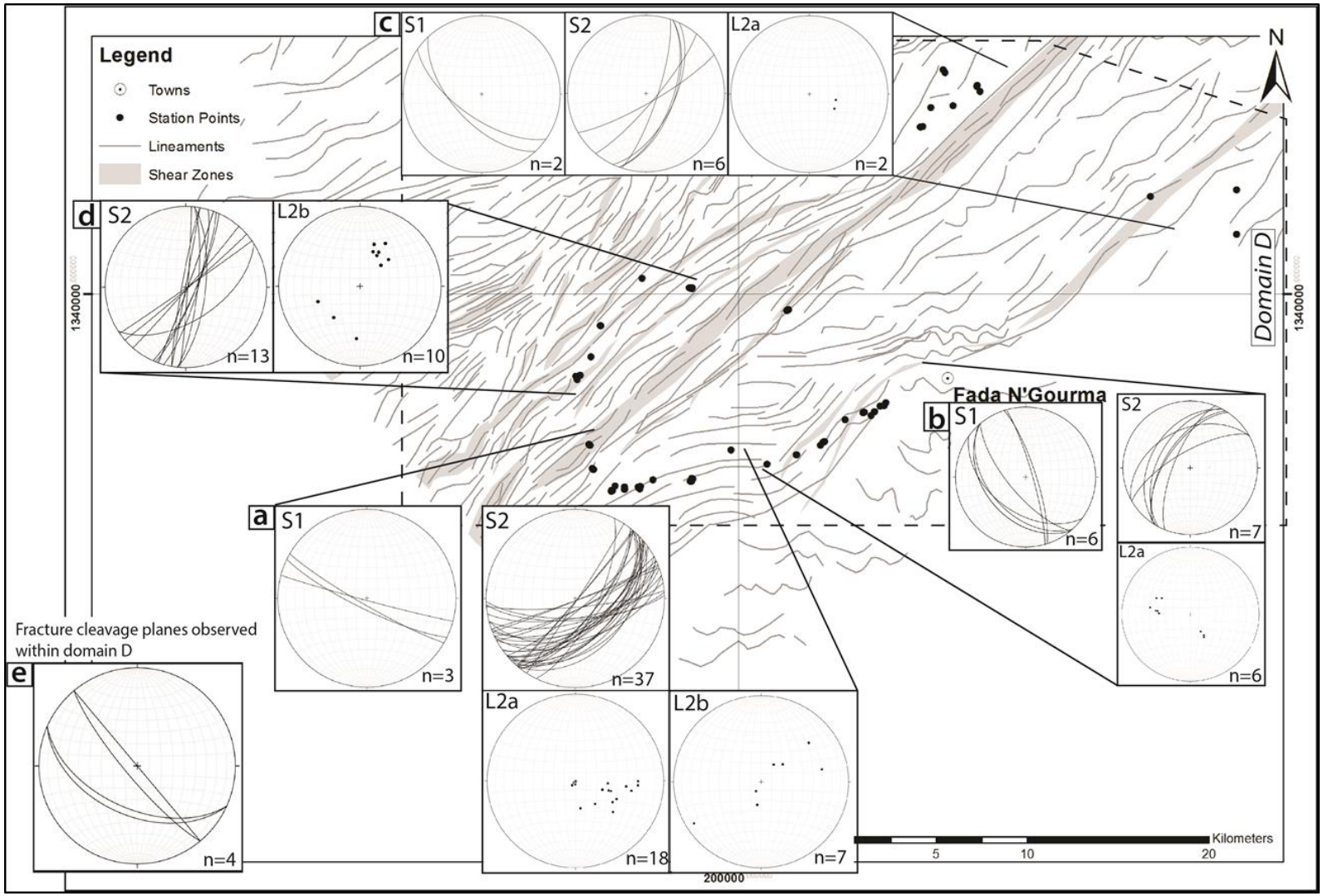


Figure 5.30: *Stereoplots of the foliation, lineation and fracture cleavage planes in domain D. Similar to domain C, S1 in domain D is defined by a NW-trending gneissic and migmatitic foliation in the granodiorites and granite. Lineation on the S2 planes is sub-divided into L2a and L2b based on the clusters with different orientations. The fracture cleavage planes have a NW trend, and they crosscut all other fabrics.*

5.4.4 Lineation- L2

A similar division of the lineation is applied for domain D as in domain C. Lineation L2a and L2b are described below, and the stereoplots of each lineation suite are presented in Figure 5.30 insert a, b c and d.

Lineation-L2a

L2a is defined by stretching minerals hornblende and minor biotite in the granite gneiss and foliated hbd-bt granodiorite. The lineations plunge to the NW and SE; the calculated average orientation for the NW plunging lineation is 49°→278°, and for the SE plunging lineation is 62°→118°. This orientation corresponds with a NW-SE compression.

Lineation-L2b

L2b is defined by stretching minerals (hornblende and feldspar, and minor muscovite). A few outcrops with a NE trending foliation have been folded and the fold axis has an orientation of 88°→226°. A migmatitic outcrop, shown in Figure 5.33 has a crenulation lineation along the foliation. The S2 orientation at this outcrop is 020°/88° SE, and the L2b orientation is 54°→028°.

5.4.5 Fractures planes- S4

Fracture planes crosscut some of the granite gneiss units in domain D. The thin fracture planes have been infilled with quartz to form veins that are mm in scale. The calculated average orientations of the fractures cleavage planes are 295°/53° SW and 320°/85° SW (Figure 5.30 insert e).

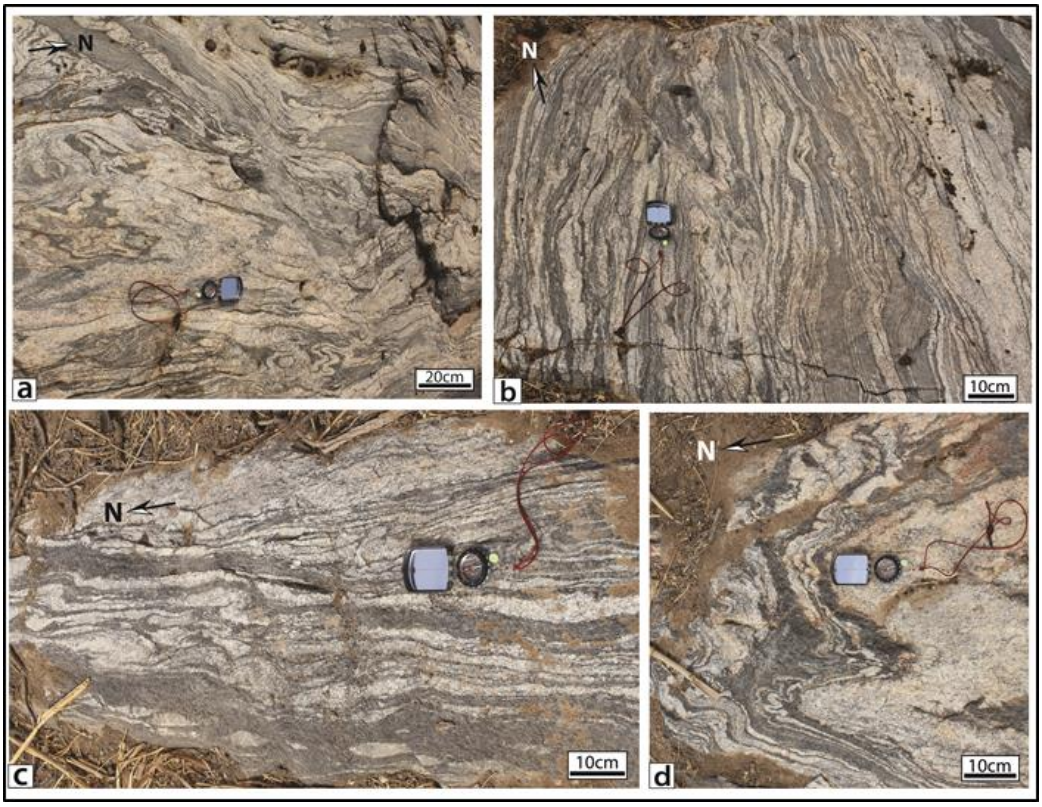


Figure 5.31: *The migmatite outcrops are dominant in domains C and D. (a) A migmatite outcrop with complex folding of leucocratic and melanocratic band. Images b, c and d are of migmatite outcrops with a near N-S oriented anatexis texture. The strike orientation of the banding is NW trending. Some outcrops have meso-scale folded bands as shown in image d.*

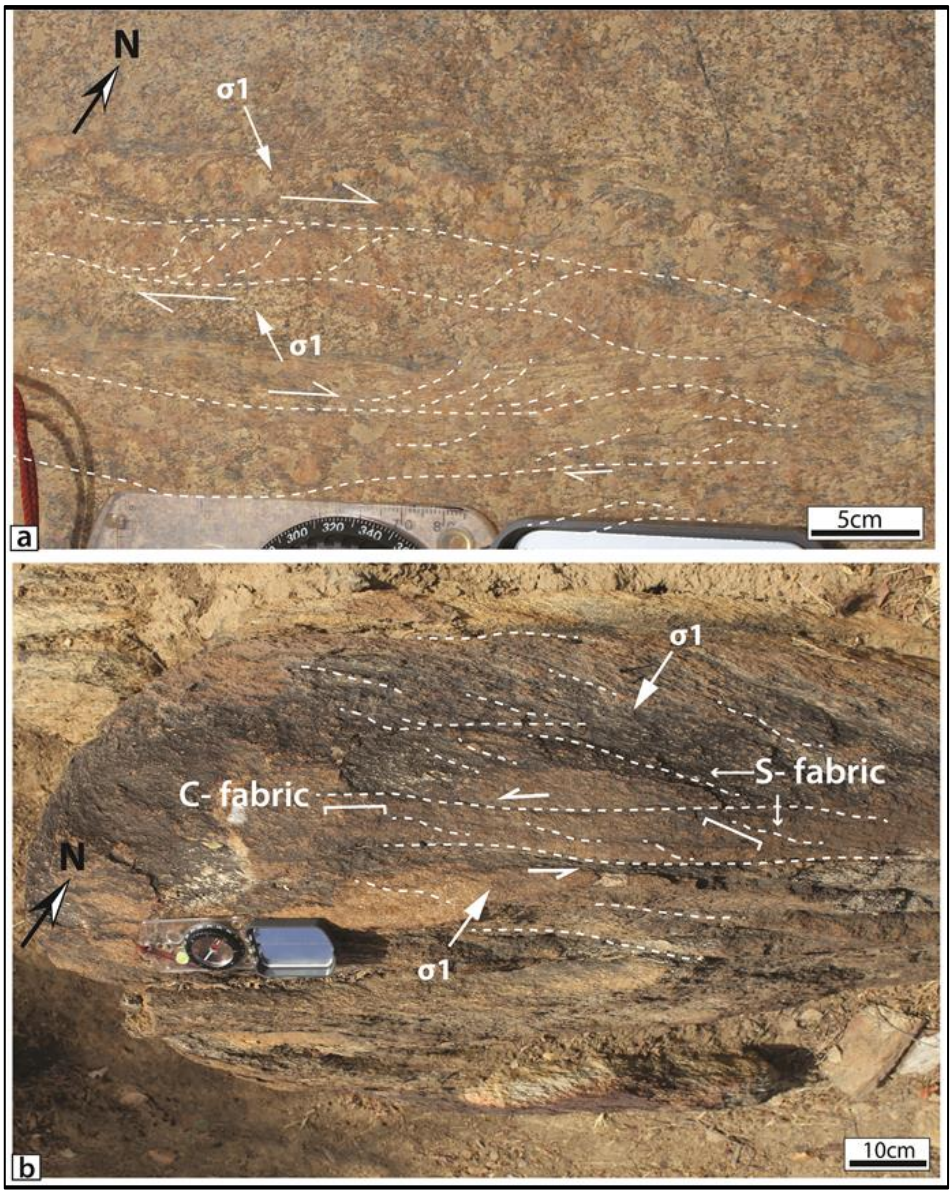


Figure 5.32: *The Bounpa Mylonite Zones outcrops; (a) The mylonite has a pink appearance in outcrop. The dominant foliation is NE trending, and the S1 orientation measured at this outcrop is 040°/70° SE. The shear sense in zone 1 is dextral, as illustrated by the S-C fabric. The σ1 orientation required for this displacement is NW-SE. (b) The second mylonite outcrop is weathered, and fine grained (<1mm grain size). An S-C fabric has developed in this outcrop; the S1 orientation is 070°/60° SE and the C1 orientation is 042°/52° SE. The shear sense in this mylonite outcrop is sinistral under a NNW-SSE stress axis.*

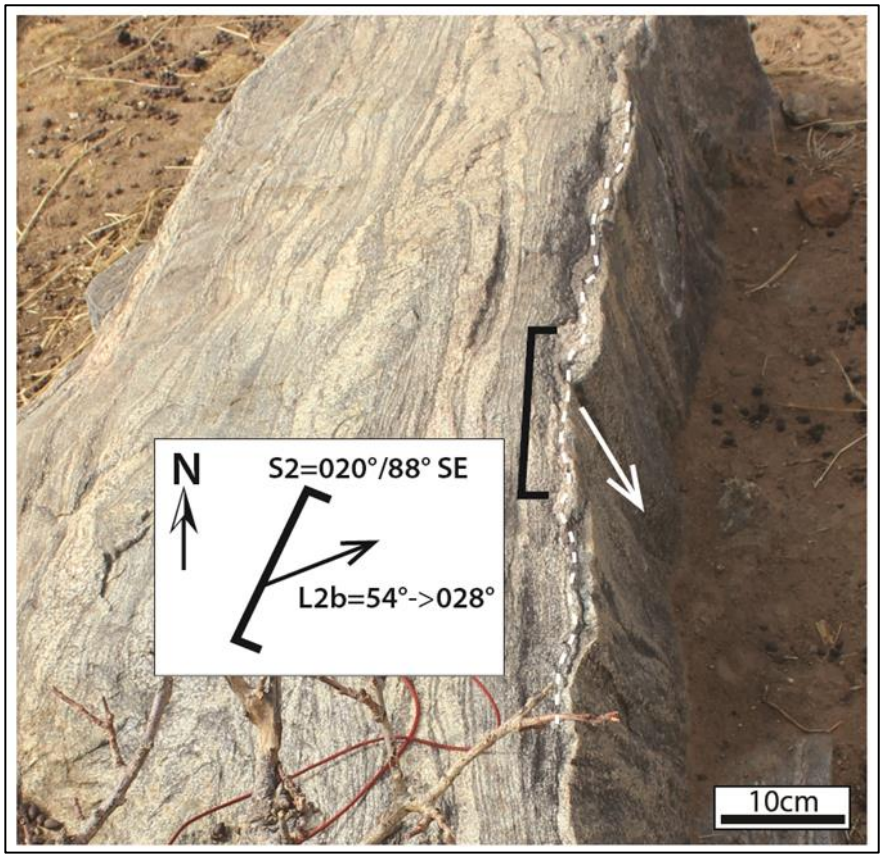


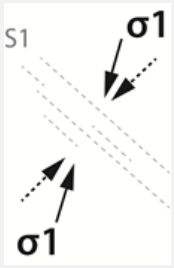
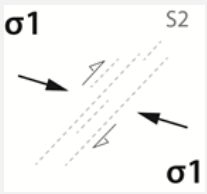
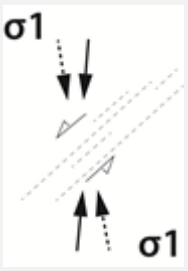
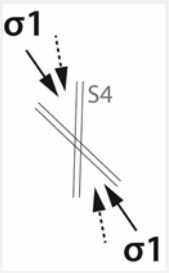
Figure 5.33: *A migmatite outcrop with a NNE trending anatexis banding and a crenulation lineation; the orientation of the foliation is 020°/88° SE and the crenulation lineation L2b is 54°→028°.*

5.4.6 Summary of the structures and sequence of deformation events in Domain D

Table 7 summarizes the deformation events to which defined structures belong to, based on the crosscutting relations seen in the field, and desktop studies on the geophysical imagery data.

Table 7: *Summary of the structures and deformation events in domain D.*

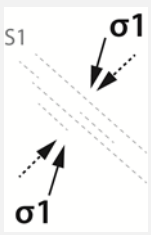
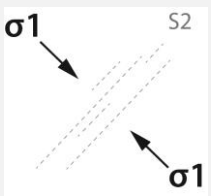
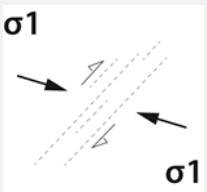
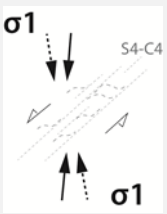
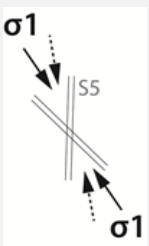
D1	D2	D3	D4
NW-trending S1 foliation	NE trending S2 foliation		NW trending S4 fracture clevage planes
Ductile deformation	Ductile deformation	Ductile deformation	Brittle deformation
	Multiple lineation deformation events; Lineation L2a: NW and SE plunging lineation		

	Lineation L2b: NE and SW plunging lineation		
NE-SW principal stress axis	Dextral displacement along NE mylonitic foliation	Sinistral displacement along NE trending mylonitic foliation; Map scale sinistral S3-C3 fabric from desktop studies	
NNE-SSW to NE-SW oriented σ1 	NW-SE oriented σ1 	NNW-SSE to NNE-SSW oriented σ1 	NW-SE oriented σ1 

5.5 COMBINED STRUCTUAL DATA FROM ALL DOMAINS AND THE DEFORMATION EVENTS FOR ENTIRE STUDY AREA

The defined deformation events for domains A and B are not inclusive of the NW trending foliation observed in domains C and D. The summarized tables therefore differ from domain to domain. This sub-section incorporates the field data from all the domains into one summarized deformation events table, based on the consistency and comparability of principal stress axis orientations, dominant structural grain, and the orientations of the fabrics in the domains. The deformation event sequence changes for some domains, and the conversion from locally defined events to regional deformation events is applied.

Table 8: *Combined summary of the structures and deformation events in the study area.*

D1	D2	D3	D4	D5
NW-trending **S1** foliation	NE trending **S2** foliation *(locally defined as S1 in domains A and B)*	Deformation along NE trending foliation	E-W to NW-SE trending **S4** foliation *(locally defined as S2 in domains A and B)*	NW trending **S5** fracture planes *(locally defined as S4 in all domains)*
Ductile deformation	Ductile deformation	Ductile deformation	Ductile-Brittle deformation	Brittle deformation
No regional **L1** identified along the NW trending S1	NW and SE plunging lineation **L2** *(locally defined as L1 L-tectonite and L2a)*	Lineation **L3**: NE and SW steeply plunging lineation *(locally defined as L2b)*	Lineation **L4**: NE and SW shallow plunging lineation *(locally defined as L2c)*	
	Late precipitation of NE trending quartz veins **V2** *(locally defined as V1)*	Deformation of V2; boudinage and en échelon veins	Crosscutting NW trending quartz veins **V4** *(locally defined as V2)*	Brittle deformation of quartz veins; quartz infilling of fracture planes- **V5**
Possible coaxial shortening to produce NW trending S1	Possible coaxial to non-coaxial shortening to produce dominant NE trending foliation	Dextral displacement along NE trending foliation; Dilational bend along FGSZ and DT	Sinistral- reverse to strike slip displacement along NE trending foliation; Map scale sinistral **S4-C4** fabric	
NNE-SSW to NE-SW oriented σ1 	NW-SE oriented coaxial σ1 	NW-SE to NWN-ESE oriented non-coaxial σ1 	NNW-SSE to NNE-SSW oriented σ1 	NW-SE oriented σ1 

CHAPTER 6: GEOCHRONOLOGY ANALYSIS OF SELECTED PLUTONIC SAMPLES

Three samples GP006, GP027 and GP043 were analyzed for U-Pb isotope data on zircon grains. Figure 6.1 is a locality map of the analyzed samples. Analysis on all three samples was conducted using the LA-ICP-MS. CL images obtained from the SEM were used to analyze the internal structure of the zircons, and to choose ideal ablation spot sites. The cores of the zircons were targeted to measure the crystallization age. The laser beam spot size was 30 µm. Detailed sample description and location, and a summary table of the LA-ICP-MS data analysis results is presented in this chapter. The ages in the Concordia diagrams are based on the $^{207}Pb/^{235}U^*$ ratio, 1SE, $^{206}Pb/^{238}U^*$ratio, 1SE and the Rho (correlation error) values.

6.1 SAMPLE LOCATIONS, DESCRIPTIONS AND LA-ICP-MS RESULTS

6.1.1 Sample GP006

This sample is located to the west of the FGSZ, within close proximities to the western meta-volcanic belt, coordinates 31P 259182.00m E 1392423.00m N (Figure 6.1). This western granitoid domain is separated from the volcanic belt by the FGSZ. In outcrop, this unit is massive with an equigranular texture, and grain size of up to ~2mm (Figure 6.2 a) The sample is composed of 70% felsic minerals (quartz, plagioclase and K-feldspar), and the minerals biotite, muscovite and hornblende make up 30% (Figure 6.2 b). The XRF data plots the sample as a quartz diorite/granodiorite, as presented in section 4.4.

Thirty zircon cores were analyzed from this sample. The zircons for this sample are sub-euhedral to euhedral; average grain size is 150µm. The zircons have well-defined oscillatory zoning indicating that they are of magmatic origin (Figure 6.2 c) (Yuanbao and Yongfei, 2004). The contrasting rims are well developed. Few of the grains have dark, inherited cores; these cores were avoided during analysis. The results for the analysis on this sample are presented in Table 9. The Concordia core age obtained for this sample, (crystallization age) is 2210±8.7Ma.

In addition to the cores analysis, four of the zircons were also analyzed for rim ages. The rim ages are indicated by the red ellipsoids in the Concordia diagram

(Figure 6.2 d), and the red entries at the bottom of Table 9. The narrow banding of the zoning and the spot-size of the laser beam did not allow conclusive metamorphic ages to be determined from such analysis (Yuanbao and Yongfei, 2004). The Concordia age for rim analyses obtained are similar to the Concordia core age, and are within the error range of the core age. The data for sample GP006 is in Table 9.

6.1.2 Sample GP027

The granite gneiss is located in-between the two NE trending volcanic belts, coordinates 31P 273432.00m E 1388876.00m N (Figure 6.1). This unit has a penetrative gneissic texture, and is intruded by granodiorites, quartz diorite, aplite dykes and pegmatites. It is a fine grained (Figure 6.3 a), equigranular unit with plagioclase (30%), quartz (30%), hornblende (20%) K-feldspar (10%) and biotite (10%). The granitic unit underwent deformation and recrystallization. The quartz grains show undulose extinction, with grain boundary migration and sutured boundary micro-scale textures (Figure 6.3 b).

The sample zircons show varied shapes of zircons in the backscatter images. There is no consistent characteristic in the zircons of this sample. These zircons are anhedral, and grain size varies from very fine grained, ≤50μm to up to 200μm. No internal structures could be identified from the CL images of the zircons for this sample (Figure 6.3 c). This may be related to a recrystallization event that overprinted any oscillatory zoning that may have existed (Pidgeon, 1992).The quality of the CL images may indicate that mounting and polishing of the grains for sample GP027 did not expose the grains well enough from the resin in the mount. Another possibility may be that the zircons had low common lead content, which affects CL imaging. Microphotographs of the mount were therefore taken and used to select grains to be analyzed. Only the centers of the grains were analyzed, on the premise that the centers represent the core of the zircon (Yuanbao and Yongfei, 2004).

Thirty-five zircons were analyzed (results in Table 10), and only five zircons gave acceptable results, and these were used for the Concordia diagram. All other zircon grains yielded ages deemed unacceptable due to high discordance, or common lead error. The Concordia crystallization age for this sample is 2239±13Ma (Figure 6.3 d).

6.1.3 Sample GP043

The granodiorite sample intrudes into the granite gneiss, and the intrusive contacts are observed in the field. Sample location coordinates are 31P 273712.00m E 1387448.00m N (Figure 6.1). It is medium grained, composed of plagioclase (30%), hornblende (30%), quartz (20%), K-feldspar (10%), biotite and minor muscovite (10%) (Figure 6.4 b). The XRF data for this unit plots between a granite and a quartz diorite (granodiorite) using the classification by Cox et al. (1979), and as a quartz monzonite using the classification diagram by Middlemost et al. (1994).

This sample has slightly elongate, euhedral zircons. The grain sizes varied from 150µm to 250µm. The cores were darker in CL images, and most grains had little oscillatory zoning (Figure 6.4 c). Obliteration of oscillatory zoning can be an indication of a metamorphic imprint on the zircon (Yuanbao and Yongfei, 2004). Some of the zircons have complex internal structures and patched zoning. Patched zoning may be associated to progressive recrystallization of a previously oscillatory zoned zircon (Pidgeon, 1992). The internal structures observed for some of the zircons revealed cracks and holes, and they were avoided for analysis as they would not yield acceptable results. A total of 30 grains were analyzed (Table 11), all at the core of the zircons (Figure 6.4 d). A Concordia age of 2167±12Ma was obtained for this sample.

Table 9: *LA-ICP-MS U-Pb analysis of sample GP006, quartz diorite. The last four analyses (in red) are rim analyses.*

Sample number	Semiquantative concentrations (ppm)		Common lead	Ratios (* asterisk indicates radiogenic lead isotope)										U-Pb Discordance		Ages (Ma)					
	U	206Pb	206Pbc(%)	206Pb/204Pb	207Pb/206Pb*	1SE	208Pb/206Pb*	1SE	207Pb/235U*	1SE	206Pb/238U*	1SE	Rho	Central (%)	Minimum rim (%)	207Pb/206Pb	1s	207Pb/235U	1s	206Pb/238U	1s
GP006-01	116	42.2	.	13271	0.13629	0.00073	0.07707	0.01348	7.05654	0.06638	0.37551	0.00291	0.823	-6.71	-3.39	2181	9	2119	8	2055	14
GP006-02	119	44.7	.	17101	0.13671	0.00075	0.11446	0.01965	7.39092	0.08643	0.3921	0.00405	0.884	-2.87	.	2186	10	2160	10	2133	19
GP006-03	77	29.1	.	7775	0.13705	0.00076	0.09935	0.01655	7.37654	0.08169	0.39037	0.00374	0.866	-3.52	.	2190	9	2158	10	2125	17
GP006-04	76	28.3	.	10121	0.13761	0.00077	0.11614	0.01979	7.35479	0.09252	0.38762	0.00436	0.895	-4.57	.	2197	9	2155	11	2112	20
GP006-05	87	31	.	16740	0.13941	0.0008	0.09055	0.01503	7.01386	0.06932	0.3649	0.00294	0.816	-11.23	-7.98	2220	9	2113	9	2005	14
GP006-06	54	20.4	.	10188	0.13742	0.00082	0.08968	0.01603	7.46418	0.1016	0.39395	0.00481	0.898	-2.88	.	2195	10	2169	12	2141	22
GP006-07	74	27.1	.	9903	0.13847	0.00081	0.13337	0.02284	7.28934	0.0998	0.38179	0.00473	0.905	-6.55	-1.35	2208	10	2148	12	2085	22
GP006-08	81	22.4	.	8113	0.13855	0.00085	0.07771	0.01314	5.51916	0.06409	0.28892	0.00285	0.851	-29.31	-26.15	2209	10	1904	10	1636	14
GP006-09	39	13.8	.	1676	0.14073	0.00088	0.10494	0.01719	7.10004	0.07448	0.3659	0.00308	0.803	-11.76	-8.38	2236	10	2124	9	2010	15
GP006-10	63	22.6	.	10409	0.13841	0.00089	0.09478	0.0158	7.27325	0.08922	0.38113	0.00399	0.853	-6.67	-2.23	2207	11	2146	11	2082	19
GP006-11	44	17	.	7165	0.13895	0.00094	0.10591	0.01871	7.56395	0.10803	0.3948	0.00496	0.88	-3.67	.	2214	12	2181	13	2145	23
GP006-12	189	40.2	.	11570	0.13871	0.001	0.12873	0.02368	4.26901	0.07071	0.22321	0.00333	0.901	-45.45	-41.77	2211	12	1687	14	1299	18
GP006-13	84	32	.	12661	0.13801	0.00097	0.13405	0.02315	7.61936	0.10101	0.40042	0.00451	0.849	-1.68	.	2202	12	2187	12	2171	21
GP006-14	46	16.8	.	10573	0.13755	0.0011	0.08323	0.01619	7.12023	0.11129	0.37543	0.00505	0.86	-7.53	-1.84	2197	13	2127	14	2055	24
GP006-15	83	31.3	.	4274	0.13864	0.001	0.11733	0.02027	7.52204	0.09633	0.39349	0.00416	0.826	-3.79	.	2210	12	2176	11	2139	19
GP006-16	113	41.6	.	6042	0.13802	0.001	0.16934	0.0295	7.29446	0.09018	0.3833	0.00383	0.809	-5.89	-1.56	2203	12	2148	11	2092	18
GP006-17	162	44.7	.	3895	0.13961	0.00107	0.10843	0.0201	5.56092	0.0811	0.28888	0.00359	0.852	-29.82	-25.86	2222	13	1910	13	1636	18
GP006-18	104	38	.	14706	0.13763	0.00119	0.11276	0.02257	7.07149	0.11489	0.37263	0.00512	0.846	-8.27	-2.48	2198	15	2120	14	2042	24
GP006-19	47	17	.	60440	0.13866	0.0011	0.12696	0.02318	7.27303	0.1029	0.38043	0.00446	0.829	-7	-2	2211	13	2146	13	2078	21
GP006-20	58	21.3	.	2598	0.13958	0.00109	0.09114	0.0162	7.40038	0.10332	0.38454	0.00445	0.829	-6.56	-1.63	2222	13	2161	12	2097	21
GP006-21	122	43.7	.	21388	0.13657	0.00114	0.06619	0.0116	7.03541	0.09376	0.37362	0.00387	0.778	-7.36	-2.85	2184	14	2116	12	2046	18
GP006-22	70	22.6	.	7446	0.1388	0.00095	0.07288	0.00952	7.08731	0.07281	0.37032	0.00285	0.749	-9.55	-6.3	2212	11	2122	9	2031	13
GP006-23	84	28.4	.	22397	0.13876	0.00095	0.08407	0.0102	7.39885	0.08095	0.38672	0.00331	0.782	-5.52	-1.79	2212	11	2161	10	2108	15
GP006-24	69	21.3	.	3131	0.14062	0.001	0.12385	0.01561	6.44032	0.08171	0.33218	0.00349	0.828	-19.83	-16.01	2235	11	2038	11	1849	17
GP006-25	69	22.2	.	5947	0.14021	0.00098	0.07723	0.00945	7.13604	0.07935	0.36912	0.00319	0.778	-10.69	-7.13	2230	12	2129	10	2025	15
GP006-26	61	19.9	.	6962	0.13959	0.00098	0.09788	0.01177	7.16297	0.07685	0.37217	0.00301	0.754	-9.57	-6.17	2222	12	2132	10	2040	14
GP006-27	65	21	.	8997	0.13941	0.001	0.12523	0.01492	7.00746	0.0816	0.36455	0.00335	0.789	-11.32	-7.57	2220	12	2112	10	2004	16

GP006-28	57	18.8	.	3274	0.1411	0.00102	0.08345	0.01003	7.37369	0.09213	0.37903	0.00386	0.814	-8.81	-4.6	2241	12	2158	11	2072	18
GP006-29	74	24.1	.	4983	0.14044	0.00103	0.09017	0.01136	7.25588	0.07748	0.37471	0.00292	0.729	-9.46	-6.17	2233	12	2143	10	2052	14
GP006-30	61	18.2	.	2528	0.14047	0.00106	0.08282	0.00932	6.83532	0.07679	0.35293	0.00293	0.739	-14.74	-11.44	2233	13	2090	10	1949	14
GP006-31-RIM	30	12.2	.	2356	0.14307	0.0011	0.1041	0.03006	7.43716	0.25879	0.37702	0.0128	0.975	-10.43	.	2265	13	2165	31	2062	60
GP006-32-RIM	48	19.2	.	8051	0.1398	0.00116	0.08127	0.02227	7.31186	0.2245	0.37932	0.01121	0.963	-7.97	.	2225	14	2150	27	2073	52
GP006-33-RIM	58	22.9	.	15334	0.13902	0.00118	0.05739	0.01814	7.14114	0.23041	0.37255	0.01159	0.965	-9.14	.	2215	14	2129	29	2041	54
GP006-34-RIM	29	11	.	3908	0.13982	0.0012	0.08728	0.02411	6.84176	0.21146	0.35489	0.01053	0.96	-13.91	-2.21	2225	15	2091	27	1958	50

Table 10: *LA-ICP-MS U-Pb analysis of sample GP027, gneissic granite.*

Sample number	Semiquantative concentrations (ppm)		Common lead	Ratios (* asterisk indicates radiogenic lead isotope)										U-Pb Discordance		Ages (Ma)					
	U	206Pb	206Pbc(%)	206Pb/204Pb	207Pb/206Pb*	1SE	208Pb/206Pb*	1SE	207Pb/235U*	1SE	206Pb/238U*	1SE	Rho	Central (%)	Minimum rim (%)	207Pb/206Pb	1s	207Pb/235U	1s	206Pb/238U	1s
GP027-01-CPb	1218	185.7	2.62	527	0.13231	0.00114	0.09916	0.04123	6.14169	0.10094	0.33666	0.00471	0.851	-13.96	-8.31	2129	14	1996	14	1871	23
GP027-02	716	115.5	.	8068	0.13918	0.00119	0.02424	0.0101	7.13959	0.17181	0.37205	0.00837	0.935	-9.36	-0.09	2217	14	2129	21	2039	39
GP027-03	328	53	.	36721	0.14117	0.00121	0.02564	0.01088	7.13496	0.16468	0.36656	0.00785	0.928	-11.86	-3.35	2242	14	2128	21	2013	37
GP027-04-CPb	906	136	3.01	449	0.13322	0.00117	0.12258	0.05093	6.07469	0.11331	0.33072	0.00544	0.882	-16.04	-9.59	2141	15	1987	16	1842	26
GP027-08-CPb	1282	203.2	0.69	1545	0.13526	0.00123	0.02447	0.01035	6.71912	0.1361	0.36029	0.00651	0.893	-9.85	-2.31	2167	16	2075	18	1984	31
GP027-10	2202	247.9	.	705	0.13552	0.00129	0.02909	0.01223	4.79108	0.11189	0.25641	0.00547	0.914	-35.96	-29.63	2171	16	1783	20	1471	28
GP027-10-CPb	2202	247.9	2.09	705	0.1252	0.00119	0.02366	0.00995	4.33407	0.10202	0.25106	0.0054	0.914	-32.24	-25.14	2032	17	1700	19	1444	28
GP027-11	141	57.8	.	5082	0.13599	0.00066	0.1308	0.03729	7.32781	0.17953	0.39082	0.00939	0.98	-2.7	.	2177	8	2152	22	2127	44
GP027-12	192	72.1	.	754	0.1395	0.0008	0.85208	0.22518	6.83836	0.13185	0.35553	0.00654	0.954	-13.57	-6.45	2221	9	2091	17	1961	31
GP027-12-CPb	285	100.7	1.69	798	0.12818	0.00088	0.83787	0.17509	6.12417	0.13131	0.34651	0.00704	0.947	-8.66	.	2073	12	1994	19	1918	34
GP027-13	79	28.9	.	357	0.15111	0.00085	0.57699	0.1548	7.30032	0.1441	0.35039	0.00663	0.959	-20.68	-14.23	2358	9	2149	18	1936	32
GP027-13-CPb	79	28.9	3.64	357	0.13227	0.00075	0.5482	0.14709	6.15804	0.12224	0.33766	0.00642	0.958	-13.68	-6.11	2128	10	1999	17	1875	31
GP027-14	162	60.2	.	625	0.14239	0.00082	0.9797	0.25877	6.87315	0.13531	0.35009	0.00659	0.956	-16.47	-9.51	2256	10	2095	17	1935	31
GP027-14-CPb	146	53.9	2.18	621	0.13178	0.00071	0.96981	0.27023	6.16787	0.12258	0.33945	0.0065	0.963	-12.92	-5.22	2122	9	2000	17	1884	31
GP027-15-CPb	73	27.2	5.65	239	0.13248	0.00074	0.6478	0.17224	6.11993	0.117	0.33505	0.00612	0.956	-14.48	-7.28	2131	9	1993	17	1863	30
GP027-16-CPb	14	5.8	18.57	67	0.14106	0.00109	0.358	0.09565	6.40773	0.13526	0.32945	0.00647	0.931	-20.72	-13.73	2240	13	2033	19	1836	31
GP027-17	48	19.2	.	16977	0.14183	0.00077	0.11524	0.03445	7.33469	0.16191	0.37508	0.00803	0.97	-10.18	-1.64	2250	9	2153	20	2053	38
GP027-18	4	2	.	26	0.42583	0.00304	0.99596	0.26493	28.47178	0.62381	0.48493	0.01004	0.945	-43.66	-39.88	4003	10	3435	21	2549	44
GP027-19	44	18.4	.	9632	0.1413	0.00074	0.1082	0.03223	7.5521	0.17712	0.38764	0.00886	0.975	-6.86	.	2243	9	2179	21	2112	41
GP027-20	9	3.4	.	160	0.18463	0.00116	0.17972	0.05208	9.24086	0.20065	0.363	0.00755	0.957	-30.06	-24.29	2695	10	2362	20	1996	36
GP027-20-CPb	9	3.4	5.86	160	0.1557	0.00104	0.1057	0.03082	7.33484	0.1612	0.34166	0.00716	0.953	-24.61	-17.89	2410	11	2153	20	1895	34
GP027-21	82	30.2	.	323	0.15531	0.00097	0.51024	0.13505	7.41044	0.15499	0.34606	0.00691	0.955	-23.48	-16.98	2405	10	2162	19	1916	33
GP027-21-CPb	82	30.2	4.22	323	0.13397	0.00085	0.47504	0.12573	6.1227	0.12859	0.33146	0.00664	0.954	-16.3	-8.6	2151	10	1993	18	1845	32
GP027-22-CPb	10	4.5	24.38	52	0.14826	0.00147	0.24729	0.06599	6.25122	0.14901	0.30579	0.00663	0.91	-29.62	-22.88	2326	16	2012	21	1720	33
GP027-23-CPb	7	2.4	11.44	88	0.15581	0.00172	0.10511	0.11211	6.42675	0.1746	0.29915	0.00743	0.914	-34.03	-26.93	2411	18	2036	24	1687	37
GP027-24	162	59.4	.	589	0.14401	0.0009	0.31436	0.0835	6.89214	0.15451	0.34711	0.00747	0.96	-18.02	-10.22	2276	10	2098	20	1921	36
GP027-24-CPb	162	59.4	2.25	589	0.13253	0.00083	0.29159	0.07745	6.20181	0.13946	0.33939	0.00733	0.96	-13.4	-4.74	2132	11	2005	20	1884	35

GP027-25-CPb	6	2.7	24.42	47	0.17649	0.00377	0.2941	0.08629	7.58432	0.26496	0.31167	0.00861	0.791	-37.85	-30.5	2620	34	2183	31	1749	42
GP027-26	66	25.1	.	763	0.15538	0.00217	0.1534	0.0411	7.73041	0.19814	0.36083	0.00775	0.838	-20.25	-12.7	2406	23	2200	23	1986	37
GP027-26-CPb	66	25.1	2.5	763	0.1427	0.00214	0.12412	0.03327	6.92708	0.18163	0.35207	0.00758	0.821	-16.16	-7.8	2260	25	2102	23	1944	36
GP027-27	55	21.8	.	8979	0.14006	0.00091	0.10558	0.02949	7.30835	0.16965	0.37845	0.00843	0.96	-8.33	.	2228	11	2150	21	2069	39
GP027-28	9	3.7	.	52	0.27847	0.00222	0.53746	0.14335	15.52672	0.36849	0.40439	0.00904	0.942	-40.76	-36.09	3354	12	2848	23	2189	41
GP027-28-CPb	9	3.7	23.13	52	0.16017	0.00167	0.28836	0.07759	6.86682	0.17469	0.31093	0.00722	0.912	-33	-26.37	2458	17	2094	23	1745	35
GP027-29-CPb	51	19.2	5.91	228	0.13709	0.00096	0.58263	0.1571	6.26584	0.14984	0.3315	0.00758	0.957	-18.09	-9.55	2191	12	2014	21	1846	37
GP027-30-CPb	51	29.3	65.17	29	0.09526	0.01404	1.31904	0.40123	2.32143	0.37032	0.17675	0.0108	0.383	-34.17	.	1533	283	1219	113	1049	59
GP027-31	315	110	.	953	0.13537	0.00121	0.65222	0.14538	6.38924	0.1964	0.34231	0.01007	0.957	-14.41	-2.67	2169	15	2031	27	1898	48
GP027-31-CPb	315	110	1.44	953	0.1281	0.00114	0.64433	0.14362	5.95875	0.18322	0.33737	0.00993	0.957	-11.01	.	2072	15	1970	27	1874	48
GP027-32	16	5.4	.	186	0.17155	0.00144	0.14021	0.03957	7.66252	0.2138	0.32395	0.00862	0.954	-33.96	-26.71	2573	14	2192	25	1809	42
GP027-32-CPb	16	5.4	5.44	186	0.14512	0.00129	0.07523	0.02131	6.12932	0.17241	0.30633	0.00818	0.949	-28.15	-19.58	2289	15	1994	25	1723	40
GP027-33	42	15.4	.	196	0.16767	0.00147	0.40025	0.10893	7.94524	0.22546	0.34367	0.00928	0.951	-28.65	-20.62	2535	14	2225	26	1904	45
GP027-33-CPb	42	15.4	6.63	196	0.13504	0.00124	0.33913	0.09234	5.98172	0.17141	0.32126	0.00872	0.948	-19.49	-9.31	2165	16	1973	25	1796	43
GP027-34	4	2	.	30	0.38495	0.00323	0.9283	0.25227	24.98858	0.74202	0.47081	0.01341	0.959	-42.41	-36.97	3851	12	3308	29	2487	59
GP027-35	46	16.8	.	241	0.16398	0.00136	0.444	0.11999	7.70001	0.22189	0.34055	0.0094	0.958	-28.02	-19.66	2497	13	2197	26	1889	45
GP027-35-CPb	46	16.8	5.41	241	0.13731	0.00116	0.39706	0.10731	6.09842	0.17642	0.32212	0.00891	0.957	-20.53	-10.4	2194	14	1990	25	1800	43

Table 11: *LA-ICP-MS U-Pb analysis of sample GP043, granodiorite.*

Sample number	Semiquantative concentrations (ppm)		Common lead	Ratios (* asterisk indicates radiogenic lead isotope)										U-Pb Discordance		Ages (Ma)					
	U	206Pb	206Pbc(%)	206Pb/204Pb	207Pb/206Pb*	1SE	208Pb/206Pb*	1SE	207Pb/235U*	1SE	206Pb/238U*	1SE	Rho	Central (%)	Minimum rim (%)	207Pb/206Pb	1s	207Pb/235U	1s	206Pb/238U	1s
GP043-01	75	20	.	3628	0.14095	0.00112	0.09164	0.01221	5.55129	0.07084	0.28565	0.00285	0.782	-31.21	-28.05	2239	14	1909	11	1620	14
GP043-03	88	28.4	.	1817	0.1371	0.00116	0.19444	0.02341	7.03718	0.09739	0.37228	0.00408	0.793	-8.02	-3.32	2191	15	2116	12	2040	19
GP043-02	80	27.8	.	1244	0.14112	0.00132	0.12312	0.01615	7.08197	0.10553	0.36396	0.00422	0.778	-12.45	-7.76	2241	16	2122	13	2001	20
GP043-04	234	72.1	.	4324	0.13176	0.00115	0.19607	0.02622	6.08289	0.0967	0.33483	0.00446	0.837	-14.09	-8.68	2122	15	1988	14	1862	22
GP043-05	169	53.7	.	2813	0.13389	0.00121	0.17289	0.02266	7.32758	0.14097	0.39694	0.00674	0.882	0.29	.	2150	15	2152	17	2155	31
GP043-06	265	86.9	.	10884	0.13289	0.00122	0.12778	0.01485	7.30831	0.12902	0.39886	0.00601	0.854	1.5	.	2137	16	2150	16	2164	28
GP043-08	91	30.4	.	6780	0.13556	0.00122	0.16272	0.01938	7.06391	0.09138	0.37793	0.00352	0.72	-5.63	-1.4	2171	15	2120	12	2067	16
GP043-09	79	24.5	.	8235	0.13605	0.00129	0.22276	0.02626	6.98649	0.1352	0.37245	0.00628	0.871	-7.31	-0.09	2177	16	2110	17	2041	29
GP043-10	144	46	.	13902	0.13537	0.00129	0.12238	0.01559	7.18461	0.13143	0.38494	0.00601	0.854	-3.75	.	2169	16	2135	16	2099	28
GP043-11	96	31.7	.	7890	0.136	0.00129	0.13997	0.01743	7.21953	0.11072	0.385	0.00463	0.784	-4.16	.	2177	16	2139	14	2100	22
GP043-12	603	101	.	7139	0.1358	0.00086	0.05261	0.0216	7.30102	0.13658	0.38994	0.00686	0.941	-2.79	.	2174	10	2149	17	2123	32
GP043-14	764	130.7	.	11724	0.13525	0.00092	0.04013	0.01653	7.4545	0.15328	0.39976	0.00776	0.944	0.04	.	2167	11	2168	18	2168	36
GP043-15	1689	291.4	.	17749	0.13357	0.00088	0.03547	0.01457	7.28442	0.13352	0.39555	0.00676	0.933	0.17	.	2145	11	2147	16	2149	31
GP043-16	626	102.6	.	5444	0.13638	0.00092	0.04628	0.01882	7.19469	0.1429	0.3826	0.00715	0.941	-5.01	.	2182	12	2136	18	2088	33
GP043-17	1324	223.8	.	8000	0.13572	0.00084	0.0344	0.01576	7.13137	0.14282	0.38109	0.00726	0.951	-4.95	.	2173	10	2128	18	2081	34
GP043-20	510	82	.	5622	0.13594	0.00091	0.0459	0.0188	7.02736	0.12426	0.37491	0.00614	0.926	-6.63	.	2176	11	2115	16	2052	29
GP043-21	483	74	.	21722	0.13704	0.00092	0.0439	0.01858	6.66128	0.12655	0.35254	0.00626	0.935	-12.86	-5.85	2190	11	2068	17	1947	30
GP043-22	1249	213.5	.	4308	0.13438	0.0009	0.02724	0.01274	6.9924	0.17662	0.3774	0.00919	0.964	-4.98	.	2156	11	2110	22	2064	43
GP043-23	480	79.1	.	13781	0.13617	0.00101	0.05245	0.02093	7.21979	0.15945	0.38454	0.008	0.942	-4.39	.	2179	12	2139	20	2097	37
GP043-24	610	95.6	.	4297	0.1364	0.00097	0.04536	0.0187	6.78255	0.11144	0.36064	0.00535	0.902	-10.47	-4.42	2182	12	2083	15	1985	25
GP043-25	438	68.2	.	8129	0.13668	0.00095	0.03898	0.01681	6.70399	0.10372	0.35574	0.00491	0.892	-11.86	-6.32	2186	12	2073	14	1962	23
GP043-26	564	88.5	.	10973	0.1364	0.00097	0.04585	0.01909	6.79511	0.10872	0.36132	0.00518	0.896	-10.3	-4.44	2182	12	2085	14	1988	25
GP043-27	335	53.6	.	2854	0.13791	0.001	0.03682	0.01535	7.01259	0.11317	0.36878	0.00532	0.894	-9.39	-3.46	2201	12	2113	14	2024	25
GP043-28	594	93.6	.	6751	0.13655	0.00097	0.04485	0.01944	6.75311	0.10893	0.3587	0.00519	0.898	-11.04	-5.18	2184	12	2080	14	1976	25
GP043-29	586	92.3	.	5426	0.13648	0.00099	0.02761	0.01181	6.77263	0.10903	0.3599	0.00517	0.893	-10.71	-4.85	2183	12	2082	14	1982	25
GP043-30	832	134.8	.	10891	0.13668	0.00107	0.05005	0.02037	7.11833	0.16944	0.37772	0.00849	0.945	-6.41	.	2186	13	2126	21	2066	40

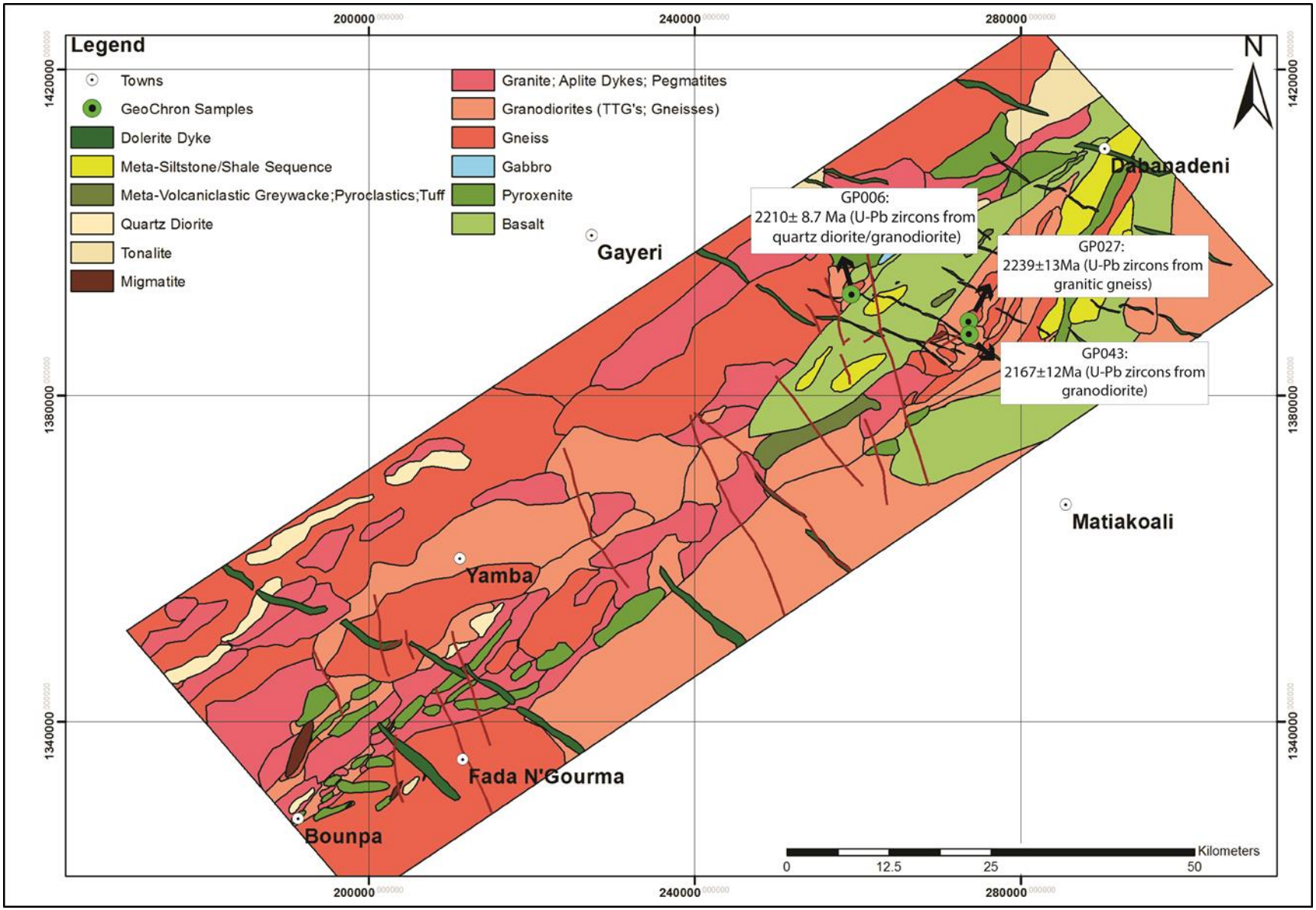


Figure 6.1: *Locality map of the three geochronology samples, and the zircon U-Pb ages of each sample.*

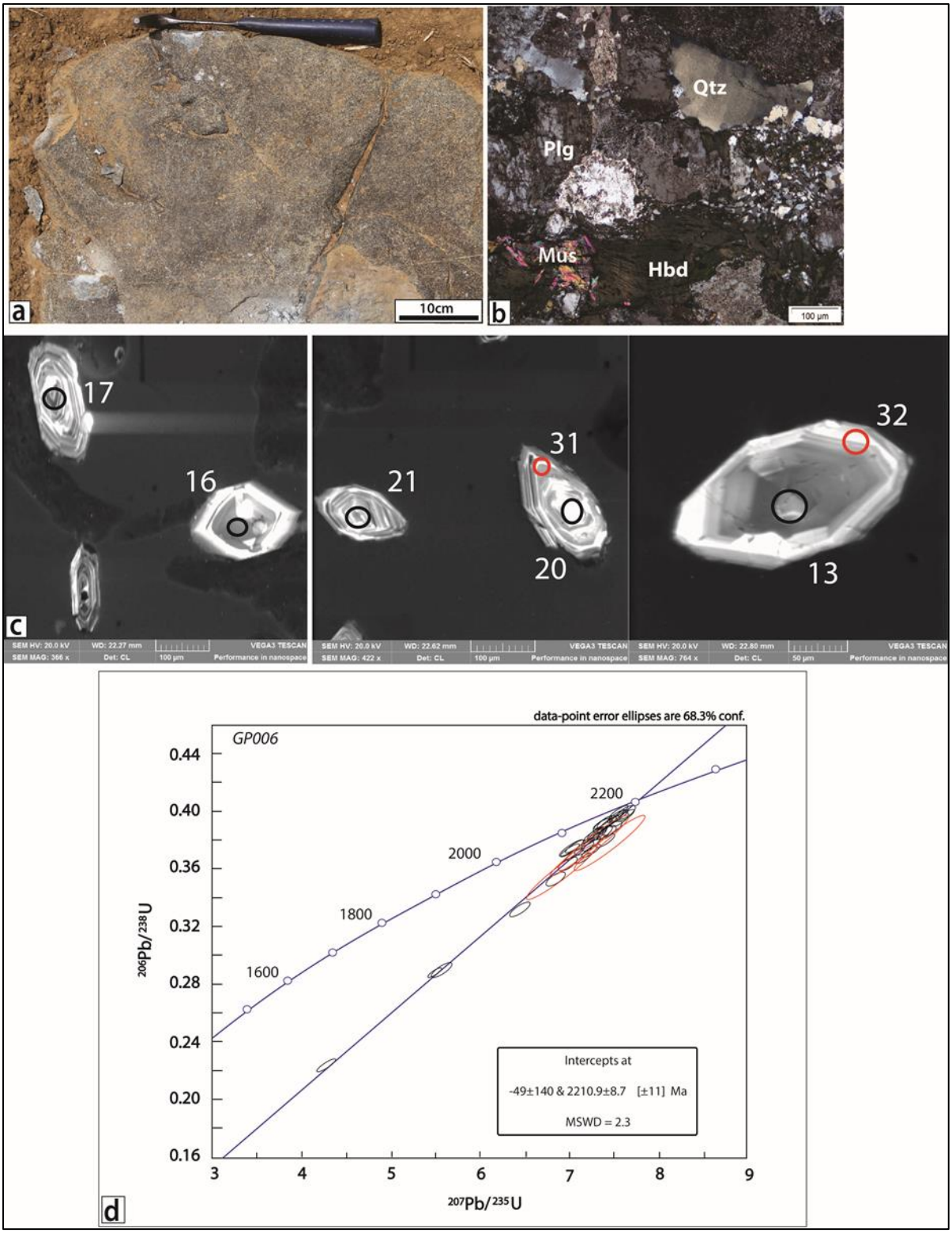


Figure 6.2: *Sample GP006; (a) Field outcrop of the quartz diorite. (b) Thin section of sample GP006 with plagioclase, quartz, hornblende and minor muscovite and biotite. The quartz has undulose extinction, and has a seriate texture with fine and course grained recrystallized quartz grains. (c) Zircons analysed using LA. The black circles indicate where core ablations spots were made, and the red circles indicate where rim ablations were made. The numbers relate to the suffix numbers in the table of results (Table 9) for sample GP006. (d) The Concordia diagram gave an age of 2210±8.7Ma.*

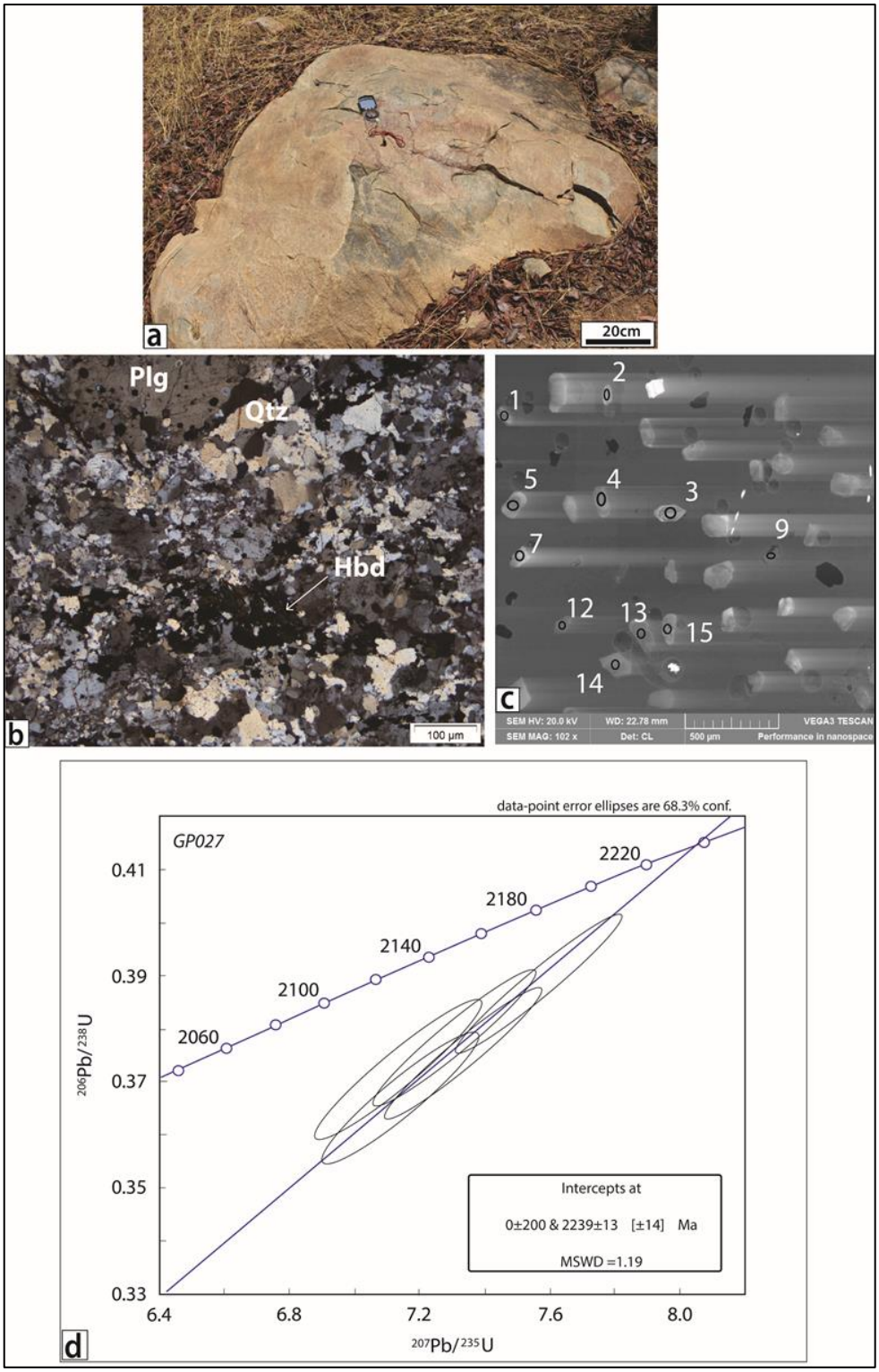


Figure 6.3: *Sample GP027; (a) the field outcrop of the granite gneiss, with intrusive contacts with the granodiorite. (b) The hand sample of the granite gneiss. This sample was cut for thin section, crushed for XRF and was separated for zircons. (c) The fine grained gneiss in thin section. The matrix is quartz and feldspar dominates, with minor hornblende and mica content. (d) The black circles indicate where ablation was done, and the number correlated with the sample number suffixes in the sample names in Table 10. (e) The Concordia age attained for sample GP027 is 2239±13Ma.*

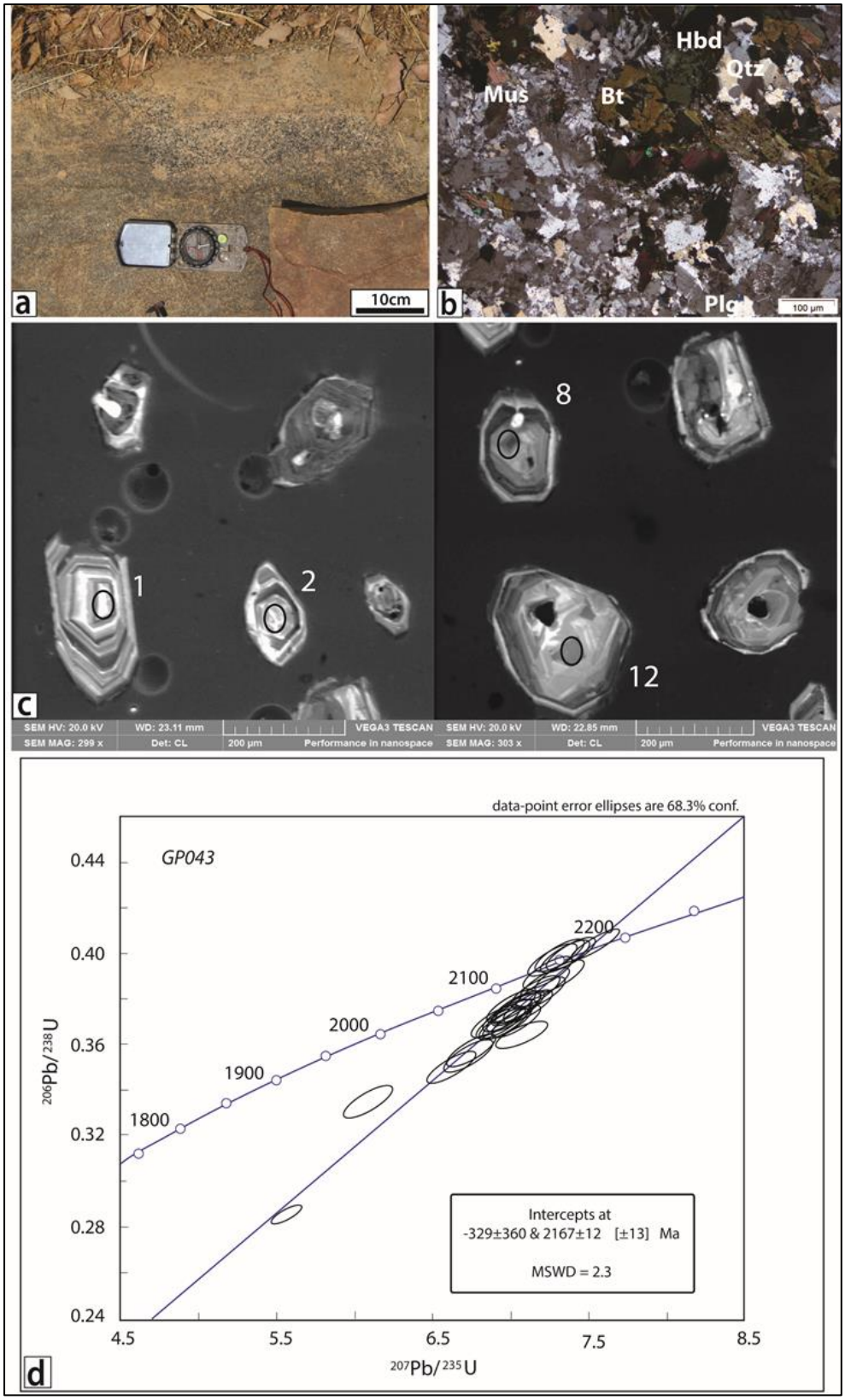


Figure 6.4: *Sample GP043; (a) The field outcrop of the sampled granodiorite. (b) Sample GP043 in thin section. It has a fine to medium grain size. (c) The zircons analysed in LA. The black circles represent were ablation was done, and the numbers correlate with the sample name suffix in Table 11. (d) The Concordia diagram for sample GP043, with an age of 2167±12Ma.*

6.1.4 Summary of Geochronology Results

The three samples give an intrusive relationship between the granite gneiss, the quartz diorite/granodiorite and the granodiorite. The oldest unit dated for this study is the granite gneiss, at 2239±13Ma. The quartz diorite/granodiorite is aged at 2210±8.7Ma. The youngest unit dated for this study is the granodiorite at 2167±12Ma. These ages will be used to constrain overall magmatic and tectonic events for the study area, and will be put in context with dated plutons from other studies proximal to the FGSZ including Castaing et al. (2003), Vegas et al. (2008) and Fontaine et al. (2017).

CHAPTER 7: INTERPRETATION AND DISCUSSION OF THE TECTONIC EVOLUTION OF THE FGSZ

The FGSZ and the related structures within the study area were studied in detail to bring into regional context the tectonic evolution of this region in eastern Burkina Faso. The interpretations of the tectonic evolution of the FGSZ and related structures were made by incorporating desktop studies, fieldwork data, geochemical and geochronological analysis. Geochemical analysis and the petrography descriptions revealed the composition of the different rock types, and specific mineral assemblages established the metamorphic grade of the region.

Age constrains of intrusive events were established by using the LA-ICP-MS zircon U-Pb age data obtained from the sampled units. The geochronology results were also implemented in constraining the ages of deformation phases based on the crosscutting structures and plutonic units identified in each domain. Interpretations made for this study are correlated with published work done in areas adjacent to the FGSZ and within the WAC, to establish whether the tectonic evolution of the study area coincides with what has already been studied in eastern Burkina Faso, and other parts of the craton.

7.1 VOLCANIC ARC ACTIVITY AND MAGMATISM

The greenstone belts in the study area are composite of metamorphosed basalt, meta-sediments and the ultra-mafic pyroxenite units. Gabbros are closely associated with the meta-basalts and pyroxenites. The meta-volcaniclastic sediments, pyroclastic, tuffaceous sequences, graphitic schist accumulated during volcanic activity. The andalusite bearing schist, which is also within the greenstone belt, is associated with contact metamorphism, or metamorphism associated with a low pressure tectonic regime (Deer et al., 2013). Graphitic schists and argillites are ubiquitous in volcanic sequences of greenstone belts, and are good indicators for mesothermal gold deposits (Barrie, 2004).

Based on the zircon U-Pb age data, the granite gneisses (dated at 2239±13Ma) belong to a suite of the oldest plutons emplaced in the study area, and they make up the basement rocks found in this region. From the Rb, Y and Nb (ppm) binary classification diagrams by Pearce et al. (1984), geochemical data indicates

that samples GP006, GP027 and GP043 represent plutons emplaced in a volcanic arc and/or syn-collisional tectonic regime.

The age of the granite gneiss sample GP027 coincides with the age of the volcanic activity dated to have occurred at the early stages of the 2250Ma-2200Ma volcanism cycle as reported by Lompo (2009; 2010). The granodiorite sample GP006 has an age of 2210±8.7Ma, and it is therefore part of a subsequent intrusive event, during which the granodiorite intruded into the host granite gneiss. Of the three magmatic cycles defined by Lompo (2009; 2010), the samples GP006 and GP027 fall with the constrains of the 2250Ma-2200Ma cycle.

The early stages of the Eoeburnean (2266Ma to 2150Ma) are reported to be generally dominated by volcanism and older granitic emplacements (Abouchami et al., 1990; Lambert-Smith et al., 2016; Parra-Avila et al., 2017). Another volcanic arc cycle is also reported at 2240Ma to 2170Ma from age data reported by Castaing et al., 2003 for Burkina Faso. The age of volcanism and magmatism for this study area, based on published work in other regions in Burkina Faso and on the crystallization age of the granite gneiss, is ~2240Ma or older (Figure 7.1).

The volcanic arc regime characterized by the geochemical results suggests that plutonism was therefore coeval with continued volcanic activity from 2240Ma to 2200Ma (Castaing et al., 2003; Gasquet et al., 2003; Lompo, 2010; Tshibubudze et al., 2013). Pluton emplacement of younger granites and granodiorites did, however, occur post 2200Ma in some regions (Feybesse et at., 2006; Lompo, 2009; Vidal et al., 20009; Lompo, 2010; Tshibubudze et al., 2013; Ganne et al., 2014). The intrusive contacts and crosscutting relationships reveal a sequence of emplacements of the different plutonic rocks. A simplified stratigraphy column illustrating the age of volcanism, sediment deposition, emplacements of intrusive units and the dolerite dykes is shown in Figure 7.2.

Sample GP043, the granodiorite, dated at 2167±12Ma has an age similar to the quartz diorite dated by Vegas et al. (2008), with an age of 2170±6Ma. The ages of these plutons are coeval with the Tangaean Event constrained to have occurred between 2170Ma and 2130Ma (Tshibubudze et al., 2009; Tshibubudze et al., 2013) or the Eoeburnean between 2187Ma and 2158Ma (Allibone et al., 2002; de Kock et al., 2011; Perrouty et al., 2012). This suggests that the granodiorite (sample GP043) was syn-tectonically emplaced during the regionally defined Tangaean Event.

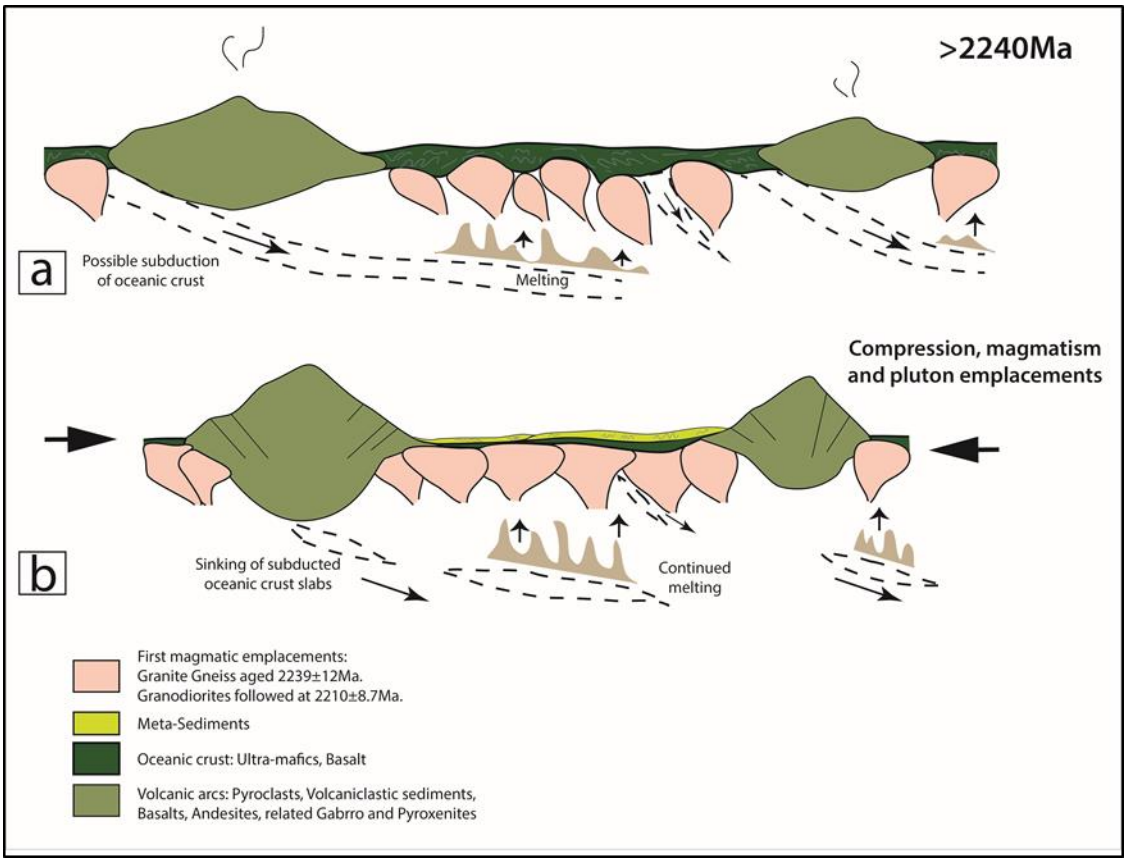


Figure 7.1: *An interpretation of the volcanic arc regime during which volcanic activity was coeval with magmatism; volcanic activity is constrained at 2240Ma or older (Castaing et al., 2003; Gasquet et al., 2003; Lompo, 2010; Tshibubudze et al., 2013). For the current study area, the oldest dated rock is the granite gneiss aged at 2239±13Ma. It is interpreted that magmatism was continuous, and the oldest granodiorite suite for this study area was emplaced ~29Ma later. The meta-sediments, the pyroclastics and meta-volcaniclastic sediments all accumulated during continued volcanic activity, and form part of the greenstone belts.*

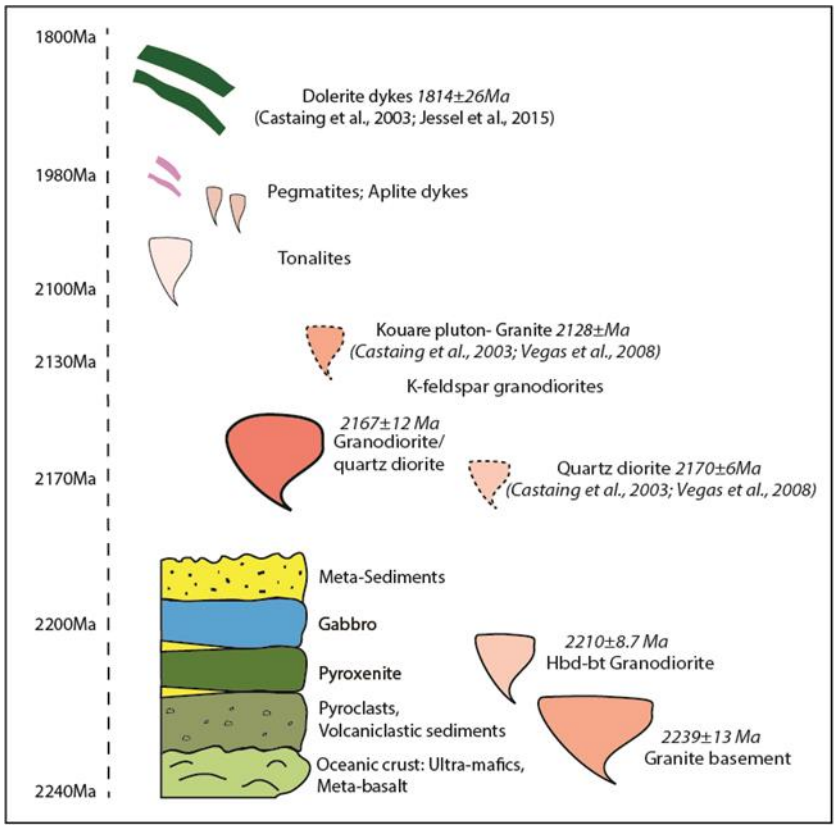


Figure 7.2: *A simplified stratigraphic column illustrating the relationships between the greenstone belt rocks, the meta-sediments and the intrusive rocks for this study. Age data of plutons from other studies in Burkina Faso have been included in the geochronological sequence (Castaing et al., 2003; Vegs et al., 2008; Jessell et al., 2015).*

7.2 REGIONAL DEFORMATIONS AND THE OVERALL TECTONIC EVOLUTION

The FGSZ has a minimum of four map-able deformation phases; D1 is responsible for the NW trending S1 foliation dominant in domains C and D. D2 is a coaxial stress that led to shortening and thrusting of terranes resulting in the dominant NE trending structural grain; D3 is a non-coaxial dextral reverse regime. D4 is a transpression deformation with sinistral shear sense. The last event, D5, represents a transition from ductile to brittle deformation that crosscuts all preceding structures. Each deformation event is described below, and the interpretations made for this study are compared with regional interpretation for other regions in eastern and southern WAC

7.2.1 Deformation Event- D1

In regions not proximal to the shear zones, the plutonic units have weakly defined fabrics or none at all. The foliated granodiorites and granite gneisses have a

NW-SE trending S1 foliation with calculated average orientation of 300°/78° SW. A NE trending meso-scale fold axial plane affects this NW-trending S1 foliation, as shown in section 5.3.4. This indicates that the NW trending foliation pre-existed and was folded by a stress axis that led to an overprinting NE trending foliation.

In northeastern Burkina Faso, NE-SW compression led to similar NW/NNW trending fabrics and structures; the deformation event is referred to as the Tangaean event (Tshibubudze et al., 2009; Hein, 2010; Tshibubudze and Hein, 2013), or the Eo-Eburnean (de Kock et al., 2011; Perrouty et al., 2012; Block et al., 2015). The NW-SE trending S1 foliation may be a remnant of the same forces that acted in northeastern Burkina Faso. The NW-trending foliation therefore defines a regional S1 that formed during a NE-SW compression, as illustrated in Figure 7.3.

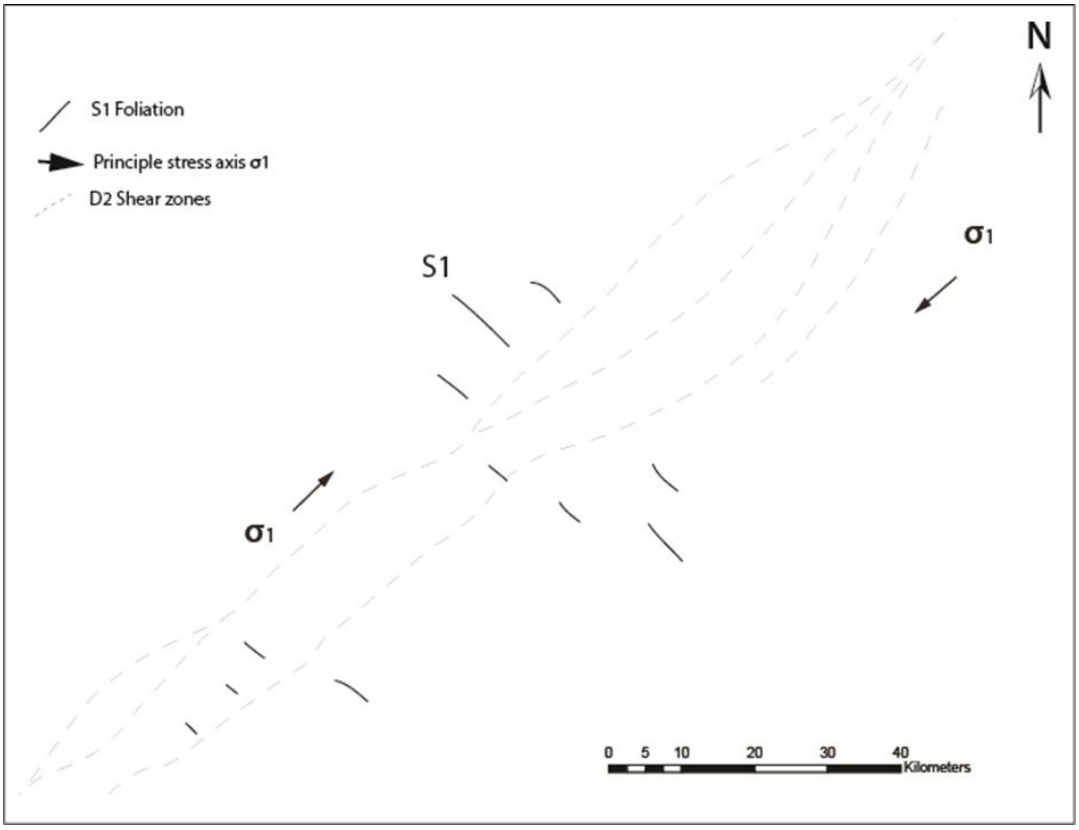


Figure 7.3: *An interpretation of the D1 event; a NE-SW oriented σ1 lead to the development of the NW trending S1 foliation. This foliation has a calculated average orientation of 300°/65° SW. This foliation pre-exists the NE trending structures.*

7.2.2 Deformation Event- D2

D2 is a ductile deformation with a NW-SE directed coaxial shortening direction (Figure 7.4). This resulted in the linear to arcuate shapes of the greenstone belts and plutons in the Fada-Gourma region and the development of the dominant NE trending structural grain. The S2 foliation has a calculated average orientation (from the domain averages) of 039°/55° SE.

The contacts between the plutons and greenstone belts are the main zones that accommodated stress, and developed into SE dipping thrust faults, as shown in cross-section A-B and C-D in Figure 7.4 and 7.5. Exhumation of the pyroxenite outcrops west of the FGSZ is interpreted to be related to the imbricate set of thrust faults. The volcanic suite of rocks developed the pervasive NE trending S2 schistosity. The chl-bt-qtz schists dominate the northern regions (domains A and B) along the tectonic contacts between the plutons and greenstone belts.

The greenstone belts caught in-between the thrust faults developed into NW-verging, tight synform folds, with NE trending fold axis as described in section 5.1.3. The NNE to NE fabric is ubiquitous in the Baoulé-Mossi Domain, and is attributed to a NW-SE shortening stress regime (Feybesse et al., 2006; Vegas et al., 2008; Baratoux et al., 2011; de Kock et al., 2012; Perrouty et al., 2012; Block et al., 2016; Fontaine et al., 2017).

Volcanic arc accretion during which linear greenstone belts were intruded into by various granitoids is reported to have occurred during the Eburnean Orogeny, constrained between 2150Ma and 2000Ma (Abouchami et al., 1990; Beziat et al., 2000; Feybesse et al., 2006). Gasquet et al. (2003) describes a continued NW-SE compression between 2160Ma and 2105Ma, during which plutons were emplaced and shear zones formed in the Dabakala area, Ivory Coast. Perrouty et al. (2012) defined a similar compressional regime as D3 in the Ashanti belt, Ghana, bracketed between 2125Ma and 1980Ma. Lompo et al. (2009) brackets the formation of the NE-SW trending major structures in the Palaeoproterozoic terranes of the WAC between 2180Ma and 2150Ma, under NW-SE directed shortening.

The vertical tectonics related to NW-SE shortening in western Ghana is reported to have occurred between 2200Ma and 2100Ma (Lompo, 2010; de Kock et al., 2012). The general consensus is that the NW-SE compression responsible for the NNE-NE trending major structures and fabrics was at the early stages of the

progressive Eburnean Orogeny that started as early as 2180Ma and lasted until ~1980Ma (Allibone et al., 2002; Feybesse et al., 2006; Tshibubudze et al., 2009; Lompo, 2010; Metelka et al., 2011; Perrouty et al., 2012).

The L-tectonite zone in-between the FGSZ and the FBSZ (domains A and B) defined as a regional L2 is evidence of a vertical to sub-vertical displacement during coaxial shortening. The plunge direction (calculated average orientation 81°→155°) is indicative of a sub-horizontal σ1. This suggests that the principal stress σ1 was horizontal and σ3 was vertical, further supporting a coaxial shortening tectonic regime.

Towards the end of this deformation phase, the first set of quartz veins precipitated along the weakness planes within the chl-bt-qtz schist and other NE trending structural weaknesses. This set of veins is therefore parallel to the dominant NE-fabric. The veins underwent a ductile, coaxial stretching during which a near-perpendicular σ1 caused stretching and boudinage structures in the σ3 plane oriented NE.

D2 Metamorphic Imprint

The gneissic S2 foliation with calculated average orientation from domains of 043°/71° SE, in the basement granite gneiss is defined by a quartz, plagioclase and hornblende compositional banding. The mineral assemblage indicates a high metamorphic grade of up to amphibolite facies during a ductile deformation with NW-SE compression. The hbd-bt granodiorites also developed a gneissic fabric and underwent recrystallization due to deformation. The hbd-bt granodiorites in the domains C and D developed a gneissic foliation in some regions, and have amphibolitic minerology in a few outcrops with and partial melting fabrics.

There is a transition from a chlorite, biotite ± muscovite, epidote and quartz dominant mineral assemblage in domains A and B to a more hornblende, biotite, muscovite, plagioclase and minor quartz in the domains C and D towards the SW along strike of the FGSZ and FBSZ. This is evident in the prevalence of the chl-bt-qtz schist in domains A and B and not so much in domains C and D. Migmatites and stromatic fabrics are more prevalent in the domains C and D, indicating that high temperature conditions dominated during a ductile deformation.

The migmatite outcrops have amphibolitic and feldspar rich layers with -complex patterns. Pons et al. (1995) and Gasquet et al. (2003) suggest that the

migmatites in southwestern Niger and Cote d'Ivoire respectively are associated with syntectonic-emplaced plutons, rather than a reworking and partial melting of pre-existing plutons. Migmatization is constrained to have occurred during Eoeburnean orogeny (2193Ma-2195Ma) at amphibolite facies metamorphic grade in central west Ghana (de Kock et al., 2012). Pyroxenites are outcropping in the NE and SW domains of the study area (geological map at the end of section 4.4). According to Ganne et al. (2011), the greenstone belts were exhumed during the progressive D2 due to volumes of granitoids that were syntectonically emplaced.

Regional high grade metamorphism is bracketed between 2140Ma and 2130Ma in NW Ghana by Block et al. (2016). This is the first metamorphic imprint , M1, and the reported conditions are 10-140kbar and 520°-600° (Block et al., 2016); this translates to granulite-amphibolite facies. This M1 is a metamorphic marker for the beginning of the Eburnean Orogeny in northwestern Ghana, concomitant with N-S crustal thickening defined as D1 by Block et al., 2016 in NW Ghana. The M2a conditions reported for the Fada N'Gourma region in Burkina Faso by Ganne et al. (2011) is a contact metamorphism related to the shortening tectonic regime that resulted in the arcuate shapes of the greenstone belts, and the pluton emplacement. The pressure and temperature conditions for the M2a are 550°-650° and 6-8kbar (Ganne et al., 2011).

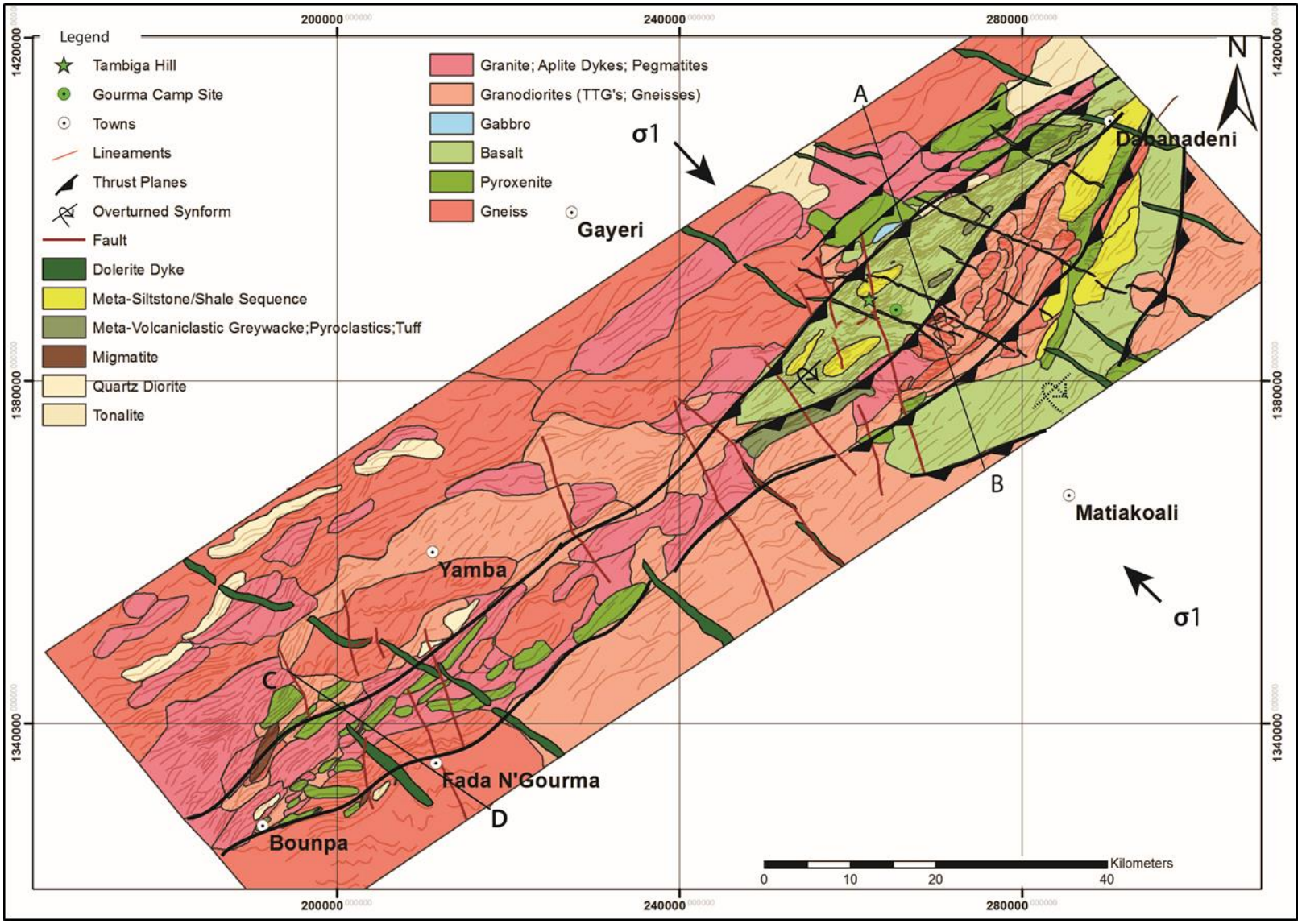


Figure 7.4: *The interpreted geological map for the study area. The lineaments extracted from aeromagnetic data show the pervasive NE trending fabric. The thrust planes are located mainly at the contacts of the greenstone belts and the plutons. Synforms are interpreted to have developed in the greenstone belts (cross-section A-B in Figure 7.5).*

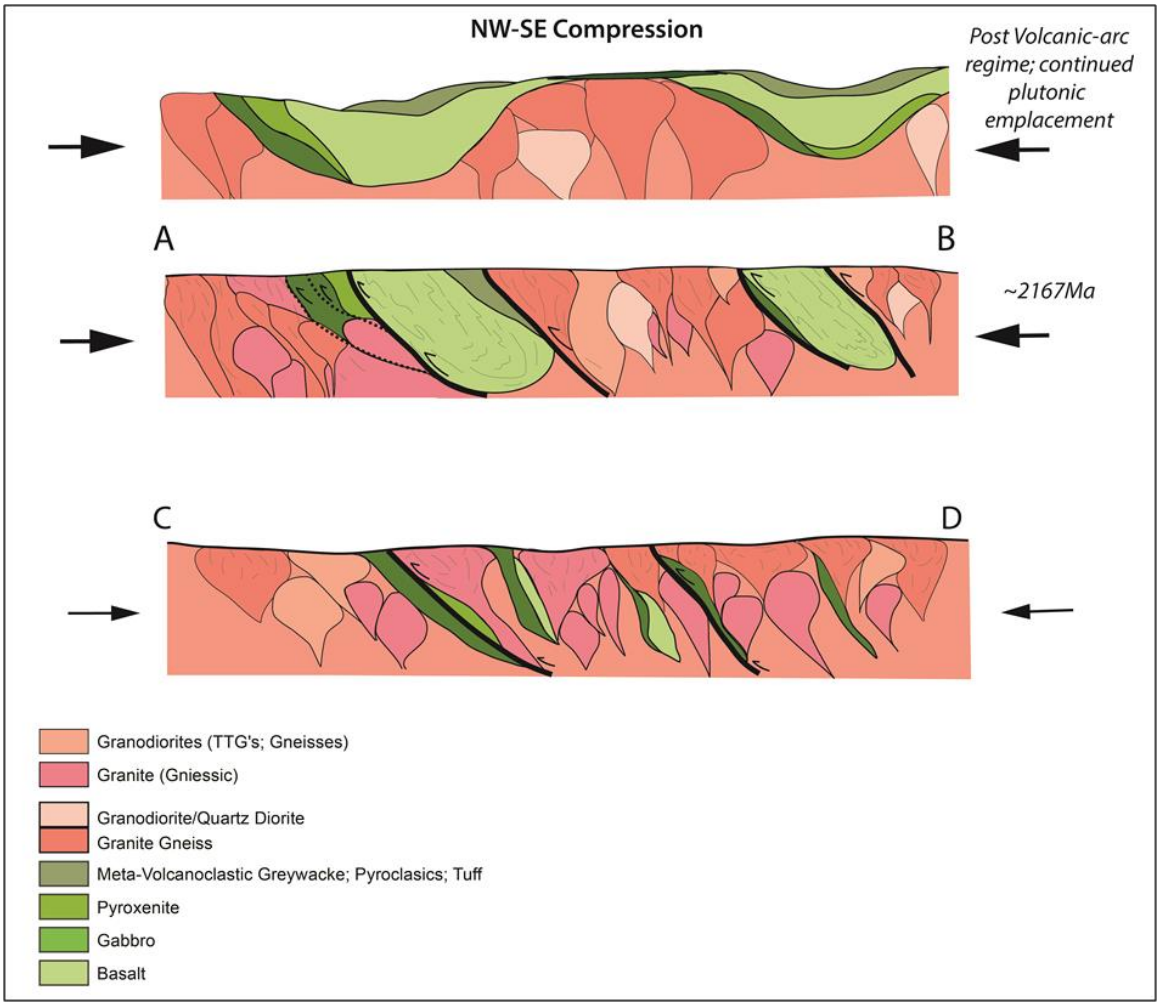


Figure 7.5: *Cross sections A-B and C-D as indicated in Figure 7.4. illustrating the coaxial shortening and thrusting deformation is in a NW-SE direction. Thrust folding of sequences occurred. The basalt, meta-volcaniclastics, pyroxenites and gabbros were all emplaced during the ≥2239Ma volcanic event. The ages of the plutons are an indicator of syn-tectonic plutonism during accretion at ~2167Ma.*

7.2.3 Deformation Event- D3

D3 had an ENE-WSW oriented principal stress axis, as shown in Figure 7.6. This deformation is a progressive transition from a coaxial shortening to a non-coaxial; the thrust faults became reactivated and shearing occurred. D3 did not cause a significant distortion of D2 structures, and the deformation occurred mainly along the NE structural grain that formed in D2. Shear sense displacement was dextral along a right stepping bend in the FGSZ and this led to the development of a dilational bend. The FGSZ (together with the DT) and the FBSZ have preserved

dextral shear senses. The overall displacement for D3 is a transpressive; dextral reverse, east block up.

In some chl-bt-qtz schist outcrops, a non-coaxial shear stress dominated and the boudins were sheared, developing sigma-clast shapes. The shear sense in these sigma-clasts is dextral (section 5.1.1). This is an indication that the veins underwent continuous ductile deformation during a non-coaxial stress dextral shear deformation in D3.

The L3 readings are steep plunging to the NE and SW (calculated average orientations from domains 60°→033° and 67°→232°), indicating a transition from NW-SE thrusting, to an oblique, transpressive deformation. This is consistent with a dextral reverse deformation.

The strain of deformation during D3 also led to mylonites forming in outcrops along the FGSZ. The Gourma mylonite zone has a NE trending foliation (calculated average orientation in the mylonite zone is 033°/44° NW) with weakly defined shear sense indicators, although a few dextral sigma clasts are identified in thin section.

Both sub-zones in the Bogueli mylonite zone have dextral displacements in the minor shear zones. The minor shear zones are NE trending (058°/80° SE) and crosscut the gneissic host rocks. The shear sense indicators in zone 1 display dextral shear S3-C3 fabrics (locally defined S2 orientations 040°/87° NW and C2 orientation 055°/88° NW). Zone 1 of the Bounpa mylonite zone has complex ductile deformation patterns, and micro-folds. The dextral shear sense along the mylonite zones is consistent with a NW-SE principal stress axis. The stress axis orientation does however vary along the FGSZ, and is WSW-ENE oriented in some regions, as illustrated in Figure 7.6.

The dextral shearing along the Bole Nangodi Shear Zone (BNSZ), an extension of the FGSZ in NW Ghana by Block et al. (2015) and an equivalent to this study's D2, is associated with an E-W shortening D3. D3 along the BNSZ is reported to have ended around 2104±1Ma (Block et al., 2015). Dextral shearing is reported to be syn-tectonic with the emplacement of the NE elongate Tenkodogo–Yamba pluton between 2150Ma and 2120Ma (Naba et al., 2004). The Tenkodogo–Yamba pluton is proximal to this study, and is located west of Fada N'Gourma.

The D2 and D3 events for this study are considered to be part of the early stages of the Eburnean Orogeny in eastern Burkina Faso, and this is comparable

with other studies in Burkina Faso and Ghana (Leube et al., 1990; Eisenlohr and Hirdes, 1992; Naba et al., 2004; Feybesse et al., 2006; Fontaine et al., 2017). Eburnean dextral shear is reported as the primary deformation regime responsible for the syn-tectonic pluton emplacement in the Yamba region, proximal to the FGSZ (Naba et al., 2004). The NW-SE D2 event responsible for the NE trending structural grain is an equivalent of Block et al. (2016)'s D3 which is constrained between 2125Ma and 1980Ma. D1, defined by Fontaine et al. (2017) is southern Burkina Faso is an E-W to WNW-ESE compression during which isoclinal folds and local shears formed. Northwest and SE shortening and a NE trending S3 and thrust faults define the D2 and D3 in the Ashanti and Damang regions in southern Ghana, as reported by Allibone et al. (2002) and Perrouty et al. (2012) respectively. Baratoux et al. (2011) constrains an E-W to WNW D1 compression at 2160Ma-2120Ma.

The metamorphic grade for this early Eburnean Orogeny is reported to be greenschist to lower amphibolite facies with conditions of 665 ± 35 °C at 8–9 kbar at 30–35 km depth (Baratoux et al., 2011; de Kock et al., 2012; Fontaine et al., 2017).

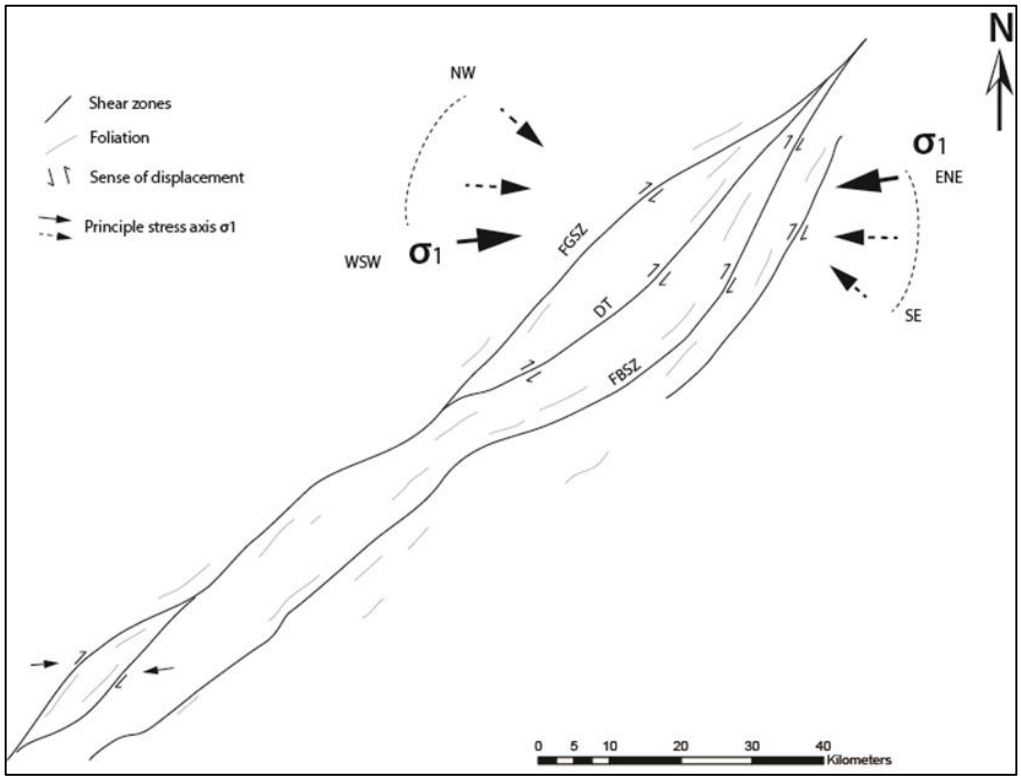


Figure 7.6: *An illustration of D3 stress axis orientation; the σ1 varies from WSW-ENE to NW-SE. This was a non-coaxial shortening and it lead to dextral shear sense along the thrust fault planes. The FGSZ developed a right stepping dilation bend with the DT on the eastern margin of the bend. Another dextral dilation bend is discernible in geophysical imagery data, but has been*

7.2.4 Deformation Event- D4

D4 represents a reactivation of the FGSZ, DT and FBSZ from a dextral deformation in D3 to sinistral strike slip. The principal stress axis for D4 was in a NNE-SSW direction (Figure 7.6). The overprinting D4 fabrics and structures are discernible in aeromagnetic imagery data. Rotational fabrics in-between the sinistral shear zones indicate clockwise rotation. Although coaxial shortening of the NW-SE striking S1 can produce similar patterns, no sufficient evidence was observed in the field to support this. The sigma structure that is in-between the DT and the FBSZ is indicative of sinistral displacement along the FGSZ and FBSZ, and map-scale S4-C4 (strikes S4= 290° and C4= 030°) fabrics are consistent with the sinistral shearing.

In some outcrops, S2=S3 has been crenulated to form an E-W to NW-SE oriented S4, as shown in Section 5.1.1 (at local scale, these fabrics were described as locally S1 and S2). The crenulation cleavage S4 is oriented 086°/82° S along the FGSZ. Some of the E-W trending measurements are along the S4 plane in the S4-C4 sinistral fabric. The S4 has an orientation of 052°/80° SE and the C4 orientation is 028°/88° SE. as described in section 5.2.6. The S4-C4 fabric orientation is slightly rotated at local outcrops, but is still consistent with an N-S to NNE-SSW σ1.

L4, by regional convention refers to the NE and SW plunging lineations (26°→032° and 37°→241° in domain A and 17°→224° and 08°→048° in domain C). Crenulation fold-axes that have an average orientation of 40°→090 ° also occur, and a few have azimuths to the west, 40°→270°. The crenulation micro-folds are asymmetrical, with a sinistral shear sense as shown in section 5.1. This is consistent with the NNE-SSW σ1 under an oblique, sinistral-reverse to strike slip regime.

The Bounpa Mylonite Zone 2 has sinistral shear sense indicators (section 5.4.3), and is consistent with the D4 structural features. This is an indication that localized mylonites formed in D4, and that D4 was a ductile deformation with high shear strain (White et al., 1980).

Another indication of a NNE-SSW oriented σ1 is along the dextral displacement on the NW-trending plane (presented in section 5.3.2). The NW-trending foliation may have been rotated during a progressive sinistral strike slip regime along the NE trend. The dextral displacement and folding on the NW foliation is consistent with Riedel shears in a sinistral strike slip regime as shown in Figure 7.7 a.

Vegas et al. (2008) propose that the z-folds that envelope the Kouare pluton are a rotation of the NW gneissic foliation in the host tonalite rock during pluton emplacement and sinistral shearing along the WKSZ (Figure 7.2 b). The foliation was at an angle to the bounding shear zones prior to shearing and rotation. Similar patterns are observed in the aeromagnetic imagery data throughout eastern Burkina Faso. The map-scale S4-C4 fabrics for this study and the D4 σ1 orientation are illustrated in Figure 7.6. In Figure 7.7, the interpretation by Vegas et al. (2008) has been incorporated with the S4-C4 foliation. These patterns are consistent with N-S to NNE-SSW directed σ1 under a sinistral shear regime.

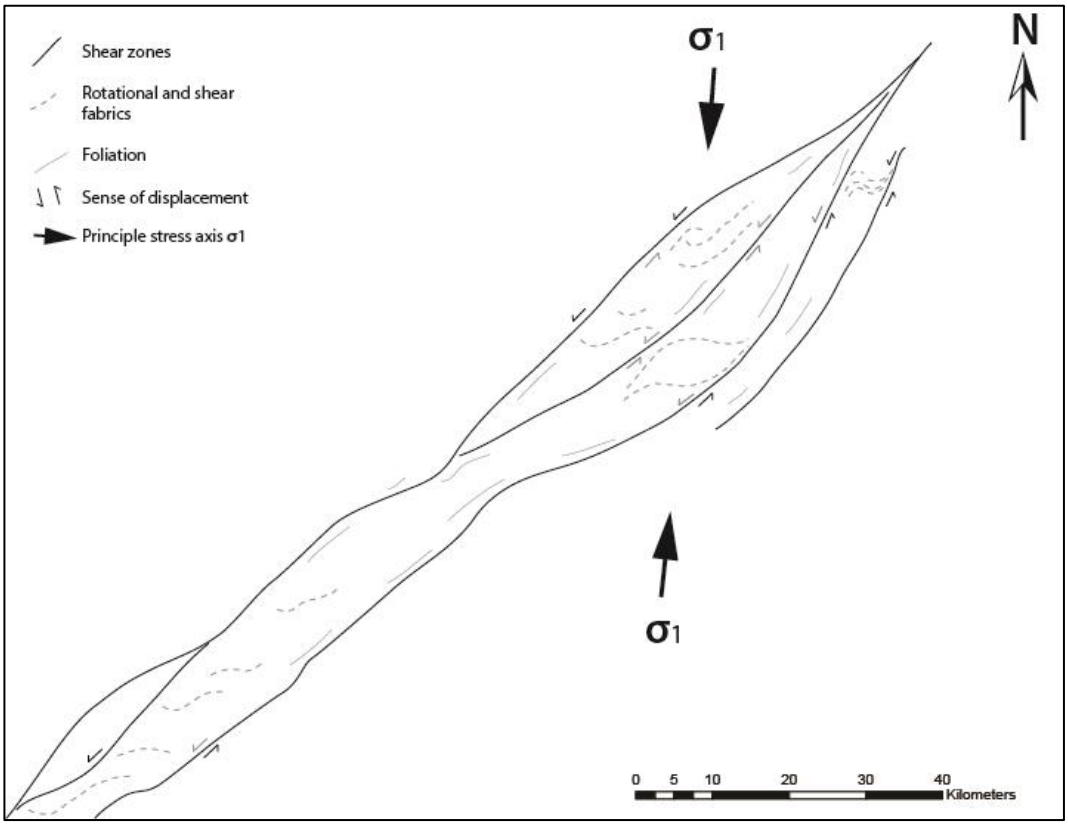


Figure 7.6: *D4 is defined by NNE-SSW directed σ1. This resulted in a sinistral shear sense along the reactivated shear zones. Rotational fabrics are discernible on the aeromagnetic imagery data.*

Studies by Tunks et al. (2004) and Perrouty et al. (2012) reported N-S to NNW-SSE shortening regimes along the NE trending major structures that host the Damang gold deposit, Ghana. This N-S shortening is subsequent to the deformation event responsible for the dominant NE structural grain (Tunks et al., 2004), and lead to E-W trending foliation. The WKSZ south of Fada N'Gourma underwent sinistral shearing and syn-tectonic emplacement of the Kouare pluton (Vegas et al., 2008).

The Kouare pluton is dated at 2128±6Ma (Pb-Pb zircon age) (Castaing et al., 2003). This gives an age constraint to the sinistral shearing along the WKSZ and possibly the FGSZ. According to Allibone et al. (2002), NE trending sinistral strike slip shears are defined as D5 in the Ashanti belt, Ghana. The stress axis for the reactivation of the NE trending thrust zone is reported to have had to be NNE-SSW (Allibone et al., 2002).

Metamorphic Imprint

The metamorphic mineral assemblage of greenschist facies of chlorite, chloritoid, biotite, quartz and feldspars and minor epidote is observed in the schists, the meta-basalts and granodiorites of this study. These minerals are common in low-grade metamorphic zone in contact metamorphism regions. Ganne et al. (2011) has constrained the second major metamorphic imprint, M2b, as part of the retrogression in the contact metamorphic conditions induced by intrusion of plutons in the Fada N'Gourma region. The reported P-T conditions are <1kbar and 200-450°C. This falls within the greenschist facies metamorphic grade.

The addition of biotite and hornblende in these greenschist units (schists, the meta-basalts and granodiorites) is indicative of an increase in metamorphic grade, and in the case of contact metamorphism, these minerals indicate a metamorphic zone closest to an intrusive body. A greenschist facies contact metamorphism in consistent with the volumes of pluton emplacement during the Eburnean Orogeny (Pons et al., 1995; Feybesse et at., 2006; Pawlig et al., 2006; Lompo, 2009; Vidal et al., 20009; Lompo, 2010; Tshibubudze et al., 2013; Ganne et al., 2014).

The graphite schists have euhedral andalusite grains, indicating medium to low temperature and pressure metamorphic conditions. Andalusite is in a P-T metamorphic zone indicative of a thermal effect that plutons had on the host rock, and corresponds to a low greenschist metamorphic grade (Deer et al., 2013). The metamorphic mineral is also indicative of a decrease in coaxial or shear stress (Deer et al., 2013). Graphitization in the Palaeoproterozoic rocks is associated with the crustal thickening and the compressive tectonic regime of the Eburnean Orogeny (Kribek et al., 2008).

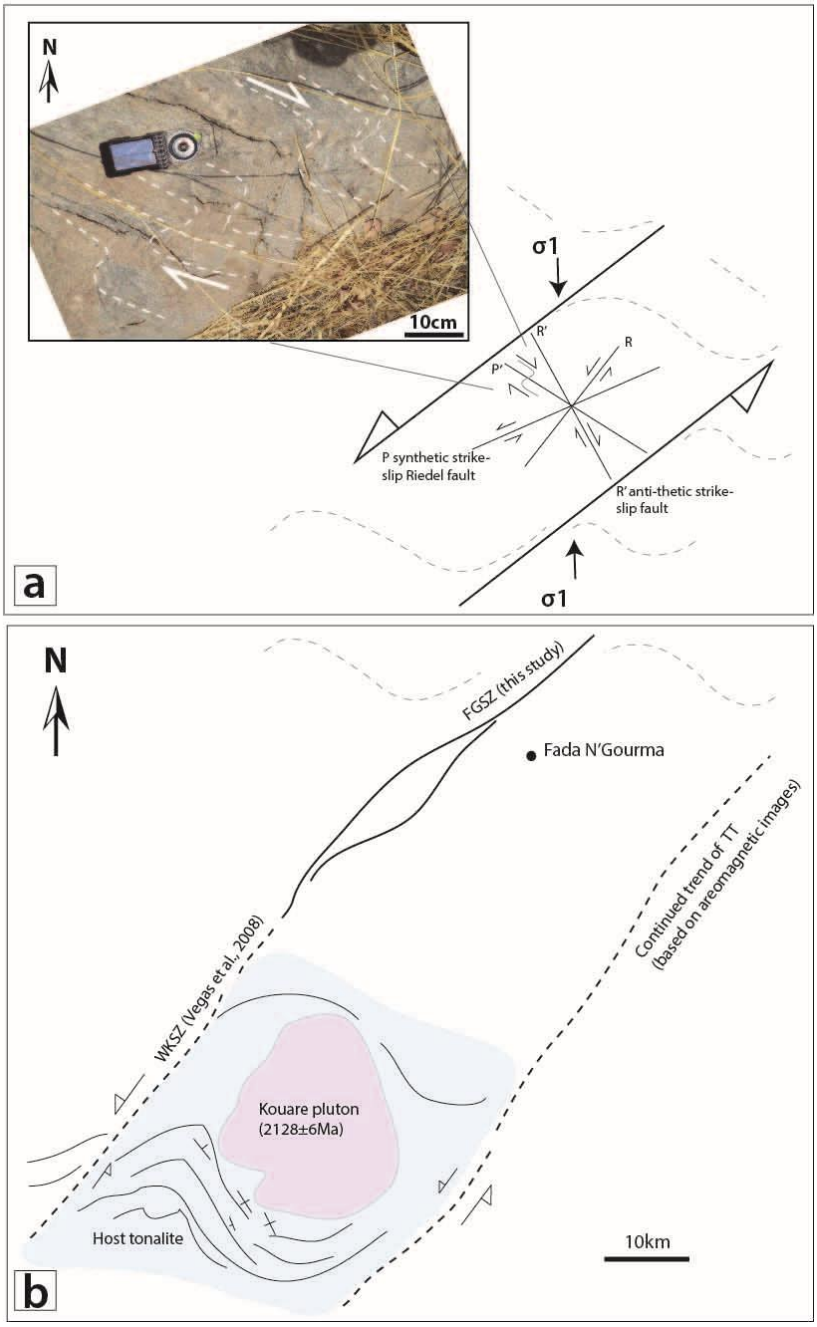


Figure 7.7: *An interpretation of the possible relation of the NW-trending foliation to the dominant NE fabrics. (a) One outcrop shows the NW striking foliation being folded and sheared (dextral shear sense). This may be part of the Riedel fault system that develops in a sinistral shear zone with NNE-SSE directed σ1. This orientation is consistent with the sinistral shear defined in D4 for this study area. (b) Southwest of the FGSZ study area, is the WKSZ as defined by Vegas et al., 2008. The Koure pluton was emplaced within a tonalitic host rock, and is dated at 2128±6Ma. The high temperature emplacement of the pluton led to the re-melting and development of the gneissosity in the tonalite, and rotation fabrics formed. Although the original orientation of the pre-existing foliation before rotation could be determined, Vegas et al. (2008) suggest that the layering before deformation was at an angle to the NNE/NE shear zones, and underwent rotation during sinistral shearing and emplacement of the pluton. The NW-trending migmatite foliation in the FGSZ study area may have developed under similar tectonic environments. For this study, NNE-SSW directed σ1 is defined as part of the D4 event.*

7.2.5 Deformation Event- D5

Subsequent to the ductile deformations D3 and D4, a brittle deformation D5 occurred. The D5 structures crosscut most of the rock types, and the D1, D2, D3 and D4 features. Fracture cleavage planes developed on the massive buck quartz veins outcrops, and on the intrusive units (section 5.1 and 5.2). These fracture cleavage planes have average mean calculated orientations of 300°/60° SW and 347°/80° SW.

Quartz veins V4 formed in a similar orientation to the NW-oriented fracture planes, and they also crosscut the NE trending V2 buck quartz veins. These veins are cm-scale in width. It is interpreted that V4 and the fracture cleavage planes may belong to the same D5 brittle deformation regime.

Infilling of the fractures by hydrothermal fluids that precipitated into quartz veins V5 indicates that these fracture planes are extensional fracture planes. The stress axis required for NW trending extensional fractures to form is NW-SE oriented.

The fracture cleavage planes observed in southern Ghana within the Damang gold deposit also formed during a NW-SE compressive brittle deformation. These fractures are reported to crosscut all other structures (Tunks et al., 2004). No relative timing of the deformations in the Damang region, Ghana, was defined but the sequence of events and orientations of principal stress axes are comparable with those of this study. De Kock et al. (2012) report brittle fracture planes and faults as part of a later D5 event in the central west Ghana; the orientation of the fractures is WNW-ESE, and in some local areas, the fractures have quartz infilling.

7.2.6 Gold Mineralization

The thrust planes, fold axes and schist units were ideal weakness planes for quartz veining to occur. A fault-valve system was a probable mechanism for fluid migration during increased and decreased lithostatic pressures in-between thrusting (Sibson, 1996; Vearncombe and Zelic, 2015). This lead to buck quartz veining, V2, parallel to S2, hosted within the chl-bt-qtz schist and meta-volcaniclastic units. The hydrothermal veining was a progressive event, with repetitive pulses of veins during the thrusting in late D2 and early D3. The veins are NE trending, and in some case have a boudinaged shape.

It is interpreted that V2 was concomitant with gold mineralization found in this region. Gold mineralization is hosted either within or along the veins, as described in section 5.1.3. The abundance of artisanal mining activity is indicative of the presence of gold in the region, and the artisanal mines are systematically located along the strike of the quartz veins. The metamorphic conditions required for gold mineralization are around 570°C (Fontaine et al., 2017), or lower between 300°C and 500°C at low pressures of <2kbar (Ganne et al., 2011).

The location of gold mineralization and deposits indicates that the first mineralization event had a structural control. The gold is associated with quartz, tourmaline and pyrite. Disseminated (often oxidized) pyrite within the schist units may also be associated with gold mineralization. The V4 quartz veins may host reworked, placer gold deposits in the form of visible gold. Fontaine et al. (2017) identified two phases of mineralization in the Kiaka deposit, SW of Fada N'Gourma. The first is a disseminated sulphide, quartz-biotite and meta-volcaniclastic greywacke hosted mineralization. The second phase is associated with alterations related to deformation and reworking along shear zones. The age constrains on the first mineralization phase is during the Eburnean Orogeny at around 2150Ma, and the second phase is constrained between 2100Ma and 2040Ma (Fontaine et al., 2017). Due to the proximity of the Kiaka deposit to this study area, these age constraints and mineralization types are considered as comparable with those in this study.

7.3 SUMMATION OF THE TECTONIC FRAMEWORK OF THE FGSZ

Timing of the deformation phases for this study is crucial in establishing the regional context relating to the tectonic evolution of the WAC. Many studies have defined local deformations and sequences of events based on available geochronology data. Local similarities in plutonic unit compositions and ages, and/or in the orientation of the major structures are the basis on which a regional context is gathered to build up the tectonic evolution of the Palaeoproterozoic terranes in the Baoulé-Mossi Domain.

Illustrated below is a schematic summary of the tectonic evolution and sequence of granitoid emplacement for this study. Referenced and included in the summary are the ages of different granitoids, and the age constrains on regional deformation events studied in other areas in Burkina Faso.

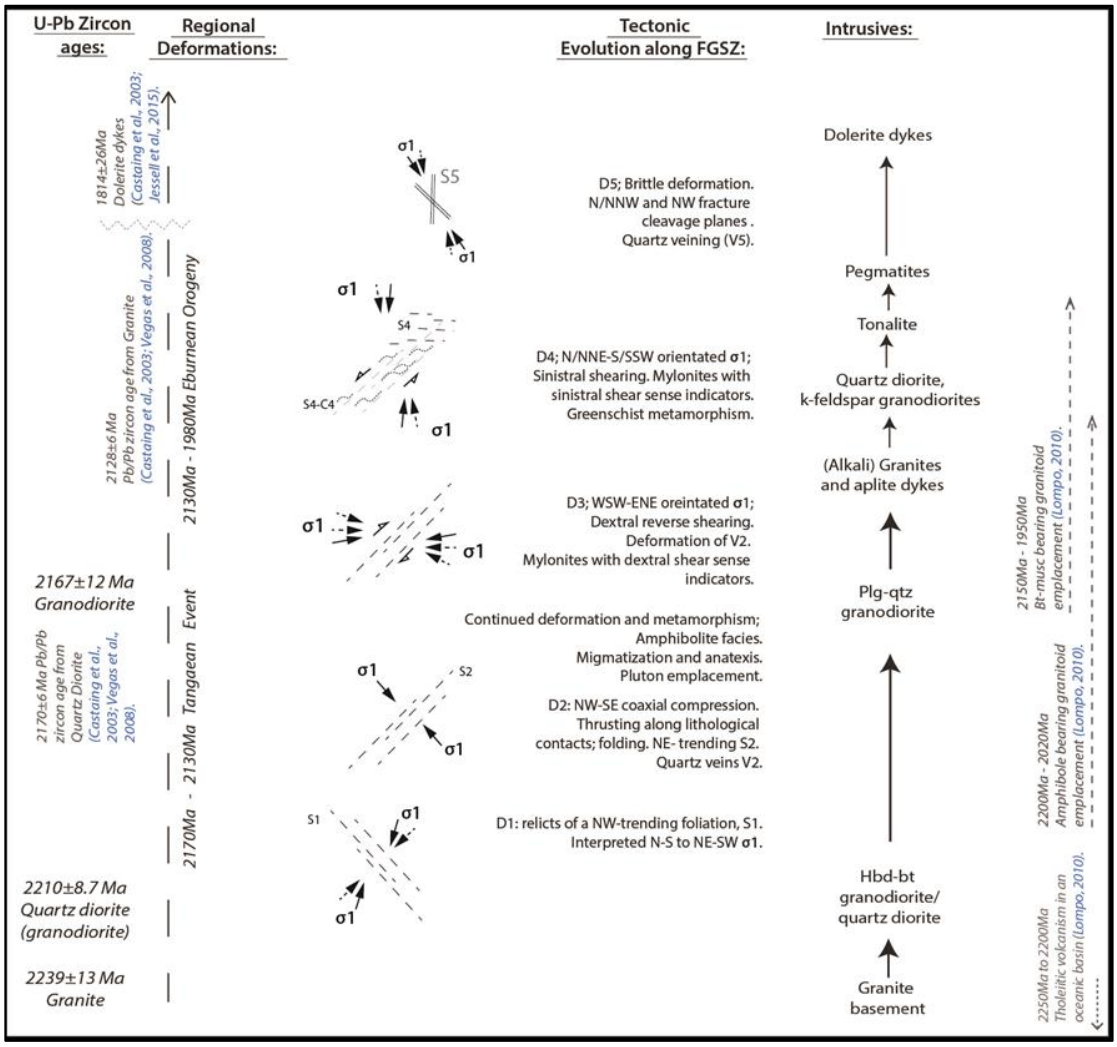


Figure 7.8: *A schematic summation of the tectonic evolution, pluton emplacement sequence incorporated with published data from other studies in Burkina Faso. The ages attained from this study reveal that the basement rocks for the Birimian terrane in the FGSZ area were granitic (granite gneiss). The crystallization age of the granite gneiss and the quartz diorite/granodiorite is within the constrained volcanic arc activity ages between 2250Ma and 2200Ma (Lompo, 2010). This suggests that magmatism was coeval with volcanic activity. Deformation event D1 is comparable with the D1 defined in NE Burkina Faso as the Tangaean event by Tshibubudze et al. (2009), Hein (2010), Tshibubudze et al. (2015). D2 and D3 form part of the early stages of the Eburnean Orogeny in eastern Burkina Faso, dominated by compression and crustal thickening. The dominating NE trending structural grain resulted from the NW-SE shortening direction. D4 is a reactivation of the shear zones during a sinistral shear sense regime. D5 is a late stage brittle deformation resulting in fracture cleavage planes. Plutons were emplaced through the deformation events. The youngest units are the dolerite dykes that crosscut all other lithologies and the structures. The dolerite dykes in*

CHAPTER 8: CONCLUSION

The structure of the FGSZ and the related shear zones, and the geology that makes up the study area are defined using geophysical imagery data together with field data. Kinematic, geometric and dynamic information was sourced from field measurements, and the tectonic regimes interpreted from the crosscutting features. Using the age data obtained from the sampled plutons, timing of magmatic events could be interpreted. These ages were integrated with the structural interpretation to constrain deformation events.

Five deformation events are defined for this study area. Although the D1 fabric has limited crosscutting evidence in the field, it is interpreted that it pre-exists the dominant NE-trending structural grain. The S1 foliation was rotated during the younger transpressional deformation events. D2 and D3 may be part of a progressive deformational event, which started out as a coaxial NW-SE shortening that later became a transpressional deformation with dextral shear sense. The change in principal stress axis from D2 to D3 is NW-SE to ENE-WSW. This phase makes up the late Tangaean Event to early Eburnean Orogeny.

High metamorphic grade of amphibolite facies was the earliest metamorphic imprint, and it dominates the southern and central domains of the study area. The greenschist facies dominate the northern domains, and is a latter metamorphic imprint. The distinction in the difference in metamorphic grade from the north to the south of the study area cannot be explained conclusively. Gold mineralization in the greenstone belt-granitoid sequence occurred under lower P-T conditions, and occurs as vein hosted gold, or disseminated gold in schists.

The intrusive contacts observed in the field aided in establishing the oldest lithologies from the youngest in this study area. This was especially the case in distinguishing the different granodiorite suites. A detailed geological map was produced for this study area, and a stratigraphic column illustrating the sequence of emplacements and deposition was also produced. The interpretations are consistent with the literature review of the Birimian Terranes in other parts of Burkina Faso, and other regions in the WAC.

The limitation for this study is the scarcity of outcrops in the field. Infilling of geology in some regions of the study area relied on interpolation of aeromagnetic imagery data interpretations. This method is useful and yields reliable results,

although it is best incorporated with field data for ground truth. Future studies can focus on the Bounpa mylonite zone 1 in domain D of the study area. Complex structural features are observed in the mylonite outcrops that, if mapped in detail and a significant number of structural measurements are taken, can yield more detail into the deformation event that acted to produce the mylonites. The study area poses potential for gold deposit exploration. The age constraints for gold mineralization in this study area are based on studies in adjacent areas. A future study may focus on the gold mineralization in the Gourma region, adding detail to the exploration prospects for the area.

REFERENCES

Abouchami, W., Boher, M., Michard, A. and Albare`de, F., 1990. A major 2.1 Ga event of mafic magmatism in West Africa: an early stage of crustal accretion.. *Journal of Geophysical Research,* Volume 95, pp. 17605-17629.

Allibone, A.H., McCuaig, T.C., Harris, D., Etheridge, M., Munroe, S., Byrne, D., Amanor, J.,Grapong, W.., 2002. Structural controls on gold mineralization at the Ashanti Gold Deposit, Obuasi, Ghana. *Society of Economic Geologists (Special Publication),* Volume 9, pp. 65-93.

Amponsah, P.O., Salvi, S., Beziat, D., Siebenaller, L., Baratoux, L., Jessell, M.W., 2015. Geology and geochemistry of the shear-hosted Julie gold deposit, NW Ghana. *Journal of African Earth Sciences,* Volume 112, pp. 505-523.

Augustin, J., Gaboury, D. and Crevier, M., 2016. The world-class Wona-Kona gold deposit, Burkina Faso. *Ore Geology Reviews,* Volume 78, pp. 667-672.

Baratoux, L., Metelka, V., Naba, S., Jessell, M.W., Grégoire, M., Ganne, J., 2011. Juvenile Paleoproterozoic crust evolution during the Eburnean orogeny (~2.2–2.0 Ga), western Burkina Faso. *Precambrian Research,* Volume 191, pp. 18-45.

Baratoux, L., Metelka, V., Naba, S., Ouiya, P., Siebenaller, L., Jessell, M.W., Nare, A., Salvi, S., Beziat, D., Franceschi, G., 2015. Tectonic evolution of the Gaoua region, Burkina Faso: Implications for mineralization. *Journal of African Earth Sciences,* Volume 112, pp. 419-439.

Barrie, C.T. and Associates Incorporated, 2004. *Geochemistry of Exhalites and Graphitic Argillites near VMS and Gold Deposits,* Canada: Ontario Mineral Exploration Technologies (OMET).

Beziat, D., Bourges, F., Debat, P., Lompo, M., Tollon, F., Zonou, S., 1998. Albitite et listve´nite: sites de concentration aurife`re ine´dits dans les ceintures de roches vertes birimiennes du Burkina Faso. Bull. *Soc. Ge´ol. Fr.* Volume 169, Issue 4, pp. 563–571.

Beziat, D., Bourges, F., Debat, P., Lompo, M., Martin, F., Tollon, F., 2000. A Paleoproterozoic ultramafic-mafic assemblage and associated volcanic rocks of the Boromo greenstone belt: fractionates originating from island-arc volcanic activity in the West African craton. *Precambrian Research,* Volume 101, pp. 25-47.

Beziat, D., Dubois, M., Debat, P., Nikiema, S., Salvi, S., Tollon, F., 2008. Gold metallogeny in the Birimian craton of Burkina Faso (West Africa). *Journal of African Earth Sciences,* Volume 50, pp. 215-233.

Black, L.P., Kamo, S.L., Williams, I.S., Mundil, R., Davis, D.W., Korsch, R.J., Foudoulis, C., 2003. The application of SHRIMP to Phanerozoic geochronology; a critical appraisal of four zircon standards. *Chemical Geology,* Volume 200, pp. 171-188.

Block, S., Ganne, J., Baratoux, L., Zeh, A., Parra, L.A., Jessell, M., Ailleres, L.,Siebenaller, L., Mensah, E., 2015. Petrological and geochronological constraints on lower crust exhumation during Paleoproterozoic (Eburnean) orogeny, NW Ghana, West African craton. *Journal of Metamorphic Geology*. Volume 33, pp. 463-494.

Block, S., Jessell, M., Aillères, L., Baratoux, L., Bruguier, O., Zeh, A., Bosch, D., Caby, R., Mensah, E., 2016. Lower crust exhumation during Paleoproterozoic (Eburnean) orogeny, NW Ghana, West African Craton: interplay of coeval contractional deformation and extensional gravitational collapse. *Precambrian Research*. Volume 274, pp. 82–109.

Bourges, F., Debat, P., Tollon, F., Munoz, M., Ingles, J., 1998. The geology of the Taparko gold deposit, Birimian greenstone belt, Burkina Faso, West Africa. *Mineralium Deposita,* Volume 33, pp. 591-605.

Castaing, C., Billa, M., Milési, J.P., Thiéblemont, D., Le Mentour, J., Egal, E., Donzeau, M. (BRGM) (coordonnateurs) et Guerrot, C., Cocherie, A., Chevremont, P., Tegyey, M., Itard, Y. (BRGM), Zida, B., Ouedraogo, I., Kote, S., Kabore, B.E., Ouedraogo, C. (BUMIGEB), Ki, J.C., Zunino (ANTEA), (2003). *Notice explicative de la Carte Géologique et Miniére du Burkina Faso à 1/1 000 000.*

Chappell, B. W. and White, A. J. R., 1974. Two contrasting granite types. *Pacific Geology,* Volume 8, pp. 173-174.

Chappell, B. W. and White, A. J. R., 2001. Two contrasting granite types: 25 years later. *Australian Journal of Earth Sciences,* Volume 48, pp. 489-499.

Cox, K.G., Bell, J.D., Pankhurst, R.J., 1979. *The interpretation of igneous rocks. George Allen & Unwin,* London.

Science Education Resource Centre @ Carleton College., 2012. *Geochemical Instrumentation and Analysis.* [Online] Available at: serc.carleton.edu/research_education/geochemsheets/techniques/Empa.html [Accessed 02 June 2016].

Davis, D. W., Hirdes, W., Schaltegger and Nunoo, E. A., 1994. U-Pb age constraints on deposition and provenance of Birimian and gold-bearing Tarkwaian sediments in Ghana, West Africa. *Precambrian Research,* Volume 67, pp. 89-107.

de Kock, G. S., Armstrong, R. A., Siegfried, H. P. and Thomas, E., 2010. Geochronology of the Birim Supergroup of the West African craton in the Wa-Bolé region of west-central Ghana: Implications for the stratigraphic framework. *Journal of African Earth Sciences.*

De Waele, B., Lacorde, M., Vergara, F. and Chan, G., 2015. New insights on proterozoic tectonics and sedimentation along the peri- Gondwanan West African margin based on zircon U–Pb SHRIMPgeochronology. *Precambrian Research,* Volume 259, pp. 156-175.

Debat, P., Nikiema, S., Mercier, A., Lompo, M., Beziat, D., Bourges, F., Roddaz, M., Salvi, S., Tollon, F., Wenmenga, U., 2003.A new metamorphic constraint for the Eburnean orogeny from Paleoproterozoic formations of the Man shield (Aribinda and Tampelga countries, Burkina Faso). *Precambrian Research,* Volume 123, p. 47–65.

Deer, W. A., Howie, R. A. and Zussman, J., 2013. *Introduction to the Rock Forming Minerals.* 2nd ed. England: ELBS.

Dentith, M., Mudge, S.T., 2014. *Geophysics for the Mineral Exploration Geoscientist.* Cambridge: Cambridge University Press.

Doumbia, S., Pouclet, A., Kouamelan, A., Peucat, J.J., Vidal, M., Delor, C., 1998.Petrogenesis of juvenile-type Birimian (Paleoproterozoic) granitoids in Central Cote-d'Ivoire, West Africa: geochemistry and geochronology. *Precambrian Research,* Volume 87, pp. 33-63.

Egal, E., Thieblemont, D. and Lahondere, D., 2002. Late Eburnean granitization and tectonics along the western and northwestern margin of the Archean Kenema–Man domain (Guinea, West African Craton). *Precambrian Research,* Volume 117, pp. 57-84.

Eglinger, A., Thebaud, N., Zeh, A., Davis, J., Miller, J., Parra-Avila, L.A., Loucks, R., McCuaig, C., Belousova, E., 2017. New insights into the crustal growth of the Paleoproterozoic margin of the Archean Kemena-Man domain, West African craton (Guinea): implications for gold mineral system. *Precambrian Research*, Volume 292, pp.258-289.

Eglinger, A., Thébaud, N., Davis, J., Miller, J., Zeh, A., McCuaig, C., Belousova, E., 2015. High-K to shoshonitic magmatism across the northern Archean Kéména Man margin (Guinea): Implications for the Eburnean orogenic gold mineralizations. *Postdoctoral research of Aurélien Eglinger,* Centre for Exploration Targeting; The University of Western Australia, Perth, WA 6009, Australia. GeoRessources, UMR 7359, CNRS-CREGU-Université de Lorraine, Nancy, France.

Eisenlohr, B.N. and Hirdes, W., 1992. The structural development of the early Proterozoic Birimian and Tarkwaian rocks of southwest Ghana, West Africa. *Journal of African Earth Sciences,* 14(3), pp. 313-325.

Ernst, R.E., 2014. Large Igneous Provinces. *Cambridge University Press,* Volume 653.

Ernst, R.E., Bleeker, W., Soderlund, U. and Kerr, A. C., 2013. Large Igneous Provinces and supercontinents: toward completing the plate tectonic revolution. *Lithos,* Volume 174, pp. 1-14.

Ernst, R.E., Jowitt, S.M., 2013. Large Igneous Provinces (LIPs) and Metallogeny. *Society of Economic Geologist Incorporated,* Special publication 17, pp. 17-51.

Feybesse, J.L., Billa, M., Guerrot, C., Duguey, E., Lescuyer, J.-L., Milesi, J.-P., Bouchot, V., 2006. The paleoproterozoic Ghanaian province: Geodynamic model and ore controls, including regional stress modeling. *Precambrian Research,* Volume 149, pp. 149-196.

Feybesse, J. L., Milesi, J.-P., Ouedraogo, M. F., Prost, A., 1990. La ceinture de Boromo-Goren (Burkina-Faso), un exemple d'interfrrence entre deux phases transcurrentes 6burn6ennes.. *Sciences de la Terre et des Planetes,* Volume 310, pp. 1353-1360.

Feybesse, J.-L. and Milesi, J.-P., 1994. The Archaean/Proterozoic contact zone in West Africa: a mountain belt of d6collement thrusting and folding on a

continental margin related to 2.1 Ga convergence of Archaean cratons?. *Precambrian Research,* Volume 69, pp. 199-227.

Fontaine, A., Eglinger, A., Ada, K., Andre-Mayer, A-S., Reisberg, L., Siebenaller, L., Le Migot, E., Ganne, J., Poujol, M., 2017. Geology of the world-class Kiaka polyphase gold deposit,West African Craton, Burkina Faso. *Journal of African Earth Sciences,* Volume 126, pp. 96-122.

Fu Yuan, W. U., 2010. Geochemical applications of in situ isotopic analyses by laser ablation. *Geochemical News,* Volume 143, pp. 1-16.

Ganne, J., De Andrade, V., Weinberg, R., Dubacq, B., Vidal, O., Kagambega, N., Naba, S., Baratoux, L., Jessell, M., Allibone, J., 2011. Modern-style plate subduction preserved in the PalaeoproterozoicWest African craton. *Nature Geoscience,* Issue 5, pp. 60-65.

Ganne, J., Gerbault, M. and Block, S., 2014. Thermo-mechanical modeling of lower crust exhumation—Constraints from the metamorphic record of the Palaeoproterozoic Eburnean orogeny, West African Craton. *Precambrian Research,* Volume 243, pp. 88-109.

Gasquet, D., Barbey, P., Adou, M. and Paquette, J., 2003. Structure, Sr–Nd isotope geochemistry and zircon U–Pb geochronology of the granitoids of the Dabakala area (Cote d'Ivoire): evidence for a 2.3 Ga crustal growth event in the Palaeoproterozoic of West Africa?. *Precambrian Research ,* Volume 127, pp. 329-354.

Gill, R., 2010. *Igneous Rocks and Processes.* London: Wiley- Blackwell.

Gueye, M., Ngom, P.M., Diene, M., Thiam, Y., Siegesmund, S., Wemmer ,K., Pawlig, S., 2008. Intrusive rocks and tectono-metamorphic evolution of the Mako Palaeoproterozoic belt (Eastern Senegal, West Africa). *Journal of African Earth Sciences*, Volume 50, pp. 88-110.

Hastings, D. A., 1982. On the tectonics and metallogenesis of West Africa: A model incorporating new geophysical data*. *Geoexplorution,* Volume 20, pp. 295-327.

Hein, K. A. A., 2010. Succession of structural events in the Goren greenstone belt (Burkina Faso): Implications for West African tectonics. *Journal of African Earth Sciences,* Volume 56, pp. 83-94.

Hein, K. A. A., 2016. The Bagassi gold deposits on the eastern margin of the Houndé greenstone belt, Burkina Faso. *Ore Geology Reviews,* Volume 78, pp. 660-666.

Hein, K.A.A., Morel, V., Kagoné, O., Kiemde, F., Mayes, K., 2004. Birimian lithological succession and structural evolution in the Goren segment of the Boromo–Goren Greenstone Belt, Burkina Faso. *Journal of African Earth Sciences,* Volume 39, pp. 1-12.

Hein, K. A. A. and Tshibubudze, A., 2016. Manganese deposits of the Oudalan province in the northeast of Burkina Faso, and Ansongo Inlier in eastern Mali. *Ore Geology Reviews,* Volume 78, pp. 645-651.

Hirdes, W., Davis, D. W., Ludtke, G. and Konan, G., 1996. Two generations of Birimian (Paleoproterozoic) volcanic belts in northeastern C6te d'Ivoire (West Africa): consequences for the 'Birimian controversy'. *Precambrian Research,* Volume 80, pp. 173-191.

Hottin, G. and Ouedrago, O. F., 1992. Carte Géologique du Burkina Faso, second edition. *Bureau de Recherches Géologique et Miniéres, Burkina Faso,* Volume 2.

Hout, D., Sattran, V. and Zida, P., 1987. Gold in Birrimian Greenstone Belts of Burkina Faso, West Africa. *EconomicG eology,* Volume 82, pp. 2033-2044.

Huhma, H., Mantarri, I., Peltonen, P., Kontinen, A., Halkoaho, T., Hanski, E., Hokkanen, T., Holtta, P., Juopperi, HThe age of the Archean greenstone belts in Finland. *Geological Survey of Finland, Special Paper,* Volume 54, pp. 74-175.

Irvine, T. N. and Baragar, W. R. A., 1971. A guide to the chemical classification of the common volcanic rocks. *Canadian Journal of Earth Sciences,* 8(5), pp. 523-548.

Jackson, S. E., Pearson, N. J., Griffin, W. L. and Belousova, 2004. The application of laser ablation-inductively coupled plasma-mass spectrometry to in situ U–Pb zircon geochronology. *Chemical Geology,* Volume 211, pp. 47-69.

Jessell, M., Santoul, J., Baratoux, L., Youbi, N., Ernst, R E., Metelka, V., Miller, J., Perrouty, S., 2015. An updated map of West African mafic dykes. *Journal of African Earth Sciences,* Volume 112, pp. 440-450.

Junner, N. R., 1940. Geology of the Gold Coast and Western Togoland. *Gold Coast Geological Survey-Accra Bulletin,* Volume 11, pp. 40.

Klemd, R., Oberth€ur, T., Ouedrago, A., 1997. Gold-telluride mineralization in the Birimian at Diabatou, Burkina Faso. *Journal of African Earth Sciences*, Volume 24, pp. 227–239.

Klemd, R., Hunken, U. and Olesch, M., 2002. Metamorphism of the country rocks hosting gold–sulfide-bearing quartz veins in the Paleoproterozoic southern Kibi-Winneba belt (SE-Ghana). *Journal of African Earth Sciences,* Volume 35, pp. 199-211.

Koffi, Y. H., Wenmenga, U. and Djro, S. C., 2016. Tarkwaian Deposits of the Birimian Belt of Houndé: Petrological, Structural and Geochemical Study (Burkina-Faso, West Africa). *International Journal of Geosciences,* Volume 7, pp. 685-700.

Kouamelan, A. N. et al., 2015. The oldest rock of Ivory Coast. *Journal of African Earth Sciences,* Volume 103, pp. 65-70.

Kouamelan, A.N., Kra, K.S.A., Djro, S.C., Paquette, J-L., Peucat, J-J., 2017. The Logouale Band: A large Archean crustal block in the Kenema-Man domain (Man-Leo rise, West African Craton) remobilized during Eburnean orogeny (2.05 Ga). *Journal of African Earth Sciences,* pp. 1-8.

Kribek, B., Sykorova, I., Machovic, V. and Laufek, F., 2008. Graphitization of organic matter and fluid-deposited graphite in Palaeoproterozoic (Birimian) black shales of the Kaya-Goren greenstone belt (Burkina Faso, West Africa). *Journal of Metamorphic Geology,* Volume 26, pp. 937-958.

Lambert-Smith, J.S., Lawrence, D.M., Muller, W., Treloar, P.J., 2016. Palaeotectonic setting of the south-eastern Kédougou-Kéniéba Inlier, West Africa: New insights from igneous trace element geochemistry and U-Pb zircon ages. *Precambrian Research*, Volume 274, pp. 110-135. 10.1016/j.precamres.2015.10.013 file.

Le Pape, F., Jones, A.G., Jessell, M., Hogg, C., Siebenaller, L., Toure, A., Boran, G., Ouiya, P., Mahamud, A., 2014. Preliminary 2D results from a Magnetotelluric survey crossing Burkina Faso and Ghana as part of the WAXI project. *Extended Abstract, 22nd EM Induction Workshop: Weimar, Germany, August 24-30, 2014.*

Leube, A., Hirdes, H. W., Mauer, R. and Kesse, G. O., 1990. The Early Proterozoic Birimian Supergroup of Ghana and Some Aspects of its Associated Gold Mineralization. *Precambrian Research,* Volume 46, pp. 139-165.

Lister, G. S. and Snoke, A. W., 1984. S-C Mylonites. *Journal of Structural Geology,* 6(6), pp. 617-638.

Lompo, M., 2009. Geodynamic evolution of the 2.25–2.0 Ga Palaeoproterozoic magmatic rocks in the Man-Leo Shield of the West African Craton. A model of subsidence of an oceanic plateau. *Palaeoproterozoic Supercontinents and Global Evolution- Geological Society, London, Special Publications,* Volume 323, pp. 231-254.

Lompo, M., 2010. Paleoproterozoic structural evolution of the Man-Leo Shield (West Africa). Key structures for vertical to transcurrent tectonics. *Journal of African Earth Sciences,* Volume 58, pp. 19-36.

Metelka, V., Baratoux, L., Naba, S. and Jessell, M. W., 2011. A geophysically constrained litho-structural analysis of the Eburnean greenstone belts and associated granitoid domains, Burkina Faso, West Africa. *Precambrian Research,* Volume 190, pp. 48-65.

Middlemost, A.K., 1994. Naming materials in the magma/igneous rock system. *Earth-Science Reviews*. Volume 37, pp. 215-224.

Milesi, J.P., Feybesse, J.L., Pinna, P., Deschamps, Y., Kampunzu, H., Muhongo, S., Lescuyer, J.L., Le Goff, E., Delor, C., Billa, M., Ralay, F., Heinry, C., 2004. Geological map of Africa 1:10,000,000, SIGAfrique project.. *20th Conference of African Geology, BRGM, Orléans, France,* 2-7 June accessed 2016-2017. http://www.sigafrique.net.

Milesi, J.-P., Ledru, P., Feybesse, J.-L., Dommanget, A., Marcoux, E., 1992. Early Proterozoic ore deposits and tectonics of the Birimian orogenic belt, West Africa. *Precambrian Research,* Volume 58, pp. 305-344.

Milesi, J.P., Feybesse, J.L., Ledru, P., Dommanget, A., Ouedraogo, M.F., Marcoux, E., Prost, A., Vinchon, C., Sylvain, J.P., Johan, V., Tegyey, M., Calvez, J.Y., Lagny, P., 1989. Minéralisations aurifères de l'Afrique de l'ouest leurs relations avec l'évolution litho-structurale au Protérozoïque inférieur. *Chronique de la Recherche Minièrre; Carte géologique au 1:2.000.000.,* Volume 497, pp. 3-98.

Milesi, J.P., Ledru, P., Ankrah, P., Johan, V., Marcoux, E., Vinchon, C., 1991. The metallogenic relationship between Birimian and Tarkwaian gold deposits in Ghana. *Mineral. Deposita,* Volume 26, pp. 228-238.

Mumin, A. H., Fleet, M. E. and Longstaffe, F. J., 1996. Evolution of hydrothermal fluids in the Ashanti gold belt, Ghana: stable isotope geochemistry of carbonates, graphite and quartz. *Economic Geology,* Volume 91, pp. 135-148.

Naba, S., Lompo, M., Debat, P., Bouchez, J.L., Beziat, D., 2004. Structure and emplacement model for late-orogenic Paleoproterozoic granitoids: the Tenkodogo–Yamba elongate pluton (Eastern Burkina Faso). *Journal of African Earth Sciences,* Volume 38, pp. 41-57.

Oberthur, T., Schmidt M.A., Vetter, U., Simon, K., Amanor, J.A.., 1996. Gold mineralization in the Ashanti Belt of Ghana: genetic constraints of stable isotope geochemistry.. *Economic Geology,* Volume 91, pp. 289-301.

Ouedraogo, B. I., Levermore, G. J. and Parkinson, J. B., 2012. Future energy demand for public buildings in the context of climate change for Burkina Faso. *Building and Environment,* Volume 49, pp. 270-282.

Parra-Avila, L.A., Belousova, E., Fiorentini, M.L., Baratoux, L., Davis, J., Miller, J., McCuaig, T.C., 2016. Crustal evolution of the Paleoproterozoic Birimian terranes of the Baoulé-Mossi domain, southern West African Craton: U–Pb andHf-isotope studies of detrital zircons. *Precambrian Research,* Volume 274, pp. 25-60.

Parra-Avila L.A., Bourassa, Y., Miller, J., Perrouty, S., Fiorentini, M.L., McCuaig, T.C., 2015. Age constraints of the Wassa and Benso mesothermal gold deposits, Ashanti Belt, Ghana, West Africa. *Journal of African Earth Sciences,* Volume 112, pp.524-535.

Passchier, C. W. and Trouw, R. A. J., 2005. *Microtectonics.* 2 ed. Germany: Springer.

Pawlig, S., Gueye, M. and Klischies, R., 2006. Geochemical and Sr-Nd isotopic data on the Birimian of the Kedougou-Kenieba Inlier (Eastern Senegal): Implications on the Palaeoproterozoic evolution of the West African Craton. *South African Journal of Geology,* Volume 109, pp. 411-427.

Pearce, J., 1996. Sources and Settings of Granitic Rocks. *Episodes,* 19(4), pp. 120-125.

Pearce, J. A., Harris, N. B. W. and Tindle, A. G., 1984. Trace element discrimination diagrams for the tectonic interpretation of granitic rocks. *Journal of Petrology,* Volume 25, pp. 956-983.

Perrouty, S., Ailleres, L., Jessell, M.W., Baratoux, L., Bourassa, Y., Crawford, B., 2012. Revised Eburnean geodynamic evolution of the gold-rich southern Ashanti Belt, Ghana, with new field and geophysical evidence of pre-Tarkwaian deformations. *Precambrian Research,* Volume 204-205, pp. 12-39.

Petersson, A., Schersten, A., Kemp, A.I.S., Kristinsdottir, B., Kalvig, P., Anum, S., 2016. Zircon U–Pb–Hf evidence for subduction related crustal growth and reworking of Archaean crust within the Palaeoproterozoic Birimian terrane, West African Craton, SE Ghana. *Precambrian Research ,* Volume 275, pp. 286-309.

Pidgeon, R. T., 1992. Recrystallisation of oscillatory zoned zircon: some geochronological and petrological implications*. *Contributions to Mineralogy and Petrology,* Volume 110, pp. 463-472.

Pigois, J.P., Groves, D.I., Fletcher, I.R., McNaughton, N.J., Snee, L.W., 2003. Age constraints on Tarkwaian palaeoplacer and lode-gold formation in the Tarkwa-Damang district, SW Ghana. *Mineralium Deposita,* Volume 38, pp. 695-714.

Pons, J., Barbey, P., Dupuis, D. and Leger, J. M., 1995. Mechanisms of pluton emplacement and structural evolution of a 2.1 Ga juvenile continental crust: the Birimian of southwestern Niger. *Precambrian Research,* Volume 70, pp. 281-301.

Roddaz, M., Debat, P. and Nikiema, S., 2007. Geochemistry of Upper Birimian sediments (major and trace elements and Nd–Sr isotopes) and implications for weathering and tectonic setting of the Late Paleoproterozoic crust. *Precambrian Research,* Volume 159, pp. 197-211.

Rollinson, H. R., 1993. *Using Geochemical Data: Evaluation, Presentation, Interpretation.* England: Prentice Hall.

Roncoli, C., Ingram, K. and Kirshen, P., 2002. Reading the Rains: Local Knowledge and Rainfall Forecasting in Burkina Faso. *Society and Natural Resources,* Volume 409, pp. 409-427.

Roncoli, C., Jost, C., Kirshen, P., Sanon, M., Ingram, K.T., Woodin, M., Some, L., 2009. From accessing to assessing forecasts: an end-to-end study of

participatory climate forecast dissemination in Burkina Faso (West Africa). *Climatic Change,* Volume 92, pp. 433-460.

Shand, S. J., 1943. *The Eruptive Rocks.* 444 ed. New York: John Wiley.

Sibson, R. H., 1996. Structural permeability of fluid-driven fault-fracture meshes. *Journal of Structural Geology,* 18(8), pp. 1031-1042.

Stern, R.A., Bodorkos, S., Kamo, S.L., Hickman, A.H., Corfu, F., 2009. Measurement of SIMS Instrumental Mass Fractionation of Pb Isotopes during zircon dating. *Geostandards and Geoanalytical Research,* 33(2), pp. 145-168.

Sylvester, J. and Attoh, K., 1992. Lithostratigraphy and Composition of 2.1 Ga Greenstone Belts of the West African Craton and Their Bearing on Crustal Evolution and the Archean-Proterozoic Boundary. *The Journal of Geology,* Volume 4, pp. 377-393.

Thieblemont, D., Goujou, J.C., Egal, E., Cocherie, A., Delor, C., Lafon, J.M., Fanning, C.M., 2004. Journal of African Earth. *Archean evolution of the Leo Rise and its Eburnean reworking,* Volume 39, pp. 97-104.

Tshibubudze, A. and Hein, K. A. A., 2013. Structural setting of gold deposits in the Oudalan-Gorouol volcanosedimentary belt east of the Markoye Shear Zone, West African Craton. *Journal of African Earth Sciences,* Volume 80, pp. 31-47.

Tshibubudze, A., Hein, K. A. A. and Marquis, P., 2009. The Markoye Shear Zone in NE Burkina Faso. *Journal of African Earth Sciences,* Volume 55, pp. 245-256.

Tshibubudze, A., Hein, K. A. A. and McCuaig, T. C., 2015. The relative and absolute chronology of strato-tectonic events in the Gorom-Gorom granitoid terrane and Oudalan-Gorouol belt, northeast Burkina Faso. *Journal of African Earth Sciences,* Volume 112, pp. 382-418.

Tshibubudze, A., Hein, K.A.A., Peters, L.F.H., Woolfe, A.J., McCuaig, T.C., 2013. Oldest U-Pb Crystallization Age For The West African Craton From The Oudalan-Gorouol Belt Of Burkina Faso. *South African Journal of Geology,* Volume 116, pp. 169-181.

Tunks, A. J., Selley, D., Rogers, J. R. and Brabham, G., 2004. Vein mineralization at the Damang Gold Mine, Ghana: controls on mineralization. *Journal of Structural Geology,* Volume 26, pp. 1257-1273.

Vearncombe, J. and Zelic, M., 2015. Structural Paradigms for Gold: Do They Help Us Find and Mine?. *Applied Earth Science,* 124(1), pp. 2-19.

West Africa Exploration Initiative, 2016. *Waxi2.* [Online] Available at: http://www.waxi2.org/ [Accessed 26 February 2016].

Vegas, N., Naba, S., Bouchez, J.L., Jessell, M., 2007. Structure and emplacement of granite plutons in the Palaeoproterozoic crust of Eastern Burkina Faso: rheological implications. *Int. J. Earth Sci. (Geol Rundsch)*, Volume 97, pp. 1165-1180.

White, S.H., Burrows, S.E., Carreras, J., Shaw, N.D., Humpphreys, F.J., 1980. On mylonites in ductile shear zones. *Journal of Structural Geology,* 2(1), pp. 175-187.

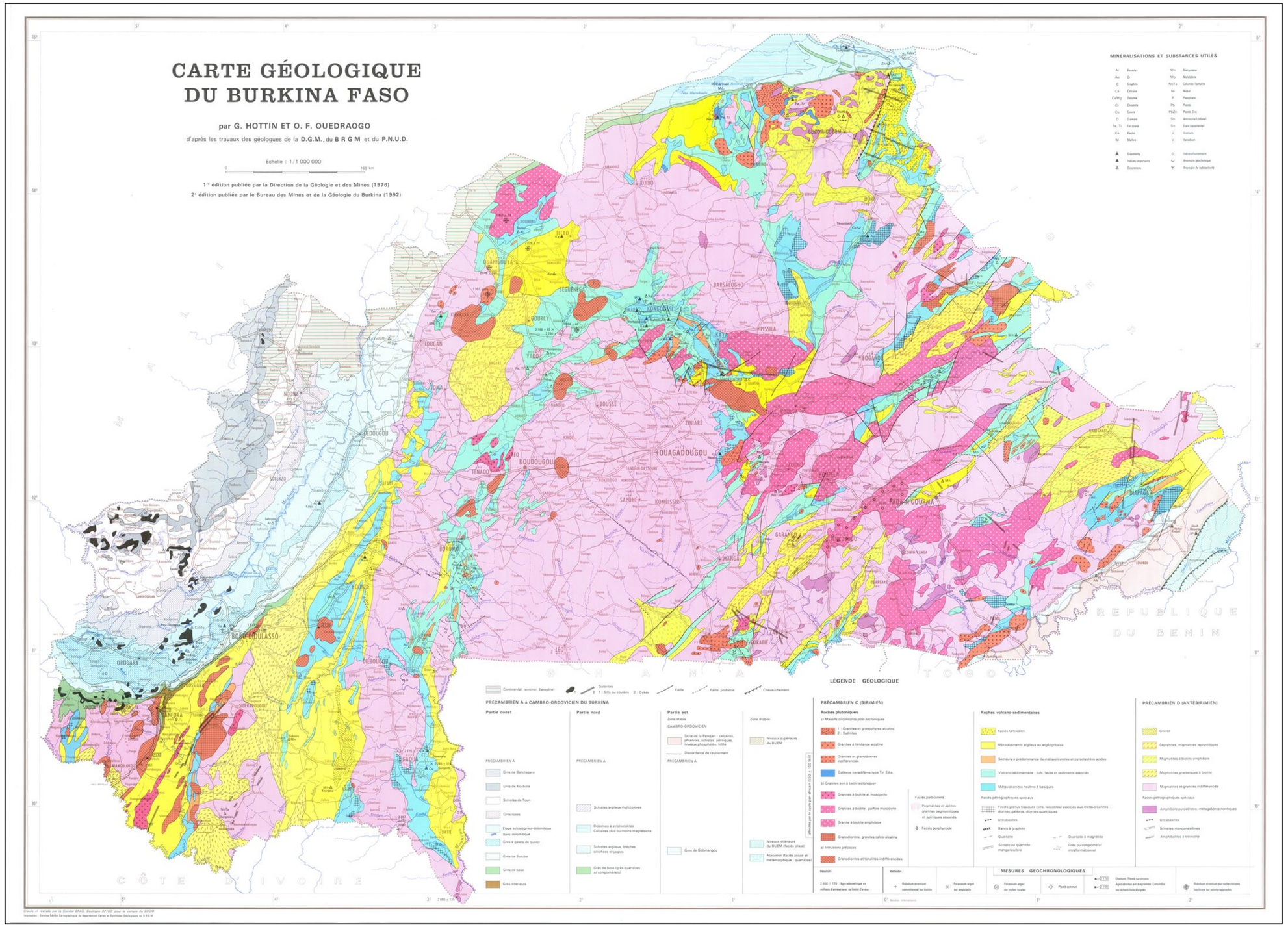
Wilson, A.H., Zeh, A., 2015. Zircon U-Pb age data and Hf isotopic signature of Kaapvaal Basement Granitoids from the Archean white Mfolozi inlier, Northern Kwa-Zulu Natal. *South african Journal of Geology,* 118(4), pp. 473-488.

Wise, D.U., Dunn, D.E., Engelder, J.T., Geiser, P.A., Hatcher, R.D., Kish, S.A., Odom, L.A., Schamel, S., 1984. Fault-related rocks: Suggestions for terminology. *Geology,* Volume 12, pp. 391-394.

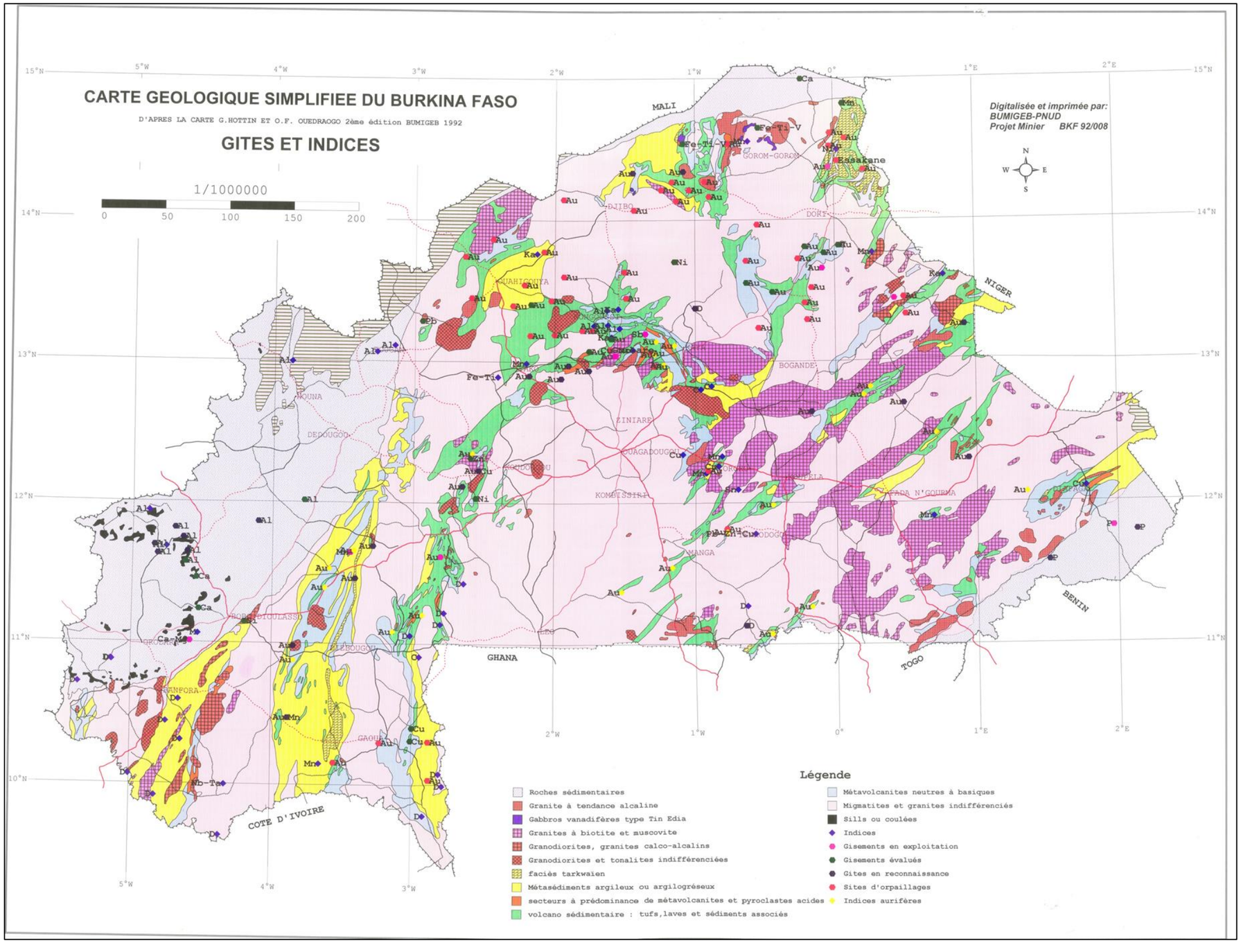
Yuanbao, W. and Yongfei, Z., 2004. Genesis of zircon and its constraints on interpretation of U-Pb age. *Chinese Science Bulletin,* 49(50), pp. 1554-1569.

APPENDIX A

1:1 000 000 Geological Map (BRGM, 1992)

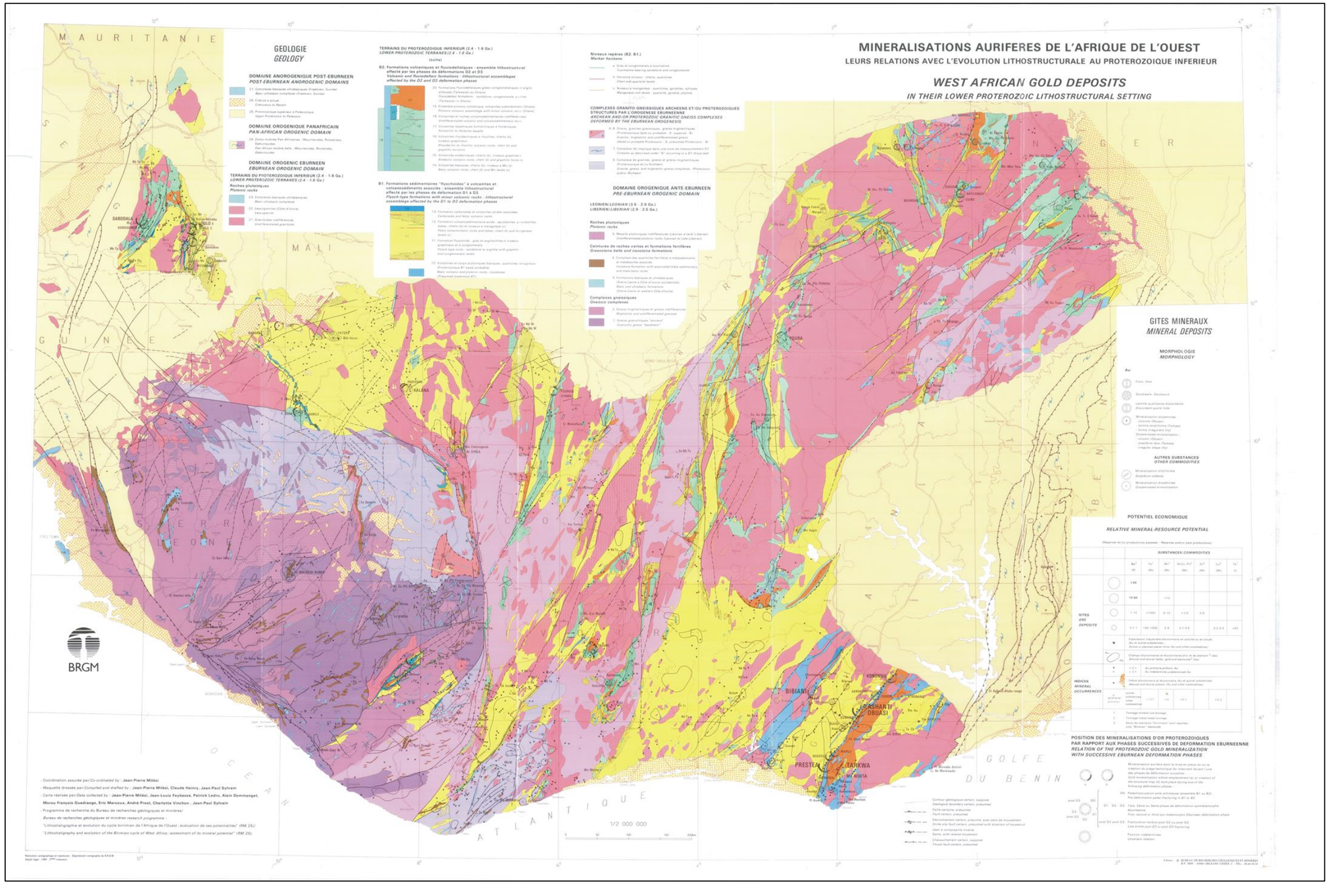


APPENDIX B
1:1 000 000 Geological Map (BUMIGEB, 1992)



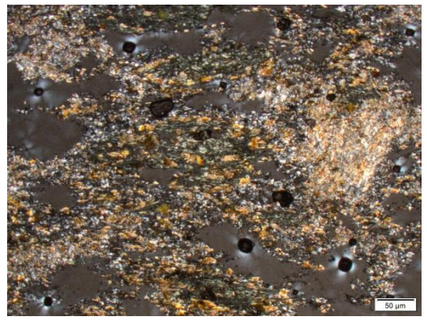
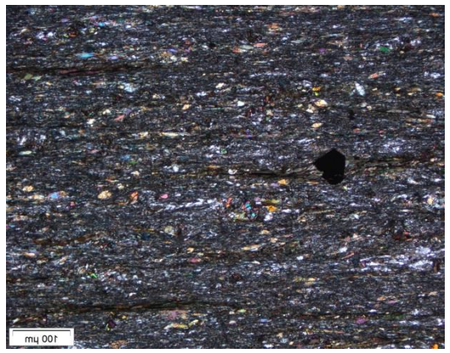
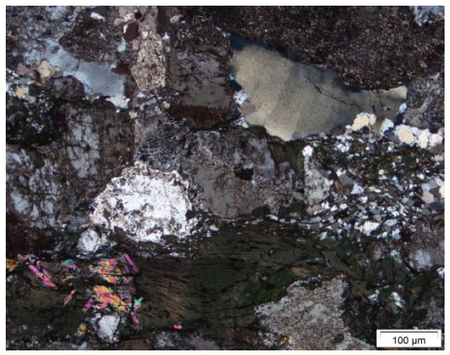
APPENDIX C

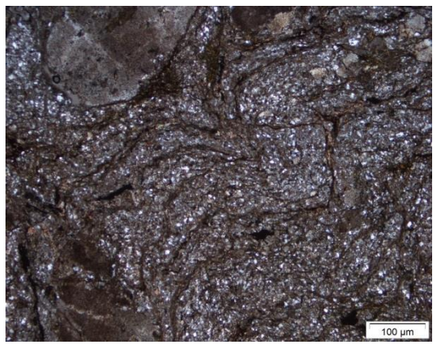
1:2 000 000 Geological Map (BRGM, 1992)

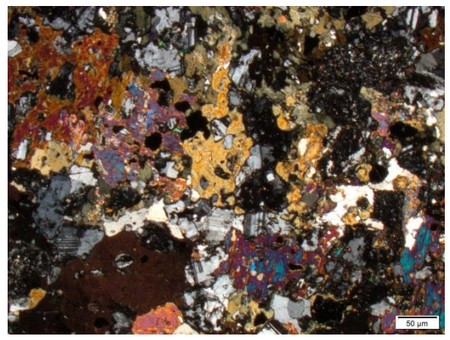
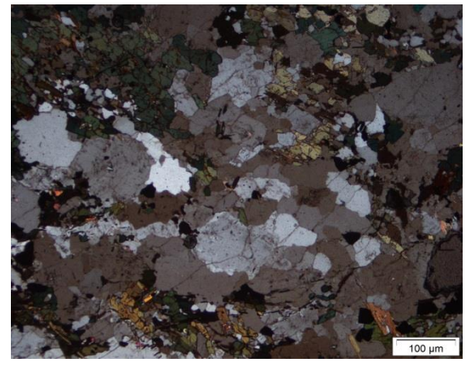


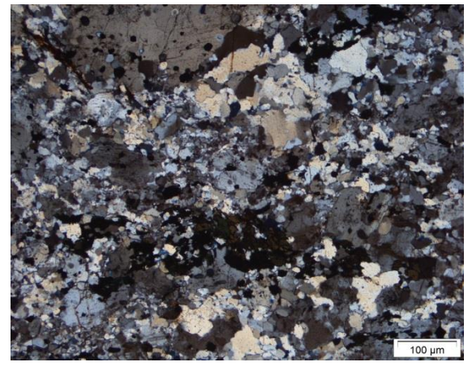
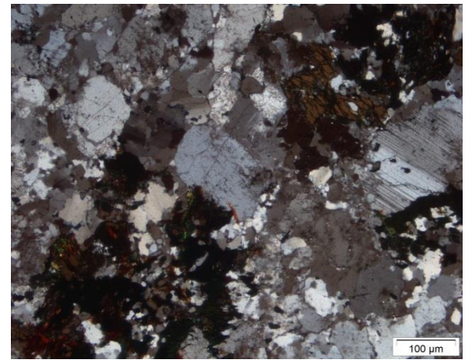
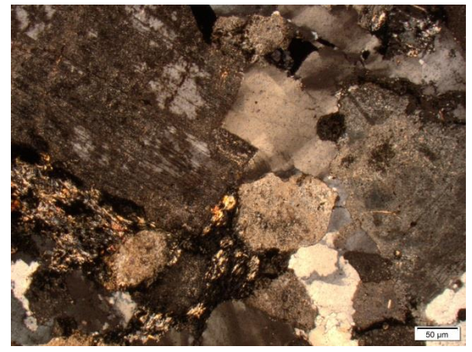
APPENDIX D

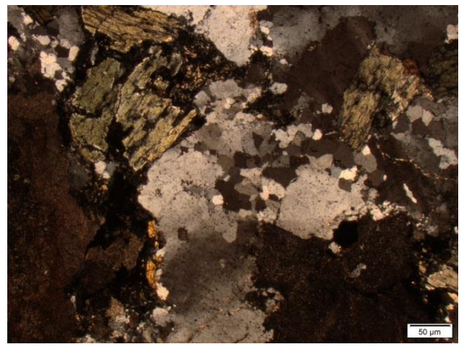
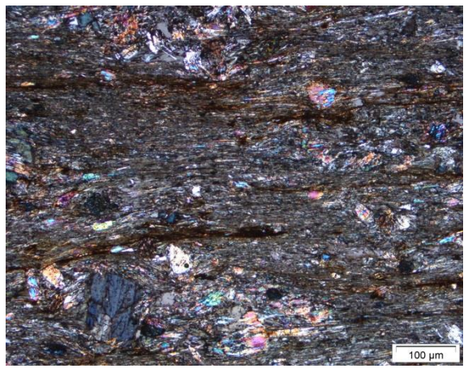
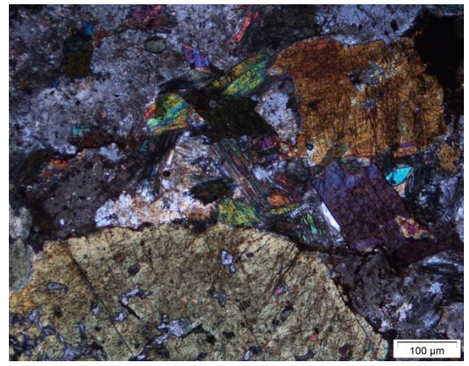
Petrographic Descriptions

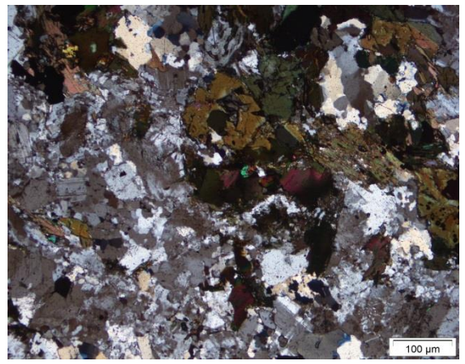
Sample no.	Northing	Easting	Modal Minerology	Rock type	Fabrics	Photomicrograph
GP002	1382546.00	260624.00	Biotite 30% Hornblende 30% Quartz 20% Feldspar 10% Muscovite 10%	Schist/Phyllite	Strongly foliated; foliation defined by biotite and hornblende.	
GP004	1390957.00	259223.00	Chlorite 40% Muscovite 30% Biotite 20% Quartz 10% Minor Sulphides (Pyrite)	Schist	Foliation defined by micas and chlorite.	
GP006	1392423.00	259182.00	Quartz 65% K-feldspar 20% Hornblende 15% Minor Epidote	Quartz Diorite/Granodiorite	Equigranular. No foliation.	

GP009	**1389476.00**	**257171.00**	**Matrix 40% Feldspars 30% Quartz 30%**	**Proto-mylonite**	**Micro-folds; shear bands; weak foliation.**	
GP010	**1393819.00**	**264871.00**	**Matrix 70% Feldspars 20% Quartz 10%**	**Mylonite**	**Micro-folds; shear bands; weak foliation.**	
GP011	**1393811.00**	**264869.00**	**Quartz and feldspar sub-angular clasts; fine grained matrix**	**Meta-Volcanoclastic Greywacke**	**No fabric.**	

GP014	**1396359.00**	**262123.00**	**Pyroxenes 65% (augite, enstatite) Feldspars 15% Olivine 5% Secondary Quartz 5%**	**Pyroxenite**	**Mega-crystic texture; no fabrics.**	
GP016	**1396451.00**	**262883.00**	**Pyroxenes 30% Hornblende 30% Plagioclase 20% K-feldspar 10% Epidote 10%**	**Gabbro**	**No fabric; medium to coarse grained.**	
GP026	**1387792.00**	**270208.00**	**Plagioclase 40% K-feldspar 30% Quartz 15% Hornblende 10% Biotite 5% ± minor pyroxenes**	**Granodiorite**	**Weak to no foliation.**	

GP027	**1388876.00**	**273432.00**	**Plagioclase 40%** **K-feldspar 30%** **Hornblende 20%** **Quartz 10%**	**Granite Gneiss**	**Weak to no foliation.**	
GP028	**1389276.00**	**274567.00**	**K-feldspar 40%** **Plagioclase 30%** **Quartz 10%** **Hornblende 10%** **Biotite 10%** **± minor Muscovite**	**Granite**	**Weak to no foliation.**	
GP029	**1400621.00**	**269173.00**	**Plagioclase 40%** **K-feldspar 40%** **Quartz 10%** **Pyroxene 5%** **Chlorite 5%**	**Gabbro/Tonalite**	**Equigranular. No foliation.**	

GP032	**1400869.00**	**269376.00**	**K-feldspar 40% Plagioclase 25% Quartz 15% Hornblende 10% Chlorite 10%**	**Alkali-Feldspar Granite**	**Seriate texture with coarse grained K-feldspar grains; no fabrics**	
GP037	**1384334.00**	**253697.00**	**Biotite 30% Muscovite 30% Chlorite 20% Quartz 10% Plagioclase 10%**	**Schist**	**Foliation defined by micas; rotated quartz and feldspar clasts.**	
GP038	**1378125.00**	**268005.00**	**Pyroxenites 80% Feldspars 10% Secondary Quartz 10%**	**Pyroxenite**	**Mega-crystic texture; no fabrics.**	

GP043	**1387448.00**	**273712.00**	**Plagioclase 30% Hornblende 20% K-feldspar 20% Quartz 20% Biotite (and minor Muscovite) 10%**	**Granodiorite**	**No fabric, medium grained. Minor pyrite in composition.**	

APPENDIX E

Field Dataset Sample

AZMTH- Azimuth; DIP DIR- Dip direction; LIN- Lineation; PLNG- Plunge; SMPL NO.- Sample number; StP- Station Point; STR- Strike.

StP	Date	Zone	NORTH-ING	EASTING 31 P	HOST ROCK TYPE	CHARACTER	S1 STR	S1 DIP	S1 DIP DIR	S2 STR	S2 DIP	S2 DIP DIR	LIN AZMTH	LIN PLNG	SMPL NO.	GEOCHONOLOGY	GEOCHEMISTRY	THIN SECTION
Gourma 2016																		
1	09/04/2016	31P	1382389.00	259554.00	Buck Quartz Vein	Tourmaline+Ankerite												
2	09/04/2016	31P	1382484.00	259618.00	Buck Quartz Vein	Tourmaline+Ankerite	64	52	SE						GP001			
3	09/04/2016	31P	1382778.00	259695.00	Schist	Chlorite+Muscovite	44	82	SE									
4	09/04/2016	31P	1382860.00	259689.00	Buck Quartz Vein	Tourmaline+Ankerite	36	80	NW									
5	09/04/2016	31P	1382163.00	260154.00	Buck Quartz Vein	Cross-cutting Chl+Musc Schist	36	40	SE									
6	09/04/2016	31P	1382467.00	260236.00	Schist	Chl-bt-muc-qtz	46	86	SE									
6	09/04/2016	31P	1382467.00	260236.00	Schist	Chl-bt-muc-qtz	26	80	SE	82	82	N						
7	09/04/2016	31P	1382477.00	260251.00	Schist	Chl+Musc, Silicified, Malachite, Qtz Veins	30	78	NW				278	74				
8	09/04/2016	31P	1382495.00	260259.00	Schist	Chl+Musc, Silicified, Malachite	24	72		68	88	N						
8	09/04/2016	31P	1382495.00	260259.00	Schist	Chl+Musc, Silicified, Malachite	24	72		82	80	S						
9	09/04/	31P	138259	260348.00	Schist	Chl-bt-muc-qtz	24	72										

	2016		8.00															
10	09/04/2016	31P	1382546.00	260624.00	Schist	Qtz+Chl+Musc+Feldspar	24	58							GP002 A+B			Yes
11	09/04/2016	31P	1383009.00	260773.00	Schist	Dark purple/grey min dominant	30	68	SE				22	10				
11	09/04/2016	31P	1383009.00	260773.00	Schist	Dark purple/grey min dominant?	32	70	SE				210	10				
12	09/04/2016	31P	1383106.00	260777.00	Schist	Chlorite+Muscovite with Fe-enrichment	40	60	SE				100	54				
12	09/04/2016	31P	1383106.00	260777.00	Schist	Chlorite+Muscovite with Fe-enrichment	40	60	SE				100	60				
12	09/04/2016	31P	1383106.00	260777.00	Schist	Chlorite+Muscovite with Fe-enrichment	40	62	SE				98	64				
13	09/04/2016	31P	1384293.00	262256.00	Siltstone/Schist Sequence	Meta-siltsone/Schist	30	68										
14	09/04/2016	31P	1385239.00	264242.00	Schist	Chlorite+Muscovite with Fe-enrichment, silicified	14	60	SE				98	58				
14	09/04/2016	31P	1385239.00	264242.00	Schist	Chlorite+Muscovite with Fe-enrichment, silicified	14	60	SE				98	60				
15	09/04/2016	31P	1385297.00	264251.00	Schist	Chlorite+Muscovite with Fe-enrichment, silicified												
16	09/04/2016	31P	1385278.00	264204.00	Basalt	Amygaloidal, schistosed	34	60	SE									
17	09/04/2016	31P	1385348.00	264290.00	Basalt	Schistosed, Meta-basalt												
18	09/04/2016	31P	1385380.00	264294.00	Basalt	Flow banding	10	68	SE									
18	09/04/2016	31P	1385380.00	264294.00	Basalt	Flow banding	14	50	SE									
19	09/04/2016	31P	1385392.00	264334.00	Buck Quartz Vein	Tourmaline												

20	09/04/2016	31P	1385370.00	264399.00	Basalt	Schistosed	10	70	E	286	88	N					
21	09/04/2016	31P	1385494.00	264305.00	Basalt	Schistosed, Meta-basalt	26	76	SE								
22	10/04/2016	31P	1386831.00	260045.00	Basalt	Highly mafic (tholeiitic), amygadloidal	20	88	NW	346	76	SW			GP003		
23	10/04/2016	31P	1389971.00	259456.00	Buck Quartz Vein	Ankerite (Fe-carbonate staining)				338	80	SW					
24	10/04/2016	31P	1390150.00	259323.00	Buck Quartz Vein	Ankerite (Fe-carbonate staining)	80	54	SE	322	88	W	222	30			
24	10/04/2016	31P	1390150.00	259323.00	Buck Quartz Vein	Ankerite (Fe-carbonate staining)							230	32			
25	10/04/2016	31P	1390957.00	259223.00	Schist	Chloritoid+Chlorite+ Muscovite	36	74	NW	310	82	W	24	14	GP004		Yes
25	10/04/2016	31P	1390957.00	259223.00	Schist	Chloritoid+Chlorite+ Muscovite+amphiboles	38	60	NW				30	12			
26	10/04/2016	31P	1391025.00	259218.00	Schist	Chloritoid+Chlorite+Muscovite+amphiboles	22	80	E	300			20	8			
27	10/04/2016	31P	1391035.00	259242.00	Schist	Chloritoid+Chlorite+Muscovite+sulphides	24	80	SE								
27	10/04/2016	31P	1391035.00	259242.00	Schist	Chloritoid+Chlorite+Muscovite+sulphides	20	84	SE								
28	10/04/2016	31P	1392047.00	259412.00	Dolerite Dyke	Dyke									GP005		
29	10/04/2016	31P	1392423.00	259182.00	Granitoid	Tonalitic composition	78	38	NW						GP006	Yes	Yes	Yes